Concentrated Solar Power on Demand

by

Daniel Shawn Codd

M.S. Mechanical Engineering
Stanford University, 1999

B.S. Mechanical Engineering
University of California, San Diego, 1997

SUBMITTED TO THE DEPARTMENT OF MECHANICAL ENGINEERING
IN PARTIAL FULFILLMENT OF THE REQUIREMENTS FOR THE DEGREE OF

DOCTORATE OF PHILOSOPHY

AT THE

MASSACHUSETTS INSTITUTE OF TECHNOLOGY

JUNE 2011

Signature of Author.....
Department of Mechanical Engineering
April 26, 2011

Certified by.....
Alexander H. Slocum
Pappalardo Professor of Mechanical Engineering
MacVicar Faculty Fellow
Thesis Supervisor

Accepted by.....
Professor David E. Hardt
Chairman, Department Committee on Graduate Students

Concentrated Solar Power on Demand

by

Daniel Shawn Codd

Submitted to the Department of Mechanical Engineering
on April 26, 2011 in Partial Fulfillment of the
Requirements for the Degree of Doctorate of Philosophy in
Mechanical Engineering

Abstract

This thesis describes a new concentrating solar power central receiver system with integral thermal storage. Hillside mounted heliostats direct sunlight into a volumetric absorption molten salt pool, which also functions as a single tank assisted thermocline storage system. Concentrated light penetrates the molten salt and is absorbed over a depth of several meters; the molten salt free surface tolerates high irradiance levels, yet remains insensitive to the passage of clouds. Thermal losses to the environment are reduced with a refractory-lined domed roof and a small, closeable aperture. The molten salt and cover provide high and low temperature heat sources that can be optimally used to maximize energy production throughout the day, even when the sun is not shining. Hot salt is extracted from the upper region of the tank and sent through a steam generator, then returned to the bottom of the tank. An insulated barrier plate is positioned vertically within the tank to enhance the natural thermocline which forms and maintain hot and cold salt volumes required for operation. As a result, continuous, high temperature heat extraction is possible even as the average temperature of the salt is declining.

Experimental results are presented for sodium-potassium nitrate salt volumetric receivers optically heated with a 10.5 kilowatt, 60-sun solar simulator. Designs, construction details and performance models used to estimate efficiency are presented for megawatt-scale molten salt volumetric receivers capable of operating with low cost nitrate or chloride salt eutectics at temperatures approaching 600 °C and 1000 °C, respectively. The integral storage capabilities of the receiver can be sized according to local needs, thereby enabling power generation on demand.

Thesis Supervisor: Alexander H. Slocum
Title: Pappalardo Professor of Mechanical Engineering, MacVicar Faculty Fellow

Table of contents

List of Figures

List of Tables

Nomenclature

Abbreviations:

CPC	Compound Parabolic Concentrator
CSP	Concentrating Solar Power
CSPonD	Concentrated Solar Power on Demand
DAR	Direct Absorption Receiver
DNI	Direct Normal Irradiance
FLC	Flow Line Concentrator
HTE	Heat Transfer Equation
HTF	Heat Transfer Fluid
IFB	Insulating Firebrick
NREL	National Renewable Energy Laboratory
RTE	Radiative Transfer Equation

Greek symbols:

α	absorptivity
α'	thermal diffusivity
β	attenuation coefficient
β'	coefficient of volumetric expansion
γ	rate of salt vaporization per unit area
δ	optical thickness
Δ	change of quantity
ε	emissivity
η	efficiency
θ	angle, non-dimensional temperature
κ	absorption coefficient
λ	wavelength
ν	kinematic viscosity
ξ	tank (conduction) storage efficiency
ρ	reflectivity, density
σ	Stefan-Boltzmann constant
σ_s	scattering coefficient
ϕ	beam-down angle
Φ	flux: solar radiation per unit area
Φ_λ^*	spectral scattering phase function
χ	exergetic efficiency
Ω	solid angle

Roman symbols:

A	area
c_p	specific heat
C	concentration ratio
D	diameter
$F_{1\text{-}2}$	view factor from surface 1 to surface 2
g	gravitational acceleration
h	convection coefficient
H	height, depth
ΔH_{vap}	enthalpy of vaporization of salt
i	$\sqrt{-1}$
I	intensity
I_λ	spectral irradiance
k	absorptive index, thermal conductivity
l	penetration depth
L	characteristic length, latent heat of fusion
m	complex index of refraction
n	refractive index
P	power
P	pressure
r	range distance
R	reflection coefficient, thermal resistance
Ra	Rayleigh number
Ri	Richardson number
Ste	Stefan number
t	time
T	temperature
v	velocity
V	absorber volume
q	heat flux
Q	heat flow rate

Subscripts:

λ	spectral
a	aperture
b	blackbody
c	cold
conv	convective
cos	cosine
crit	critical
decomp	decomposition
div	divider plate
e	electric
ele	parasitic electrical
eff	effective

eq	equivalent
h	hot
hx	heat exchanger/steam generator
i	incident
in	input
ip	illuminated pond
ir	infrared
l	lid
l-a	lid to aperture
m	mean
melt	melting
max	maximum
opt	optical
os	overshoot
p	nominal/design pond
p-a	pond to aperture
p-l	pond to lid
r	reflected
rad	radiative
rec	receiver
solid	solidified
sys	system
t	thermal, transmitted
vap	vaporization
vis	visible
0	initial
∞	ambient

Acknowledgments

"That's it! You people have stood in my way long enough. I'm going to clown college!"

- Homer Simpson

Initial support was provided by The Cyprus Institute, led by Prof. **C.N. Papanicolas** in Nicosia, Cyprus, for the Cogeneration of Electricity & Desalinated Sea Water using Concentrated Solar Power (CSP-DSW) study. This project was part of an interdisciplinary collaboration between The Cyprus Institute, Prof. **John G. Georgiadis**' group at the University of Illinois at Urbana-Champaign, the Electricity Authority of Cyprus and the Massachusetts Institute of Technology. The Chesonis Family Foundation provided generous funding through the MIT Energy Initiative for continuing research during the 2010-2011 academic year.

The work described in this dissertation would not have been possible without guidance and support from numerous individuals and institutions. I would like to thank my magnanimous advisor, committee chair and the CSPonD project Principal Investigator, Prof. **Alex Slocum**, for giving me the opportunity to contribute to a really hot and timely topic. Thanks, dude!

I'd also like to thank my cellmates in the Precision Engineering Research Group for creating an awesome lab environment, providing technical support, laughter and distractions all while juggling interesting projects of their own. Special thanks to PERGies **Danielle, Nevan, Zac & Conor**. I would like to acknowledge all the members of the MIT CSPonD team and associated student researchers, all of whom I gratefully acknowledge here with my sincere thanks:

Faculty and research staff:

J. Buongiorno, C. Forsberg, T. McKrell, A. Mitsos, J.C. Nave, A. Slocum (PI)

Postdoctoral researcher:

A. Ghobeity

Graduate students:

A. Lenert, C. Noone, S. Passerini, F. Rojas, V. Somani, C. Williams

Undergraduates:

A. Adames, J.R. Alvarado, A. Carlson, A. Paxson, J. Rees

I would also like to thank Prof. **Alexander Mitsos** and Prof. **Ronald Ballinger** for serving on my thesis committee and providing valuable insight and constructive critique throughout the duration of the project. Thanks to Dr. **Tom McKrell** and the NS&E Green Lab for housing the solar simulator. **John Barry**, President of Ajax Electric Co., PA; **John** and **Kevin O'Meara**, President and Manager of Metallurgical Solutions, Inc. RI and Dr. **Stephen Fantone**, President and CEO of Optikos Corp., MA, all provided much needed practical industrial wisdom regarding molten salt bath furnaces and optics. Additionally, I wish to thank Prof. **Jacob Karni** of the Weizmann Institute and Dr. **Robert Copeland**, formerly of the Solar Energy Research Institute (now NREL), for graciously sharing solar power receiver and thermal storage design experiences and lessons learned. I would also like to thank Dr. **Aris Bonanos** and Dr. **George Tzamis** for their technical contributions to the CSP-DSW study and hospitality showing me around Cyprus.

And of course, I'd like to thank my parents, sister, and my niece and nephews for their prayers and encouragement along the way.

Cambridge, Massachusetts, in April 2011

Danny Codd

In memory of my Grandpop,

whose sunbathing skills would have put
the world's best solar power collection systems to shame...

R.I.P. 1918-2010.

CHAPTER 1: Introduction

Motivation

Solar thermal power technologies offer much promise for satisfying global energy needs and can be used for "clean" power generation – but current solutions fail to be widely implemented due to their relative inefficiencies and high costs. Nevertheless, Concentrating Solar Power (CSP) is still considered one of the most promising technologies for large scale renewable power generation. In the southwestern United States alone, 45 CSP projects exceeding 11 GW_e are planned for development [1]. However, conventional designs are at best modestly efficient and resource intensive resulting in levelized costs of energy far exceeding fossil-powered plants. Widespread adoption to achieve aggressive goals, such as California's 33% Renewable Portfolio Standard prescribing 15-20 GW_e of renewable energy by 2020, will require advanced technology development and rapid deployment.

Solar Thermal Power

CSP technologies

A robust renewable energy portfolio is likely to include systems that enable energy storage with electricity production when there is limited sunlight. Conventional photovoltaic panels convert direct and diffuse sunlight into direct-current electricity, which can be inverted into alternating-current line voltages and frequencies (Fig. 1.1). However, instantaneous electrical output is directly related to the instantaneous sunlight, or solar insolation, striking the photovoltaic panel. Currently, storage of electrical energy for later use is costly and impractical at larger scales. In contrast, CSP systems use reflective or refractive optics to focus incoming direct sunlight onto an absorber. This absorber, or receiver, can achieve high temperatures and heat can be extracted for industrial or chemical processes, or to drive a heat engine and generate mechanical or electrical power. Energy storage is simplified by the use of sensible, latent or chemical heat storage means. CSP with thermal energy storage has the potential to produce

around-the-clock baseload power, or meet peak electric power demands, irrespective of instantaneous solar fluctuations.

Conventional high temperature CSP systems have evolved to utilize a central power tower, whereby mirrored heliostats focus sunlight on a receiver placed atop a tower, designed to reduce heliostat shadowing and increase optical efficiency. Point-focus systems can achieve high optical concentrations, typically greater than 600 'suns' (1 sun = 1 kW/m^2), resulting in high receiver temperatures and improved power cycle efficiencies relative to line-focus (e.g., parabolic trough, linear Fresnel) or non-concentrating solar collectors [2]. Central receiver systems allow for large, more efficient, centralized power conversion equipment and simplified thermal storage as compared to small distributed parabolic dish units (Fig. 1.2).

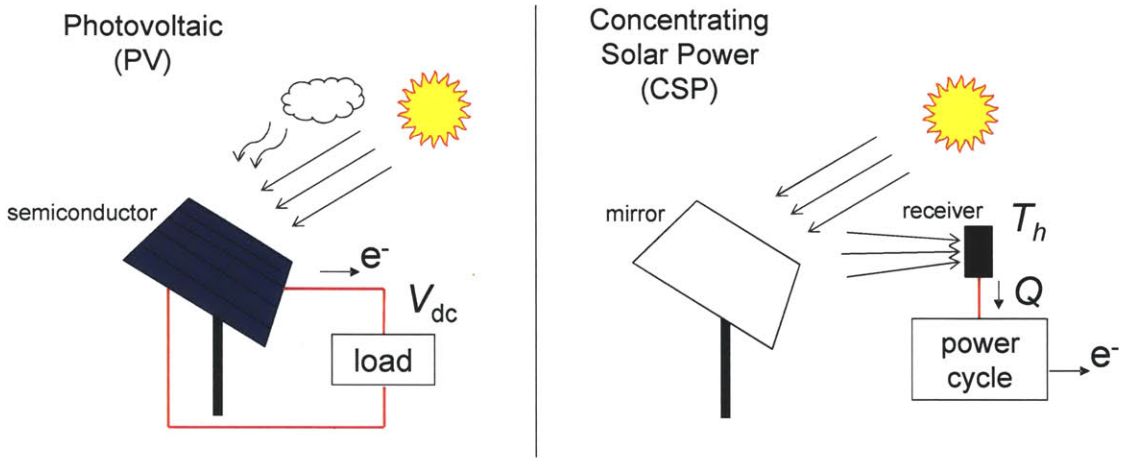

Figure 1.1 - Solar power: PV vs. CSP

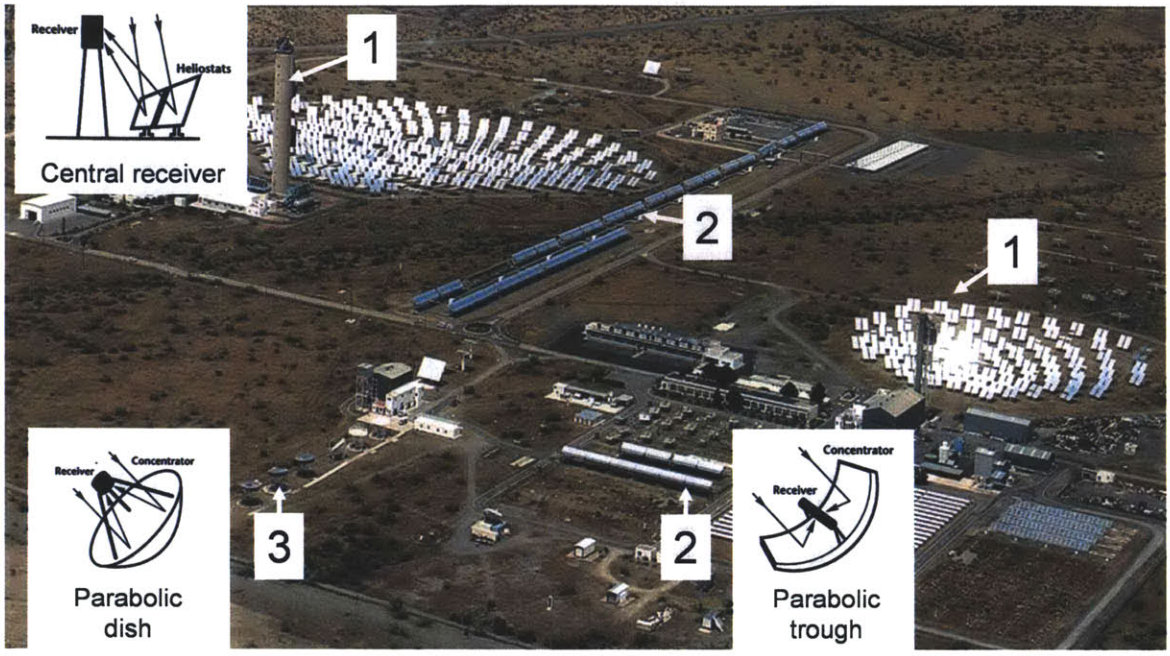

Figure 1.2 - CSP collection technologies
(courtesy E. Blanco, PSA)

CSP Receiver designs

There are numerous CSP receiver designs in the realm of point focus solar power towers, each attempting to address the functional requirements of capturing and converting concentrated sunlight into usable, high temperature heat. Receiver collection efficiency can be defined as the ratio of collected energy to incident energy, and ranges from 0.72-0.90 [2], [3]. Collection inefficiencies include surface reflection losses of the incident concentrated solar flux, radiative, convective, and conductive losses to the surrounding environment, and parasitic pumping power requirements for active heat transfer fluid (HTF) flow within the receiver. For an ideal absorber of concentrated solar flux, an upper bound to the collection efficiency η_{rec} can found as [4], [5]:

$$\eta_{rec} = \frac{\text{collected energy}}{\text{incident energy}} = \alpha - \frac{\varepsilon}{C} \cdot \frac{\sigma T_{rec}^{4}}{\Phi_0} \tag{1.1}$$

where the receiver's absorptance and emittance are denoted by α and ε, respectively, Φ_0 is the incoming solar radiation, C is the optical concentration ratio and σ is the Stefan-Boltzmann constant.

In general, collection efficiency improves as receiver surface temperature, T_{rec}, and effective emissivity ($\varepsilon' = \varepsilon/C$) decreases, favoring designs which can tolerate high flux collection and whose geometry approaches that of an ideal black-body absorber [4]. Physical systems have additional convective and conductive losses that can be minimized by increasing concentration, thereby reducing exposed surface area and insulating the receiver. Surface-receiver reflection losses can be minimized by applying high absorptivity coatings to receiver surfaces, tuned to be highly absorbing in the visible spectrum and having low emissivity in the infrared spectrum. However, Kirchhoff's law must hold true (i.e., for every wavelength $\alpha_\lambda = \varepsilon_\lambda$) and as receiver temperature increases, the emissive power spectrum shifts towards lower wavelengths and the net "spectral selectivity" decreases. However, high HTF temperatures result in improved power cycle efficiency, which is limited by Carnot efficiency η_{th} calculated as:

$$\eta_{th} = \frac{\text{useful work output}}{\text{heat from receiver}} = \frac{W}{Q_{rec}} = 1 - \frac{T_\infty}{T_{rec}} \tag{1.2}$$

where W is the work done by the power cycle, Q_{rec} is the heat supplied to the power conversion cycle by the receiver and T_∞ is the ambient temperature. Equation (1.2) provides a theoretical upper bound to the power cycle efficiency; real systems are subject to losses and irreversibilities and the resulting power cycle efficiency is reduced, particularly as the rated unit size decreases.

Overall solar-to-electric system efficiency, $\eta_{solar\text{-}electric}$, can be found as the product of individual efficiencies:

$$\eta_{solar-electric} = \eta_{opt} \cdot \eta_{rec} \cdot \eta_{th} \cdot \eta_{ele} \tag{1.3}$$

where, η_{opt} is the optical efficiency, a function of collector (heliostat field) geometry, mirror reflectivity, cleanliness and shape, and η_{ele} is the electrical conversion efficiency, which includes conversion and parasitic power consumption losses. It can be seen from Equations (1.1) to (1.3) that high receiver efficiencies require low operating temperatures; however this results in low power cycle and overall system efficiencies. Low solar-to-electric efficiencies require more heliostat collection area, increasing capital costs and subsequent levelized costs of energy that the CSP plant produces.

Conventional receiver designs

Conventional surface absorption tube-based receivers have been studied and tested, only to exhibit low capture efficiencies, parasitic fluid pumping losses and raise long term durability concerns [2], [6], [7]. Tubular receiver designs circulate a heat transfer fluid through an array of tubes onto which concentrated sunlight is focused (Fig. 1.3a & 1.3b). As a result, the highest temperature of the receiver is the tube's exterior surface, which must conduct the heat inwards to the colder, flowing heat transfer fluid (Fig. 1.4a). Daily and instantaneous solar variations create large temperature gradients, thermal strains and high temperature creep which all must be mitigated to avoid low-cycle fatigue failures of the tubing. Consequentially, maximum allowable flux values are limited to avoid thermal degradation of the receiver tubing [8]. Lata et al. cites the tradeoffs between tube diameter, wall thickness, receiver durability and pressure drop in conventional tubular receiver designs while describing a "new" external tubular receiver capable of achieving slightly higher maximum fluxes, up to 1.0 MW/m^2, thereby reducing receiver surface area and losses while increasing overall plant efficiency [9].

Volumetric absorption can reduce radiative and convective losses to the environment while increasing HTF operating temperature and capture efficiency [10]. Figure 1.3c depicts a typical volumetric air receiver [11]. Volumetric absorption reduces the susceptibility of receiver or HTF overheating and failure due to transient solar fluctuations. Ideal volumetric receivers have

a peak temperature located within the HTF that is hotter than the receiver surface temperature, reducing radiative losses, as shown in Fig. 1.4b.

Receivers can be utilized with efficient north heliostat fields (in the northern hemisphere) in cavity or directional designs, whereby a concave receiving surface can be used to reduce convective and radiative losses at the expense of the receiver's acceptance angle (Fig. 1.3a & 1.3c). Alternatively, an external receiver presents a constant area target for heliostats, regardless of azimuthal position (Fig. 1.3b). However, a full 360° circular field is non-optimal, as heliostats south of the receiver suffer from poor optical (cosine) efficiencies. As a result, the southern perimeter of an external receiver experiences reduced concentrated flux relative to the northern side of the receiver, and is typically used for HTF preheating [7], [9].

Unfortunately, both surface and volumetric receiver designs are subject to surface reflection losses. Incoming concentrated flux is reflected, directly and diffusely, away from the receiver surface and back into the environment. Conventional cavity (Fig. 1.3a) and external (Fig. 1.3b) tube-based receivers, such as those used in the PS10, PS20 and Solar I and II CSP test sites, respectively, are designed so that incoming flux strikes the tube near-normally to its surface. A fraction of the incident light is reflected off the receiver's surface and cannot be recaptured. Much effort and costs are spent applying spectrally selective solar absorption coatings, or relying on surface oxides to grow and reduce the tube's reflectivity – but the absorptivity of the tube surface presents an upper bound to tube-based receiver efficiency. Similarly, conventional volumetric absorption receivers rely on quartz aperture windows to isolate the HTF from the environment. Even with advanced conical aperture windows (as shown in Fig. 1.3c) designed to reduce surface reflection losses, a portion of the incident flux is returned to the environment. Additionally, aperture windows will absorb some of the incident energy throughout the solar spectrum, and completely block the small but non-zero contribution in near infrared portion for which quartz and sapphire are opaque. Perhaps more significantly, large aperture windows are costly, fragile components and require active cooling in high-concentration systems.

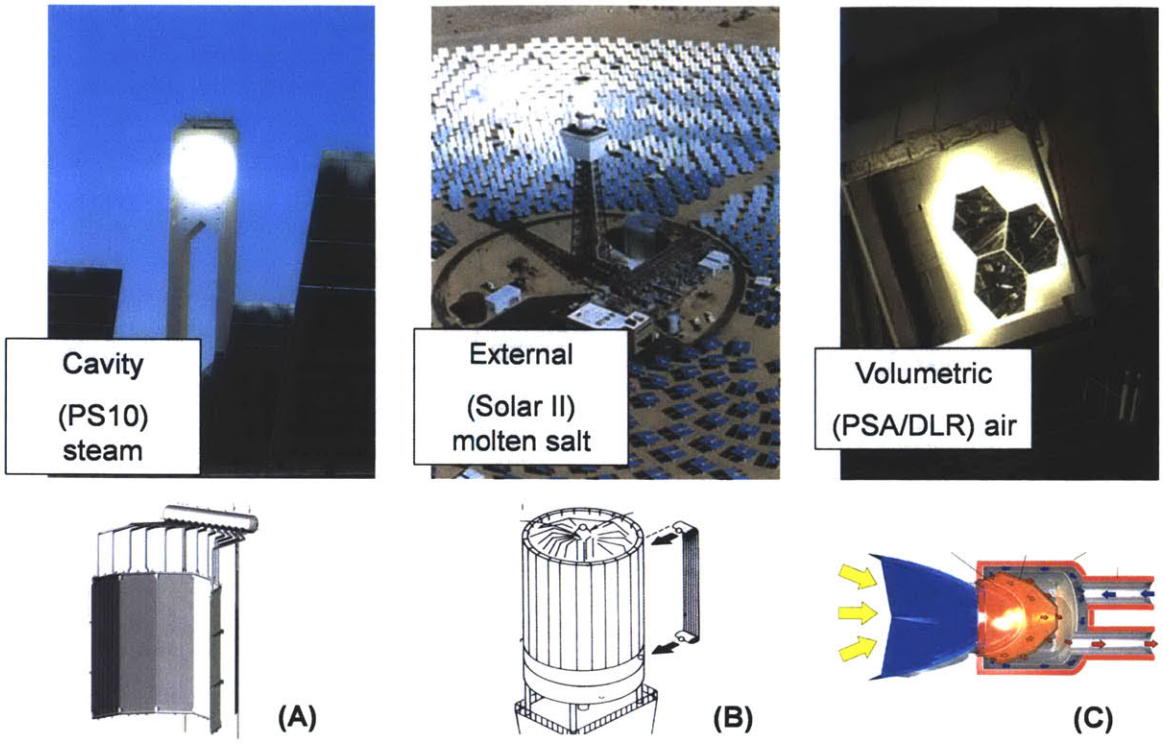

Figure 1.3 - Central receiver designs

From [2], [6], [7], [11]

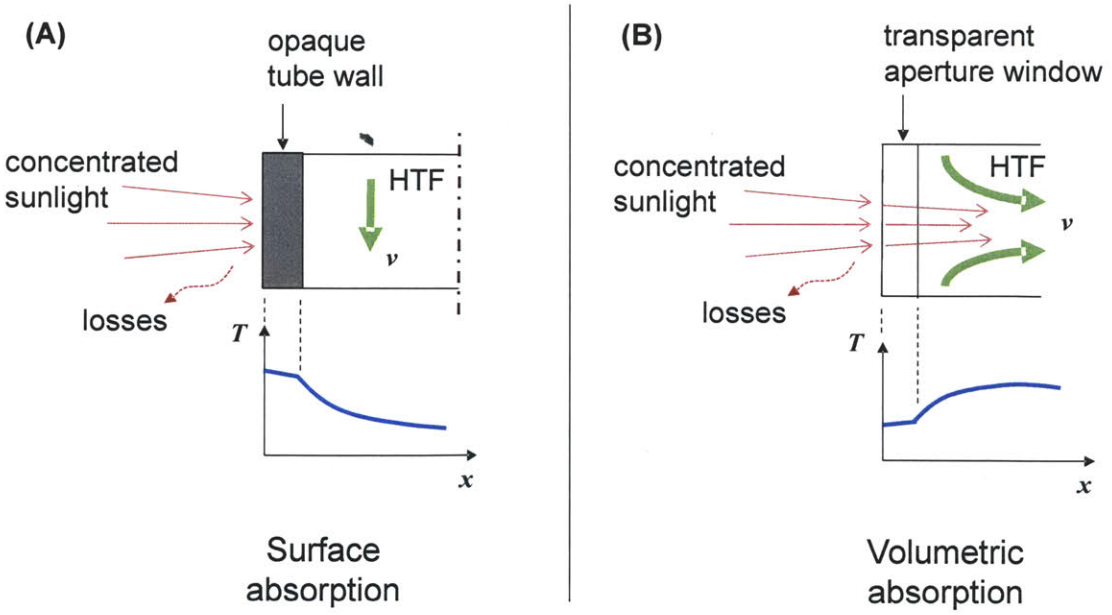

Figure 1.4 - HTF flow and temperature profiles in conventional receivers

Heat transfer fluid

The design of a receiver depends significantly upon the choice of HTF. Working temperatures, system sizing, materials compatibility, ease of energy transfer, toxicity and cost are key parameters used to select fluids. Materials besides fluids can be used as the primary heat transfer "fluid" within the receiver, including fluidized particle beds which transfer heat to a working HTF [5]. Some receivers are designed as high temperature chemical reactors, whereby the working fluids are the reactants and products themselves [10]. Typical HTFs include water/steam, air, molten salts (also known as fused salts) and liquid metals [12].

Early central receiver solar thermal power plants were designed with closed-loop direct steam generation receivers, creating pressurized steam fed directly into a power cycle. The receiver simply acted as a solar-powered boiler for a conventional Rankine power cycle [3]. Volumetric absorbers have been designed to heat air, typically as part of a solar-assisted gas turbine (i.e., Brayton) power cycle [11]. However, hot steam and air are low density fluids and subsequent thermal storage dictates energy transfer to a more efficient storage medium [13], [14]. Heat exchangers are needed each time energy is transferred to a new medium, increasing system cost and complexity.

Utilizing molten salts as the working fluid enables simple subsequent thermal storage, due to their high heat capacities and wide operating temperatures. Tube-based receiver designs have migrated to using molten salt as the primary HTF and storage medium [6], [9], [14]. While molten salts possess ideal heat transfer properties, relatively low viscosities and low costs, they can freeze. The binary sodium-potassium nitrate "solar salt" mixture (60-40 wt.%), which has seen widespread adoption in central receiver CSP plants, has a freezing temperature of 222 °C [6]. Molten salt can be kept circulating in the receiver piping throughout the night, or the receiver can be drained as the sun is setting. Unfortunately, both methods require ancillary heaters and present additional risks should the salt freeze, requiring electric heat tracing on long piping runs,

valves and manifolds. Despite these measures, operating problems still occur; for example, the Solar Two CSP demonstration plant was disabled by frozen salt in pipes and clogged preheater manifolds during the daily filling process [6].

Alternative receiver designs

An alternative approach to volumetric absorption, initially proposed by Sandia in 1974, utilizes a cascading molten salt waterfall in a Direct Absorption Receiver (DAR), as shown in Fig. 1.5 [15-19]. A portion of the concentrated flux is absorbed within the salt film, and the remainder is absorbed on a darkened alloy sheet that supports the salt film, effectively transferring thermal energy into the salt. Experiments using centimeter-thick molten salt waterfall films were found to be marginally absorbing to incoming sunlight, and the salt was doped with high absorptivity particles to collect the required energy within the salt film [15]. Unfortunately, the exposed active fluid flow, surface reflection losses, film instabilities, variations in output HTF

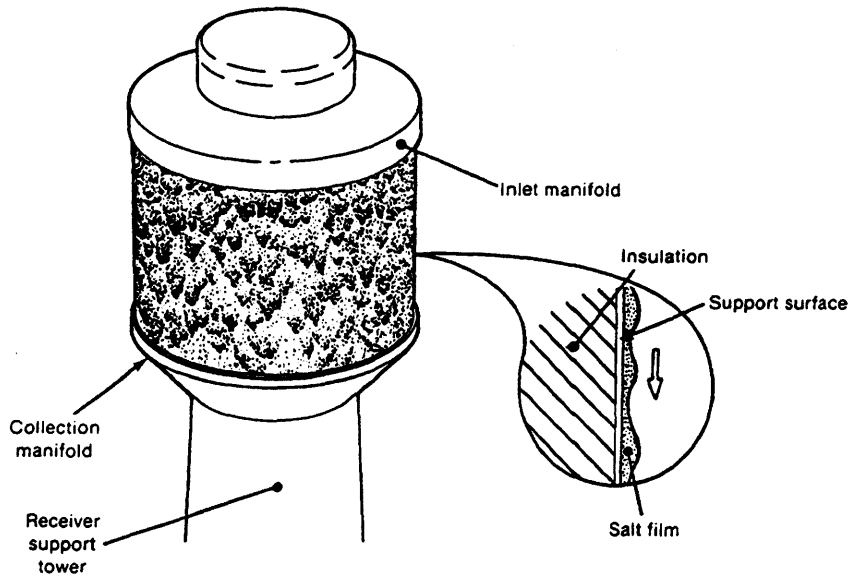

Figure 1.5 - Molten salt waterfall Direct Absorption Receiver (DAR) concept From [16]

temperature as a function of varying solar flux, and the cost of pumps, manifold and piping preheaters limits the practicality of such systems [20].

Additional receiver designs are possible if the traditional power tower approach is abandoned. Beam down systems, as originally proposed by Rabl in 1976, seek to relocate the receiver to ground level to avoid some of the tower-based receiver constraints [21]. To achieve this configuration, a secondary reflector is positioned atop a tower which redirects concentrated light from the heliostat field to the receiver. Typical Cassegrain optical geometry is employed, utilizing a hyperbolic secondary mirror. Heliostats aim at the (virtual) upper focus, above the secondary reflector, and the receiver is placed at the lower focal point. A ground-level receiver enables the use of novel materials and geometries for receiving concentrated sunlight–notably a liquid free surface (Fig. 1.6) [22], [23]. Similarly, Yogev [23] and Epstein [24], [25] suggested a beam down system where the light was to be beamed into the central region of a metallic annulus, whereby molten salt or molten metal flows and is heated in the outer annular region. Since Rabl's proposal in 1976, significant experimental work has occurred on beam down towers and ground receivers, especially for reforming materials [22], [26].

However, beam down optics are costly, incur additional reflection losses and pose high-flux durability issues. The maximum flux impinged on the secondary mirror is typically limited to 35 kW/m^2 to avoid active cooling and optical degradation, which dictates a relatively large mirror area [27]. A tower still needs to be constructed, and it may shade a significant portion of the heliostat field. Tertiary concentrators are needed to compensate for the increased sun spot size due to the increased focal length created by the beam-down geometry. Non-imaging optics are used as tertiary concentrators to increase flux levels at the receiver aperture, the most common being Compound Parabolic Concentrators, or CPCs [28]. Unfortunately, CPCs require active cooling to reject heat and, both from high-flux reflection losses within the CPC and heat from the receiver itself. Additionally, the use of quartz aperture windows to isolate the receiver chamber reflect and absorb a portion of the incident energy and raise long term durability concerns [24], [26].

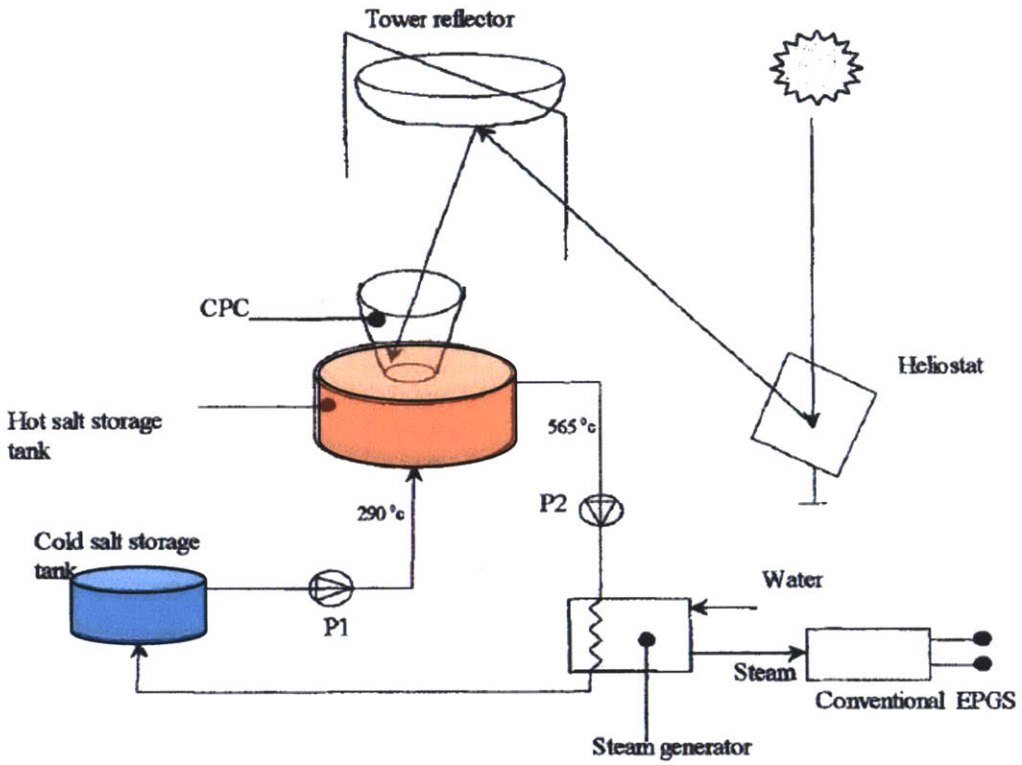

Figure 1.6 - Beam down system with ground level molten salt receiver concept
CPC concentrates light before passing through aperture window (not shown) and into receiver. Two-tank thermal storage is illustrated. From [24]

There is a precedent for solar collection systems which do not utilize an overhead secondary mirror, but instead take advantage of natural terrain. Solar furnaces are used for high temperature materials characterization and synthesis, not for power production. Two high-flux solar furnaces, one in Odeillo, France and the other in Parkent, Uzbekistan, utilize hillside mounted heliostats to collect light and direct it horizontally into a large parabolic mirror having a horizontal optical axis. This parabolic mirror further concentrates the light onto a small area at its focus (Fig. 1.7). The Odeillo solar furnace facility uses 63 south-facing flat mirror heliostats to track the sun's movement and focus it down on the north facing parabola focused on a target built into one wall of a building that holds offices and laboratories [29]. This system can achieve flux levels above 16 MW/m^2 (albeit across a few cm-wide focal spot), capable of heating objects

beyond 2800 °C, with a total power of 1 MW_t [30]. The NREL high-flux solar furnace system also employs a heliostat which redirects light near-horizontally towards a ground-based, horizontal axis secondary reflector system.

The primary drawback to multiple reflection designs is up to 10% of the energy is lost with each reflection [31]. Research beam down CSP and solar furnace systems achieve high concentrations with large, precision optical elements – whose cost and durability have prevented the commercial adoption of similar geometries to ground-level based receiver CSP systems.

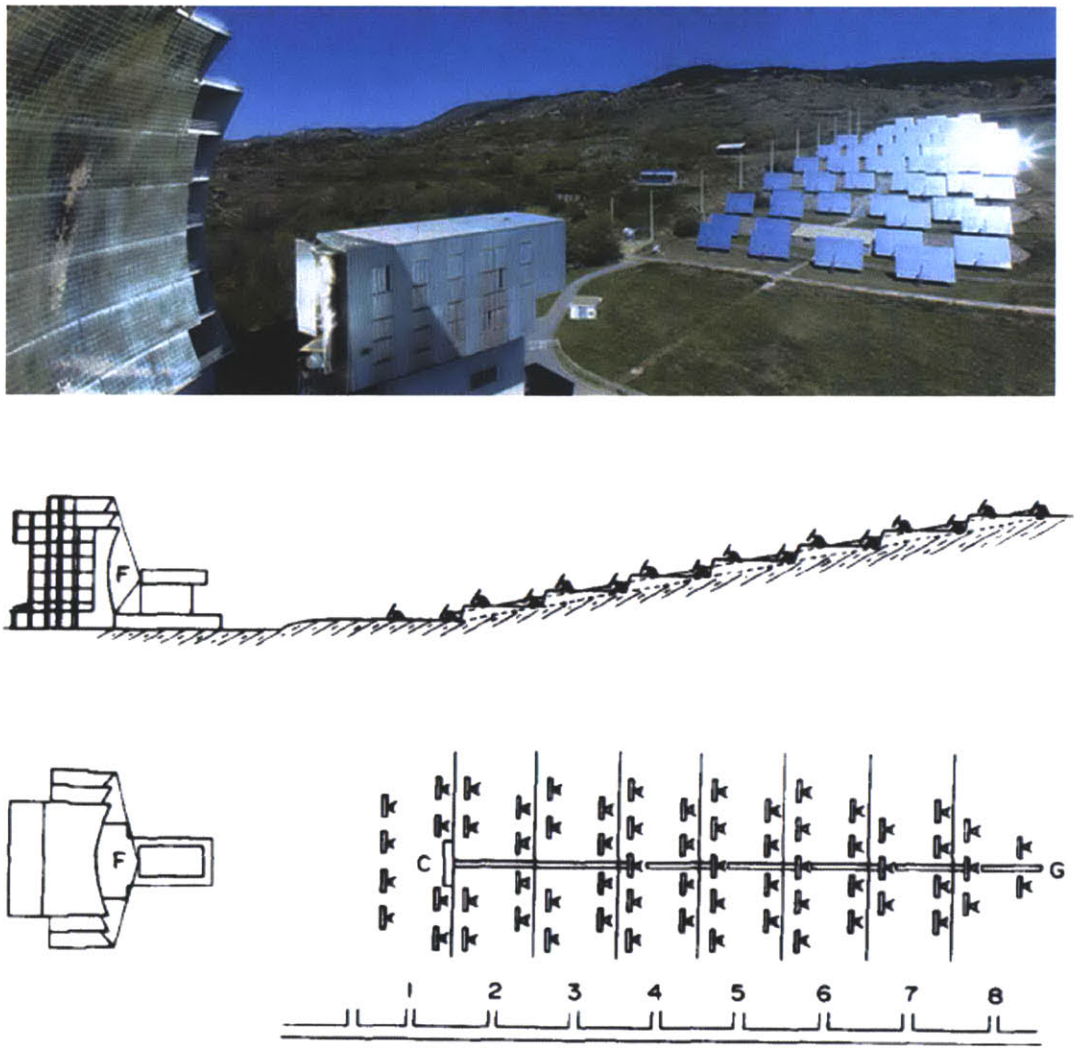

Figure 1.7 - Odeillo 1 MW_t solar furnace utilizing hillside heliostats
From [29]

Thermal storage

Regardless of the receiver design, CSP systems benefit from thermal storage for dispatchable energy production. CSP plants without storage can only produce power while the sun is shining – although the thermal inertia of the receiver allows for some flexibility due to cloud transients, on the order of a minute or so, as opposed to the truly instantaneous output of photovoltaic systems. A well-designed thermal storage system allows for heat extraction irrespective of instantaneous solar conditions so power production can occur shifted (minutes, hours or even days) relative to the maximum solar resource. However, some demonstration CSP plants have been designed with a co-firing gas turbine scheme as an alternative to thermal storage systems [11]. This provides the turbine with constant input power, regardless of solar fluctuations. Unfortunately, the gas turbine is driven at nights and during periods of low insolation, offsetting the truly "clean" energy benefits the CSP field may provide.

Thermal energy storage can be divided into three categories: sensible, latent or chemical [13], [32]. Sensible heat systems rely on a temperature increase within media to store energy. Latent heat storage utilizes phase change materials, usually at constant temperature, releasing their enthalpies of fusion or vaporization. Alternatively, reversible endothermic reactions can be used to provide chemical heat storage. Regardless of the means of thermal storage, functional requirements include high energy density, operating temperature compatibility, excellent heat transfer characteristics, low losses, ease of control, safety, durability, mechanical and chemical stability and low storage system costs.

Current CSP systems which address thermal storage utilize remote sensible heat storage of various designs, dependent on the receiver HTF: tanks of pumped molten nitrate salts, banks of thermal oil-filled steel pipe bundles encased in concrete, or hot-air heated hollow refractory brick chambers [13], [14]. These designs require an active heat-transfer fluid flow, with associated high-temperature pumping issues and costs.

Molten salt thermal storage

Molten salt is a preferred media for high temperature "direct" thermal storage, whereby a single fluid functions as both the receiver HTF and the sensible heat storage medium. Direct systems eliminate the need for a heat exchanger between the receiver HTF and the storage media. Molten salts have high densities and specific heats, which increases volumetric storage efficiency. Additionally, they can be formulated to operate across various temperature ranges and have very low vapor pressures, enabling them to be used in unpressurized systems. Molten salts are cheaper and more environmentally friendly than organic heat transfer oils used in parabolic trough systems [33]. However, as mentioned previously, molten salts have relatively high melting temperatures.

Two designs are used for molten salt direct thermal storage: two-tank systems and single tank thermocline systems. In a two-tank system, salt is heated by the receiver and directly stored in a "hot" tank. From the hot tank, salt is pumped to a heat exchanger, or steam generator, for the power cycle, where heat is extracted and its temperature is reduced. From here, it is pumped to a "cold" storage tank; the cycle repeats when the salt is then pumped to the receiver to be reheated (Fig. 1.6). The advantage to the two-tank system is that the cold and hot salts are stored separately; however, two tanks must be constructed with each capable of storing the entire system volume [34]. Daily temperature and pressure cycling of the tank walls are severe as the salt volume is transferred nearly completely from one tank to the other.

In contrast, a thermocline system uses one tank, whereby the hot and cold salts are stored in the same tank. In traditional CSP systems, cost-savings have been obtained with single tank systems relying on temperature stratification via natural thermocline formation [35]. The hot salt, with reduced density, floats above the cold salt. Hot salt is extracted from the top of the tank and cold salt is returned to the bottom. Care must be taken to design the tank proportions and locate the extraction and return ports so fluid motion does not disturb the thermocline [33], [36]. The

stratification which forms can be enhanced with the use of solid filler materials within the tank, reducing mixing and stabilizing the "thermocline" zone that forms between the hot and cold fluids. Tests using dual media thermocline tanks with silica particles (sand) in molten nitrate salts, while confirming chemical stability, have shown the filler material tends to settle and pack over time due to the vertical cycling of the thermocline's position, as the system is charged and depleted repeatedly [37].

Divided single-tank storage

Copeland et al. has shown "rafted thermocline" designs effective at boosting thermal stratification in water tanks, with suggested designs for molten salt thermal storage tanks (Fig. 1.8a) [38-40]. Similarly, Andrews describes a water storage tank with a movable, internal baffle designed to separate hot and cold layers [41]. In these designs, an insulated, horizontal barrier plate is weighted to achieve neutral buoyancy directly at the thermocline interface. Hot fluid is removed (or added) from the top of the storage tank, and cold fluid is returned (or removed) to the bottom, and the barrier plate follows the thermocline position. As described by Wang et al. [42], "a unique problem occurs with thermocline systems at high temperatures because radiant heat transfer becomes significant: transparent liquid salt offers no resistance to radiative transfer, and radiation between a hot ceiling and a cool bottom can induce convection currents that destroy the thermocline." The barrier plate would limit both conductive and radiative transfer within high temperature storage systems, increasing tank utilization. However, passive rafted thermoclines would rely on two parameters difficult to control in high temperature molten salt tanks: maintaining neutral buoyancy at the hot-cold thermocline interface; and a near perfect seal with the side walls to prevent leakage around the divider raft. Indeed, tests performed in water showed the neutrally buoyant raft design may display instabilities and tilt and/or jam in the storage tank [38].

An alternative design was suggested by Laing, whereby a movable, radial wall is positioned between hot and cold salt volumes. (Fig. 1.8b) Although Copeland's and Laing's concepts would reduce thermal losses relative to two-tank and dual media thermocline designs, sealing at high temperatures with high temperature gradients would prove problematic.

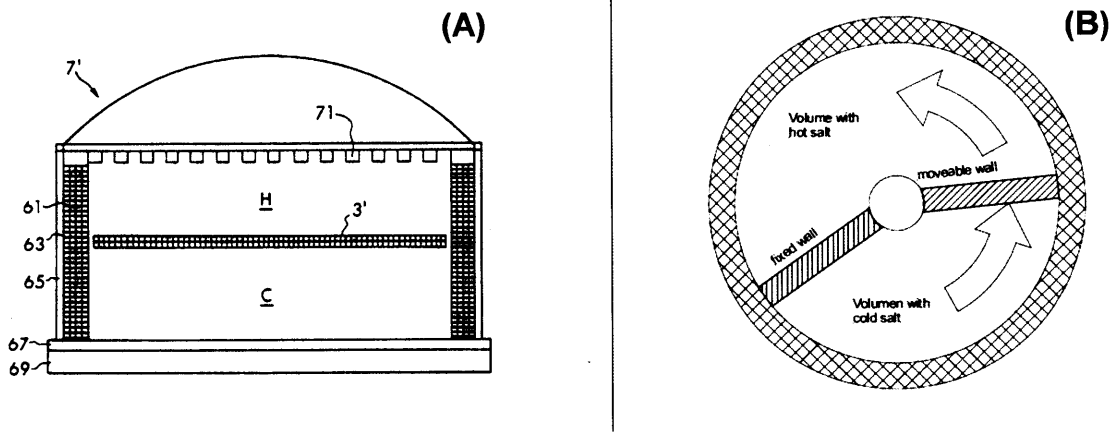

Figure 1.8 - Divided single tank molten salt thermal storage concepts
(A) Rafted thermocline (side view); From [40]
(B) Radial partition (top view); From [43]

Objectives

For widespread adoption, CSP designs must show improved efficiency, robustness, energy storage and exhibit low capital and operating costs. Designs capable of increased working fluid temperatures will be favored for the resulting flexibility in choosing and improvements in power cycle efficiencies. For example, the helium Brayton cycle, operating at temperatures exceeding 800 °C, and supercritical CO_2 power cycles, operating at 700°C turbine inlet temperature and 20 MPa pressure, are expected to exceed supercritical steam Rankine cycle efficiencies [44].

Scope of Thesis

To address these concerns, this thesis describes the design of a high-temperature CSP system with integral energy storage. In the proposed system, concentrated light is beamed through an aperture directly into a large molten salt filled thermal receiver. The light that enters this salt pond will penetrate, scatter, and be absorbed through the volume of salt, rather than on a surface. As a result, salt temperatures of up to 1000°C and a large thermal energy storage capacity can be achieved in a relatively small volume. The salt pond receiver acts as a buffer between the diurnal and instantaneous variations of the heliostat field's solar flux and the power generation unit – providing dispatchable Concentrated Solar Power on Demand (CSPonD).

This work builds on preliminary research done at MIT by an interdisciplinary team led by Prof. Alex Slocum. Collaborating with researchers from MIT's nuclear, mechanical, materials science and chemical engineering departments, designs have been evaluated and refined for reliable, cost-effective performance. Over the course of the project, the team has examined the various building blocks of the CSPonD system: optical and thermal salt properties; receiver structure; convective salt flow fields; heat extraction configurations; optimal heliostat layout and power block operation.

This thesis will provide design guidelines for CSPonD receivers: scaling laws, material selection, performance estimates, operational guidelines and cost information. Chapter 2 describes the CSPonD concept, including the functional design of the molten salt receiver. Optical, thermal and economic performance estimates are given in Chapter 3 for the proposed receiver. Chapter 4 details experimental work conducted at MIT using lab-scale test receivers, heated with a high-flux solar simulator designed specifically for that purpose. Chapter 5 outlines a typical CSPonD system design for idealized hillside heliostat field geometry. Finally, Chapter 6 summarizes the salient points of the CSPonD system and future research paths are identified.

CHAPTER 2: The CSPonD Concept

System overview

A new high-temperature CSP system with integral energy storage is presented, whereby concentrated light is beamed through an aperture directly into a large molten salt filled thermal receiver. The light that enters this salt pond will penetrate, scatter, and be absorbed through the volume of salt, rather than on a surface. The salt pond will act as a buffer between the diurnal and instantaneous variations of the heliostat field's solar flux and the power generation unit – providing dispatchable Concentrated Solar Power on Demand (CSPonD).

Concentrated sunlight penetrates and is absorbed by a passive eutectic molten salt pool, also acting as single tank assisted thermocline storage system. Absorption through a significant depth tolerates rapid changes in solar intensity without receiver damage; single tank thermocline storage enables high temperature thermal energy to be fed into a power cycle, even as the average temperature in the receiver decreases [45]. Concentrated Solar Power on Demand (CSPonD) could provide 24/7 power and thus help fill a critical need in solar power, that of energy storage [46].

Figure 2.1 depicts a schematic of the CSPonD system. Heliostats mounted on a hillside beam light directly into a molten salt receiver at the base of the hill, or into a one-bounce system with the receiver at the top of the hill. This eliminates costly beam-down optics, reflective losses and a tall receiver tower. Cosine effect losses associated with hillside heliostats beaming light downwards to the receiver are offset by the elimination of a tower and separate hot and cold storage tanks and their associated high-pressure, high-flow pumping systems.

The CSPonD DAR simplifies the system by eliminating the conventional tower-based receiver, materials-driven temperature limits on receiver structure, remote thermal storage system and high pressure pumps. Volumetric absorption results in increased performance and durability: higher temperatures, improved power cycle efficiency; and enables a collocated & smaller storage

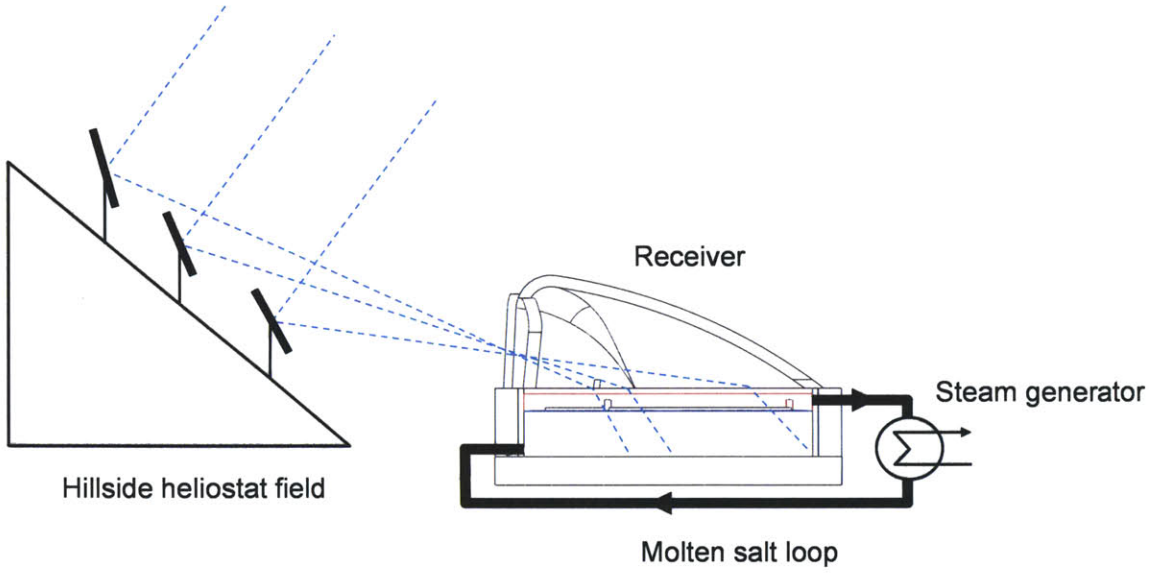

Figure 2.1 - CSPonD beam down system architecture

system. The molten salt surface is self-healing – tolerating high solar flux transients without irreparable sudden or cumulative damage to the receiver. A small aperture and refractory-lined domed roof reduce losses to the environment and reflect thermal radiation back into the pond. Hot salt is pumped from the top of the tank through a steam generator and then returned to the bottom of the tank. An insulated barrier plate is positioned within the tank to provide a physical and thermal barrier between the thermally stratified layers, maintaining hot and cold salt volumes required for continuous operation. As a result, high temperature thermal energy can be provided 24/7 or at any desired time.

For the near term, a salt commonly used in CSP plants can be used: sodium-potassium nitrate (i.e., solar salt: 60/40 wt.% $NaNO_3$-KNO_3) which has a low melting point of 222°C. Although above 600°C solar salt decomposes and becomes corrosive and dangerous, systems have been built and operated to pump it between hot and cold storage tanks and a steam generator [34], [47]. The power block, including salt pumps, heat exchanger/steam generator and power generation device, for a nitrate salt based CSPonD system will be very similar to those that can be

commercially obtained. Hence, for a near term CSPonD system, a steam power cycle will be assumed with peak steam temperatures of 500-540 °C.

The amount of storage required depends on local needs and economic conditions. Assuming a 300 K temperature swing, solar salt provides roughly 540 kJ/kg or 240 kW_th/m^3 sensible heat storage. With a conservative thermal-to-electric conversion efficiency of 30%, one can assume it takes about 14 $m^3/MW_e/h$ of nitrate salt for non-sunshine operation. For example, 2500 m^3 of salt can provide 180 MW_eh of energy storage, capable of powering a 50 MW_e turbine for 3.6 hours without additional solar input. This volume of salt can be contained in a 5 m deep, 25 m diameter CSPonD receiver. Obviously, supplying a large power cycle will require a large heliostat field, necessitating a large receiver aperture with increased losses. However, local economic conditions may dictate mid-afternoon and early evening power production – whereby a smaller heliostat field can charge a CSPonD receiver throughout the morning and then used to meet demand. Thus, the CSPonD system can be rated by continuous power production, not peak power as is typical of traditional CSP systems without thermal storage.

Inspiration

It is known that volumetric absorption results in higher working fluid temperatures and reduced thermal losses, as discussed in Chapter 1. Absorption over a depth reduces temperature gradients within the working fluid, in contrast to surface absorbers with localized heat fluxes. Additionally, many fluids are solar selective: nearly transparent to visible light and highly opaque in other wavelengths. A fluid with this characteristic allows for efficient volumetric absorption over a significant depth, while at the same time preventing excessive radiative transfer within the fluid. An analog found in nature is water, such as oceans or deep lakes. In clear, particle-free water, the penetration depth l (also termed characteristic length or mean free path) of visible light is 10-30 m; for infrared energy with a wavelength of 1.5 μm, l is less than 0.5 mm [48].

The selective absorption behavior of fluids are exploited in engineering systems – notably solar ponds, otherwise known as salt gradient ponds. In these one-sun solar thermal collection systems, incoming sunlight penetrates through a depth of saline water before striking a darkened pond bottom. The water is stratified with a freshwater layer added on top of the salt water, so that a vertical salinity and density gradient are established in the near-stagnant pool. The pond bottom is typically a black plastic liner which is highly absorbing in the visible spectrum. As a result, the solar energy is converted to thermal energy at the bottom of the pond. The heavier, yet warmer salt water remains in the bottom region of the pond due to the stabilizing salinity gradients, forming a non-convective zone between the top and bottom layers. Natural convection is suppressed even with the existence of an inverted temperature profile. Thermal transfer is limited to conduction across the vertical layers of the pond, with reduced convective losses due to cooler surface temperatures. Even without additional concentration, these large area collectors can achieve temperatures in excess of 90 °C in the lower storage zone [49].

Since solar ponds operate at relatively low temperatures with large exposed areas, the primary methods of heat loss are surface convection and evaporation. However, increasing optical concentration allows the exposed surface area to be reduced or working temperatures to be increased, or both, as in the proposed CSPonD receiver. Obviously, a working fluid other than water is needed for high temperature operation; hence the choice of molten salts.

Initial design concept

The initial objective was to develop a new type of CSP system to simultaneously receive and store thermal energy in a volume of molten salt using a beam down solar power tower. As initially proposed by Slocum et al., an insulated storage tank filled with transparent molten salts containing nanoparticles replaces the solar boiler and thermal storage system of traditional CSP central receivers [46]. Light from the primary heliostats is focused and reflected downward by secondary mirrors on the beam down tower through a small aperture into an insulated graphite

lined salt-filled tank on or underground (Fig. 2.2). This beam down reflector can either be a monolithic or tiled hyperbolic reflector or an array of servo controlled secondary reflectors which can better control the focus.

The aperture acts as a thermal diode to let large amounts of energy in, but little out. Light is absorbed by nanoparticles in molten fluoride or chloride salts which transfer their heat by conduction to the bulk salt and by scattering light to graphite walls. The container walls serve to increase the heat capacity of the system. The use of nanoparticles would allow controlled bulk heat absorption in the transparent salt and thus allows for much higher radiation fluxes. Natural circulation of salt is upward where heated and then downward through graphite blocks with cooling channels. The hottest salt is at the top of the tank where it can be extracted and fed to a heat exchanger associated with the power cycle. The reservoir acts as a capacitor so full power can always be directed into it, regardless of time of day or a passing cloud, and the steam generator can extract heat as needed on a continual basis.

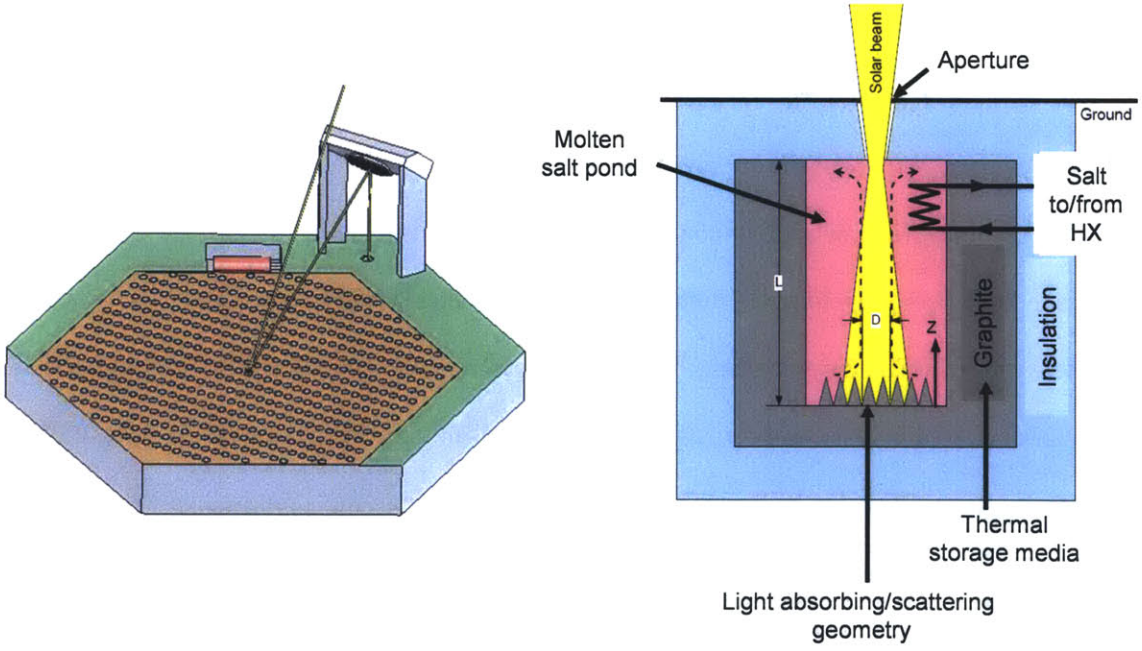

Figure 2.2 - Initial CSPonD system concept

Beam down secondary reflector (left) directs concentrated sunlight into a ground-level molten salt receiver (right; cross-section shown). From [46]

As the project progressed, it became clear that some aspects of the initial concept must change. Most revisions were motivated by cost savings and design simplifications; particularly elimination of a beam down secondary mirror as described in the next section. Experimental testing revealed some flaws with other aspects of the design. For example, nanoparticle-enhanced salts were found to be too absorbing and difficult to keep well mixed. Some salt eutectics initially selected for the system reacted in the presence of an oxidizing atmosphere. Similarly, graphite container materials were consumed in high temperature atmospheric salt melt testing; keeping either would necessitate an inert purge gas over the system with possibly a transparent aperture window. Modifying the design to eliminate these risks enables a more robust system with reduced complexity and capital costs. However, the distinguishing feature of the CSPonD concept has remained: absorption of the light through a significant depth of the salt.

Hillside heliostats

As described in Chapter 1, there is precedence for the location of heliostats on a hillside to direct sunlight to a secondary reflector, then redirecting the power to a receiver on the ground [29]; however, up to 10% of the energy is lost with each additional reflection, not to mention high-flux secondary mirror cooling concerns, operation and installation costs. Meanwhile, there appears to have been a "land rush" for acquiring rights to flat, sunny land perceived to be needed for other types of solar power systems, which have increased the overall costs of traditional CSP systems. Motivated by these concerns, plus the fortuitous initial CSPonD evaluation site of the hilly southern coastal region of Pentacomo, Cyprus, a new design was proposed which eliminates the beam down secondary reflector.

The system presented here thus reflects the solar energy from a heliostat field on a hillside directly into a receiver. Hillside mounted heliostats simultaneously collect sunlight while also acting as the beam down optic, reducing overall system complexity and cost. In the northern

hemisphere, a south-facing hillside field allows for direct beam down entry into the molten salt pond as shown in Fig. 2.3a. Alternatively, a receiver can be placed atop a north-facing hillside, creating a beam up "virtual tower" configuration with a reflective lid cover (Fig 2.3b). CSPonD collector fields can be built on otherwise undesirable steep terrain, further reducing system costs. With the correct site selection, heliostat packing density can be increased even as shading and blocking losses are decreased – without altering the landscape. Blake et al. describes a site having a natural slope to the south of 10-13°, accommodating heliostat terracing with minimum excavation, resulting in increased collection efficiency for power tower systems [50]. Methods developed by utility companies for emplacing utility poles on moderately steep terrain can be used for heliostat installation, and automated spray systems can be utilized for cleaning the mirrors.

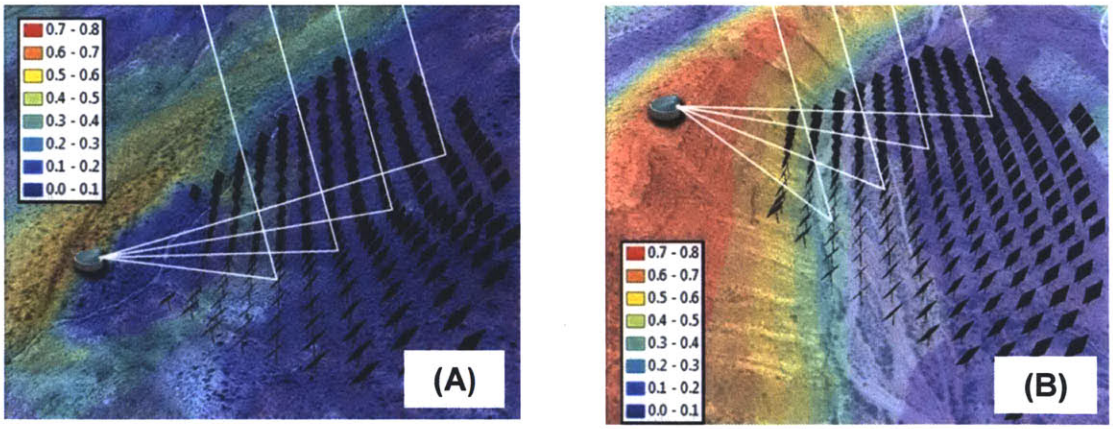

Figure 2.3 - Representative hillside CSPonD sites in White Sands, NM
(A) Beam down. (B) Beam up, whereby lid acts as short-bounce secondary reflector. From [51]

Noone et al. describes a numerical tool developed to evaluate potential sites for beam up and beam down CSPonD configurations [51]. Optimal sites not only have excellent solar insolation, specifically direct normal isolation, but also possess ideal terrain features. For

example, 10,000 km^2 areas were examined in White Sands, NM and China Lake, CA, both located in high solar resource areas and mountainous regions. For those cases, optimal beam down receiver locations were found to have efficiencies of 70% and 68%, respectively. In the beam up configuration, both case sites have optimal receiver locations with efficiencies of 77% [51]. These efficiencies take into account cosine efficiency, shading and blocking losses due to the terrain; optical losses due to reflectivity, mirror shape and tracking errors are not included.

Representative sites with highest efficiency from the White Sands, NM area are shown in Fig. 2.3. The 10,000 km^2 White Sands area examined could provide 20 GW_e of power 24/7, assuming that 15% of the land can be utilized and of this land 30% is covered by heliostats, with a solar-to-electric efficiency of 22% and a modest direct normal insolation of only 4.8 $kW/m^2/day$, which averages out to 200 W/m^2 over a 24 hour basis. Similar results are obtained for China Lake; the remainder of the high insolation region of the southwest US can be analyzed similarly, opening up new territory for renewable power generation.

Volumetric receiver pond

Concentrated solar flux passing through the aperture can follow one of three paths: refracted into the molten salt; reflected off the salt surface towards the inside surface of the receiver lid; or directly impinged on the inner surface of the lid (Fig. 2.4). A collection efficiency analysis, while the receiver is "on sun" is presented in Chapter 3. In general, capture efficiency increases with input flux concentration as the system geometry approaches that of a blackbody; the self-healing nature of the molten salt surface tolerates higher fluxes than conventional tube based receivers – and can achieve greater efficiencies as heliostat field technology and achievable concentration improves. The unique dual heat-source nature of the salt and lid in CSPonD receivers will allow more flexibility for operators to maximize useful heat extraction for their particular system.

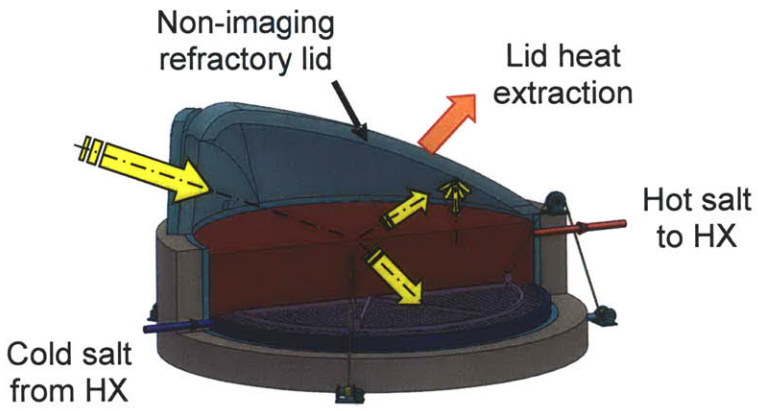

Figure 2.4 - CSPonD receiver cutaway view
Yellow arrows denote light path within receiver.

Absorption of radiation within salt

The energy that is transmitted through the salt will decay as a function of the optical path length δ, according to the Beer-Lambert law:

$$I_\lambda = I_{\lambda,0} e^{-\beta_\lambda \delta} \tag{2.1}$$

where the attenuation (or extinction) coefficient β_λ varies strongly with wavelength and moderately with temperature. The attenuation coefficient is defined in terms of the absorption, κ, and scattering, σ_s, coefficients as:

$$\beta_\lambda = \kappa + \sigma_s \tag{2.2}$$

The attenuation coefficient is related to the absorptive index, k, in the complex index of refraction, $m = n - ik$, where n is the refractive index, as:

$$\beta_\lambda = \frac{4\pi k}{\lambda} \tag{2.3}$$

All three coefficients physically represent the inverse of exponential characteristic lengths and have the dimensions of length^{-1} [52]. The attenuation coefficient describes the mono-directional penetration of the light inside the medium, while absorption and scattering coefficients are used to distinguish between the two physical phenomena causing the light attenuation [53]. For the CSPonD DAR, the attenuation and absorption coefficients allow estimation of both the light penetration into the pond, and how much of the solar light can be absorbed by the salt itself. Unfortunately, the distinction between scattering and absorption is not trivial experimentally; the measurement of the combined effects into the attenuation coefficient is much simpler [53-56].

Historically, molten salts have been considered weakly absorbing, or even fully transparent (i.e., $k = \beta_\lambda = 0$) in the visible region [16], [54-56]. Indeed, this was the motivation to "seed" the molten salt with a suspension of highly absorbing nanoparticles as described in the initial concept. However, recent experiments using longer path lengths through molten salt, on the order of 10 cm, have obtained non-zero values for the attenuation coefficient, which includes both absorption and scattering. Passerini's experiments have found attenuation coefficients for molten nitrate, carbonate and chloride salts of interest are on the order of 0.01 cm^{-1} over the visible spectrum [53]. For example, a 5 m path length through molten salt would absorb 99% of the incoming concentrated visible radiation. Molten salts have been shown to be strongly absorbing and opaque in the infrared spectrum, for $\lambda > \lambda_c$, where the cutoff wavelength λ_c is determined by the spectral absorption characteristics of the liquid [57]. Typically, λ_c ranges from 1.5 to 3.5 μm [54-56]. Figure 2.5 plots values for the complex index of refraction for molten nitrate salts.

The measured attenuation coefficient of solar salt at 350 °C has been applied to the reference AM1.5 solar irradiance plot of ASTM G173-03, as shown in Fig 2.6. AM1.5 refers to an "air mass" of 1.5; that is, 1.5 times nominal atmosphere thickness, corresponding to a solar zenith angle of 48.2°, and is typically used to for characterization of solar power systems [5]. Even though the range of valid experimental data is only from 400 to 800 nm, nearly 55% of the

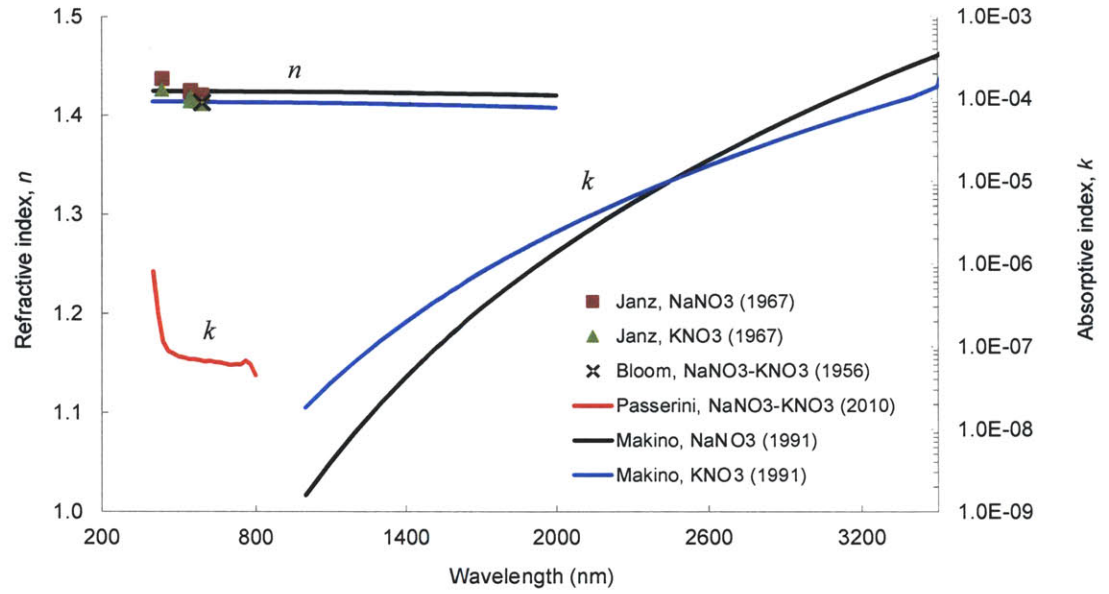

Figure 2.5 - The complex index of refraction for molten nitrate salts

Refractive (n) and absorptive (k) indices compiled from: $NaNO_3$, KNO_3 at 347 °C [56]; $NaNO_3$-KNO_3 (solar salt) absorptive index at 350 °C [53] and refractive index at 350 °C [58], [59].

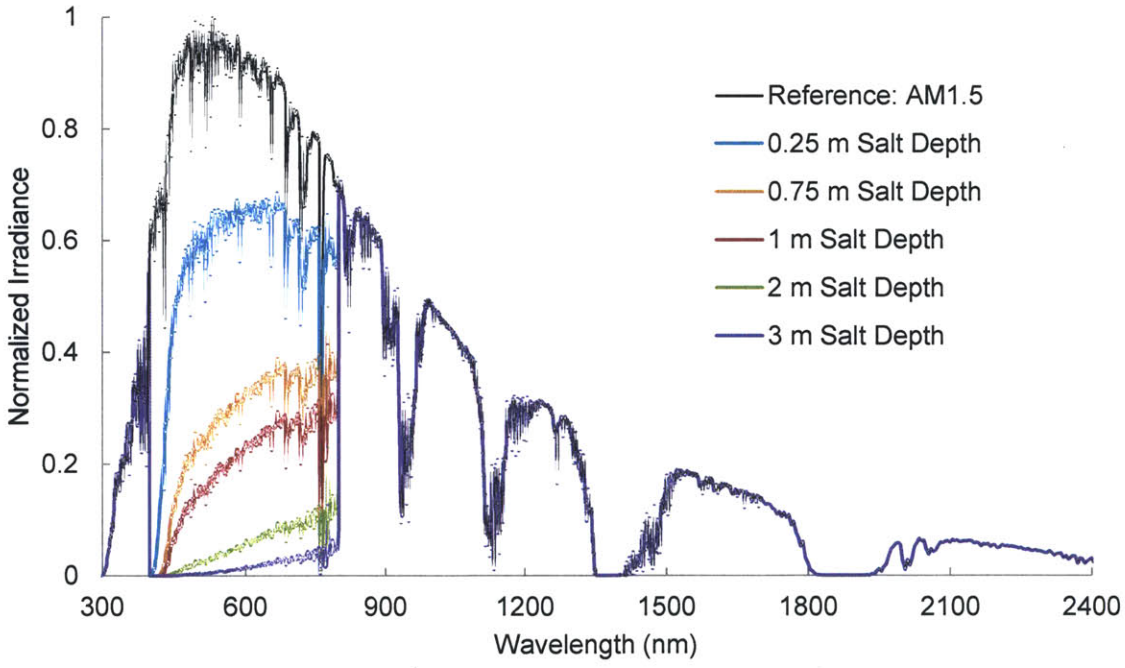

Figure 2.6 - Solar irradiance attenuation for various molten salt depths

This figure uses experimentally measured attenuation coefficients for a 60/40 wt.% sodium-potassium nitrate mixture at 350 °C in the wavelength range of 400-800 nm. From [53]

terrestrial solar insolation falls within this range. At a depth of two meters, 93% of the solar energy from 400 to 800 nm is absorbed by the nitrate salt.

The light attenuation characteristics are critical as they strongly affect temperature gradients within the salt and overall system design. For example, in large deep ponds created for large amounts of thermal storage, forced circulation of the salt could be required to prevent overheating of the top surface of the salt. Conversely, if the salt is found to be too transparent, overheating of the container structure could occur.

Thermal transport within salt

The radiative transfer equation (RTE) is used to calculate the radiative heat transfer rates within, and to the bounding wall of, a participating medium:

$$\frac{dI_\lambda}{ds} = \hat{s}\cdot\nabla I_\lambda = \kappa_\lambda I_{b\lambda} - \beta_\lambda I_\lambda + \frac{\sigma_{s\lambda}}{4\pi}\int_{4\pi} I_\lambda(\hat{s}_i)\Phi_\lambda^*(\hat{s}_i,\hat{s})d\Omega_i \qquad (2.4)$$

where Φ_λ^* is the scattering phase function, describing the probability that radiation is scattered from direction $\hat{s}_i$ into direction $\hat{s}$. Equation (2.4) states that the spectral radiative intensity I_λ along a path s in the direction of $\hat{s}$ is modified by three factors: spectral emission of the fluid at elevated temperatures; extinction or absorption and outscattering (scattering of radiation away from $\hat{s}$); and in-scattering (scattering from all other directions $\hat{s}_i$ into direction $\hat{s}$) [52]. The blackbody, spectral intensity, $I_{b\lambda}$, of the fluid at temperature T is given using the Planck function:

$$I_{b\lambda}(\lambda,T) = \frac{n^2 2C_1}{\lambda^5\left[\exp\left(\frac{C_2}{\lambda T}\right)-1\right]} \qquad (2.5)$$

The constants C_1 and C_2 are equal to 0.59544×10^{-16} W·m^2 and 14388 μm·K; n is the refractive index of the medium into which the black body emission is being evaluated. Equation (2.5)

evaluates $I_{b\lambda}$ in vacuum/air, not in the medium. It is desirable to keep track of the radiative energy in terms of the incident wavelengths that have been measured outside the fluid (i.e., in air), as the wavelength of a given bundle of radiative energy can vary as it propagates along a medium with varying properties as a function of temperature [60].

The RTE must be solved, followed by integration over all directions and all wavelengths to obtain the radiative heat flux q_r:

$$q_r = \int_0^\infty \int_{4\pi} I_\lambda(\hat{s})\hat{s}\, d\Omega d\lambda \tag{2.6}$$

Unfortunately, as Modest writes, solutions to the RTE

> *...which is an integrodifferential [sic] equation in five independent variables (three space coordinates and two direction coordinates), is a truly daunting task for all but the most trivial situations, even at the spectral level. Integration over all wavelengths, due to the complicated nature of radiative properties, tends to add another dimension to the level of difficulty."* [52]

The ultimate goal is to solve the RTE simultaneously with the heat transfer equation (HTE) and the Navier-Stokes equations to fully describe the fluid flow and temperature fields within the receiver as a function of the incoming intensity distribution. The difficulty is interfacing these equations: the RTE describes the ballistic transport of photons inside a medium which has a certain optical thickness; the HTE describes the diffusion of heat thru molecular and lattice vibrations, and the Navier-Stokes equations describe the motion of the fluid particles themselves [61], [62].

That simultaneous analysis is beyond the scope of this thesis; Nave presents a numerical tool for cases where scattering can be ignored [63]. However, a simplified one-dimensional analytical model can be used to give insight into the system's behavior. The HTE in one dimension, x, is:

$$\rho c_p \frac{\partial T}{\partial t} = k \frac{\partial^2 T}{\partial x^2} + q_{gen} \tag{2.7}$$

where q_{gen} is the volumetric heating from the incident solar radiation, including any volumetric heat loss due to thermal re-radiation from the medium at high temperatures, which is simply the negative of divergence of the radiative heat flux:

$$q_{gen} = -\nabla \cdot q_r \tag{2.8}$$

Scattering effects can assumed to be small compared to absorption for pure fluids such as molten salts, and the RTE can be simplified to: [53], [64]

$$\frac{dI_\lambda}{dx} = \kappa_\lambda I_{b\lambda} - \beta_\lambda I_\lambda \tag{2.9}$$

A multi-region approach can be used, whereby a gray medium approximation is used so that the extinction coefficient is equal for all wavelengths in the region; that is $\beta = \beta_\lambda$ [52], [64]. For the simplified case where only the incident solar radiation is considered, omitting the blackbody emission term, the volumetric heating becomes: [65], [66]

$$q_{gen}(x) = -\frac{dI}{dx} = \beta I_0 e^{-\beta x} \tag{2.10}$$

Lenert presents numerical solutions to Eqs. (2.7) to (2.9) using a two-region gray body approach for no-flow volumetric receivers [64]. Region I represents wavelengths smaller than 2 μm, while Region II wavelengths are greater than 2 μm. Figure 2.7a depicts the volumetric heating profile for a receiver with a Region I optical thickness is $\beta L = 4$, such that 98% of the incident solar radiation is attenuated within one pass of the receiver. The optical thickness of Region II is set to infinity, such that the fluid is a black body radiator in the IR. Figure 2.7b shows

the developing temperature profiles over time for the same receiver, subject to surface convection and radiation losses.

Initially the temperature profile closely resembles the heat release profile; however, an inverted temperature profile develops as time progresses. The gradient at the top of the receiver is dominated by the heat loss from the top surface, while volumetric heating dictates the profile towards the bottom of the receiver. As the temperature of the fluid increases to high temperatures (above 900 K), the medium begins to radiate in the spectral region which is no longer "optically thick," as predicted by Eq. (2.5). Hot spots inside the receiver will re-radiate more intensely so the temperature profile begins to average out.

To further avoid hot spots and minimize system complexity, natural convection within the salt is needed. Temperature inversions beyond critical values (i.e., Rayleigh numbers exceeding the critical value for the particular geometry and molten salt) will incite buoyancy driven flow and natural convection loops. This can be designed into the pond using numerical methods [63]. Preliminary results using the full variable-property Navier-Stokes equations to produce direct numerical simulations show thermal gradients can be used to create plumes to mix the salt [67].

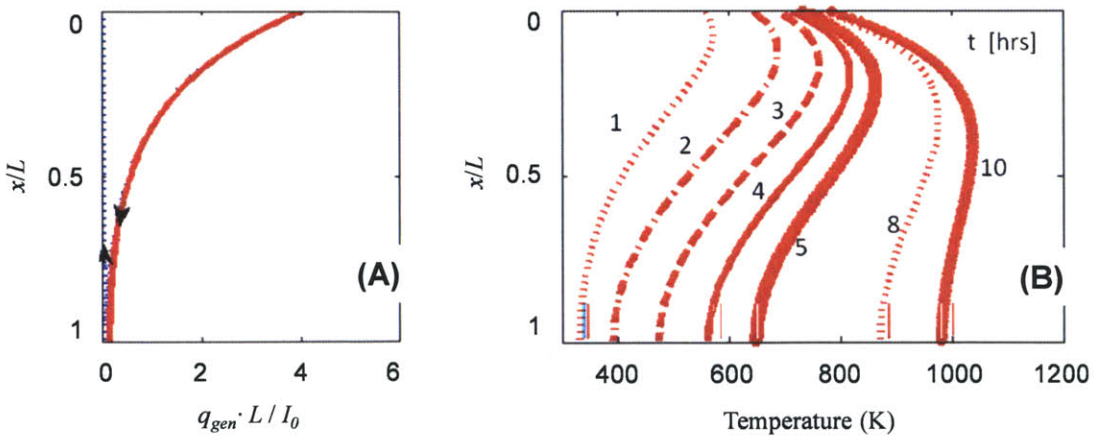

Figure 2.7 - Volumetric absorber heating profile
(A) Volumetric radiative heating profile, $\beta L = 4$. (B) Temperature distribution within fluid. From [64]

Non-imaging lid

The hillside heliostat field allows for direct entry into the molten salt pond for a majority of rays; any that are reflected or off-target can be redirected or absorbed by a grazing incidence, non-imaging cover over the pond (Fig 2.3). An important design goal is to shape the cover to function as a diffuse reflecting concentration booster, not unlike the CPC units used in beam down towers [68], [69]. This cover serves two additional purposes: to reduce losses to the environment and to condense a majority of the vaporized salt which otherwise would be carried away.

Both the molten salt pond and the lid will exchange heat with each other and to the environment by radiation, convection and conduction; the primary heat transfer mechanism is through radiation. The system cover will be lined with refractory firebrick and backside cooled, so the salt vapor rises and condenses on the inner surface of the cover, akin to frost collecting on evaporator coils within a refrigerator. The resulting white surface will grow until the thickness results in a thermal resistance that condenses the salt vapor, but the surface continually melts and returns liquid salt to the pond. The liquid/solid interface is expected to act as a diffuse reflector to incoming light that reflects off the surface of the salt, which serves to further insulate the pond and reflect radiation into the molten salt. Solidified salt has a very high reflectivity in the visible and near-infrared spectrum ($\rho \sim 0.9$) and behaves nearly as a Lambertian reflector; liquefied salt will be subject to grazing-angle Fresnel surface reflections and as such, much of the light impinged onto the lid will be reflected back to the pond [70]. The energy that is transferred to the lid is from lower-temperature, longer wavelength radiation from the salt surface. Only a small fraction of incoming photon energy is converted to thermal energy at the lid.

The vapor pressures of molten salts are fairly low, on the order of 0.001 bar for chloride salts at 900 °C. As a result, the overall fuming rate is low, given as 0.2 kg per square meter of exposed salt area per hour for a chloride salt bath at 870 °C [71]. For the 5 m deep x 25 m diameter, 180 $MW_e h$ system discussed previously, this equates to roughly 100 kg/h, or less than

0.06% of the entire salt mass. Lower temperature nitrate CSPonD systems will have lower salt vapor pressures and mass transfer, and reduced radiative transfer between the salt surface and the lid as compared to higher temperature carbonate or chloride salt systems.

The lid is not dependant on mass transfer for cooling – active cooling will be employed to obtain the desired lid operating temperature. Cooling loops would be concentrated in high heat flux regions, and various zones can be employed for temperature control throughout the lid. It may be found that the optimal lid design is not isothermal, but has varying temperature to limit radiative transfer and convective losses. As a result, the shape and temperature of the lid, and aperture location with respect to the lid structure, can be configured to minimize losses to the environment [72-76].

The collected cover energy, unique to CSPonD systems, can vary from 2-20% of the incident solar power and this intermediate-temperature heat is used elsewhere in the plant [77]. This depends primarily on the plant layout: hillside topology, operating temperatures, and seasonal and diurnal position of the sun. As analyzed by Ghobeity et al., in a dual-purpose desalination and electricity production plant using the CSPonD concept, heat collected by the cover can be used for preheating feed water to the steam generator or desalination feed water [77-79]. The CSPonD receiver can thus provide two heat extraction loops: low temperature from actively cooling the pond cover, and high temperature directly from the heated molten salt. These can be optimally controlled to maximize power output, even when the sun is not shining.

Integral Divided Thermocline Storage

The top surface of the salt needs to remain at a constant level for consistent solar absorption; hence, the tank is split into two zones with a moving barrier plate. The top zone is the hot salt side, and the bottom zone is the cold salt side, as shown in Fig. 2.8. A corrosion and creep resistant "divider plate" axially separates these two zones, providing a physical and thermal

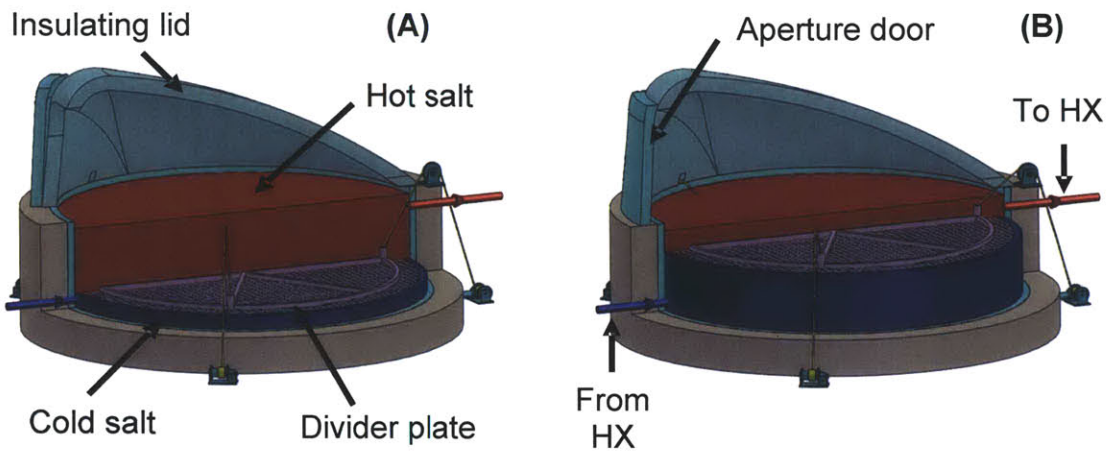

Figure 2.8 - CSPonD storage system at various states of charge

(A) At end of a sunny day, divider plate has moved down and the hot salt region is fully charged. (B) After prolonged heat extraction without solar input, the divider plate has moved up and the cold side is full.

barrier between the thermally stratified hot and cold layers within the tank. The divider plate is well insulated and near-neutrally buoyant; it is moved axially by small actuators with negligible power consumption to maintain the hot and cold salt volumes required for continuous operation. Hot salt is extracted from the top of the receiver tank, sent to a steam generator and returned to the bottom of the receiver tank at a lower temperature.

There is a generous annular clearance between the divider plate edge and tank walls. This clearance prevents binding and allows for annular salt flow past the plate during daytime charging of the system, where colder salt from below moves past the annular clearance space between the barrier plate and tank wall to be reheated. Incoming light penetrates deeply and a portion of it will be absorbed on the divider plate causing convection currents, heating the hot salt to a uniform high temperature. As the system collects more energy and the top hot section grows in thickness, the divider plate is lowered in the tank. Nighttime energy extraction, with a closed aperture, is accomplished by raising the divider plate, following the natural thermocline progression upward

as the hot salt volume decreases. As a result, high-temperature steam can be provided even as the average temperature of the salt in the tank decreases.

Figure 2.8a shows the end of a sunny day: the divider plate has moved down and the hot side is fully charged. Figure 2.8b depicts the system after a prolonged period of heat extraction without any solar input: the aperture is sealed with an insulated door, reducing losses to the environment and the divider plate has moved up and cold side is full.

Design and control

The annular gap between the divider plate and tank walls can have a significant effect on system performance. An excessively large gap will fail to limit conduction, mixing and radiative transfer (which dominates as temperatures increase and the molten salt begins to radiate more energy in shorter wavelengths where the extinction coefficient is low) between the hot and cold salt layers; a very small gap may cause jamming due to thermal strains on the divider plate, and could possibly create salt freezing failures between the divider plate and tank walls, immobilizing the system. As the divider plate is lowered when the aperture is open and the tank is being heated by sunlight, colder salt from below moves past the annular clearance space between the barrier plate and tank wall to be reheated (Fig. 2.9). Semenyuk describes a means to calculate exergy losses for mixing two working bodies differing only in temperature [80]. For a nitrate CSPonD receiver with hot salt at 823 K, cold salt at 523 K and ambient temperature of 300 K, the exergetic mixing efficiency (1 = no losses) is found as 0.935; this value approaches 1 in higher temperature systems as the salt temperatures increase.

The salt-filled annular clearance between the loose fitting divider plate and tank walls acts as a buffer by limiting thermal gradients as the divider plate moves. Degradation of the tank walls due to thermal shock is reduced compared to well-sealed barrier thermoclines with sharp thermal interfaces [39]. Clearly, for constant divider plate speeds, the blow-by salt velocity is inversely proportional to the annular gap area.

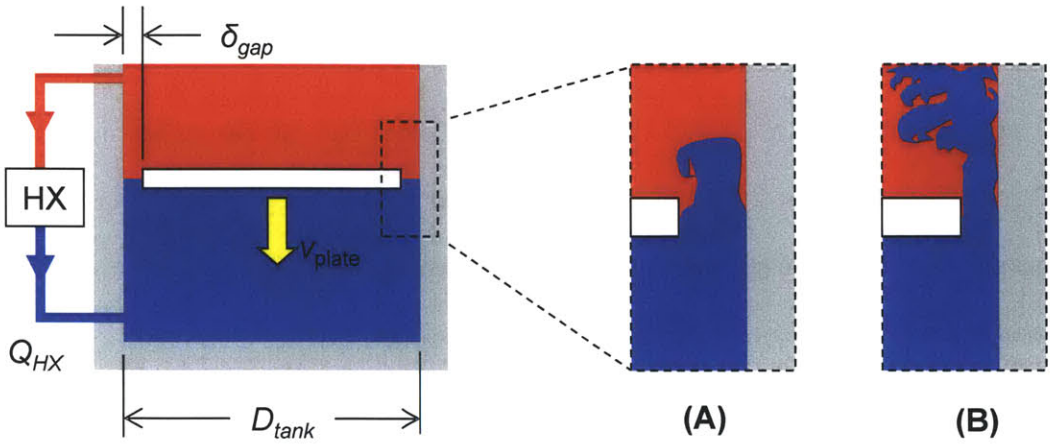

Figure 2.9 - Schematic of divider plate motion during charging
Salt blow-by plumes (A) wide gap: weak, low momentum; (B) narrow gap: high momentum.

For a cylindrical tank, with gap clearance δ_{gap} much less than the tank diameter D_{tank}, the annular gap area can be approximated as:

$$A_{gap} = \pi D_{tank} \cdot \delta_{gap} \tag{2.11}$$

The total volumetric flow of the gap blow-by salt is the sum of the heat exchanger volumetric flow Q_{HX} and the volume of salt displaced by the moving divider plate, acting as a piston:

$$Q_{gap} = Q_{HX} + \pi D_{tank}^{2} \cdot v_{plate} \tag{2.12}$$

where v_{plate} is the velocity of the plate. The average velocity of the annular salt flow becomes:

$$v_{gap} = Q_{gap} / A_{gap} \tag{2.13}$$

As depicted in Fig. 2.9, different gap clearances will result in different flow and mixing patterns. Previous work on buoyancy-driven laminar thermal plumes and turbulent thermal and

jet plumes provides insights into probable plume geometry, fluid entrainment mixing and plume spreading angles [81-83]. Figure 2.9a shows a relatively wide clearance, which results in very slow velocities past the divider plate, and weak laminar plumes of cold salt. However, Fig. 2.9b depicts a gap sized to ensure a well-mixed plume of cold salt. In this case, cold salt has enough momentum to penetrate far into the heated salt region; subsequent Rayleigh instabilities (to be discussed in Chapter 4) and the laminar-turbulent or fully turbulent nature of the plume promotes good mixing. However, relative "blow-by" salt velocities are slow (much less than 1 cm/s for a nominal 10-20 cm annular clearance on typical systems) during the daily "charging" downward motion of the plate, displacing fluid and pumped cold salt returning from the heat exchanger.

Additionally, the gap should not be made so small that the expelled molten salt creates a high drag force as the divider plate is positioned. A very small gap would result in high velocity salt blow-by flow, with increased flow resistance; a large drag force on the divider plate would require larger positioning actuators. An estimate for the drag force on the divider plate can be found as:

$$F_{drag} = \tfrac{1}{2}\, \rho_{salt}\, v_{gap}^{2}\, C_d\, A_{plate} \tag{2.14}$$

where ρ_{salt} and A_{plate} are the density of the molten salt and area of the divider plate, respectively. For a circular flat plate perpendicular to the fluid flow, the drag coefficient, C_d, is 1.12 [61].

Modifications to the flat concentric disc divider plate geometry can be envisioned which alter the thermal and physical separation and mixing characteristics. For example, bypass holes, perforations, or grooves of appropriate size can be employed on the divider plate to alter performance, creating areas of differential flow which cause plume instabilities and promote mixing in the upper region. Figure 2.10 illustrates a design flowchart for obtaining desired divider plate gap performance.

The divider plate would likely be a ribbed steel or corrosion resistant alloy plate. Without insulation, however, it would be heavy; yet only a modest thickness of insulating firebrick is

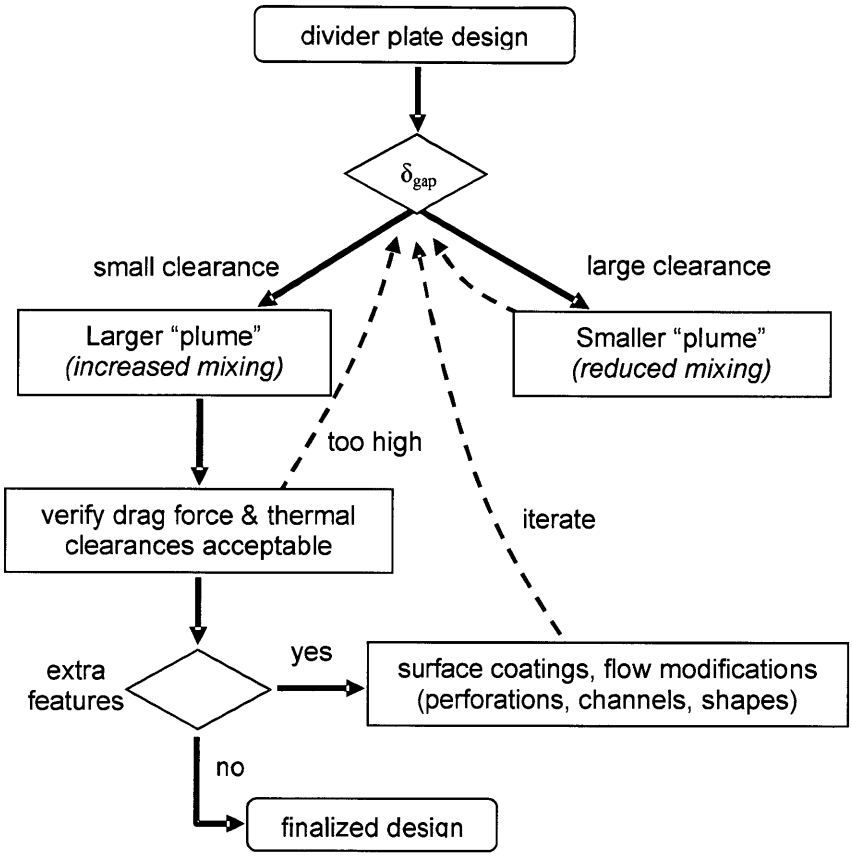

Figure 2.10 - Design process for divider plate gap

needed to make it near-neutrally buoyant in the molten salt. Alternatively, a hollow tubular structure can function to thermally separate the hot and cold sides while maintaining near-neutral buoyancy. The hollow chambers could be designed with a slight internal pressure at the operating temperature to minimize hydrostatic stresses in the chamber walls. This could be achieved by making the divider from a series of capped pipes. Another method of construction would entail a fluid-tight outer shell, utilizing insulative filling material. The upper surface of the divider plate would likely be made from stainless steel or other suitable high temperature alloy, compatible with molten salts. Over time, a rough oxide layer will form, increasing the surface's absorptivity

and causing the reflected energy to be diffusely scattered. This will enhance the development of hot spots and create a temperature inversion within the upper hot salt layer, initiating convective mixing cells. The upper surface of the divider plate may even employ three-dimensional features to magnify this effect.

As identified by Lata et al., thermal deformations in service pose additional concerns [84]. With the upper surface of the divider plate at the hot temperature, and the lower surface at the cold temperature, an overall state of bending deformation is developed due to thermal strains. This spherical domed shape would decrease the working height of the storage tank, in addition to potentially triggering structural problems in the divider plate. Not to mention that a curved divider plate would alter the naturally plane interface between the two salt layers, and thus, the overall effectiveness and insulating properties of the assisted thermocline would be altered. However, simply adding ribs and other features to increase the geometrical stiffness and/or preforming the divider plate can alleviate all of these problems. Additionally, ribbing or corrugating reduces the chance of local buckling – mitigating the risk that the divider plate would morph into a giant wavy "potato chip" over time.

An optimal design will be near-neutrally buoyant and well insulating, yet still promote adequate mixing of the annular salt plume. When these objectives are achieved, the drag and restraining forces on the divider plate become negligible; the radial clearance between the divider plate and the tank walls creates Stokes-like flow of the slowly moving plate and salt. As a result, low cost actuators can be utilized to position the slowly moving divider plate. An additional element of operational control is gained by actuating the divider plate, avoiding raft instabilities and jamming failures inherent in passive divided thermocline systems. Figure 2.11 depicts a possible control scheme for divider plate position in the tank. This strategy is illustrated in Fig. 2.12 over two day/night cycles: one "ideal day" and one mostly cloudy "transient day." As a general rule, if the instantaneous solar input to the CSPonD receiver is less than the rate of heat extraction (equal to the mass flow rate of salt to the heat exchanger multiplied by the product of

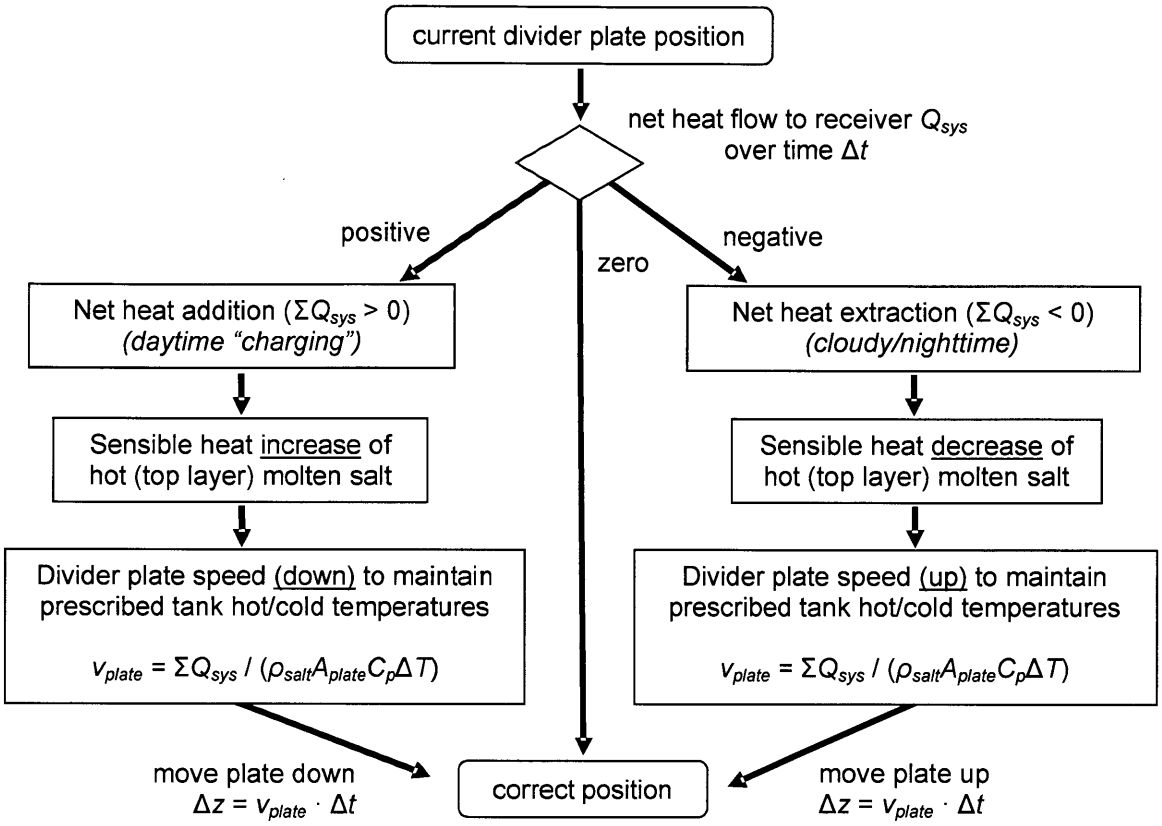

Figure 2.11 - Position control strategy for divider plate
C_p is the specific heat capacity of the molten salt.

the specific heat of the salt and its corresponding temperature drop) , the divider plate would be moved up in the tank to maintain the required hot & cold volumes. Figure 2.12a illustrates a CSPonD receiver designed to provide continuous, 24/7 power extraction; Fig. 2.12b depicts the same CSPonD receiver used in a larger load-shifting application for several hours each afternoon and early evening. In both cases, the CSPonD receiver is able to supply the power cycle with the design load regardless of instantaneous or diurnal solar variations.

Greater power cycle efficiencies can be realized with the use of larger steam turbines. This can be accomplished with larger CSPonD receivers or several smaller units feeding a

common power block. However, many locales will favor the use of CSP-generated power for peaking purposes, with greatly reduced storage needs, as in Fig. 2.12b. After peak demand subsides, heat extraction can be stopped and nighttime losses from the well-insulated receiver are minimal.

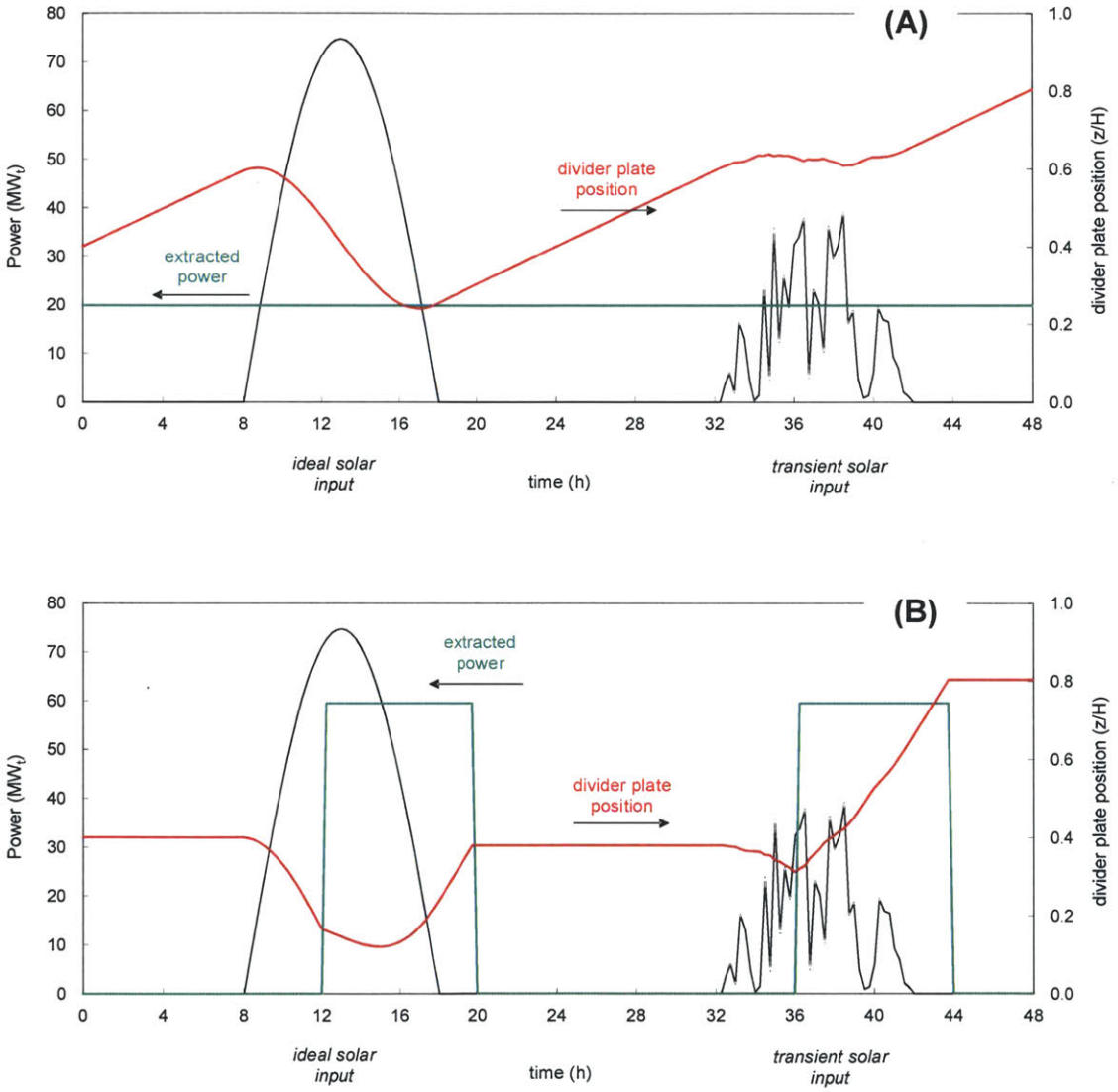

Figure 2.12 - Simplified divider plate positioning example for two day/night cycles
Ideal solar input (left) and transient, cloudy solar input (right).
For a constant 20MW$_t$ extraction system (A) and a load-shifting eight hour, 60 MW$_t$ system (B).

Heat extraction

The power block salt pumps and heat exchanger/steam generator considered for a near-term nitrate salt CSPonD system are commercially available and have been proven on CSP parabolic trough plants with separate molten salt storage systems [34], [47]. The CSPonD system could likely support increased power cycle temperature requirements and the two zone tank could still be used. A high temperature CSPonD could supply hot salt directly to the power block heat exchanger; alternatively, two salt loops can be used where hot salt is blended with some cold salt recycled from the heat exchanger to create a constant salt temperature entering the heat exchangers. The power extraction system in high temperature designs can be leveraged from salt handling and power cycle technology developed for the molten salt reactor (MSR), part of the Aircraft Nuclear Propulsion Program [85]. The MSR program successfully tested reactor designs with salt temperatures over 800 °C, a primary salt to secondary salt intermediate heat exchanger, and a secondary heat transfer loop with a pump that rejected heat to an air-blast heat exchanger. Liquid salt pumps were tested up to 6,000 L/minute at temperatures exceeding 700 °C [86], [87].

Typical molten salt systems employ vertical shaft centrifugal pumps which insulate and mount the drive motor above the salt storage tank. A conventional bearing assembly supports a long vertical shaft and impeller, with salt-lubricated lower bearings suspended into the liquid salt tank [20], [88]. The pump could be mounted towards the rear of the CSPonD DAR with a salt pickup located to extract hot salt from the upper region of the tank. The cold salt return can be accomplished with a vertical pipe whose exit is near the tank bottom, preferably diametrically opposite the hot salt pickup. This accomplishes two design simplifications: it eliminates any radial protrusions into the tank walls, and establishes a unidirectional flow pattern within the receiver. However, a cold salt return pipe which does penetrate the tank at a lower elevation would allow for a passive gravity draining, an ideal countermeasure in a worst-case emergency tank draining and shutdown.

Weir flow extraction

As an alternative to the vertical shaft centrifugal pump method, a weir, or waterfall edge can be built into the back wall of the receiver. Similar to "infinite edge" pools where water spills over a horizontal edge into a catch basin and is pumped back into the pool, a molten salt weir would provide a simple means of hot salt extraction for the heat exchanger, before being pumped back into the lower zone of the divided thermocline tank. There are several precedents besides swimming pools for the design; high temperature variants include chemical refining bath skimmers and glass tank furnaces, whereby a notched platinum weir plate is used to limit molten glass flow at temperatures approaching 1300 °C [89], [90]. A CSPonD weir plate need not be made from costly refractory alloys; chromium-nickel high temperature alloys will suffice.

Weir-based salt extraction would provide several benefits. Any surface scum or debris would be continually swept over the weir, providing a clean salt surface for light penetration. Further, as in pool systems, a weir reduces liquid-container surface wave propagation – in effect "smoothing" the pond should a severely choppy surface develop. Additionally, the catch basin or trough below the weir can be sized to accommodate thermal expansion of the entire volume of salt, so that a separate expansion tank is not needed to keep the salt surface at a constant height within the receiver.

A centrifugal pump can be used to flow the salt from the catch basin through the heat exchanger, thereby forcing cold salt to return to the bottom of the tank, as shown in Fig. 2.13a. Alternatively, the weir's position can be controlled to alter the static head present in the catch basin. If the nominal pressure drop on the molten salt side of the heat exchanger is designed to correspond with the nominal salt level in the catch basin, alterations to the catch basin level will cause a corresponding change in flow through the heat exchanger. Figure 2.13b depicts a schematic of such a system. The cold return would obviously need to be pumped back into the CSPonD DAR – but the colder salt temperatures would dramatically improve pump reliability

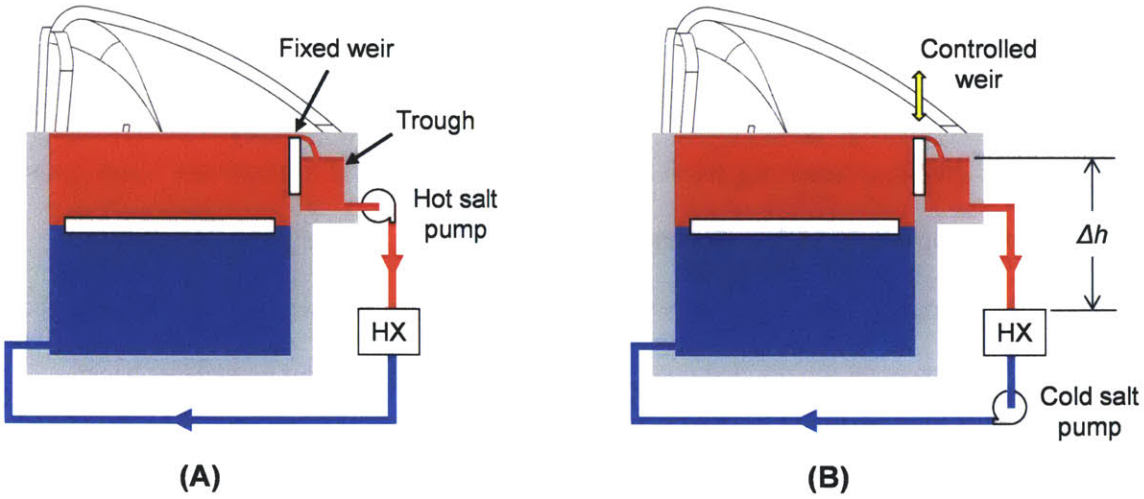

Figure 2.13 - Weir hot salt heat extraction scheme
Weir provides "skimming" action on pond surface: (A) hot salt can be pumped to HX; (B) static pressure head in catch basin can be used to control flow to HX.

and performance. An order-of-magnitude check shows the concept feasible only if a low pressure drop heat exchanger is employed: a 5 m nitrate solar salt (density of 1740 kg/m^3 at 550 °C) column results in 85 kPa static pressure head. Existing nitrate salt evaporators and superheaters have been designed with full load salt side pressure drop limits of 450 kPa (65 psi) [47].

System sizing considerations

In the range from 1 kW_e to 100 MW_e, power block efficiency increases with size, while the cost per unit power produced decreases. Conversely, due to the divergence of the sun's rays, light spillage and collection efficiency decreases with increasing field area and heliostat range. Even with perfectly focused heliostat optics, the sunspot image at the receiver is equal to the heliostat range multiplied by angle subtended by the sun, 0.52° (0.09 radians). As an example, a range of 10 m results in roughly a 90 cm diameter image; a one-kilometer range creates a 9 m diameter sunspot with appropriately spherically shaped mirrors. For each locale, there is an

optimal heliostat field size which maximizes collected power while still maintaining a small solar image and aperture size to so radiative losses are manageable.

Thus the CSPonD system may be deployed in arrays with the option of multiple CSPonD systems feeding a common central power generation plant. There are large economics of scale associated with steam turbines; but, there are complications in long-distance heat transport and coupling multiple power sources. Fortunately there are examples, such as multiple coal plants including the Tennessee Valley Authority's Bull Run plant, where two boilers feed a common steam plant. More recently, up to 8 modular nuclear reactors are planned to feed high-temperature steam to a single turbine in a Chinese program to develop modular high-temperature nuclear reactors. A two-reactor station is under construction to demonstrate the reactor and combined steam system [91].

Materials selection

Molten salt selection

Janz has compiled a comprehensive database with a wide array of property data for thousands of molten salt mixtures of varying composition [59], [92]. More recently, Williams has examined molten salts for use in the Next Generation Nuclear Plant (NGNP) [87]. As previously mentioned, some salt eutectics that appeared ideal on paper (e.g., low melting point, wide operating temperature range) were found to be reactive in lab furnace melting experiments. For example, the presence of a moist atmosphere triggered the formation of an acidic gas (HCl) in a candidate magnesium-sodium-potassium chloride salt mixture above 450 °C. While these salts may be ideal for use in sealed, non-oxidizing NGNP cooling loops, using similar salts at high temperatures would necessitate an inert purge gas over the CSPonD system – possibly requiring a transparent aperture window. In keeping with the intent to develop a low-cost, open receiver

system, there is renewed interest in alternate salt mixtures capable of operating in air without degradation.

Fortunately, commercially available molten salt baths, successfully used in open-bath metallurgical heat treating processes for several decades, provide promising salt candidates for CSPonD receivers. There is a large industrial experience base with water-soluble, inorganic salts used in the thermal processing of metal components moved in and out of the salt bath [71], [93]. Low-cost eutectic salt mixtures achieve the desired operating ranges: low temperature (130-600 °C) quenching/tempering nitrate-nitrite and nitrate salts; high temperature (400-800 °C) tempering/drawing carbonate salts; and neutral high-speed hardening (850-1100 °C) chloride salts (Fig 2.14). All salts are very fluid at their respective working temperatures, with low viscosities and surface tensions. Table 2.1 lists common metallurgical heat treatment salt compositions and representative properties.

Figure 2.14 - Open air NaCl-KCl salt bath at 900 °C for metal heat treating (Picture taken at Metallurgical Solutions, Inc. in RI)

The heat treating industry has developed standard methods to test and control the salt chemistry using chemical rectifiers and periodic removal of metallic oxides which settle to the bottom of the tank. The rate of impurity buildup will be much lower for CSPonD than for a heat

treatment bath with its daily throughput of steel parts. Regardless, it is anticipated that impurities in suspension will have a significant effect on the attenuation properties of the salt and will therefore have to be closely monitored and controlled.

Table 2.1 - Representative metallurgical heat treatment salts appropriate for CSPonD

Salt type	Composition (wt. %)	Freezing point (°C)	Decomposition temp. (°C)	Volumetric heat capacity (kJ/m^3-K)
Binary nitrate (solar salt)	60:40 $NaNO_3$:KNO_3	222	593	2920
Ternary carbonate (Cartescal)	32:35:33 Li_2CO_3: K_2CO_3:Na_2CO_3	397	850	3560
Binary chloride (#4 high speed hardening)	60:40 NaCl:KCl	660	1000	1740

Nitrate and chloride data from [92], [94]*; carbonate from* [92], [95].

Upon first glance at Table 2.1, it would appear that the carbonate ternary eutectic salt is an excellent choice for all CSPonD DARs. It possesses a relatively low melting point and a wide operating temperature range, and has a high volumetric heat capacity. Unfortunately, this salt contains a significant amount of lithium carbonate, which increases the salt price relative to binary mixtures which contain cheaper commodity-based salts of sodium and potassium. Indeed, the ternary carbonate salt may prove economical on small-to-medium size systems where the cost of salt needed is small in relation to the overall system cost. Water introduced into carbonate salts has been shown to cause hydrolysis of the molten solvent, forming bicarbonate and hydroxide ions [96]. Purification and regeneration can be accomplished by bubbling carbon dioxide through the melt.

Nitrate salt mixtures are well known in the thermal processing industry, and favored in CSP and chemical processing applications for their relatively low melting temperatures and

chemical stability up to their peak operating temperature. A common ternary eutectic salt is potassium nitrate, sodium nitrite and sodium nitrate (i.e., Hitec® Heat Transfer Salt: 7:53:40 wt.% $NaNO_3$:KNO_3:$NaNO_2$) which melts at 142 °C and can be safely heated to 450 °C. However, when heated to higher temperatures in an open system, the nitrite is slowly oxidized by atmospheric oxygen into nitrate, which raises the freezing point.

The sodium-potassium nitrate solar salt (60:40 wt.% $NaNO_3$:KNO_3) previously mentioned as ideal for a near-term CSPonD system, which is widely used for CSP thermal storage, has a melting point of 222°C. In contrast to the carbonate eutectic, water has a significant solubility in the binary nitrate melt; it can be rapidly and reversibly taken up or removed from the melt up to 600 °C. Over the temperature range 500-620 °C, there is thermal decomposition of the nitrate ion to form nitrite and oxygen [97]. Additionally, pure carbon dioxide attacks the melt at all temperatures above 250 °C, producing carbonate ions. The solubility of carbonate is strongly temperature dependent and is approximately 5 mol% near the eutectic point [98]. Such a high solubility presents little concern for a thermal storage system because an extremely long time would be required to absorb enough CO_2 from the atmosphere to saturate a large mass of molten salt, however thermal cycling may result in carbonate precipitation, causing problems in pipes and the heat exchanger. If carbonate and nitrite buildup is a significant problem, then regeneration of clean melt can be achieved by bubbling pure nitrogen dioxide, or a nitrogen dioxide/oxygen gas blend through the salt [99]. Carbonate ions, dissolved water and nitrite ions can be detected by direct in situ electrochemical measurements; the CSP plants using nitrate salts have not had problems regarding salt contamination or impurity precipitation [7], [34], [47]. However, both nitrate and nitrite-nitrate salt mixtures can produce hazardous and corrosive nitric acid fumes if heated beyond 700 °C.

The long term goal is to design a CSPonD system capable of using very low cost, stable salts, such as the sodium-potassium chloride mixture (60:40 wt.% NaCl:KCl) that can operate

safely up to 1000°C. Such a high temperature source could easily power more advanced, efficient power cycles, increasing overall solar-to-electric efficiency. As mentioned previously, some chloride salts can generate small quantities of gaseous hydrogen chloride as a hydrolysis product during their melting. Hydrogen ions can be introduced into molten salts from atmospheric moisture, from the bath lining, or it can be present in incompletely dried salt. The quantities are far below any hazardous limits based on thermodynamic calculations and industrial experience. If required, there are two control strategies: (1) salt additives (i.e., sodium hydroxide) to reduce the thermodynamic potential for HCl generation, and (2) controlled atmosphere blanketing of the salt to minimize moisture input. Fortunately, the potential for HCl generation using the binary chloride salt is low, as evidenced by decades of successful use in the metallurgical industry. Common chloride salt rectification methods include bubbling gaseous methyl chloride through the salt, or adding ammonium chloride pellet blends as needed.

The short list presented of three candidate salts should not be considered final by any means. Much research is being conducted on new salt formulations which have reduced freezing temperatures and wider operating ranges, in the hopes of developing more robust sensible heat thermal storage fluids. For example, Bradshaw and Brosseau describe quaternary nitrate salt mixtures which melt at temperatures below 100 °C and have thermal stability limits beyond 500 °C [98], [100]. These mixtures contain calcium nitrate and lithium nitrate to depress the melting point of a sodium-potassium nitrate solar salt mixture. These and other candidate salt formulations can be evaluated for use in CSPonD systems based on thermal and optical properties, cost and availability.

Safety

Molten salt baths create a special set of hazards due to their high working temperatures. The salts previously described are not inherently dangerous to the environment when at ambient temperature: solar salt is used extensively as fertilizer and the components of the binary chloride

salt are used in food preparation. Lithium, potassium and sodium carbonate are used in medicines, soaps and water softening agents, respectively. But molten salts can create burns, fires or even trigger explosions if the conditions are right. Lipsett describes violent explosions and damaging shock waves as molten metals come into contact with water – molten salts can have the same behavior [101]. Care must be taken so that the salt pond is thoroughly protected in the case of inclement weather and driving rain.

Nitrate and nitrite salts, while operating at lower temperatures than other molten salts, can cause explosions. These mixtures are powerful oxidizing agents, and in the molten state they become highly active [102]. This requires extra care in handling and temperature control, because, as mentioned, nitrate salts are subject to rapid breakdown with emission of toxic and reactive fumes when overheated.

The use of quartz windows was considered to reduce thermal losses and eliminate mass transfer across the aperture. However, as mentioned in literature and as observed in testing, quartz crucibles in contact with many salts tend to lose their optical clarity with time [103]. The salts chosen as appropriate for CSPonD systems have limited toxicological and environmental effects should some condense outside the receiver; however, any system which regularly loses heat transfer fluids (other than steam) to the environment will likely be denied an operational permit. Fortunately, the salt bath heat treating industry provides guidance. Taken from the ASM Handbook on heat treating, regarding the evaporative nature of a NaCl-KCl bath [71]:

> *Salt bath furnaces that operate at temperatures above 650 °C (1200 °F) will fume.... Sodium chloride and potassium chloride are both edible; however, in large quantities they can be a nuisance. The best way to overcome this nuisance is to capture it at the source.*

Salt bath furnaces employ ventilation hoods, either offset from the salt surface or directly overhead to capture salt fumes at their source (Fig. 2.15). The salt vapors are drawn into the intake, and condense on the intake plenum. The accumulated salt is scraped off during routine

maintenance. A similar system can be installed above the aperture or integrated into the lid of the CSPonD receiver, perhaps utilizing an intake plenum with an automated salt scraping and collection system. Salt vapor and thermal losses can also be mitigated with the use of air curtains installed across the aperture [104].

Figure 2.15 - Side draft fume hood used to collect salt vapors
Fume extractor at rear of 600 °C tank with condensed salt buildup
(Picture taken at Metallurgical Solutions, Inc. in RI)

Pond construction

There is a wealth of knowledge in regards to commercial salt bath furnace construction [93]. Stainless or carbon steel tanks are used to contain nitrate salts, depending on their operating temperatures, and are externally heated using combustion or resistance heating methods. Typical high temperature chloride salt baths utilize internal mortarless refractory firebrick insulation, followed by a mild steel outer casing and external ceramic fiber insulation. A "freeze plane" is formed within the alumina-silica firebrick, and as a result, the steel tank is not exposed to corrosive molten salts. These internally-insulated tanks are heated using submerged or over-the-top electrodes, whereby electrical current (on the order of kiloamperes AC) heats the salt through Joule heating.

A similar internally-insulated design is used to construct the CSPonD receiver. The tank is internally insulated with mortarless insulating refractory brick, whose thermal resistance and mass limits temperature swings at the mild steel tank shell, as depicted in Fig. 2.16 [105]. If needed, a thin corrugated alloy liner can be employed which reduces erosion and spalling of the refractory brick in the tank [106]. As demonstrated in CSP hot salt storage tank designs, thin, thermally conductive corrosion-resistant liners can be used to reduce axial thermal gradients and thermal shock to the internal firebrick from fluctuating salt levels. This internally-insulated design has been shown to be more cost-effective than a stainless steel tank with external

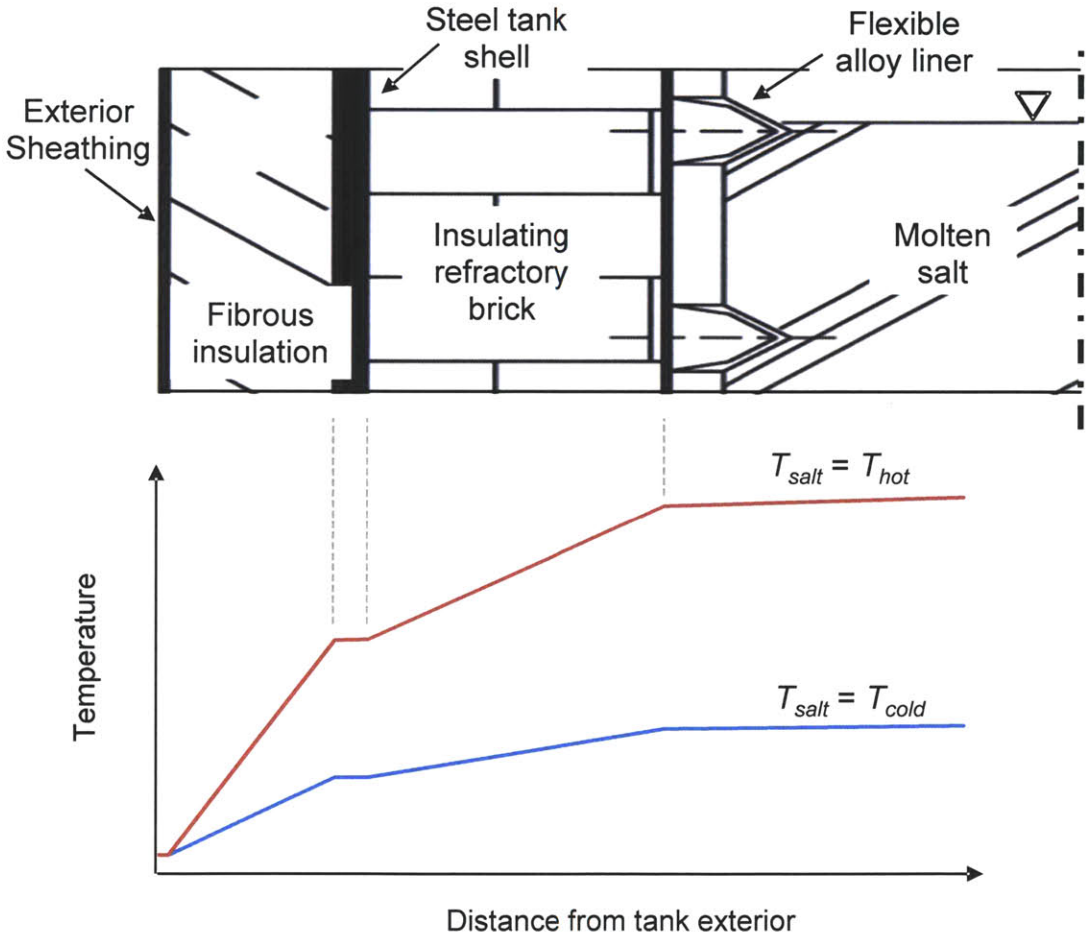

Figure 2.16 - Tank wall insulation schematic
Cross-section adapted from Kolb [104] and Gabbrielli and Zamparelli [105].

insulation [106]. Metallurgical salt baths have proven commercial "super-duty" alumina/silica or pure silica fireclay bricks adequately resist corrosion from molten nitrate or chloride mixtures [71]. Recent tests have verified the cyclic stability of silica particles in molten sodium and potassium nitrate at the temperatures considered [37]. The hydrostatic pressure is transferred directly to the steel vessel through the flexible liner and the firebrick layer. Brackets can be welded to the steel shell to provide stability of the firebrick column. Electric heating elements can be embedded in the tank floor insulation as a contingency, to prevent the salt from freezing during extended periods of inclement weather.

The lid and closeable aperture doors can be lined with refractory bricks or lightweight insulating refractory board. As mentioned previously, the cover will be backside cooled to enhance the buildup of salt that condenses on the inner surface of the cover. However, the salt vapors would also condense on the inner surface of quartz aperture window, reducing its effective transmission. This fogging is a primary reason why a quartz window for the aperture is not being considered.

The external surface of the receiver is wrapped in a layer of ceramic fiber insulation, which is in turn, covered by a thin aluminum protective cladding. The entire system is surrounded within a secondary containment area, whereby molten salt can gravity-drain into a catch basin or culvert in cases of severe emergencies or major overhauls [34].

Corrosion considerations

While metallurgical salt baths have short (1-3 year) service lives before being rebuilt, CSP systems utilizing molten salts as a thermal storage medium need to operate for 20 years or more. As a result, extensive research has been conducted to determine the corrosive effects of molten salts on container and piping materials [6], [37], [47], [88], [107-110]. Similar to heat treatment baths, nitrate salts are compatible with stainless steels and mild steels depending on operating temperatures. Goods et al. describes solar salt (nitrate) corrosion rates as linear with

respect to time [108], [109]. At 570 °C, the annualized rates of metal loss were found to be between 6-15 μm/year for AISI type 304 and 316 stainless steel specimens, depending on salt impurity content. The same mixtures at 316 °C result in corrosion rates of 1-4 μm/year in A36 mild steel. Similarly, Gabbrielli and Zamparelli suggest the use of AISI type 321 stainless for hot salt tank liners, whereby the increased alloy content reduces corrosion rates [106]. A corrosion allowance can be incorporated into metallic CSPonD tank components, such as the flexible tank liner.

Carbonate salts are known to be compatible with stainless steels, nickel-based alloys and high chromium alloys up to 700 °C; electrofused alumina ceramics can be used with oxidizing atmospheres up to 1000 °C [111]. However, molten carbonates can dissolve significant amounts of silica; any refractory materials in contact with carbonate salts should not contain any significant silica content.

Chloride salts are more troublesome, due to their increased working temperatures and inherent corrosive nature with ferrous alloys. As Seybolt writes [112]:

> *When Ni-20Cr alloys and stainless steels are oxidized while submerged in molten [chloride] salt, readily oxidizable alloy components, such as chromium, and in some cases iron, migrate to the surface to form non-adherent, granular and thus nonprotective oxides. This loss of alloy constituents causes a counter current flow of vacancies which condense into an interconnecting pore network filled with salt.*

This mechanism of intergranular corrosion with non-adherent oxide layers removed by the molten salt can lead to premature container failure. However, higher nickel alloys such as Alloy 600 can be used, and alternative Fe-Cr-Ni-Si austenitic (UNS S30815) and Fe-Cr-Si ferritic stainless alloys have been shown to form protective silicate layers limiting corrosive attack [113], [114]. Both alumina and silica refractory materials are compatible with molten chlorides; hence, common Al_2O_3-SiO_2 insulating firebricks are used extensively as low cost high temperature molten salt container materials.

CHAPTER 3: CSPonD Performance

Receiver heating and efficiency analysis

Irradiance distribution within receiver

For a central heliostat located on the optical axis of the receiver aperture, the input flux will be restricted to an ellipse of major axis D_{ip} projected on the salt surface, calculated as:

$$D_{ip} = D_a / \sin \phi \tag{3.1}$$

where D_a is the aperture diameter and ϕ is the nominal beam-down angle measured from horizontal. A portion of the incoming concentrated light is reflected off the molten salt-air interface. This reflected fraction can be calculated from the Fresnel equations describing light as it moves between media of different refractive indices. The reflection coefficients for *s*- and *p*-polarized light are: [115]

$$R_s = \left[\frac{\sin(\theta_t - \theta_i)}{\sin(\theta_t + \theta_i)} \right]^2 \tag{3.2}$$

$$R_p = \left[\frac{\tan(\theta_t - \theta_i)}{\tan(\theta_t + \theta_i)} \right]^2 \tag{3.3}$$

The angles that the incident, reflected and refracted rays make to the normal of the interface are given as θ_i, θ_r and θ_t, respectively, and related by Snell's Law and the law of reflection:

$$n_{salt} \sin \theta_t = n_{air} \sin \theta_i \tag{3.4}$$

$$\theta_r = \theta_i \tag{3.5}$$

where

$$\theta_i = 90° - \phi \tag{3.6}$$

Since the incident light is unpolarized, containing an equal mix of *s*- and *p*-polarizations, the reflection coefficient, *R*, is:

$$R = (R_s + R_p)/2 \tag{3.7}$$

Equation (3.7) can be used to find the percentage of the incident energy which is reflected onto the lid. Most CSPonD beam down systems will be designed to operate with a 10° beam down angle or greater. Below this value, the surface reflection intensity increases dramatically, increasing the heat load to the lid as shown in Fig. 3.1. For the sample case of nitrate solar salt with $\phi = 20°$ and $n_{salt} = 1.413$ [58], 84.7% of the incoming radiation refracts into the salt while 15.3% reflects onto the lid. It is important to recall that this reflected intensity is not necessarily lost to the environment as in traditional designs; the lid can, and should, be designed to reflect this radiation back to the salt and/or capture this energy. The reflected intensity calculated here

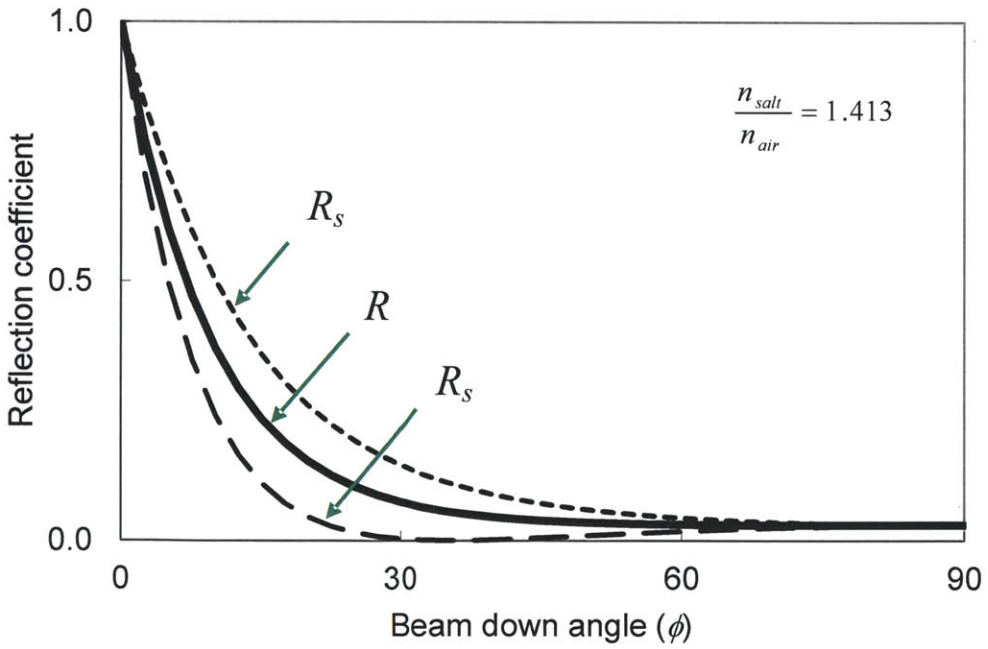

Figure 3.1 - Reflection coefficient for various beam down angles

for a smooth surface represents an upper-bound, as the salt surface will likely have small surface waves due to convective and extracted salt flows. Haltrin et al. has shown wavy water interfaces to have reduced reflection coefficients as compared to smooth interfaces [116].

The intensity of the refracted light at various salt depths is then found with Equation (2.1). Figure 3.2 illustrates the incoming solar irradiance distribution for a centralized heliostat on the optical axis of the receiver, simulated using MATLAB. An entire heliostat field array can be aimed to create a circular illumination distribution on the salt surface; much of the incoming radiation will be absorbed near the top of the salt surface and towards the rear of the tank. Hence, it is logical to extract high temperature salt in this location for the power cycle.

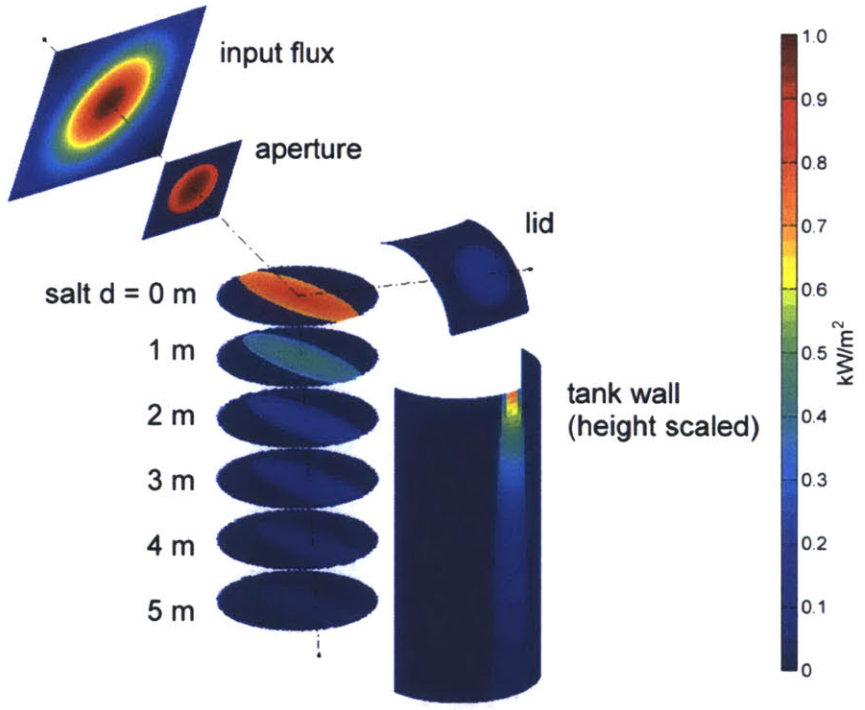

Figure 3.2 - Irradiance distribution within CSPonD receiver

Relative irradiance for a single heliostat along the CSPonD receiver's optical axis, normalized to 1 kW/m² peak intensity. A complete heliostat field can be aimed to create a circular illumination on the salt surface.

Capture efficiency analysis

A simplified model can be used to give first order efficiency estimates while the proposed CSPonD receiver is "on sun." Key assumptions include:

- Uniform input flux is completely captured by the aperture
- Lid is well insulated to the outside environment
- Energy directed to the lid is completely absorbed
- Air/salt vapor above the pond is at the lid temperature
- No mass transfer through aperture (i.e., salt vapors from pond surface condense onto lid)

"Capture efficiency" ($\eta_{capture}$) is defined as the fraction of incoming energy entering through the aperture that is retained by the receiver – used to heat both the pond and the lid. Unique to CSPonD receivers are these dual zones for heat rejection available at different temperatures. Operators can choose to utilize low temperature lid designs for power cycle preheating, or hybrid needs such as desalination feedwater heating or combined heat and power. High temperature lid heat can be employed for primary power cycle heating, followed by superheating with the higher temperature molten salt heat reservoir. Figure 3.3 depicts an energy balance diagram on a simplified CSPonD DAR.

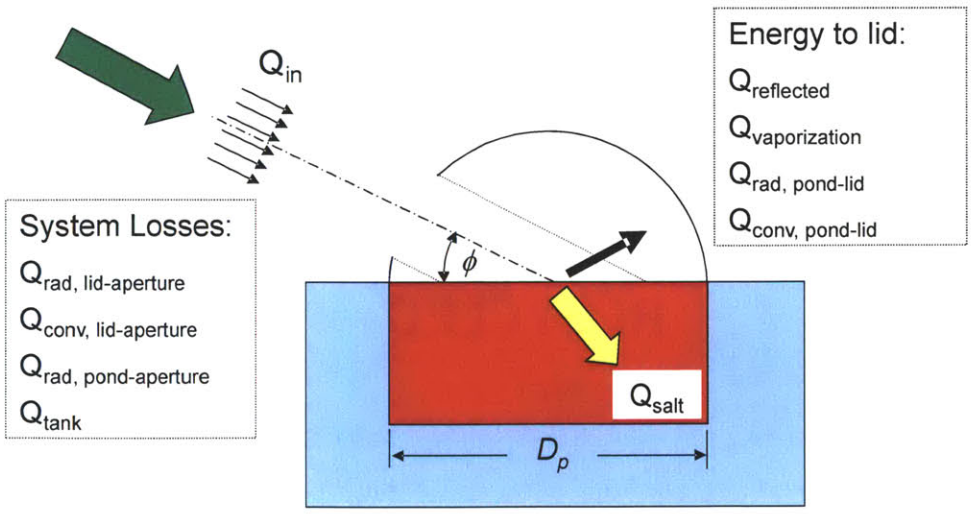

Figure 3.3 - Simplified CSPonD DAR geometry and energy balance diagram

Figure 3.4 shows the design inputs used to calculate collection efficiency. Lid and salt pond temperatures are just some of the key parameters needed to characterize a CSPonD receiver. Others include input flux concentration, nominal pond diameter and average beam down angle of the incoming concentrated light. Aperture size is driven by system sizing and input flux concentration, and is used to calculate the system's geometrical view factors needed for accurate radiative loss estimates to the environment. Other losses include conduction though the tank walls and convection to the outside environment. The collected energy can be separated into net amounts which are absorbed into salt and into the lid.

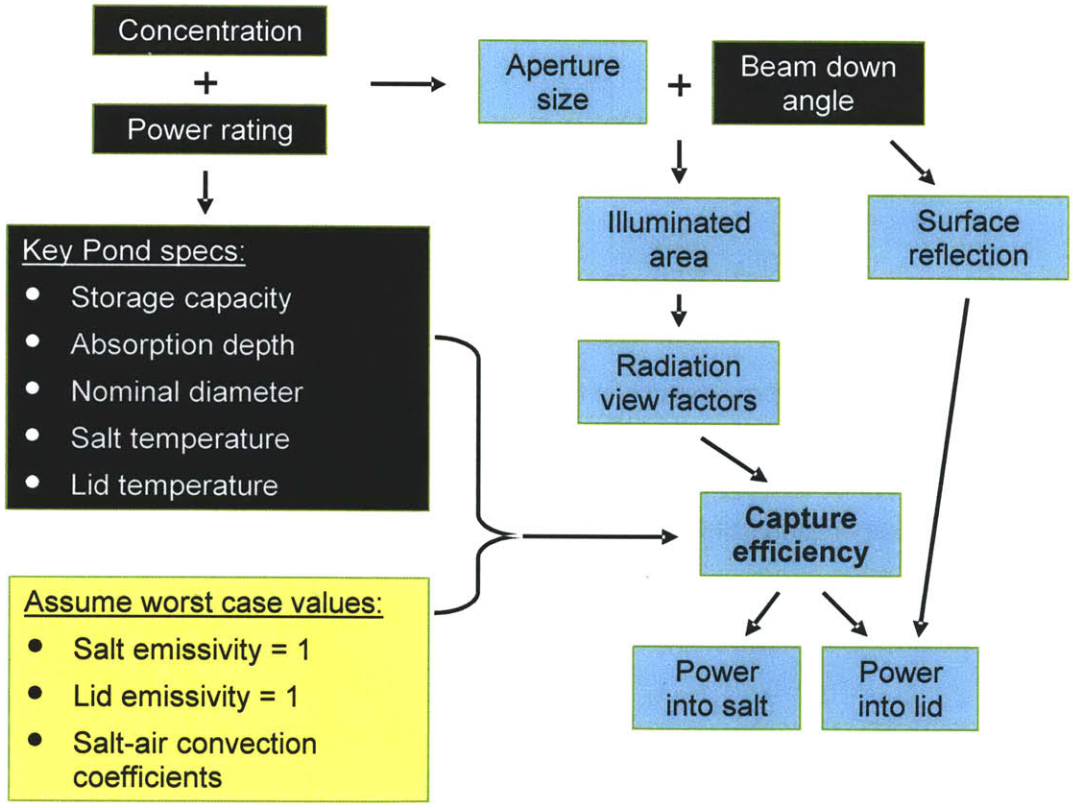

Figure 3.4 - Schematic of CSPonD receiver "capture efficiency" calculation
System design parameters are indicated in black boxes

Aperture area is determined by system sizing and input flux concentration Φ:

$$A_a = Q_{in} / \Phi \tag{3.8}$$

and is used to calculate the system's geometrical view factors needed for accurate radiative loss estimates to the environment. For a central heliostat located on the optical axis of the receiver aperture, the input flux will be restricted to an ellipse of major axis, D_{ip} given by Eq. (3.1).

Clearly, if D_{ip} is greater than or equal to the nominal design pond diameter, D_p, a portion of the incoming light will 'spill' onto the inside of the lid structure. A hemispherical lid cover is assumed, which has a surface area:

$$A_l = 2 \pi D_l^2 \tag{3.9}$$

where

$$D_l = \min(D_{ip} , D_p) \tag{3.10}$$

and

$$A_p = \pi/4 \cdot D_l^2 \tag{3.11}$$

The following view factor relationships can be derived using the radiation view factor for any finite area of any shape on interior of hemisphere to the hemisphere's entire base [117], the view factor reciprocity relationship, and the fact that the pond surface "sees" only the lid and aperture areas:

$$F_{p\text{-}l} = 1 - \tfrac{1}{2} (A_a/A_p) \tag{3.12}$$

$$F_{p\text{-}a} = \tfrac{1}{2} (A_a/A_p) \tag{3.13}$$

$$F_{l\text{-}a} = \tfrac{1}{2} (A_a/A_l) \tag{3.14}$$

The radiative heat transfer from the pond to the lid, from the pond to the aperture, and from the lid to the aperture can be found using:

$$Q_{rad,1\text{-}2} = F_{1\text{-}2}\, A_1\, \varepsilon_1\, \sigma(T_1^4 - T_2^4) \tag{3.15}$$

Emissivities of unity were assumed to set an upper bound on heat losses through the aperture as the view factors vary with aperture size and input flux concentration; in physical systems the salt surface is expected to have an emissivity ~ 0.9, and the lid may have emissivity values ranging from 0.1-0.9. In fact, the lid emissivity, temperature and geometry may be tailored throughout the lid's surface to lower the overall heat losses to the environment.

The convective heat transfer from the pond to lid and from the lid to the aperture can be approximated as:

$$Q_{conv,1\text{-}2} = h\, A_1\, (T_1 - T_2) \tag{3.16}$$

where standard correlations for a heated surfaces can be used to find estimates for the natural convective coefficient, h, for the salt and lid geometry.

An evaporation rate, γ, defined as the mass of salt per exposed surface area per unit time vaporized, can be assumed to calculate vaporization heat transfer from the pond's surface:

$$Q_{vap} = \gamma\, \Delta H_{vap}\, A_p \tag{3.17}$$

Conductive heat loss through the tank walls can be assumed as a percentage of the overall system capacity:

$$Q_{tank} = \xi\, Q_{in} \tag{3.18}$$

Using Equations (3.2), (3.3) and (3.7) to find the reflection coefficient, the incoming power absorbed directly into the salt becomes:

$$\text{if } D_{ip} \leq D_p:$$
$$Q_{direct,salt} = Q_{in}(1 - R) \tag{3.19}$$
$$\text{if } D_{ip} > D_p:$$
$$Q_{direct,salt} = Q_{in}(1 - R) \cdot (D_p / D_{ip})^2 \tag{3.20}$$

The incident power reflected and spilled onto the lid is:

$$Q_{reflect} = Q_{in} - Q_{direct,salt} \tag{3.21}$$

The net power to the salt is:

$$Q_{salt} = Q_{direct,salt} - (Q_{rad,p\text{-}a} + Q_{tank}) - (Q_{vap} + Q_{conv,p\text{-}l} + Q_{rad,p\text{-}l}) \tag{3.22}$$

and similarly, the net power to the lid becomes:

$$Q_{lid} = Q_{reflect} - (Q_{rad,l\text{-}a} + Q_{conv,l\text{-}a}) + (Q_{vap} + Q_{conv,p\text{-}l} + Q_{rad,p\text{-}l}) \tag{3.23}$$

The capture efficiency, $\eta_{capture}$, can be calculated as:

$$\eta_{capture} = \frac{Q_{in} - Q_{losses}}{Q_{in}} \tag{3.24}$$

where

$$Q_{losses} = Q_{rad,l\text{-}a} + Q_{conv,l\text{-}a} + Q_{rad,p\text{-}a} + Q_{tank} \tag{3.25}$$

The exergetic efficiency, or ratio of useful work available versus the incoming solar flux, for the pond, lid and overall CSPonD receiver can be calculated using Carnot cycle efficiencies, with an ambient rejection temperature of T_∞:

$$\chi_{salt} = (Q_{salt} / Q_{in}) \cdot (1 - T_\infty / T_p) \tag{3.26}$$

$$\chi_{lid} = (Q_{lid} / Q_{in}) \cdot (1 - T_\infty / T_l) \tag{3.27}$$

$$\chi_{sys} = \chi_{salt} + \chi_{lid} \tag{3.28}$$

Table 3.1 lists the nominal design values used to find overall CSPonD capture efficiencies for a 600 MW_th storage system. The capture efficiency as defined by Eq. (3.24) is plotted for the high (chloride) and low (nitrate) temperature designs, each with an assumed lid temperature set at the freeze point of its respective salt (Fig. 3.5). At this lid temperature, a self-sustaining salt vapor condensation and recycling loop is expected to develop within the receiver's cavity, limiting heat and mass transfer outside of the receiver. For comparison, Solar I and Solar II peak and average receiver collection efficiencies are shown [7]. Note peak concentrations are limited to less than 1000 suns to avoid receiver tube failure for both Solar I and II receivers.

Table 3.1 - Nominal CSPonD design values for capture efficiency analysis

Parameter	Design value
Peak power rating, Q_{in}	65 MW_t
Thermal storage	600 MW_th
Salt volume	2500 m^3
Pond diameter, D_p	25 m
Average beam down angle, ϕ	21.4°

Tube based-receivers, such as those used in Solar I and II, are designed so that incoming flux strikes the tube near-normally to its surface. Unfortunately, a fraction of the incident light is reflected off the receiver's surface and cannot be recaptured. In contrast, the CSPonD receiver captures reflected light with the lid and converts it to useful heat, or depending on lid temperature and construction, redirects it back into the salt. Both designs are subject to radiative and convective losses – but the proposed CSPonD receiver aperture area can be reduced as the centroid of the aperture plane, by definition, functions as a virtual focal point for the heliostat field and can be minimized without concern for material limitations. The incoming concentrated light diverges after passing through the aperture; in addition, volumetric absorption throughout the molten salt tolerates higher incoming fluxes since it is distributed over a significant depth. As a result, overall efficiency is superior in high concentration CSPonD systems.

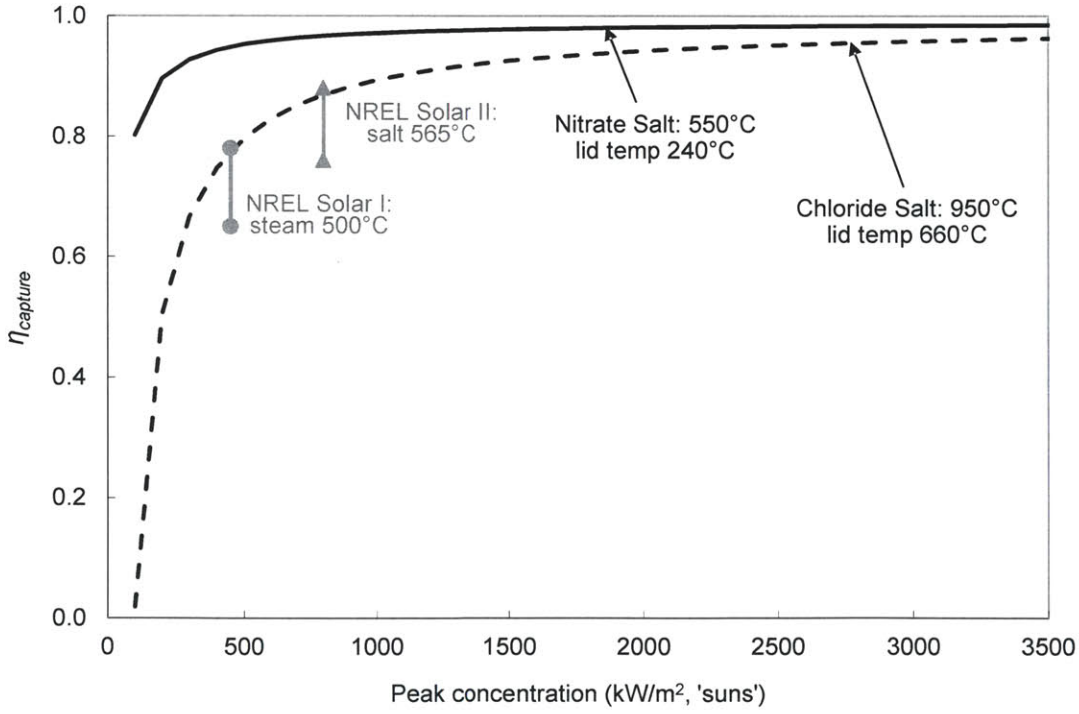

Figure 3.5 - CSPonD DAR capture efficiency

Nitrate salt: pond at 550 °C, lid at 240 °C; Chloride salt: pond at 950 °C, lid at 660 °C. Solar I and Solar II peak and average receiver efficiency values shown, from [7].

Figure 3.6 plots the availability, or exergetic efficiency, of the CSPonD receiver. The useful captured energy flows of the pond and lid are calculated using Eqs. (3.26) , (3.27) and (3.28) with Carnot efficiencies for salt and lid temperatures, rejecting heat to the environment at 25 °C. The chloride salt design, with high salt and lid temperatures (950 °C and 660 °C), exhibits greatest overall system availability. It is interesting to note at low input flux concentrations, nearly all of the captured energy is available at the lid; very little is directed to the molten salt pond. The simple explanation is that low concentrations require large apertures and large illuminated pond areas, both of which increase losses from the molten salt to the lid and the environment.

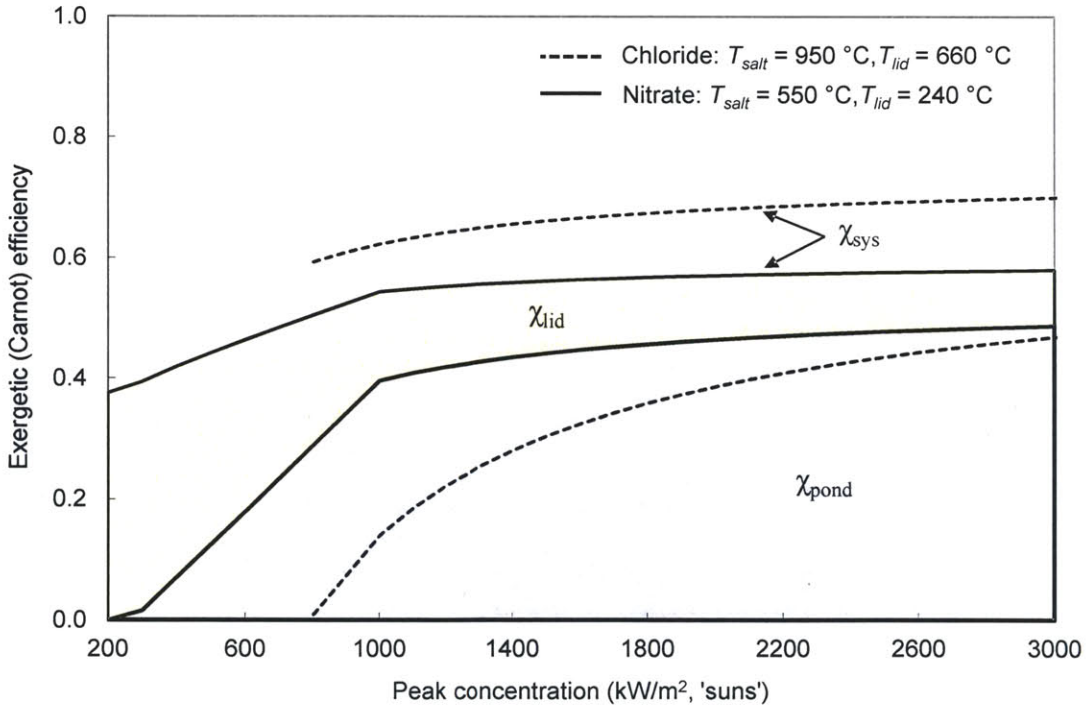

Figure 3.6 - Exergetic capture efficiency of CSPonD receiver
The useful energy of the pond and lid are calculated for their respective temperatures, rejecting heat at 25 °C.

Design parameter sensitivity analysis

Figures 3.7-3.9 examine the sensitivity of the 65 MW_t nitrate salt (T_{salt} = 550°C) CSPonD receiver's efficiency to various design parameters: nominal pond diameter, average beam down angle, and lid temperature. Varying the nominal pond diameter can drastically shift the amount of power directed to the pond or lid (Fig. 3.7). Three receiver regimes are illustrated: (a) Pond undersized: a portion of the incoming is light spilled onto lid walls, the amount of this spillage and heat gain onto the lid decreases as the input flux concentration increases; (b) Pond exactly sized for a specific aperture and particular beam-down geometry; (c) Pond oversized: the exposed pond surface can be reduced to match the illuminated area, increasing concentration enables further reductions in exposed salt surface area, further reducing losses and heat gain onto the lid.

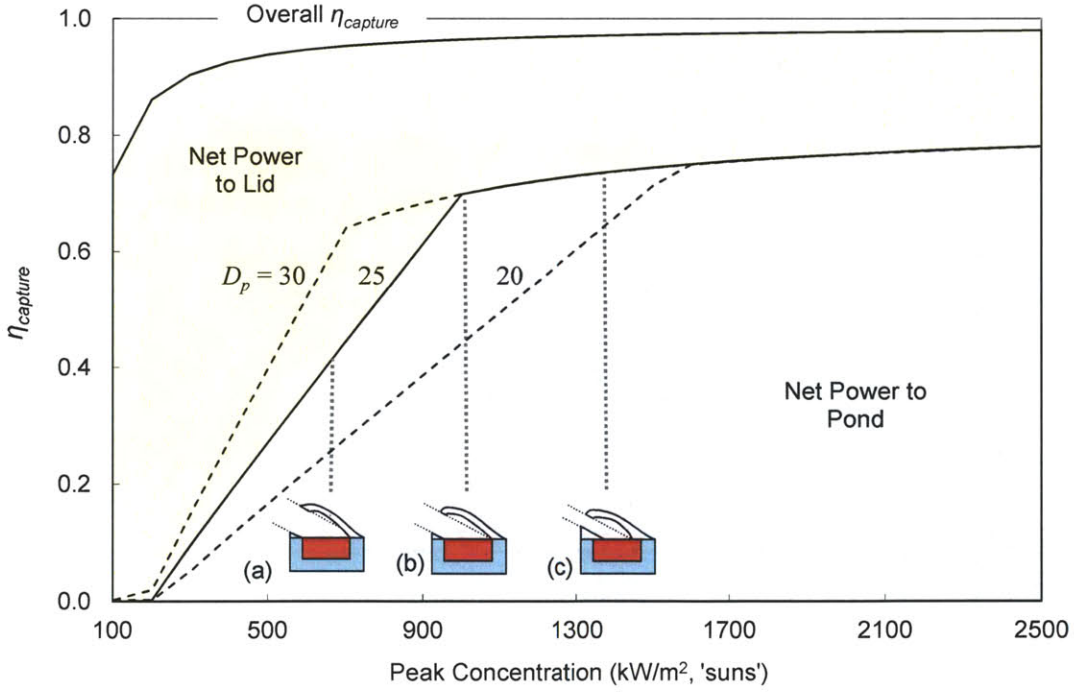

Figure 3.7 - Effect of pond diameter on capture efficiency
Constant ϕ =21.4°, T_{salt} = 550 °C, T_{lid} = 240 °C

Again, at low input flux concentrations nearly all of the captured power is available at the lid; very little is directed to the molten salt pond.

The abrupt change in slope of the net power to the salt and lid occurs at regime (b), corresponding to the specific input flux concentration which results in a projected aperture height exactly equal to the nominal pond diameter for a specific beam down angle. Below this point, the required aperture area is larger than the projected pond area and the power delivered to the salt decreases linearly with concentration, intercepting the x axis at the input flux concentration which corresponds to the radiative and convective losses off of the salt's surface towards the lid and aperture. Above this input flux concentration the aperture, exposed salt area and losses are reduced, which incrementally increases power to the salt.

Similarly, Fig. 3.8 shows larger beam down angles (i.e., steeper hillsides for the heliostat field) are effective at directing more of the incoming energy into the salt. A steeper beam down angle has two effects: firstly, the illuminated or projected area of the aperture on the horizontal molten salt pool is decreased, reducing required exposed salt area and subsequent losses. Secondly, Fresnel reflections off of the salt surface are reduced, reducing the fraction of incident light which is reflected onto the lid. The net heat to the lid approaches Fresnel reflection limits for unpolarized light at very high concentrations.

Figure 3.9 shows reduced capture efficiency with increasing lid operating temperatures, due to larger radiative and convective losses through the aperture. On the other hand, a higher lid temperature reduces radiative exchange from the salt pond to the lid – effectively keeping more energy in the salt. For example, with 240 °C lid and 550 °C salt temperatures, roughly 18 kW/m^2 is lost from the salt surface to the lid. For the 2500 m^3, 25 m diameter salt tank, this is roughly 14% of the incoming power when the receiver is on sun at the 65 MW_t design point. With the aperture closed for 16 hours, salt-lid radiative transfer would result in nearly 140 MW_th of energy transferred to the roof – nearly one-quarter of the 600 MW_th (equivalent to180 MW_eh at η_{th} =

0.30) storage capacity. This upper bound assumes a fully-exposed salt surface and a constant salt surface temperature.

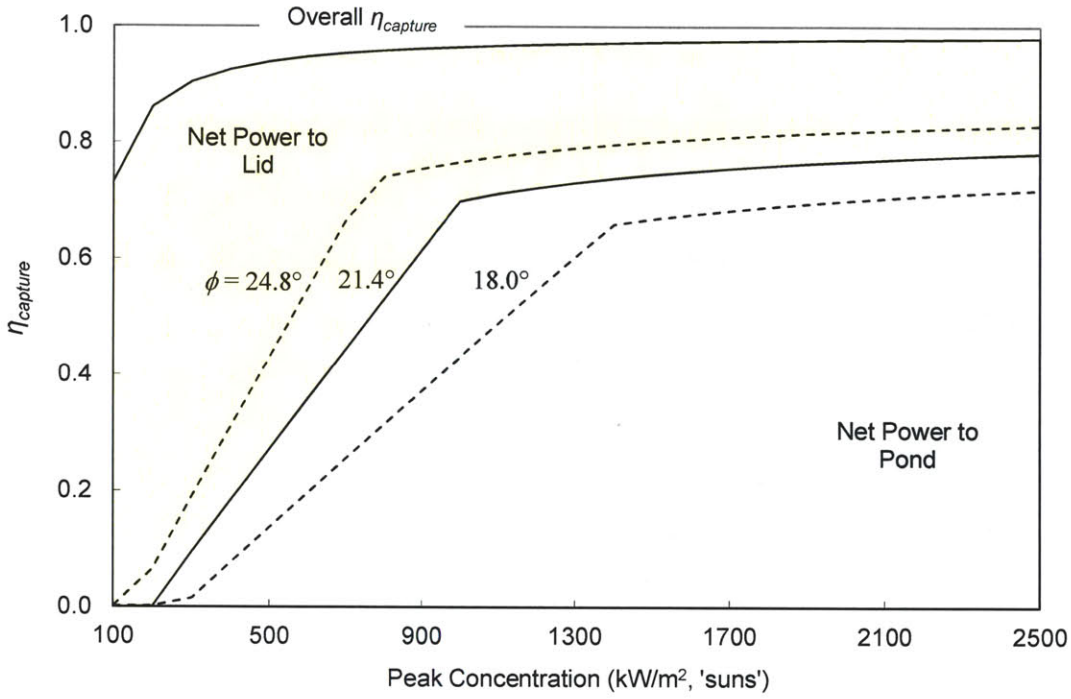

Figure 3.8 - Effect of beam down angle on capture efficiency
Constant D_p = 25 m, T_{salt} = 550 °C, T_{lid} = 240 °C

Fortunately, high solar concentration enables reductions in exposed salt surface area, further reducing losses and heat gain from the salt to the lid. As mentioned in Chapter 2, shaping the lid to function as an integrated "concentration booster", or CPC, will allow for increased irradiance on the salt surface while minimizing exposed salt area. The lid can be designed so high flux regions on the optical axis of the receiver pass through the aperture to the salt unabated, while lower intensity peripheral light skims the narrowing lid internal contours with grazing angle reflections before striking the salt, as depicted in Fig.3.10.

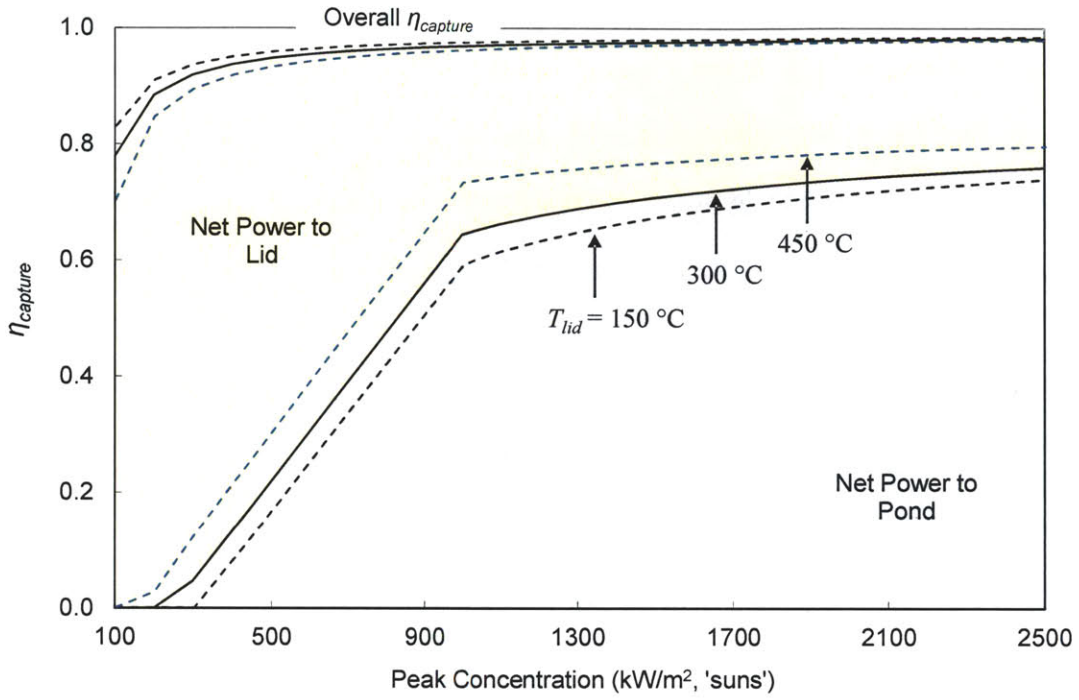

Figure 3.9 - Effect of lid internal temperature on capture efficiency
Constant D_p = 25 m, ϕ =21.4°, T_{salt} = 550 °C

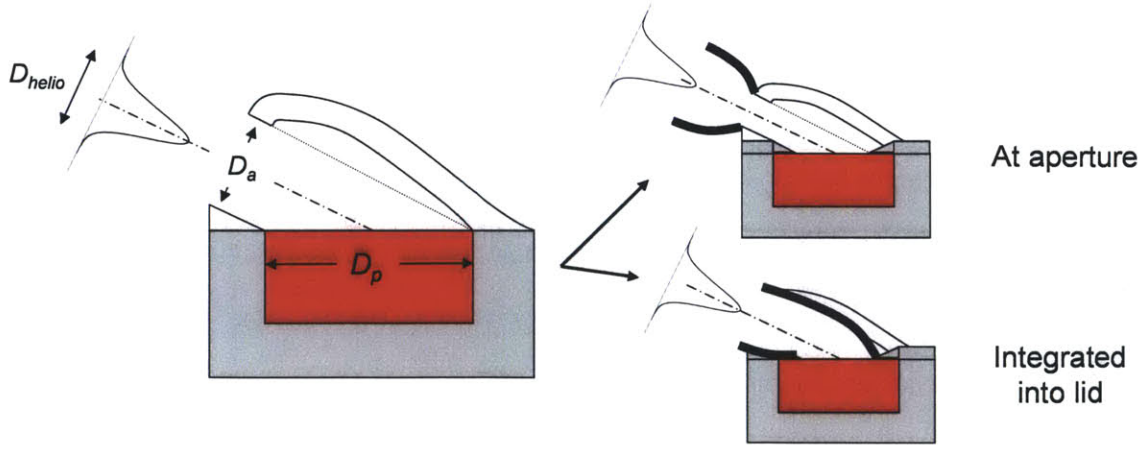

Figure 3.10 - Integrated concentration booster geometry in lid reduces exposed salt area

Also, the pond free-surface will cool due to radiative, as well as internal convective heat transfer while off-sun. As a result, heat transfer from the pond to the lid will decrease. Additionally, if energy was not extracted from the lid at a sufficient rate, the lid temperature will increase; low lid thermal mass will result in quicker heat up and reduced nighttime losses. One possible operational strategy would slow or stop energy extraction from the lid towards the end of the day while still on sun, allowing the lid temperature to equilibrate with the salt, reducing radiative transfer. An extreme implementation of this strategy could blast cooling air over the salt surface, creating a protective, solidified salt shell surface which limits radiative transfer to the lid. The salt crust layer could easily be melted away with concentrated sunlight during the next daytime heating cycle. Yet another strategy would be to deploy a "radiation shield" over the salt surface when the receiver is off-sun to substantially reduce radiative transfer to the lid. This device could be as simple as a sliding metallic shield or a folding trap door, with or without insulation throughout its thickness, whereby the upper surface of the metal has a significantly lower emissivity than the molten salt [118].

Lid temperature control

Even with a fully-exposed salt surface area, the lid temperature can be controlled by varying the amount of heat extracted from its cooling loops. Figure 3.11 depicts lid temperature as a function of lid heat extraction while the CSPonD receiver is on sun for various salt temperatures and input flux concentrations. Directionally-dependent lid absorptivity and emissivity features can be incorporated to reduce overall heat loading impinged on the lid. Similarly, lid lining materials which are spectrally selective and have stronger absorption and emission in the infrared can reduce lid temperatures. Fortunately, both solidified salts and refractory materials possess this characteristic [70].

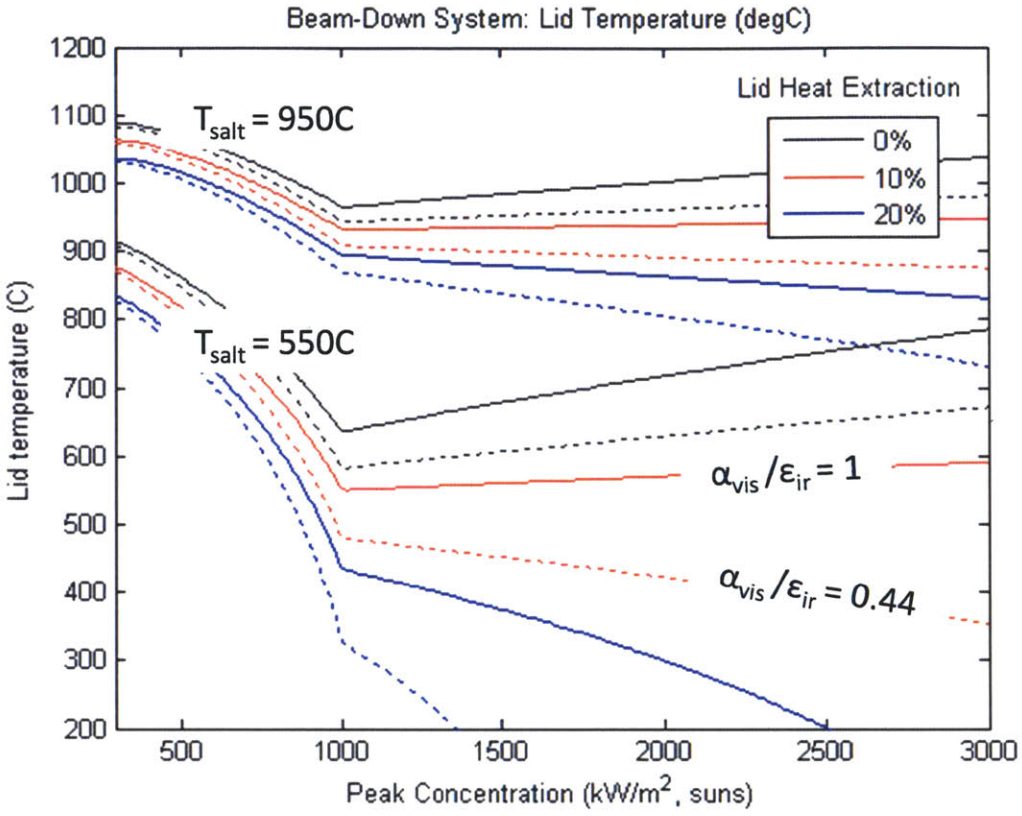

Figure 3.11 - On sun lid temperature for various lid heat extraction percentages Spectrally selective lid linings (i.e., condensed salt vapors) result in cooler lid temperatures.

Figure 3.12 plots lid temperatures explicitly as a function of salt surface temperatures, for a spectrally-selective lid surface ($\alpha_{vis}/\varepsilon_{ir} = 0.44$) while the receiver is on sun. The stagnation temperature is shown in Fig. 3.12a, whereby no heat is extracted from the lid. Figure 3.12b illustrates much cooler lid temperatures can be achieved with 20% lid heat extraction during the daytime. At night, when there is no incoming light reflected onto the lid, temperatures can be controlled with much less lid heat extraction, using the methods described in the previous section to minimize pond-to-lid radiative losses.

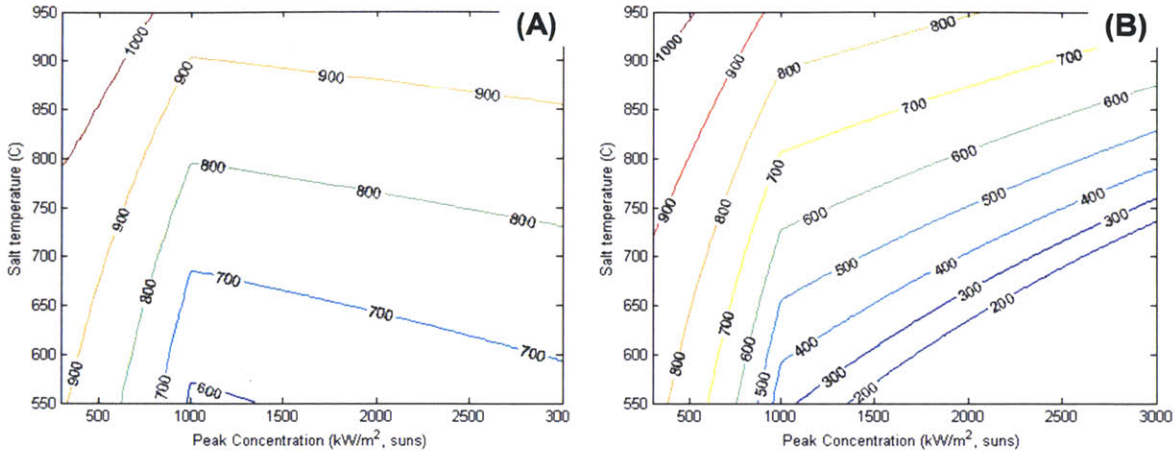

Figure 3.12 - Lid temperature maps as a function of salt temperature while on sun (A) Stagnation temperature, no lid heat extraction; (B) 20% lid heat extraction.

In contrast, Fig. 3.13 plots lid temperatures for beam up systems (as was depicted in Fig. 2.3b). In the beam up configuration all of the incoming concentrated light is directed at the lid. The fraction of incoming energy reflected into the salt, given by $\rho_{vis} = 1 - \alpha_{vis}$, is drastically reduced as compared to a beam down system. As a result, the lid temperatures are dramatically higher and relatively insensitive to salt temperature and heat extraction rates. The option of using spectrally selective lid material becomes invalid as the lid temperatures rise and begin emitting more energy in the visible spectrum. Lid temperatures higher than salt temperatures would suggest making the lid the source for the primary heat extraction loop, for increased power cycle options and efficiencies. This is all possible; it is just important to note that the receiver for a beam up CSPonD system will need to be designed differently than a beam down CSPonD system. Also, while these lid temperatures are in the operating range of high quality refractory ceramics, the diurnal cycling and extreme thermal strains while the receiver is on-and-off sun will likely cause incrementally accumulating degradation and premature failure of the lid lining materials.

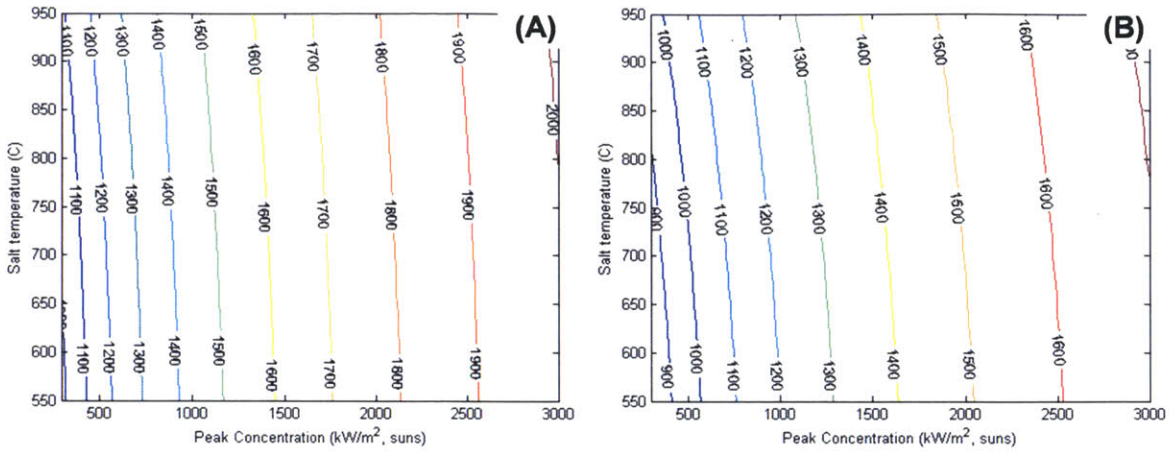

Figure 3.13 - Lid temperature maps for a beam up system on sun
(A) Stagnation temperature, no lid heat extraction; (B) 20% lid heat extraction.

If highly reflective lid materials are used, lid temperatures can be kept much cooler. Figure 3.14 depicts lid temperatures for the case of $\rho_{vis} = 0.9$ with a 20% lid heat extraction rate. This reflectivity is a realistic upper bound, as higher quality mirror surfaces would likely be damaged in such close proximity to the salt bath. An active gas-purging scheme would likely be needed to keep the lid surface clean and free from oxidation at elevated temperatures, adding complexity and risk. An alternate scheme would limit heat extraction from the lid, so a flowing salt film can be circulated from the salt pond onto the lid to be heated, as a hybrid between a CSPonD receiver and the salt film receivers presented by Bohn and others [15-19].

In summary, estimates for CSPonD receiver capture efficiency show improved performance relative to conventional tube-based CSP receiver designs. To maximize the net heat gain to the molten salt pool, and minimize the heat input to the lid, the following design objectives are emphasized: beam down angle and lid temperature are maximized while the pond exposed surface area is minimized. Losses are reduced and capture efficiency is improved with increasing input flux concentrations, whereby the system's cavity-like geometry approaches that

of a blackbody absorber. It is known that smaller apertures reduce reradiation losses but intercept less sunlight; as a result the optimum aperture size becomes a site-specific compromise between maximizing radiation capture and minimizing radiation losses [119].

However, these efficiency calculations have assumed that the lid captures all of the internal losses from the pond (convection, salt vaporization, salt-to-lid radiation) and it can be fully utilized. A real system is expected to have additional losses from the lid to the environment. Nevertheless, the unique dual heat-source nature of the salt and lid in CSPonD receivers will allow more flexibility for operators to maximize useful heat extraction for their particular system.

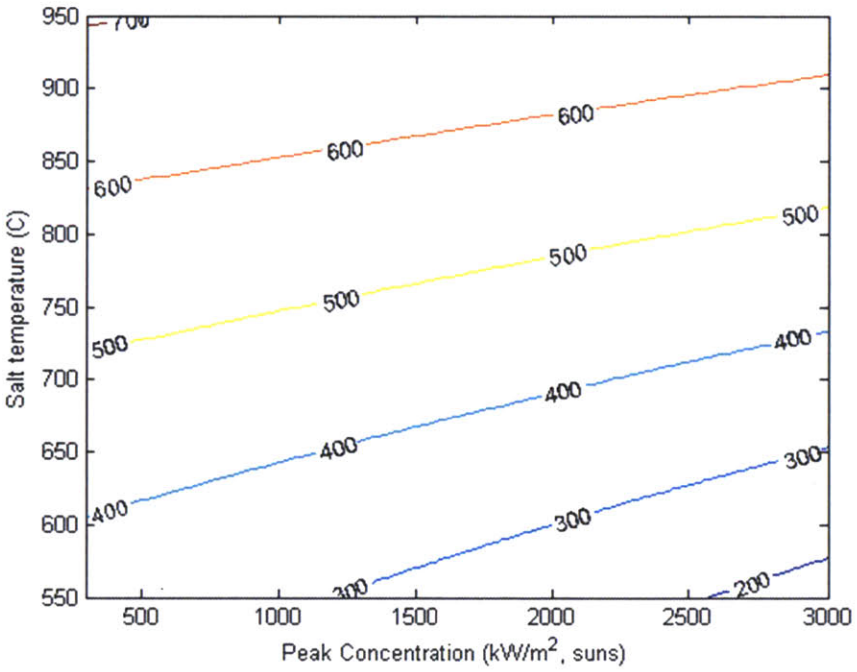

Figure 3.14 - Lid temperatures for a highly reflective lid beam up system on sun 20% lid heat extraction, $\rho_{vis} = 0.9$.

Operational issues

Optimal control

As presented by Ghobeity, Noone and Mitsos, heat collected by the cover can be used for preheating feed water to the steam generator or desalination feed water in a dual-purpose CSPonD desalination and electricity production plant [77], [78]. Optimal operating conditions result in highest income while ensuring the most efficient use of both the low and high exergy streams, which varies with local energy and water cost structures.

Similarly, the use of the two heat extraction loops for electricity production can be optimally controlled to maximize power output, even when the sun is not shining. Local economic conditions and power requirements will dictate whether the CSPonD DAR is best suited for continuous heat extraction or, alternatively, used to supply peaking load power cycles.

Risks and countermeasures

Table 3.2 lists risks and associated countermeasures with the CSPonD system. Similar to metallurgical salt baths and CSP molten salt thermal storage systems, salt freezing is a significant and catastrophic concern. In molten salt heat treatment tanks, if the heating electrodes fail or power is disrupted for several days and the tank is not drained properly, large frozen salt masses must be broken up with a jackhammer, usually destroying the container in the process. Fortunately, CSPonD operators can slow or stop heat extraction from the system if a prolonged period of inclement weather is forecasted. In severe cooling scenarios, the divider plate can be lowered to the bottom of the tank, expelling the cold layer at risk of freezing to the upper region of the tank which allows direct heating with incoming light. The CSPonD receiver will be well-insulated to minimize conductive losses to the environment; similar to CSP hot salt storage tanks, the salt temperature is expected to drop only 1-3 degrees per day when heat extraction is stopped with a sealed aperture [33]. Even so, it is prudent to follow CSP hot salt storage tank precedent

and install a supplementary heating element in the receiver. Typical heater installations are beneath the tank bottom to eliminate conductive transfer to the earth below; the divider plate itself also presents an excellent location for in-tank immersion heating should the need arise.

Minor salts leaks in pipes and valves can be repaired if shutoff valves are incorporated into the plumbing circuit. Major leaks will require immediate attention and the salt must be evacuated to a suitable area. For imminent emergencies, the entire CSPonD DAR can be sited within a bermed earth area cleared of flammable debris, or positioned to gravity-drain out of a low-lying valve into a lined culvert. The evacuated salt will solidify and can be removed without worry of environmental damage. For planned system shutdown, salt can be pumped to a small (few meters high) "prilling tower" where it is sprayed into the air and freezes into small particles. As mentioned in Chapter 2 and described by Paxson, salt fumes near the CSPonD DAR's aperture can be contained with a fume extraction system [104]. If this is not sufficient, an air curtain can be used to eliminate mass transfer across the aperture. Spent salt can be recycled into the system or sold for agricultural or commercial uses.

Rain can be prevented from entering the system with weather monitoring stations and a well-sealed aperture door. Unanticipated sprinkles can be mitigated with a visor-like feature above the aperture. It is unlikely that birds or other animals will enter the system, as has been observed with other high-flux CSP central receivers. If organic material did enter the molten salt bath, it would likely be flash-pyrolyzed and the remains would be slowly dissolved in the melt. Dissolved or suspended impurities can be removed with chemical rectifiers, either in solid or gaseous form, added to the salt. Larger floating debris and scum can be removed from the pond surface with the weir heat extraction method described in Chapter 2. Filters can be employed upstream of the pump and heat exchanger to prevent clogging.

Table 3.2 - CSPonD risks and countermeasures

Risk	Countermeasure
Salt freezing	Stop heat extraction; supplemental heater
Salt leaks	Shut off valves in plumbing circuit; catch basin for entire system
Salt fumes	Fume extraction system; air curtain
Salt impurities	Chemical or gaseous rectifiers
Rain	Aperture door & visor
Animals entering system	Flash-fry barbeque*
Floating debris	Weir "skimming" salt extraction; debris filtering
Uneven heating of salt surface	Heliostat aiming strategy
Hot spots within salt	Natural convection; textured divider plate; bypass salt circulation
Long startup times	Combustion-assisted heating

**Animals are known to keep away from intense heat; thus, systemic organic contamination does not pose a measurable risk*

The salt surface may become illuminated unevenly depending on the sun's position and direct normal irradiance available. However, the heliostat aim points (particularly the near-field heliostats with solar image sizes much smaller than the aperture) can be shifted to produce a uniform distribution. A dynamic optical mixing strategy can be employed by allowing the near-field heliostats' projected sunspots to traverse across the salt surface in regular synchronized patterns, effectively "stirring" the salt. By design, hot spots within the salt are mitigated by natural convection cells, which can be enhanced by texturing and altering the reflective properties of the upper surface of the divider plate.

System startup provides another concern. As discussed before, unmelted salts have low emissivity and absorptivity, with resulting high reflectivity in the visible spectrum. Incoming concentrated light will be mostly reflected off an unmelted, salt-filled pond. As a result, more thermal energy is needed to melt the entire salt mass in a reasonable amount of time. The salt can

be premelted in a separate combustion-fired melting line and pumped to the receiver, as is the case with conventional molten salt CSP systems. Alternatively, gas burners can be installed in the roof of the receiver, similar to gas-fired glass furnaces. The combustion jet will convectively heat and melt the salt, and also heat the lid, which will radiate back to the salt. The aperture can be opened during the daytime to provide solar-assisted melting.

Melting behavior

Solidified eutectic salt mixtures are essentially opaque, even in small granular form, and can be modeled as a diffusely reflecting surface. The fraction of the concentrated radiation Φ impinged on solidified salt that is absorbed, independent of direction, is denoted by the absorptivity, α_{solid}. The next heat flux to the salt becomes:

$$q = \alpha_{solid} \cdot \Phi \tag{3.29}$$

If α_{solid} is small for the wavelength of radiation considered, the net heat flux to the solidified salt will be low. However, the energy that is transmitted to the opaque salt will be absorbed over very short distances, and as a result, localized heating still occurs.

Assuming the penetration depth of the radiation is small compared to the container depth, wall effects and surface losses are neglected, the unmelted salt can be modeled as a semi-infinite medium heated by a constant surface flux, q. The temperature distribution is given as: [120]

$$T(x,t) = T_0 + \frac{2q}{k}\sqrt{\alpha' t}\left[\frac{1}{\sqrt{\pi}}e^{-\xi^2} + \xi\, erf(\xi) - \xi\right] \tag{3.30}$$

where

$$\xi = \frac{x}{2\sqrt{\alpha' t}} \tag{3.31}$$

and

$$erf(\xi) = \frac{2}{\sqrt{\pi}} \int_0^{\xi} e^{-y^2} dy \tag{3.32}$$

x represents the depth into the heated medium; k is the thermal conductivity, and $\alpha' = k/\rho c_p$ is the thermal diffusivity of the medium (the symbol α' is used to avoid confusion with absorptivity, α) which are assumed to be constant with temperature. Equation (3.30) is used to calculate the surface temperature for various concentrated sunlight intensities impinged on the salt surface as a function of time, assuming a solar-weighted average $\alpha_{solid} = 0.1$ [70] (Fig. 3.15). Average properties for solidified nitrate solar salt at 150 °C are used: $k = 0.9$ W/m-K, and $\alpha' = 3.0 \times 10^{-7}$ m^2/s [121], with an initial temperature $T_0 = 25$ °C.

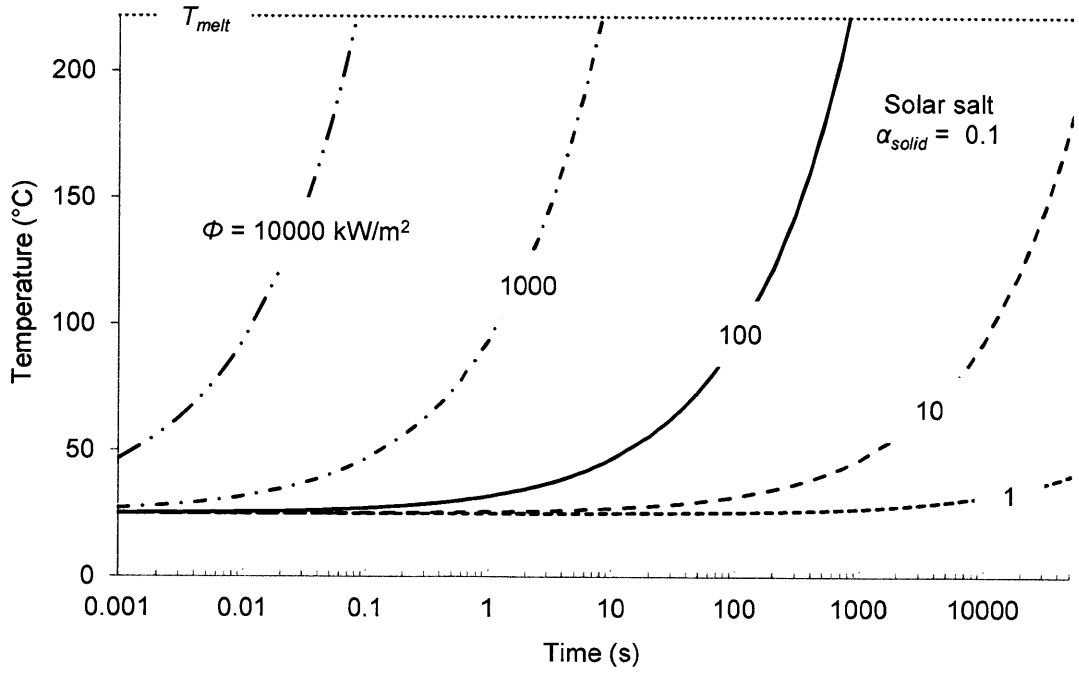

Figure 3.15 - Surface temperature progression for illuminated solid nitrate solar salt

As Fig. 3.15 shows, relatively long times are needed to melt the salt when the irradiance is low. For the range of concentrations achievable with current heliostat technology (Φ = 500-1500 kW/m^2), the time needed to heat the uppermost salt surface to the melting temperature T_{melt} is on the order of 1-10 seconds, not accounting for radiative or convective losses.

Once the salt reaches T_{melt}, energy is absorbed as the solid begins to melt. Landau solves the one-dimensional Stefan problem to describe the temperature distribution in a homogeneous medium heated by a constant surface flux q and undergoing a phase change, whereby the liquid is removed immediately on formation [122]. The heat equation is solved with the Stefan boundary condition on the evolving boundary, whose position is denoted by $s(t)$, between its two phases:

$$q = -k\frac{\partial T}{\partial x} + \rho L\frac{ds}{dt} \tag{3.33}$$

where L is the latent heat of fusion of the medium. The non-dimensional Stefan number is defined as the ratio of specific heat to latent heat for the solid salt as:

$$\text{Ste} = \frac{c_p\left(T_{melt} - T_0\right)}{L} \tag{3.34}$$

Assuming constant thermal properties, the time when an infinitesimally thin layer begins to melt is given as:

$$t_{melt} = \left(\frac{\rho L\sqrt{\pi\alpha'}}{2q}\cdot\text{Ste}\right)^2 \tag{3.35}$$

And the steady-state velocity v of the melt front is found as:

$$\frac{ds}{dt} \rightarrow v = \frac{q}{\rho L\left(1+\text{Ste}\right)} \tag{3.36}$$

Figure 3.16 plots t_{melt} and v as a function of q for the chloride and nitrate salt mixtures. The thermal properties of the solid chloride and nitrate salt mixtures are listed in Table 3.3. The chloride salt, with its larger heat of fusion and thermal diffusivity than the nitrate salt, takes longer to melt and melts at a slower rate. However, both salts will begin melting within 1-10 seconds at current maximum central receiver CSP input fluxes of $\Phi = 1500$ kW/m^2 (considering Eq. (3.29) → $q \sim 150$ kW/m^2), agreeing with the results of Eq. (3.30) and Fig. 3.15. The relatively slow steady-state melting speed can be increased by supplementing the solar energy with the resistive heating elements under the tank and possibly integrated into the divider plate for freeze protection. Another, perhaps more costly way to accelerate melting would utilize radiative and convective heating from overhead gas-fired burners as mentioned previously.

The small penetration depth assumption in the above analysis can be justified by the fact that frozen salt is composed of many randomly oriented crystalline grains, each much larger than the wavelength of the incident energy. The macrocrystalline structure is opaque to visible light; causing multiple internal reflections at crystal grain boundaries and defects. Additionally, solidified industrial salt is usually in the form of small (1-5 mm) spherical granules which further serves to scatter incoming radiation. As such, the energy which is not diffusely scattered is absorbed within a short distance.

Table 3.3 - Thermal properties of solid salt media

Salt	ρ (kg/m^3)	k (W/m-K)	c_p (J/kg-K)	L (kJ/kg)	α' (m^2/s)	Ste
Nitrate	1812	0.9	1339	147	3×10^{-7}	1.80
Chloride	1603	1.2	837	426	9×10^{-7}	1.25

Data from [13], [92], [121], [123].

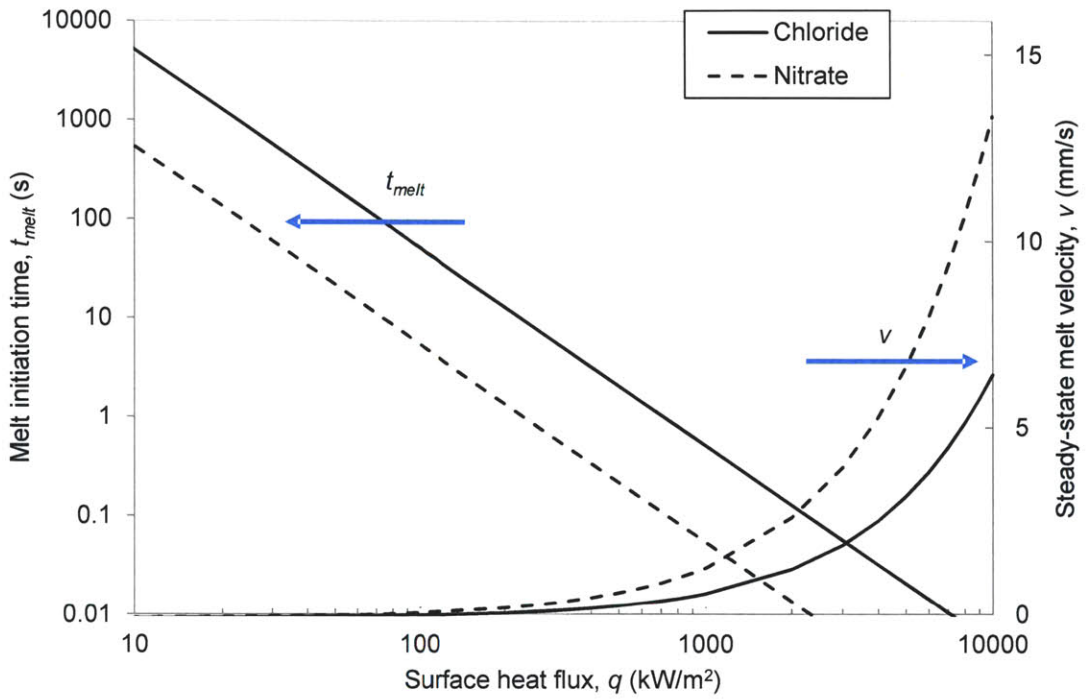

Figure 3.16 - Melt initiation time and steady-state melting velocity for surface heated salt Semi-infinite salt region; liquid removed immediately upon formation.

Maximum flux limitations

Once the salt begins melting, it will flow by gravity through the voids in the unmelted salt granules, cool and refreeze as it loses heat to its surroundings. At first, the molten salt will completely disappear into the porous media below and the assumptions of the previous analysis hold. But after some time, the melt will accumulate at the top of the unmelted bed and not run off. This modified Stefan problem has been analyzed by several researchers, some even modeling the "mushy" two-phase zone that develops in semi-transparent media [124-126].

The modeling of the two-phase melt zone progression is beyond the scope of this thesis; however, an analogy can be made from laser processing of materials concerning solid-liquid-vapor behavior. Melt pools formed by high-intensity laser beams are subject to rapid convective mixing, controlled by density and surface tension gradients in the liquid phase [127-129]. As

such, the molten salt puddle will experience the same effects and become well mixed as at it grows within the pond. Interactions with the solidified salt boundary will limit localized overheating of the rapidly growing salt puddle.

The only concern lies at the onset of heating, whereby an infinitesimally thin layer is melted and cannot flow to equilibrate its temperature. In this scenario, laser welding and machining provides guidance as to the maximum allowable surface flux before thermal decomposition, or worse, vaporization takes place. Schumacher shows that a surface layer will be melted or vaporized from a solid by a beam of radiation without significant heat conduction losses (i.e., quasi-adiabatic) if the beam power density exceeds a critical amount, found as: [130]

$$q_{crit} = \frac{\pi \rho L^* \alpha'}{l} \tag{3.37}$$

where l is the penetration depth of the radiation and L^* is total specific heat up to the temperature of interest, including the latent heat of melting and/or the heat of vaporization. In the CSPonD case, L^* includes the specific heat of the solid from ambient to the melting point, the latent heat of melting, and the specific heat of the liquid up to its decomposition temperature T_{decomp}.

If the absorbed flux is greater than q_{crit}, heat will not be transferred quickly enough into the surrounding solid and the salt will overheat. A value must be assumed for l due to a lack of data for solidified eutectic salts; as explained before, the penetration depth is likely small and on the order of the crystal size for the opaque salts. Therefore an average l = 1 mm was assumed for solid salt, or equivalently, an attenuation coefficient of β_λ = 10 cm^{-1} and absorptive index for peak visible light λ = 550 nm of $k = 4\times10^{-5}$, found using Eq. (2.3). Representative values for the critical flux on the solidified salt mass, Φ_{crit}, found by Eq. (3.29) and (3.37) are listed in Table 3.4 and are much greater than what is possible with conventional central receiver heliostat technology. It is important to note that these flux limits are based on flux impinging directly on the salt surface. A simple beam down CSPonD receiver without concentration booster geometry integrated into the

lid will have a flux projection factor of $1/\sin\phi$ as described by Eq. (3.1) that reduces the apparent intensity from the aperture plane to the horizontal salt surface.

A different approach is used to find the maximum achievable temperature imposed on the salt during high flux melting. Dabby and Paek present an analytical model for material removal from the front surface of a semitransparent solid illuminated by a high-intensity laser beam [131]. Their one-dimensional model finds that transient subsurface temperatures may exceed the surface temperature, potentially causing explosive removal of material. This technique can be used to improve productivities during laser drilling; unfortunately, explosive liquid salt removal is not a goal in the CSPonD system. However, their model can be used to find the maximum value for temperature overshoot during melting:

$$\frac{T_{max}}{T_{melt}} = \frac{1+\mathrm{Ste}}{\mathrm{Ste}} \tag{3.38}$$

This occurs when the non-dimensional quantity $B \rightarrow 0$

$$B = \frac{kL^*}{qlc_p} \rightarrow 0 \tag{3.39}$$

Peak overshoot temperatures during melting are listed in Table 3.4 for the nitrate and chloride salt mixtures. The value for the nitrate salt is well beneath the salt's decomposition temperature; the value for the chloride salt is excessively high due to the salt's high latent heat and high melting temperatures. However, as Eq. (3.39) shows, $B \rightarrow 0$ requires a very large heat flux q to be imposed on the system. Approximate overshoot flux intensities on the solidified salt mass, Φ_{os}, found by Eq. (3.29) and setting $B = 0.1$ in Eq. (3.39) are listed in Table 3.4, and again, are much greater than what is possible with conventional central receiver heliostat technology. Simply limiting q to a reasonable value will eliminate the temperature overshoot to acceptable values.

Table 3.4 - Maximum allowable flux and peak temperature overshoot during melting

Salt	L^* (kJ/kg)	Φ_{crit} (MW/m^2)	T_{max} (°C)	Φ_{os} (MW/m^2)
Nitrate	969	16.6	496	65.1
Chloride	1327	60.1	1406	190.2

L^* calculated from [13], [92], [121], [123].*Φ values based on Eqs. (3.29),(3.37),(3.39) with* $\alpha_{solid} = 0.1$.

Once the entire volume of salt is molten, a temperature profile similar to Fig. 2.7b will develop. Surface losses (radiation, convection) will create a negative temperature gradient in the uppermost salt layer, whereby a temperature inversion will be created. This in turn, will create buoyancy driven convective motion, mixing the salt. All of this occurs during heating regardless of incident flux intensity. However, if incident flux levels are high enough, one could foresee a situation whereby the subsurface temperature exceeds the allowable limits for the salt, particularly if power removal from the system is small compared to the incoming solar radiation.

A method to control salt temperatures during high incoming solar fluxes is shown in Fig. 3.17. A bypass loop is added parallel to the heat exchanger loop so hot salt can be extracted from the upper surface and purposely mixed with the bottom cold salt layer. The resulting warm salt return flow will convect upwards, mix with the cold salt and depending on the divider plate velocity, flow past the annular clearance and facilitate additional mixing in the upper region. Figure 3.17a depicts the concept for low heat exchanger extraction rates. Alternatively, Fig. 3.17b shows the bypass loop in use when there is no heat extraction through the heat exchanger. This method would allow for nearly any realistically achievable CSP flux intensity to be impinged on the salt surface, provided the bypass loop mixing flow is sufficiently high enough. As a prior art reference, a similar bypass method was utilized on the Solar II molten salt steam generator loop when molten salt flow extraction from the storage tank was greater than heat exchanger energy demands [47].

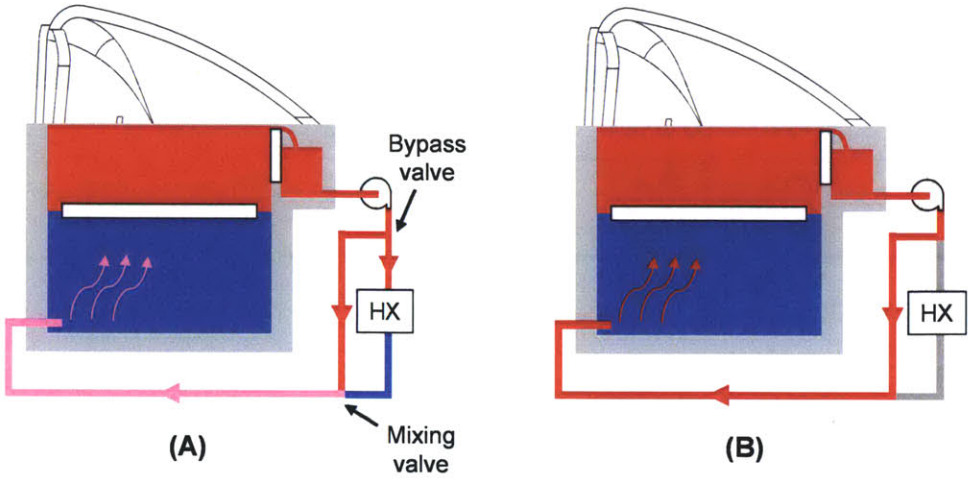

Figure 3.17 - Salt bypass loop to prevent hot side salt overheating

Bypass and mixing valves can be incorporated to prevent upper salt layer overheating during high solar flux periods for: (A) moderate heat extraction rates (B) no heat extraction.

Economics

CSPonD systems are expected to benefit from reduced capital costs and result in lower levelized costs for energy produced. A majority of the cost in CSP systems is the heliostat field and although hillside beam-down geometry results in significant cosine losses compared to conventional beam-up configurations – the CSPonD receiver is expected to exhibit an increased collection efficiency. Additionally, the capital and operating cost for a CSPonD receiver is significantly reduced with extensive use of low-cost refractory materials, extremely low-cost salts as the HTF and storage medium and lack of high pressure heat transfer fluid pumps.

Thermal storage costs

The proposed molten salts are attractive in terms of cost per unit energy stored. Table 3.5 presents a comparison of energy storage costs for the different salts as compared to synthetic oil,

widely used as the HTF (and in some cases the thermal storage fluid) in parabolic trough CSP plants. Although these costs are solely for the sensible heat storage media and do not include tank structure or ancillary equipment, there appears to be strong economic benefit to using chloride and nitrate salts.

Table 3.5 - Sensible heat thermal energy storage media costs

Energy storage medium	Temperature		Heat capacity (kJ/kg-K)	Costs per kg ($/kg)	Costs per kW_th ($/$kW_th$)
	Cold (°C)	Hot (°C)			
Synthetic oil	250	350	2.3	3.00	43.0
Nitrate salts	250	550	1.6	0.50	3.7
Carbonate salts	450	850	1.8	2.40	11.0
Chloride salts	700	950	1.1	0.13	1.7

Chloride costs from [87]*; others from* [13].

System costs

CSPonD system cost estimates including conservative as well as optimistic estimates for subsystem performance, as calculated by Mitsos and presented by Slocum et al., are presented in Table 3.6 [67]. NREL's solar System Advisor Model (SAM) was used along with the economic assumptions by US Department of Energy for Call DE-FOA-0000104 set for 2020, including some incentives [3]. The optimistic scenario gives an optimistic economical levelized cost of 0.07 $/kW$_e$h, while the conservative estimate is 0.33 $/kW$_e$h [67].

This economic analysis was conducted for a 4 MW_e continuous electrical generation system, capable of producing 24.5 to 31.5 GWh per year. This equates to a capacity factor of 0.70 to 0.90, much higher than is possible with solar photovoltaic or even conventional CSP systems

with limited storage. Although the levelized cost of energy produced is high compared to present fossil fuel costs, it is not necessarily high compared to conventional CSP systems. The wide range of uncertainty in the economic estimates clearly demonstrates the need for further research, in particular with regards to i) the detailed large-scale design and simulation of the receiver along with selection of salt and materials, ii) the best use of the site-specific land available via optimal placement of heliostats and iii) the optimal integration of the receiver's salt pond and lid with the power cycle, including a cogeneration scheme.

Table 3.6 - Upper and lower bounds for predicted CSPonD levelized cost of energy

Property	Units	Conservative	Optimistic
Rating and efficiencies			
Average specific direct normal radiation	kW/m^2	0.25	0.30
Nameplate capacity	MW_e	4.0	4.0
Heliostat overall efficiency	MW_t/MW_t	0.5	0.6
Pond efficiency	MW_t/MW_t	0.6	0.9
HX efficiency	MW_t/MW_t	0.9	1.0
Power cycle efficiency	MW_e/MW_t	0.3	0.4
Availability*Capacity factor*(1-Derate)		0.7	0.9
Capital cost. Excluding contingencies, tax and land which are included in SAM			
Heliostat specific cost*	$\$/m^2$	215	150
Pond cost	$MM	4.8	1.9
Heat exchanger cost	$MM	0.2	0.1
Power block cost	$MM	4.8	2.4
Utilities, piping, site work*	$MM	8.6	3.5
Operating costs	$MM/yr	2.0	0.5
Calculated properties			
Overall efficiency	MW_e/MW_t	0.08	0.22
Direct normal radiation required	MW	49.4	18.5
Heliostat area required	m^2	197,530	61,730
Heliostat cost	$MM	42.5	9.3
Operation	hours/yr	6,132	7,884
Yearly electricity produced	GWh/yr	24.5	31.5
Capital cost	**$MM**	**61**	**17**
SAM results	**$/kWh**	**0.33**	**0.07**

**Heliostat installation cost included in "Utilities, piping, site work" category*

From [67]

CHAPTER 4: Experimental Testing

A high-flux large-area solar simulator has been designed and characterized for the purpose of studying lab-scale CSPonD volumetric molten salt receivers. The light from seven 1500 W metal halide outdoor stadium lights is concentrated with a specular aluminum cone, achieving fluxes greater than 60 kW/m^2 (60 suns) at the output aperture [132]. The details of its design and characterization are presented in the Appendix. The following sections describe the design and testing of various lab-scale molten salt receivers, used to validate the CSPonD concept.

Single tank volumetric receiver

Optical heating tests of a single tank, volumetric molten salt receiver were performed to examine the temperature distribution of industrial-grade molten nitrate salt (Coastal Chemical Hitec® Solar Salt 60:40 wt.% $NaNO_3$:KNO_3 mixture; melting temperature 220-240 °C). A well-insulated AISI type 316L stainless steel receiver, 67 mm inner diameter x 250 mm long, was fabricated from NPS 2 ½ Sch 10S pipe (73 mm OD x 3 mm wall thickness) and instrumented along its length with eight type K sheathed thermocouples. Four thermocouples protrude into the volumetric receiver to measure centerline temperatures, while the remaining four are positioned near the receiver wall (Fig. 4.1). Low expansion, high strength reinforced silica matrix refractory board (Zircar RSLE-57) with a 63.5 mm aperture was mounted to the bottom of the concentrator to limit heating to only the exposed salt surface.

The salt mixture was premelted to approximately 250 °C using a hot plate, as the 60-sun peak flux provided by the MIT CSP simulator would take several hours to melt an otherwise adiabatic salt container, and then the filled receiver was placed under the solar simulator to be optically heated (Fig. 4.2). The simulator was successful in heating the nitrate salt and keeping it molten. Figure 4.3 shows the appearance of the molten salt-filled receiver, removed from the simulator, and illuminated with a laser pointer to demonstrate the transparent nature of the salt.

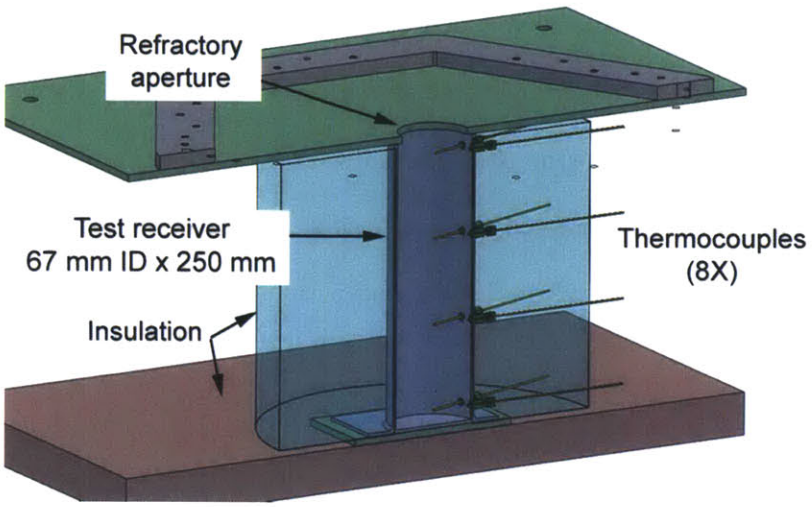

Figure 4.1 - Schematic of single tank test receiver
For optical heating tests with molten nitrate (60/40 Na-K) salts.

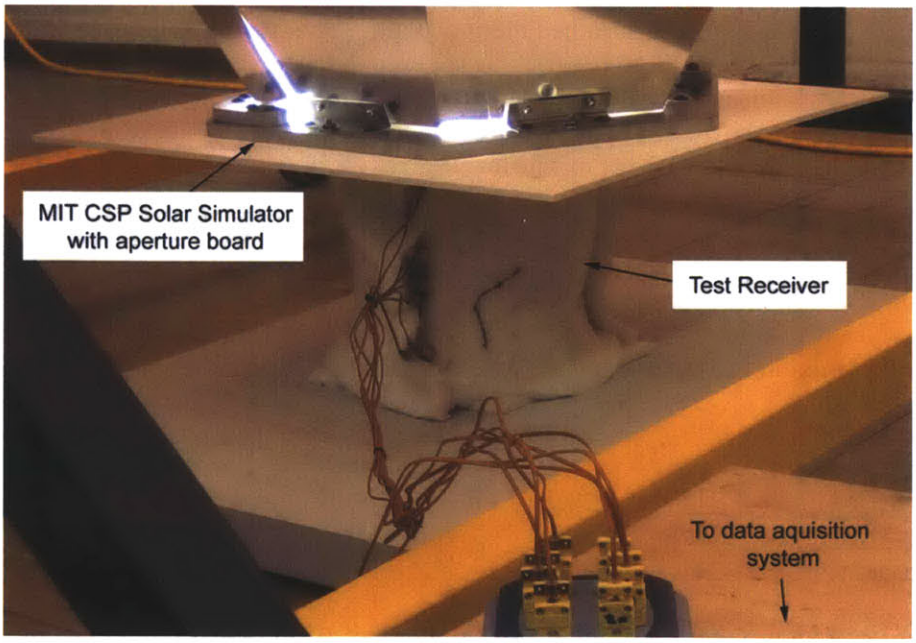

Figure 4.2 - Solar Simulator with single tank volumetric receiver at aperture.

Figure 4.3 - Molten nitrate solar salt mixture in single tank test receiver
Premelted, then optically heated to 330 °C by MIT CSP solar simulator – removed for photo. The red light is from a laser pointer used to demonstrate the transparent nature of the salt.

Figure 4.4 plots the temperature distribution in the single tank volumetric receiver at various heating times. Thermal stratification was observed, although the upper third of the salt was nearly at the same temperature as the surface, indicating volumetric energy absorption throughout that region of the receiver. It is interesting to note that the uppermost tank wall temperature, denoted by the unfilled data points, is hotter than the salt surface temperature. One explanation for this could be the divergent nature of the output rays from the simulator's non-imaging secondary concentrator (shown in Fig. A.12). As a result, the absorptive receiver walls are heated selectively in the upper region, which in turn, heat the salt in near the top of the receiver more than volumetric heating effects alone.

As an aside, it is worth discussing the significant heat losses through the bottom of the test receiver. The bottom of the cylindrical vessel was formed by welding on a 3.2 mm thick AISI type 316L stainless steel plate. This plate was made oversized (152 x 152 mm) to provide a large

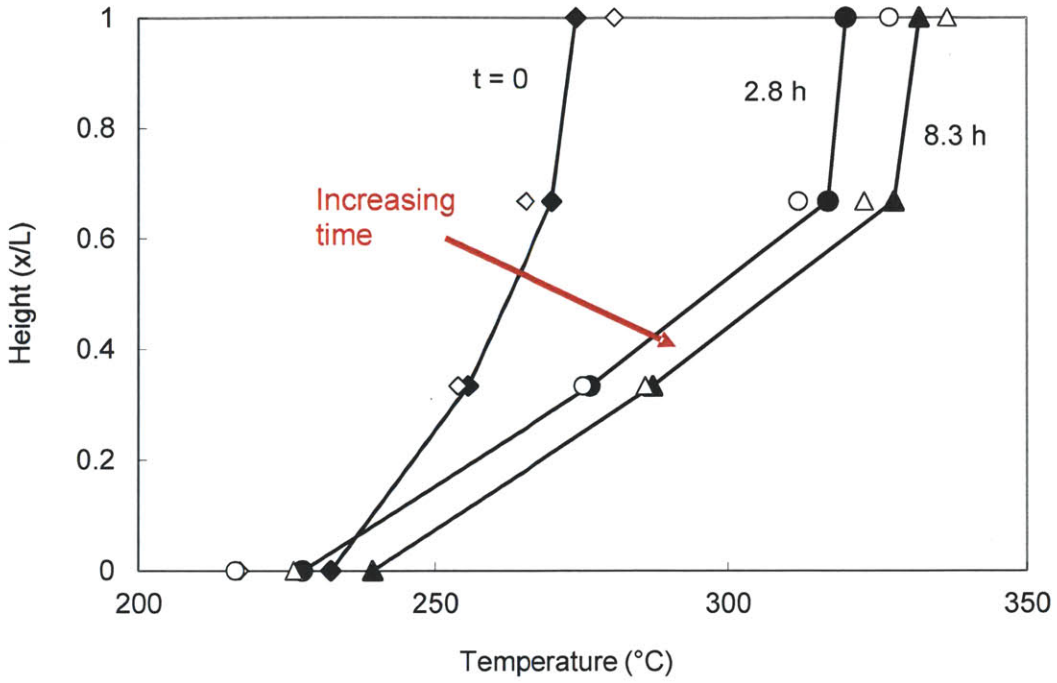

Figure 4.4 - Temperature distribution of nitrate salt mixture in single tank test receiver Heated by solar simulator; tank wall temperatures are denoted by the unfilled data points.

base and stability for the tall aspect-ratio receiver. Unfortunately this caused the plate to function as a heat sink, dissipating heat similar to a thermal fin. The heat losses leaving the test receiver are dominated by the bottom plate as evidenced the slope of the temperature curves on Fig. 4.4., even though the vessel was placed on a 2" (50 mm) thick slab of insulating calcium silicate. Large-scale systems will obviously be constructed with an adequate thickness of better performing insulation, mitigating a significant portion of the conduction losses out of the bottom.

It is interesting to compare the temperature evolution in the test receiver with that of an idealized volumetric absorber model presented by Lenert, as shown in blue on Fig. 4.5 [64]. For comparison, the temperature evolution for an equivalent power, surface-flux heated receiver is denoted by black curves. There is good agreement between the simplified volumetric absorption model presented in Chapter 2 and illustrated by Fig. 4.5, and the experimental data, as indicated by the qualitative agreement between the curves. Even though the test system has significant

conduction losses through the bottom as compared to the insulated boundary condition imposed on the model, it is clear that the experimental receiver is not behaving as a surface-flux heated system.

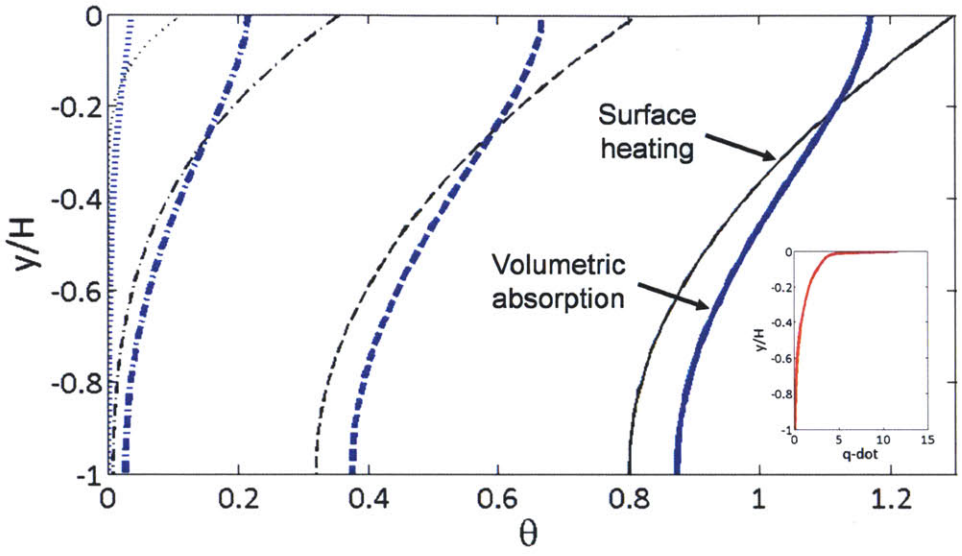

Figure 4.5 - Volumetric versus surface heating temperature profiles

Non-dimensional temperature (θ) progression at various times; volumetric heating (blue) versus surface heat flux (black). Exponentially decaying volumetric heating profile (red) shown in inset. From [64]

Divider plate equipped receiver

Additional tests were carried out using a volumetric molten salt receiver equipped with a movable divider plate, designed to partition the receiver into two thermally separated regions (Fig. 4.6). A 316L stainless steel receiver was designed with proportions similar to the aforementioned 600 MW_th receiver to fill the nearly the entire simulator aperture area: 280 mm inner diameter x 80 mm high. The divider plate was constructed from 3.2 mm thick 316L stainless steel with a 6.4 mm thick layer of rigid silica insulation board (Zircar RSLE-57) affixed

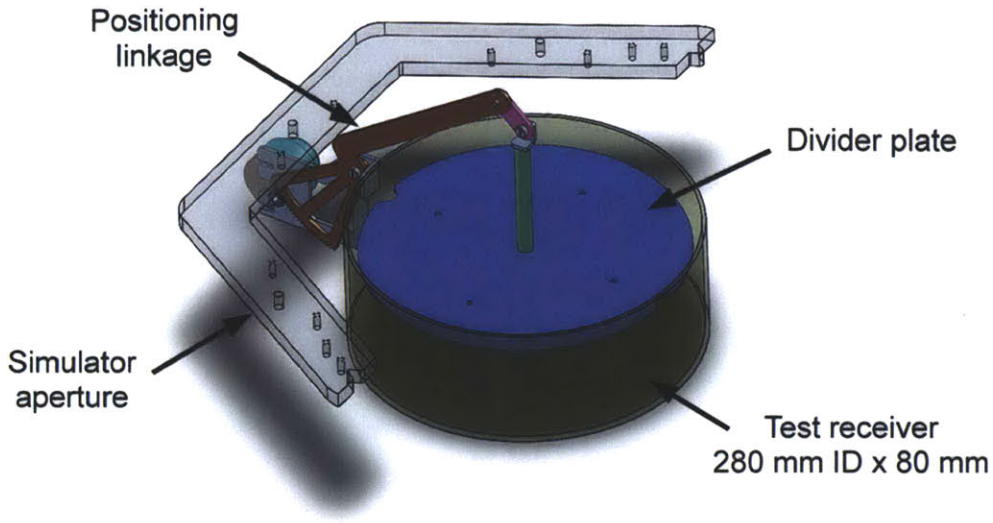

Figure 4.6 - Schematic of movable divider plate test receiver

to the underside, and given a nominal 8 mm annular clearance to the tank walls. The divider plate position was controlled via a crank-slider mechanism driven by a gearmotor installed outside the receiver. The receiver and divider plate were instrumented at several locations with type K thermocouples and the receiver was wrapped with ceramic fiber insulation followed by layers of fiberglass insulation. 5 L of Hitec® Solar Salt was premelted to 250°C and optically heated with MIT CSP solar simulator. Figure 4.7 shows the salt-filled receiver in, and removed, from the simulator. As in the single tank experimental receiver, the molten salt appears virtually transparent when melted.

Figure 4.8 depicts the temperature distribution of the volumetric receiver for different positions of the divider plate. The divider plate succeeds in providing excellent thermal separation between the upper (hot) and bottom (cold) sections. The bare stainless steel top surface of the divider plate absorbs much more energy than the relatively transparent salt; as a result, the hottest region of the receiver is the top surface of divider plate. This is excellent for establishing natural convection cells in the top region and promoting uniform, isothermal conditions which maximize thermal storage in a given volume of salt.

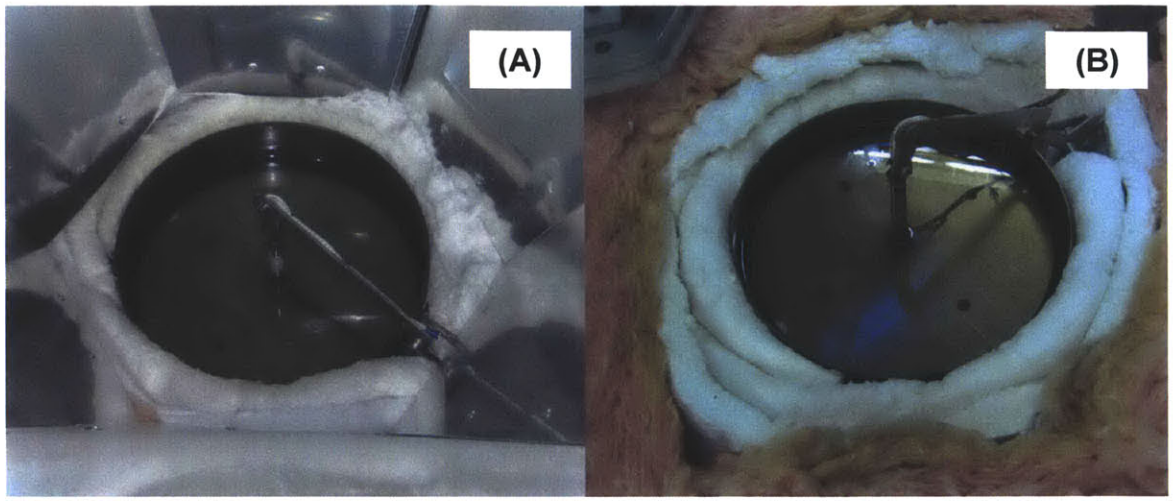

Figure 4.7 - Molten nitrate solar salt in movable divider plate test receiver
Volumetric receiver (A) inside solar simulator output aperture; (B) removed from simulator. The divider plate is clearly visible in its raised position near the surface of the salt.

Unfortunately due to packaging constraints, there is insufficient thermal resistance across this small-scale divider plate resulting in significant conduction losses to the lower cold region. The conductivity of the RSLE-57 silica board is 0.64 W/m-K, nearly the same as the molten salt. Even though the divider plate prohibits mass transfer and convective mixing between the layers, the observed temperature difference of 30 K implies a conductive heat flux of nearly 3 kW/m^2 across the plate (area times thermal resistance: $A \cdot R_{th} \sim 0.01$ m^2·K/W); far too much for this small, low-power testbed. Full scale systems would utilize significantly more effective insulation, on the order of 10-20 cm with reduced thermal conductivity, providing a greater thermal resistance and limiting heat transfer while providing the design value of 300 K across the divider plate.

The light mostly penetrates to the divider plate in this small scale test system – and cannot accurately predict how a full scale machine would truly work. In a larger and deeper system, the upper surface of the divider plate will receive less radiation. However, with full-thickness insulation on the divider plate, conduction through the bottom plate will decrease. It is expected that natural convection in the upper hot salt region will remain of the same magnitude

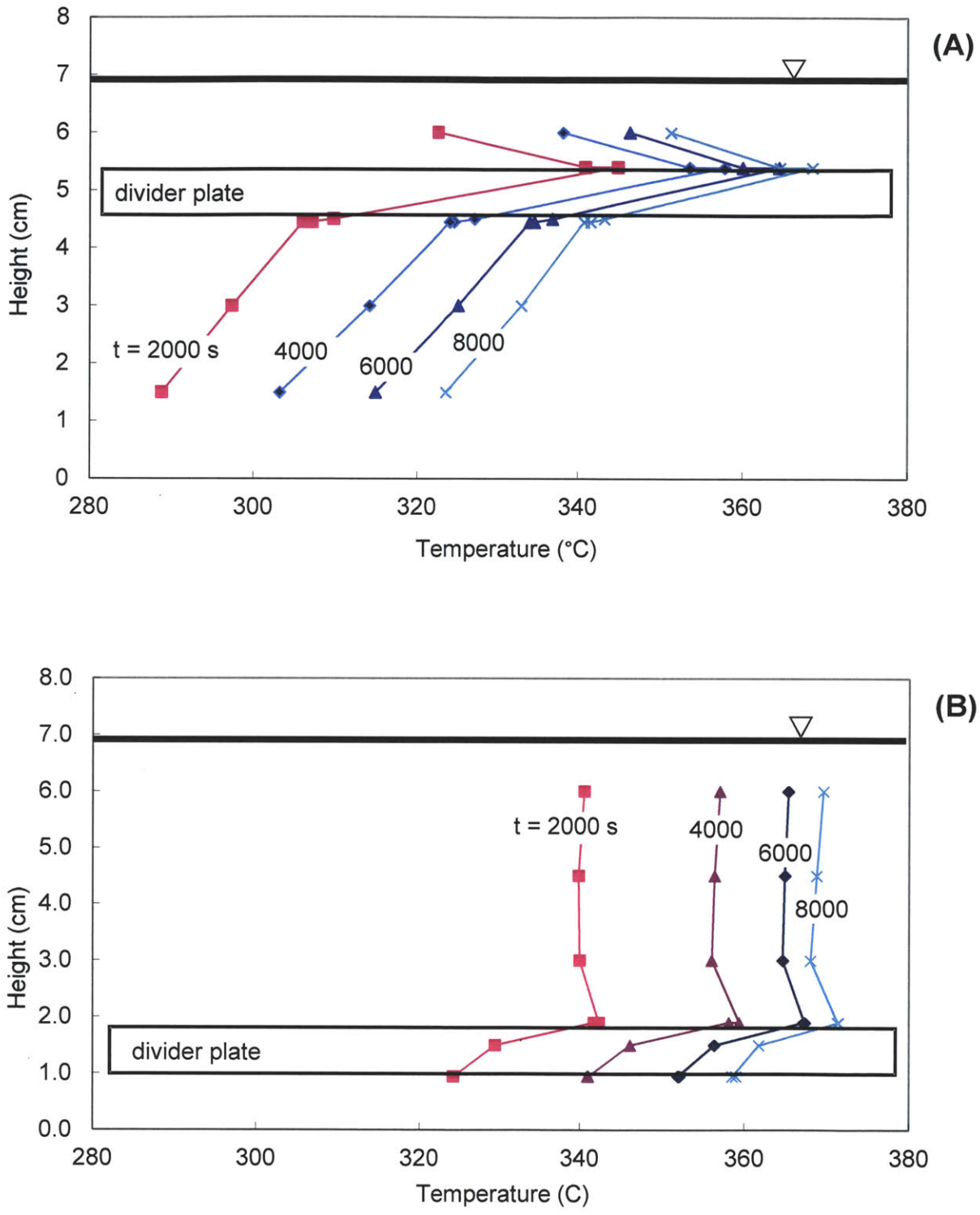

Figure 4.8 - Temperature distribution of nitrate salt in divider plate test receiver Heated by MIT CSP solar simulator; the movable divider plate is denoted by the box located (A) near the salt surface and (B) near the bottom of the test receiver.

since radiant flux intensities will be greater in full-scale systems, and a temperature inversion should still occur in the hot salt region. Accordingly the Nusselt number (the ratio of convective to conductive heat transfer across the divider plate) is similar to this experiment.

Natural convection characterization

The nearly isothermal upper salt region, clearly evident in Fig. 4.8b, is a result of convection above the divider plate. This type of natural convection occurs when buoyancy forces overcome viscous forces in a plane of fluid heated from below. Hexagonal recirculating flow cells, termed Bénard cells, develop when the horizontal fluid layer becomes unstable. Ignoring container effects, the critical temperature difference between the lower heated surface, T_h, and colder upper surface, T_c, for this flow to begin corresponds to the critical Rayleigh number:

$$\mathrm{Ra} = \frac{g\beta'(T_h - T_c)\delta^3}{\nu\alpha'} = 1708 \tag{4.1}$$

where δ is the thickness of the fluid layer and g is the acceleration due to gravity. β', ν and α' represent the fluid's coefficient of volumetric expansion, kinematic viscosity and thermal diffusivity, respectively [120]. If Ra < 1708, the viscous forces overcome the buoyancy forces and the fluid remains motionless with heat transfer progressing solely by conduction. On the other hand, turbulent convection sets in if the temperature difference $T_h - T_c$ increases to a value corresponding to Ra = 50,000, destroying the regular cellular flow patterns.

Figure 4.9 maps the three distinct heat transfer regimes for various fluid thicknesses and temperature differences. Fluid properties correspond to the nitrate solar salt used in this experiment, taken at a temperature of 350 °C giving $\beta' = 3.7 \times 10^{-4}$ 1/K, $\nu = 1.3 \times 10^{-6}$ m^2/s, and $\alpha' = 1.8 \times 10^{-7}$ m^2/s [92]. Clearly, for all but very thin fluid layers, even the smallest temperature difference will produce convective mixing in the salt layer above the divider plate. In the scale model, there is approximately a 2 cm salt thickness above the divider plate in the "up" position

(Fig. 4.8a) – the measured 15-20 K temperature inversion is sufficient to induce turbulent mixing. Similar behavior is seen in the "down" position (Fig. 4.8b) for 5-10 K temperature difference in the 5 cm salt layer.

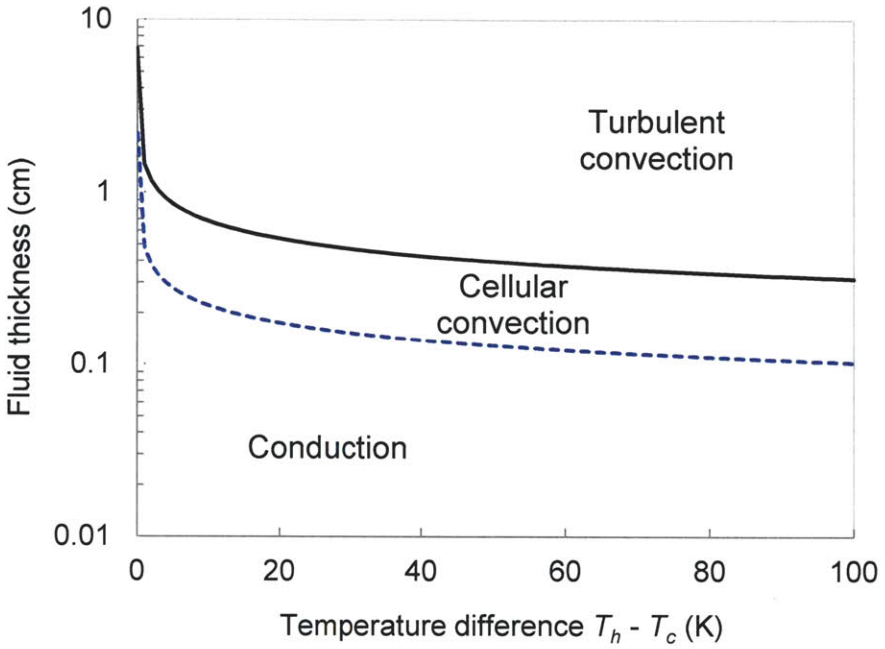

Figure 4.9 - Heat transfer regimes for hot nitrate salt layer above divider plate

Active flow receiver

Further testing was conducted using a divider plate-equipped volumetric receiver integrated into a natural convection loop. The solar simulator heats the receiver, which is at a lower elevation than a non-insulated fluid storage reservoir. Buoyancy force drives the hot, less dense fluid through the receiver outlet pipe and into the higher elevation reservoir. Heat is rejected at the reservoir, causing the cooler, denser fluid to return to the receiver, whereby it is reheated and the cycle is repeated (Fig. 4.10). The "thermosiphon" driving force for the flow is

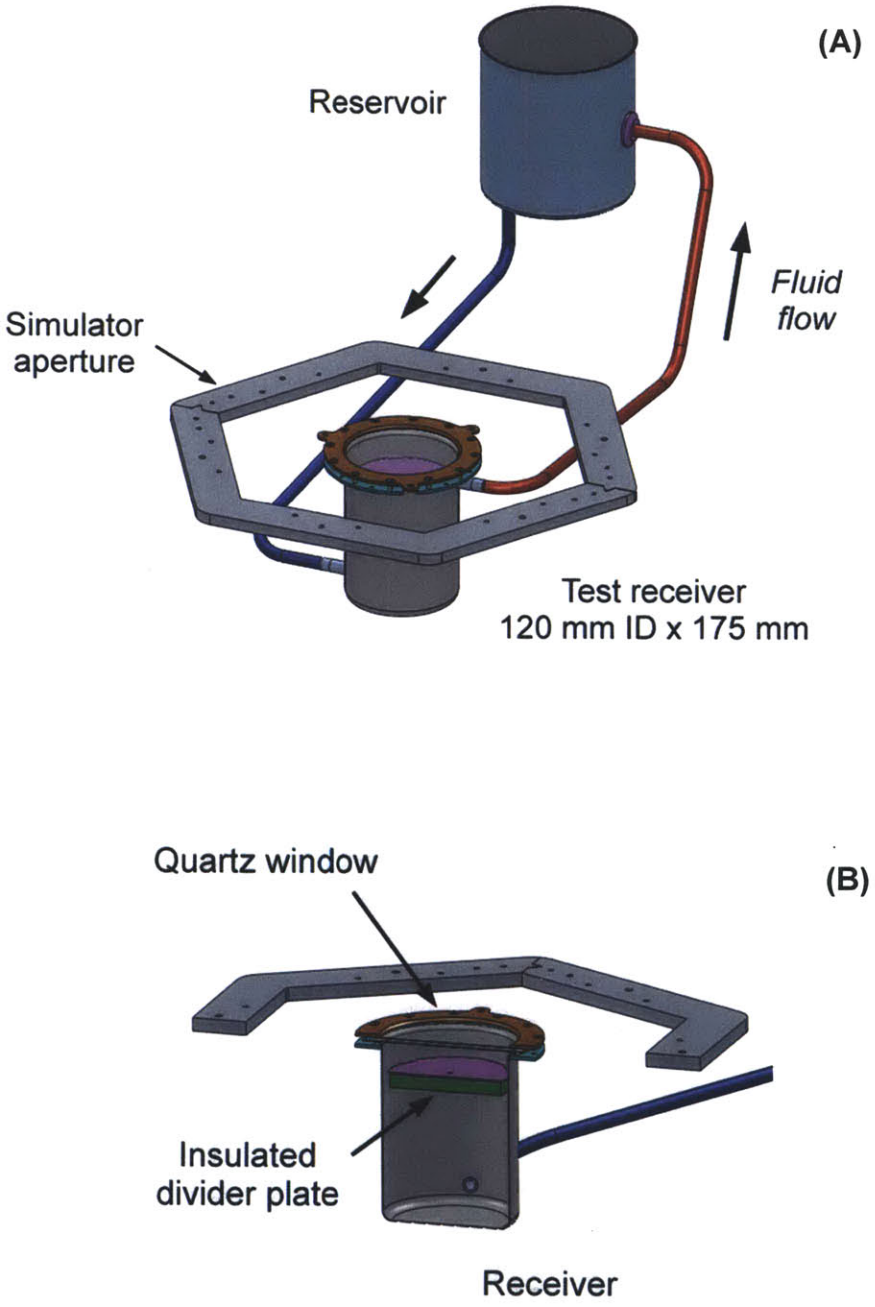

Figure 4.10 - Schematic of active flow thermosiphon test receiver

(A) Fluid in the receiver is heated by the MIT CSP solar simulator, flows upwards to the reservoir, cools, and then returns to the receiver to be reheated; (B) Cool fluid enters the bottom and flows past the divider plate before exiting the top of the test receiver.

the loop buoyancy, which is the difference in weight of the columns of fluid in the loop, and is exactly dissipated by the friction pressure drop $\Delta P_{friction}$ around the system: [133]

$$\Delta P_{friction} = \oint \rho(T) g dz \tag{4.2}$$

where the fluid density $\rho(T)$ varies with temperature.

A 120 mm inner diameter x 175 mm high 304L stainless steel bucket was modified for use as the thermosiphon receiver. Inlet and outlet ¼" NPT port fittings were silver brazed on diametrically opposite sides near the bottom and top, respectively. Additional ports were installed on the receiver bottom to facilitate fluid draining, mounting a central 3.2 mm 316L sheathed type K thermocouple profile probe, and securing a divider plate actuation rod. A quartz window, 3.2 mm thick, was sandwiched between upper 6061-T6 aluminum and lower 304L stainless steel clamping flanges with a 3.2 mm high temperature silicone sheet gasket as shown in Fig. 4.11.

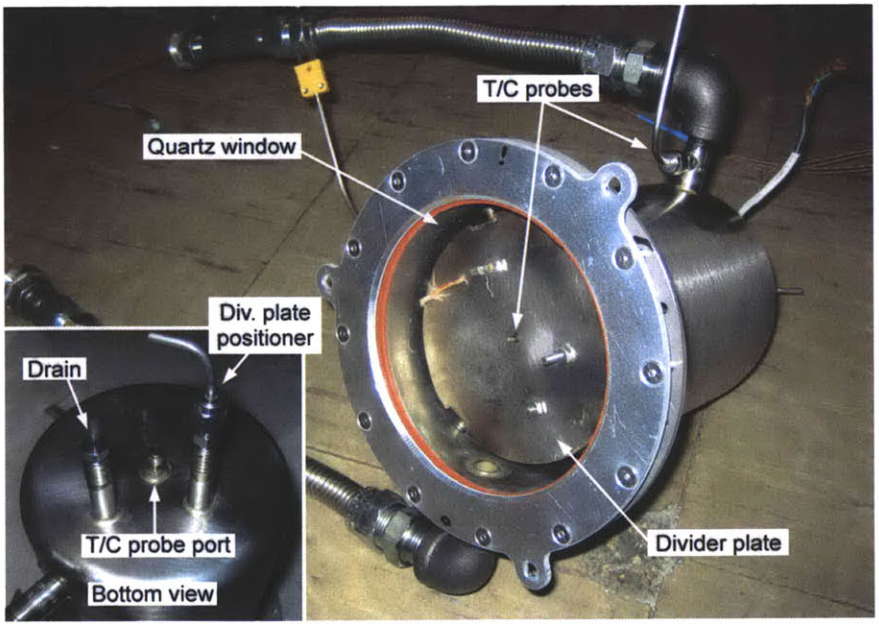

Figure 4.11 - Active flow test receiver construction details

The quartz window was necessary to contain the fluid as the receiver was mounted at a lower elevation than the fluid reservoir, a necessary condition for thermosiphon flow. Flexible and rigid 304L stainless steel pipes (nominal ½" NPS) connect the receiver to a 170 mm diameter x 193 mm cylindrical type 304L reservoir; the entire system was externally insulated using ceramic fiber and fiberglass insulation. A divider plate was fabricated from 170 mm diameter x 1 mm thick type 304L, providing a 5 mm annular gap to the receiver wall for the blow-by fluid flow. A 25.4 mm slab of closed-cell rigid glass insulation (Foamglas®: $k \sim 0.04$ W/m-K; $\rho \sim 120$ kg/m^3) was affixed to the underside of the stainless divider plate. Additional type K thermocouples were mounted at the connection pipe fittings on both the receiver and reservoir and to the top and bottom surfaces of the divider plate. The thermosiphon system was designed with a nominal 5 L capacity; when filled with this volume, the free surface of fluid in the reservoir is approximately 140 mm above the top of the receiver. The system was validated using water as the working fluid. Optical heating data using the solar simulator are depicted in Figs. 4.12 and 4.13.

As Fig. 4.12 shows, the solar simulator was successful in inducing thermosiphon flow in the water-filled system. However, the heating rates were much too intense and the simulator easily boiled water above the divider plate, as shown on Fig. 4.13. Surging steam flow cycles are evident, created by vapor pockets within the upper portion of the receiver that remain trapped and block thermosiphon loop flow. Once pressure increases, the slug of steam is forced out of the receiver outlet pipe, allowing the receiver to fill and the process to repeat again.

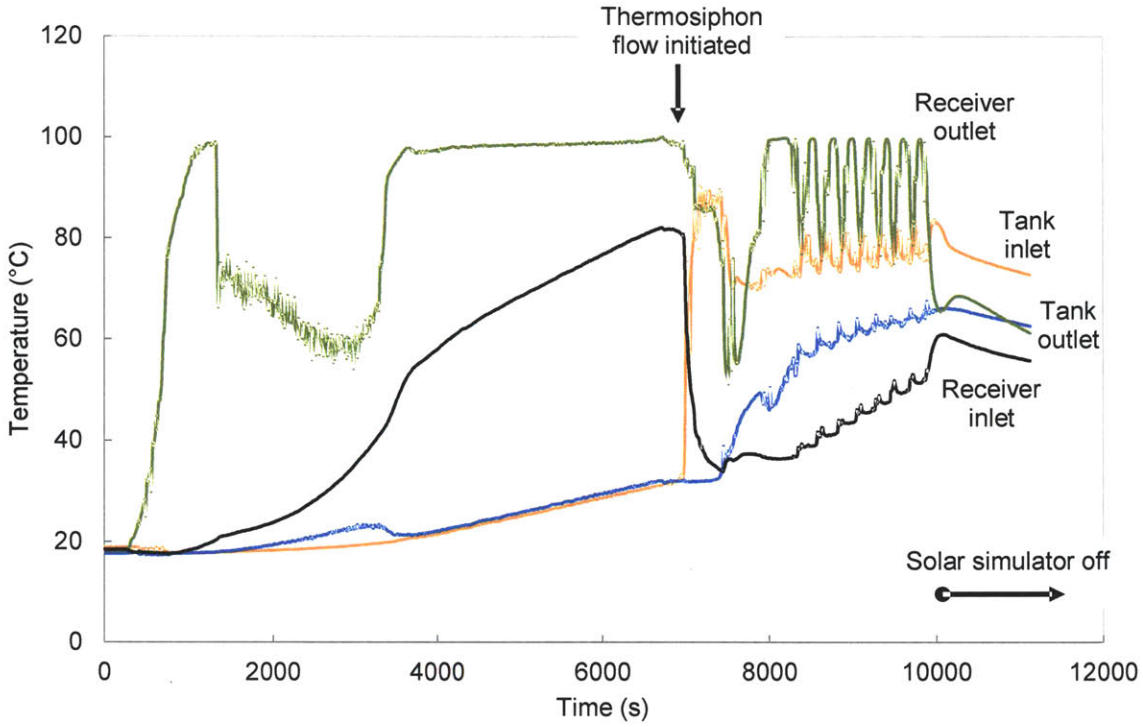

Figure 4.12 - Temperature evolution in thermosiphon system: water

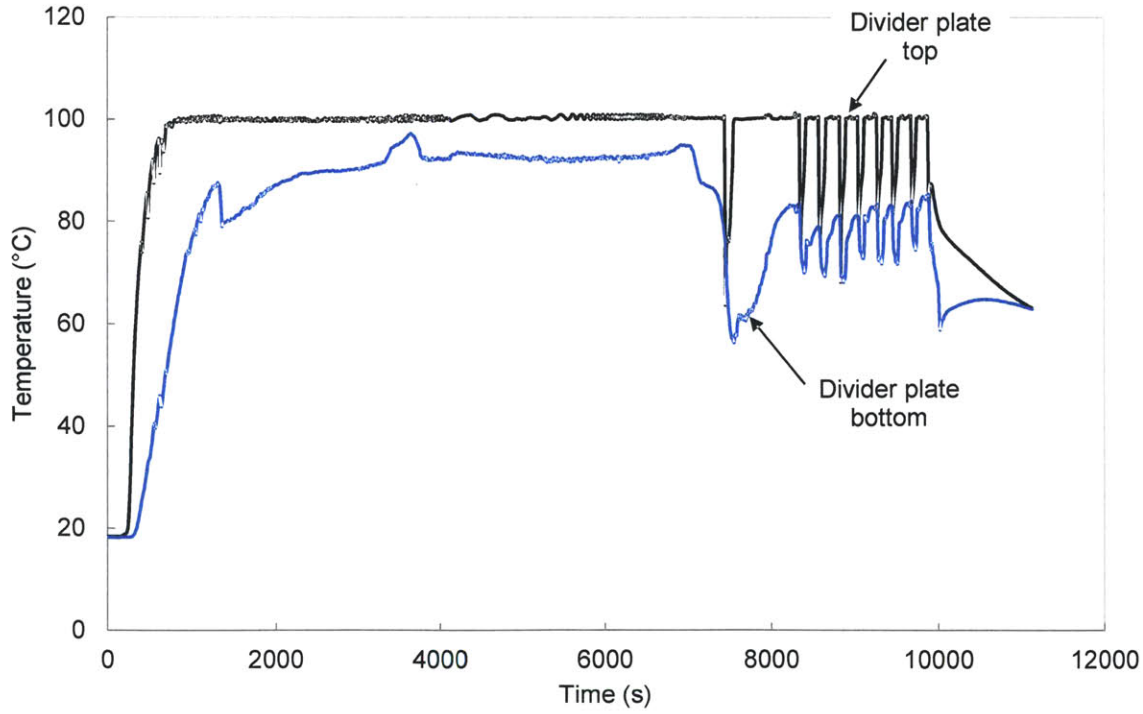

Figure 4.13 - Divider plate temperature in thermosiphon system: water

Fortunately, removing the external insulation on the receiver, reservoir and piping and adding a cooling fan directed at the reservoir were found to eliminate the percolations (Fig. 4.14). Once flow is initiated, the forced convection of air over the reservoir tank's exterior serves to cool the water entering the reservoir quicker, resulting in reduced receiver inlet temperatures, faster thermosiphon flow and minimal boiling rates. The ripples in divider plate temperature in Fig. 4.14 are the result of moving divider plate within the receiver: every 10-15 minutes the divider plate was moved upwards approximately 10 mm along the receiver's axis.

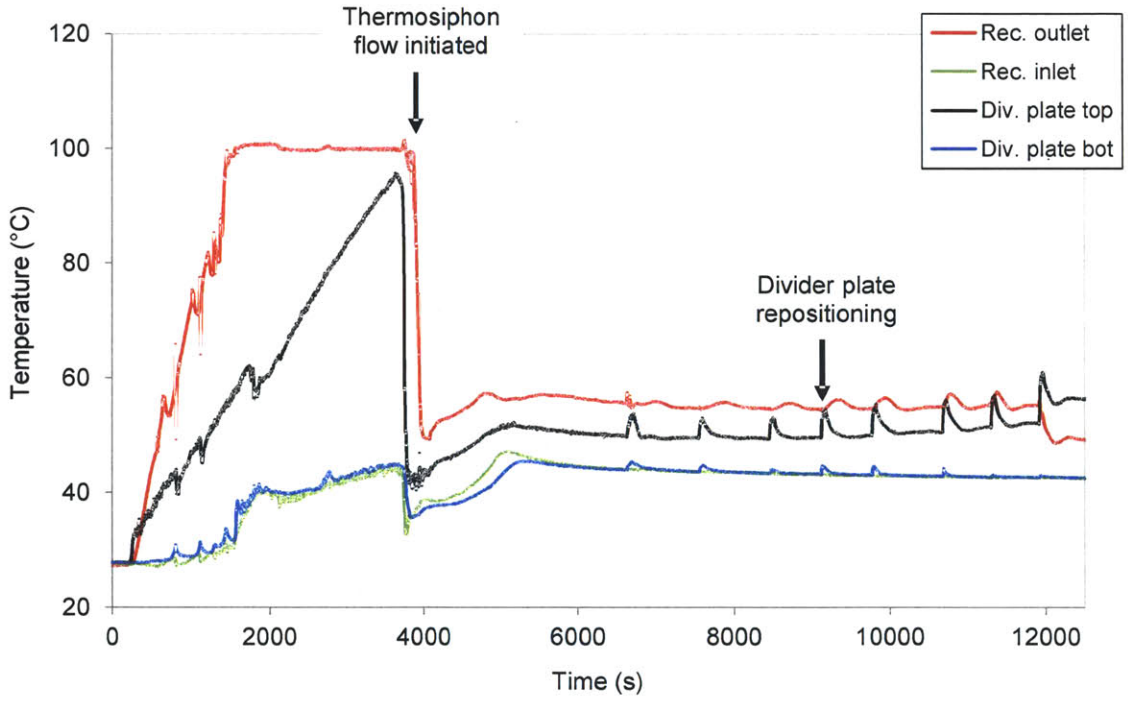

Figure 4.14 - Temperature evolution in non-insulated thermosiphon system: water
The divider plate is moved upwards approx. 10 mm every 600-900 s beginning at t = 6500 s.

Figure 4.15 plots the vertical temperature profile within the receiver after the divider plate is repositioned and temperatures reach steady-state values. For convenience, the non-dimensional temperature θ is plotted, defined as:

$$\theta = \frac{T - T_{\infty}}{T_{inlet} - T_{\infty}} \tag{4.3}$$

The upper surface of the divider plate increases in temperature as it is moved up within the receiver, while the fluid region below remains isothermal, regardless of divider plate position. It is also important to note the receiver outlet temperature (Fig. 4.14) remains nearly constant even as the divider plate is moved within the receiver (except for the anomaly at t = 12000 s, where the divider plate is moved above the receiver outlet port). These observations support the original design intent of maximizing thermal storage within the receiver and providing constant high temperature output, even as the system's overall state of charge varies.

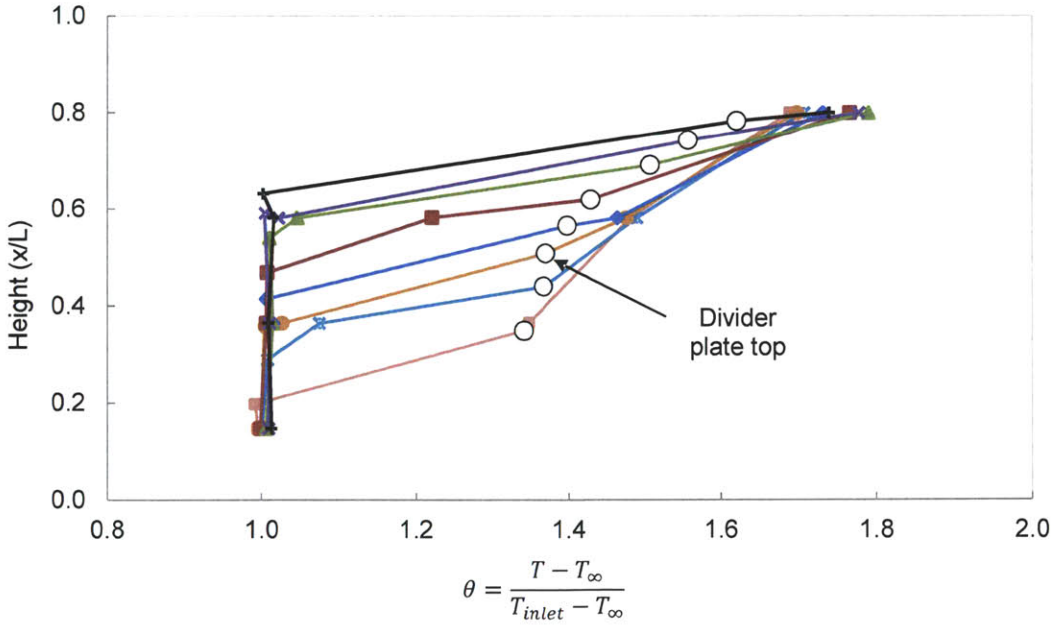

Figure 4.15 - Temperature profile within active flow test receiver: water

Next, the thermosiphon system was prepared for use with molten nitrate solar salt. External resistance wire and band heaters, totaling 3.2 kW_e, were added to the receiver, reservoir and piping to preheat the system above the 222 °C freezing point of the salt. Figure 4.16 shows the system outfitted with heaters and insulation in preparation for the premelted salt addition. Each heater was wired in independent zones, manually controlled to prevent localized overheating. Additional thermocouples were added near the heaters on the exterior of the tanks and piping to monitor hot spots and system temperatures.

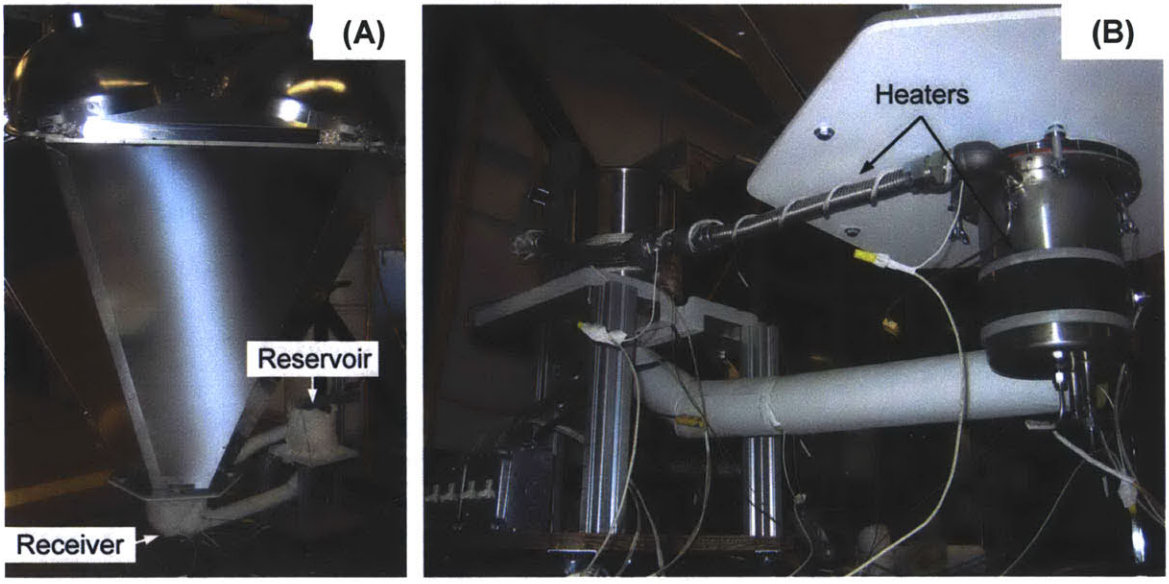

Figure 4.16 - Active flow test receiver for use with molten nitrate solar salt
(A) Receiver sits a lower elevation w.r.t. the fluid reservoir; all piping and tanks are well insulated; (B) Supplemental heaters preheat the components prior to molten salt addition.

Once the system was sufficiently heated, 5 L of premelted Hitec® Solar Salt was added. The reservoir and piping heaters were turned off, while the receiver heater was left running until thermosiphon flow was established. The lid was left off the reservoir container to allow heat to escape and cool the hot salt before it flowed back into the receiver to be heated. The receiver

heater was then turned off and the solar simulator was turned on, providing optical heating to the flowing system (Fig 4.17).

Unfortunately, the solar simulator was not powerful enough to prevent the system from cooling. This is due to the increased surface area of the thermosiphon system components, as compared to the divider plate-equipped receiver with the same system volume presented in the previous section. However, as shown in Fig. 4.17, the MIT CSP solar simulator did alter the cooling rates within the receiver, notably the upper surface of the divider plate and upper regions of salt.

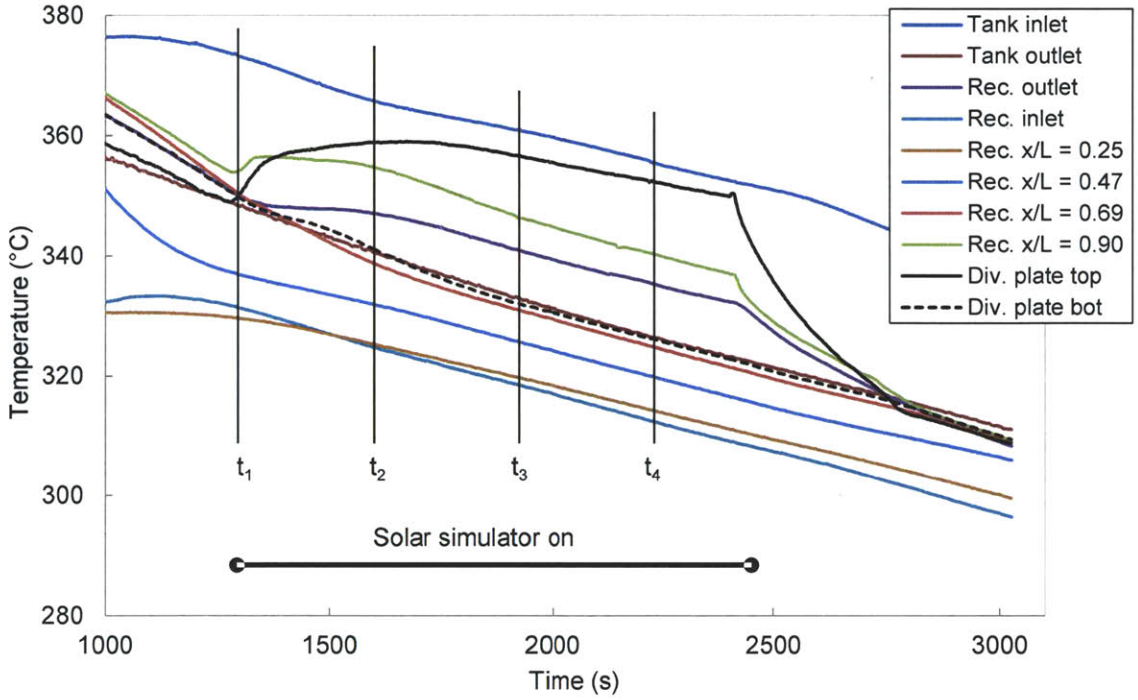

Figure 4.17 - Temperature evolution in thermosiphon system: nitrate salt

Figure 4.18 plots snapshots of the salt temperature profile at various times ($t_4 > t_3 > t_2 > t_1$), for a constant divider plate position, during the optical heating period depicted in Fig. 4.17.

This profile is noticeably different than the water-filled receiver as shown in Fig. 4.15. This is due to the higher operating temperatures of the salt-filled receiver, with significantly increased heat losses. For example, the bottom surface of the water-filled receiver is nearly adiabatic, as evidenced by the constant temperature profile below the divider plate. The salt-filled receiver, on the other hand, has a noticeable temperature gradient in the lower salt region from non-negligible heat losses. Similarly, the high temperature salt receiver exhibits a negative temperature gradient above the divider plate, due to increased surface radiation and convection losses on the quartz window.

Irrespective of the additional system losses, it is interesting to note the temperature difference across the divider plate increases as time progresses, even with the active fluid flow. Also, the region of salt below the divider plate acquires a more uniform temperature distribution as compared to the initial condition without simulator heating input.

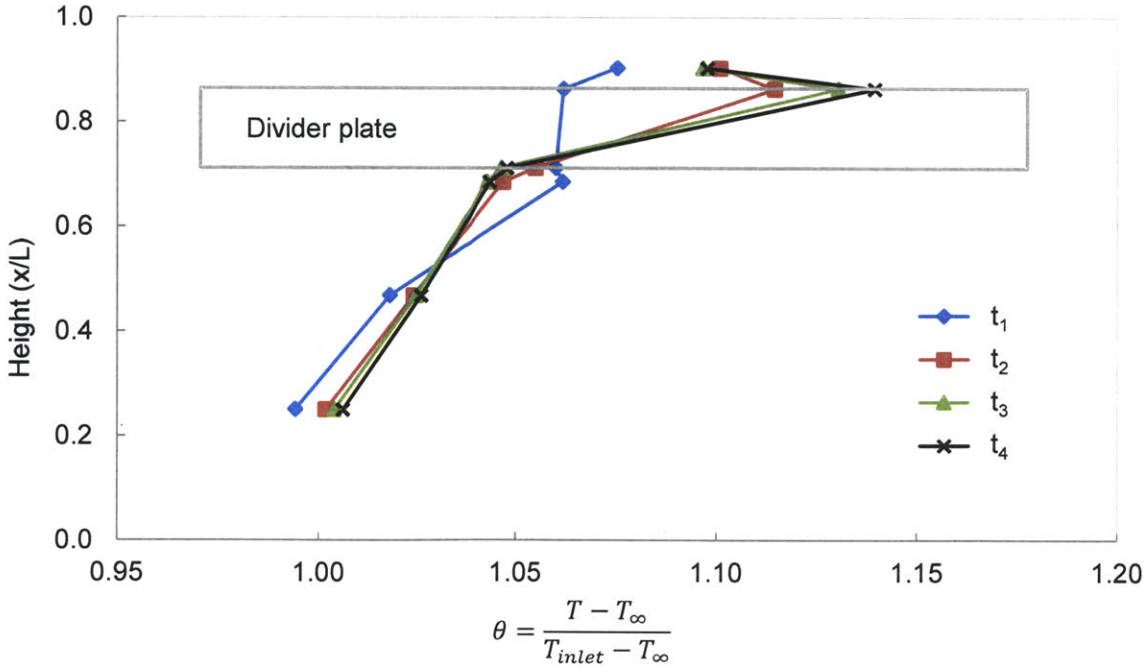

Figure 4.18 - Temperature profile within active flow test receiver: nitrate salt

Flow velocity characterization

Although the thermosiphon loop flow velocity was not directly measured (available measuring devices would impose significant pressure drops, altering or eliminating the thermosiphon flow), it was estimated using Schlieren flow visualizations of the hot fluid entering the reservoir. The flow pattern is illustrated in Fig. 4.19 for water and in Fig. 4.20 for solar salt using a thermal imaging camera. In both cases, the flow was estimated to be on the order of 1 cm/s out of the ¼" NPT (9.2 mm ID) pipe fitting; equivalent to a volumetric flow rate of 660 mm^3/s or 2.4 L/h. Assuming a uniform velocity across the 5 mm annular gap, the fluid would pass at a velocity of 0.4 mm/s – relatively slow, similar to that of a full-size system.

The Richardson number, Ri, is the dimensionless ratio of potential to kinetic energy, relating the importance of natural convection to forced convection in fluid flows with active heat transfer. For the active flow receiver, it can be defined as:

$$\mathrm{Ri} = \frac{g\beta' \Delta T L}{v^2} \tag{4.4}$$

where $\Delta T = T_{div} - T_{inlet}$ is the temperature difference between the upper surface of the divider plate and the inlet fluid temperature, v is the fluid velocity in the tank-divider plate annulus, and L is a characteristic length, which, in this case, equals the depth of the divider plate's upper surface. Natural convection is negligible when Ri < 0.1, forced convection is negligible when Ri > 10, and neither is negligible when 0.1 < Ri < 10 [120]. For 35 < L < 120 mm, Ri = 0.5-1.6 × 10^4 for the water-filled test receiver (β' = 2.1 × 10^{-4} 1/K, ΔT = 10 K); for the solar salt-filled receiver (β' = 3.7 × 10^{-4} 1/K, ΔT = 30 K), Ri = 2.4-8.2 × 10^4. Obviously the Richardson number varies with divider plate position, but these values indicate natural convection dominates.

Additional trials were conducted with varying reservoir-receiver height differentials (140 ± 60 mm), but this did not have a noticeable effect on the apparent fluid velocity. This implies the flow was limited by the small diameter fittings and ports which imposed significant restrictions to

the flow. Nevertheless, pipe sizes were kept small in order to keep flow velocities relatively high, as it is known that low salt flow velocities in sections of unheated pipe are prone to freezing [134].

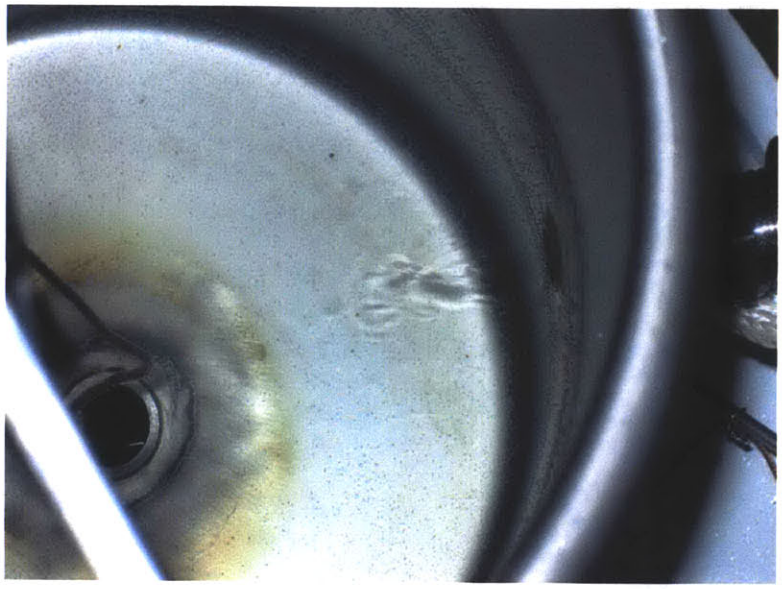

Figure 4.19 - Flow visualization in reservoir of active flow test receiver: water

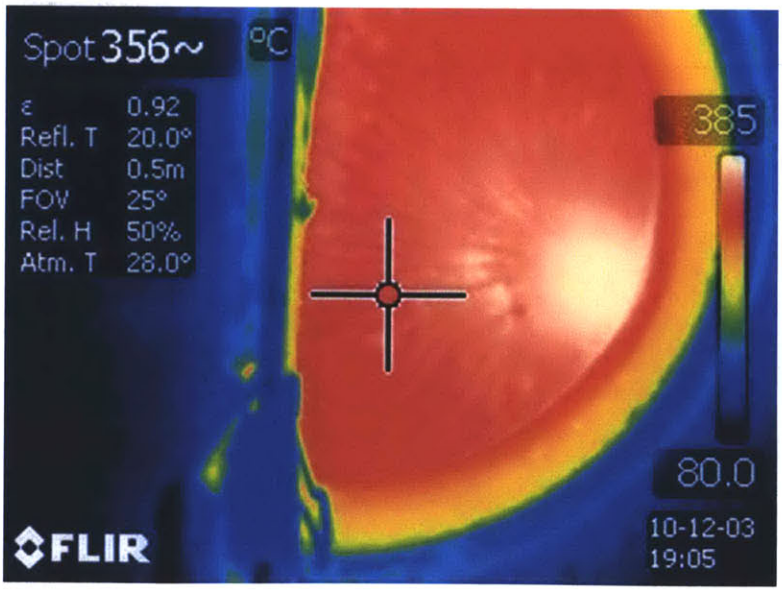

Figure 4.20 - Infrared flow visualization in reservoir of active flow test receiver: nitrate salt

Quartz aperture window

One of most interesting observations during the active flow receiver testing was the appearance of the quartz aperture window. Figure 4.21 shows the quartz window after several hours operating with water as the working fluid, and again at various intervals with molten salt in the thermosiphon system. Obviously, condensed water vapor remains a liquid on the heated window surface. On the other hand, condensed salt vapor builds up and solidifies on the cooler aperture window and reduces its effective transmittance. After a short period (0.5 h) the window is significantly clouded and the energy input to the system is decreased. After a long run under the simulator (4 h), the window is essentially opaque and what little heating that is accomplished progresses via conduction from the obscured quartz window's inner surface.

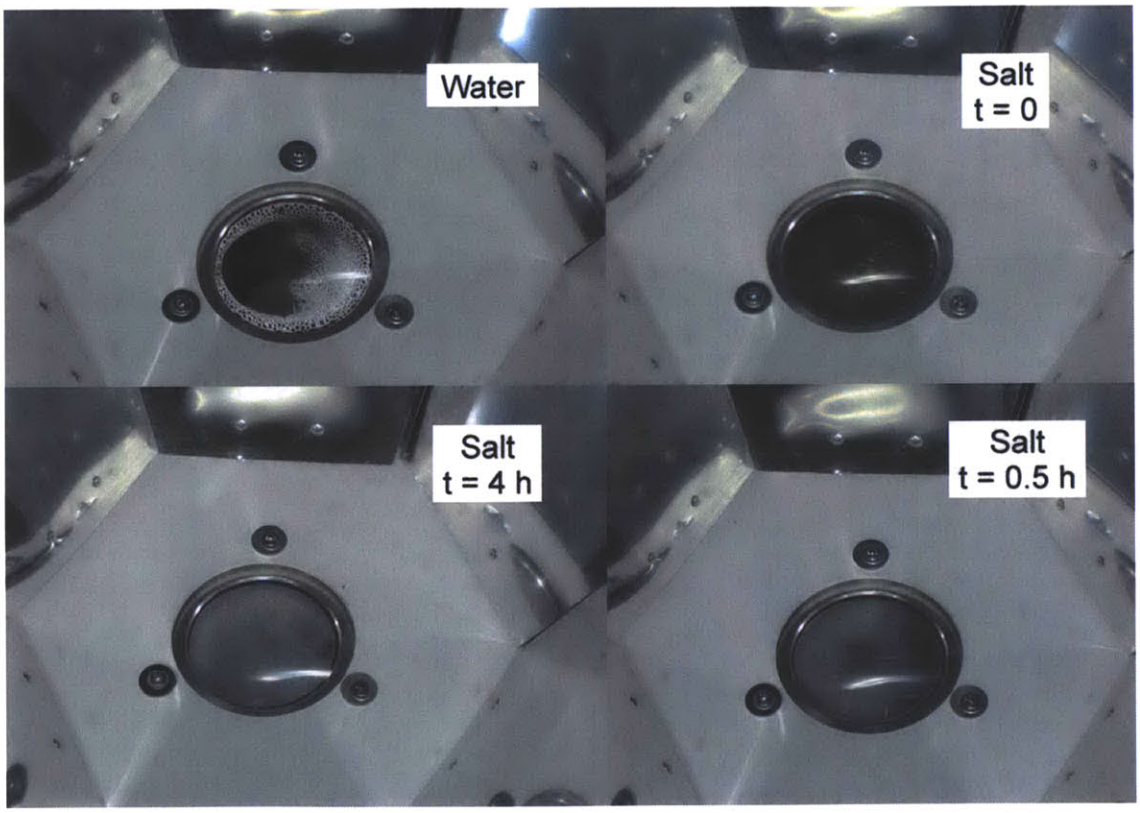

Figure 4.21 - Quartz aperture window appearance on active flow test receiver

This clouding is one of the main reasons that a sealed system complete with a transparent aperture window is not being considered for a large scale CSPonD receiver. Even if the inner surface of the window was kept cool and isolated with a protective gas shield, as is done on high flux volumetric receiver-reactor vessel designs, a significant portion of the incident flux is reflected off or absorbed within the window material. The same holds true for high temperature aperture window variants, operating above the salt's melting temperature, which would allow for transparent liquid salt to condense on its inner surface.

Heating considerations

Regrettably, the 60-sun solar simulator was not capable of heating the salt above 380 °C in any of the test receivers. This was to be expected with high system losses: conductive losses from the small receivers with their large surface area-to-volume ratios; plus radiative and convective losses from the salt surface. In fact, CSP trough plants operating with optical concentration ratios ranging from 40-80 have difficulty heating working fluids in excess of 350 °C, so it is no surprise that the MIT CSP solar simulator could not achieve higher temperatures [2]. However, the simulator proved sufficient to demonstrate the volumetric absorption, convective salt mixing, and movable divider plate concepts.

In general, a perfect receiver without any conductive or convective losses will have a "stagnation temperature" T_{max} found by setting the receiver efficiency $\eta_{rec} = 0$ in Eq. (1.1) as: [4]

$$T_{\max} = \left(\frac{\alpha_{eff} \Phi}{\varepsilon_{eff} \sigma} \right)^{1/4} \tag{4.5}$$

where the effective absorptivity and emissivity are denoted by α_{eff} and ε_{eff}, respectively. For this highest temperature to be achieved, a perfect receiver must be radiating energy at the same rate at

which it is receiving it. This implies no heat extraction and capture efficiency $\eta_{capture} = 0$, as in Eq. (3.24).

For these test receivers, no "useful" heat was extracted; assuming a perfect receiver and $\alpha_{eff} = \varepsilon_{eff}$, the minimum flux Φ required to obtain $T_{max} = 380$ °C is only 10.3 kW/m^2. This confirms that there were significant conduction and surface losses. These small scale experiments cannot provide insight to how a full scale machine would truly work; hence, numerical modeling is required to design the full scale tank and divider plate system, and then testing of a deep tank system. Full scale systems will utilize much greater flux levels with an insulated system cover. The geometry will approach that of a blackbody absorber and have significantly reduced system losses, which will increase achievable salt temperatures.

Salt melting for the experiments

For all tests, the nitrate solar salt was premelted on a hot plate before being placed under the solar simulator. Initial single tank receiver trials attempted to heat and melt the salt optically, but were unsuccessful. Figure 4.22 shows the unmelted salt appearance in the single tank receiver, prior to being placed under the simulator.

The solid salt granules are very reflective in the visible spectrum (evidenced by their white appearance), and as a result, they absorb only a small minority of the incident power. As discussed in Chapter 3 and plotted in Fig 3.15, very long times are needed to melt the salt at low input flux concentrations. For example, the 60 kW/m^2 solar simulator would require a few hours to create a melt puddle on the salt surface. Unfortunately, this long time constant also allows for the diffusion of thermal energy radially outwards, and in the case of these small receivers, the container wall-effects dominate at longer times – preventing optical melting of the salt.

Figure 4.22 - Appearance of unmelted solar salt used in tests
"Prilled" (pre-mixed) pellets, 1-3 mm diameter.

Figure 4.23 plots the measured salt surface temperature profile as compared to Eq. (3.30), the surface temperature of a semi-infinite body subject to a uniform heat flux. Initially, there is good agreement between the measured and predicted temperatures, but the wall-effects become noticeable after only one hour under the simulator.

An alternate optical melting strategy demonstrated by Rojas utilized metallic pieces embedded or placed on top of the solidified salt surface [135]. The metal has a higher absorptivity than solid salt; hence the metallic pieces achieve higher stagnation temperatures and heat more quickly. The heat from these "melting seed" components is transferred to and initiates melting in the surrounding salt. Tests were conducted with stainless steel spheres (1-5 mm diameter) and short lengths (10-30 mm) of stainless and copper tubing, with the complete volume of salt in various 5-10 L receivers optically melted by the MIT CSP simulator within a few hours. Once fully melted, the metallic melting seed components sank to the bottom of the receiver and remained for the duration of testing.

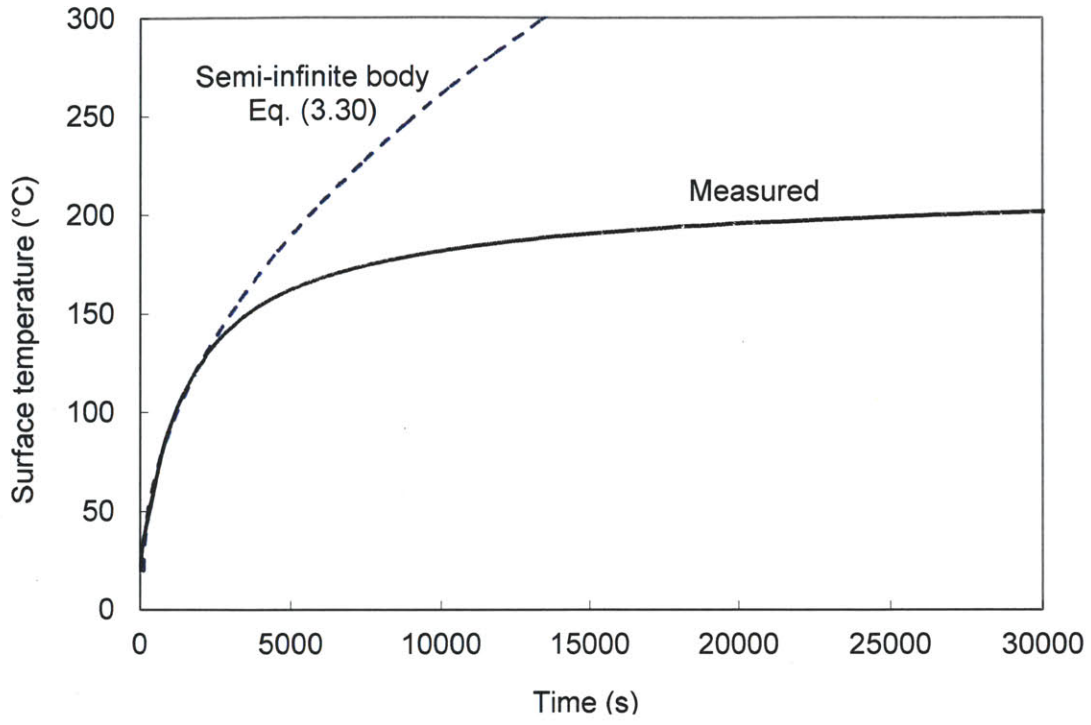

Figure 4.23 - Solid salt temperature during heating with solar simulator

Measured surface temperature as compared to Eq. (3.30) for a semi-infinite body subject to a uniform surface heat flux on the surface; reflectivity of solid salt estimated to be ~ 90%.

Another interesting occurrence worth mentioning is the appearance of freshly melted salt. When melted for the very first time, the industrial solar salt mixture developed a foamy, brownish scum on the surface, as shown in Fig. 4.24. This floating layer was not observed in salt mixtures prepared from chemically pure reagent grade materials, although it was noted by prior researchers and salt bath thermal processors using the commercial grade salts [3], [53], [105].

A call to the salt manufacturer indicated that the floating layer was likely due to anti-caking additives added to the salt, and would dissipate after a several hour "bake out" period. Samples were collected and solidified from the clear lower salt region and the floating scum layer, depicted in Fig. 4.25, and sent for analysis. Figures 4.26 and 4.27 show X-ray diffraction data for the clear and scum layers, respectively.

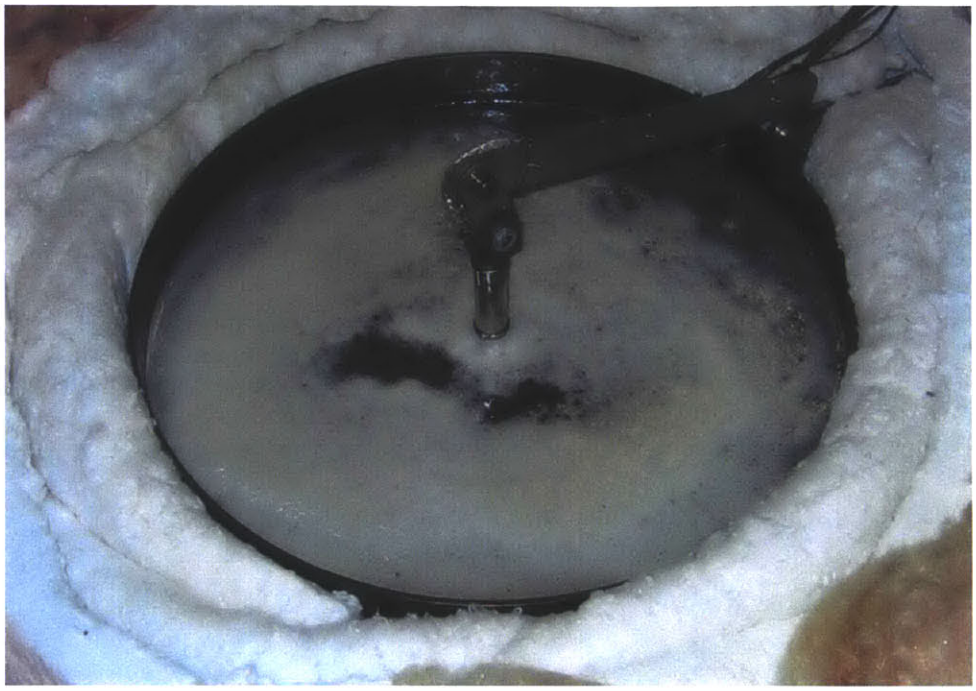

Figure 4.24 - Virgin melted solar salt with foamy surface scum

Figure 4.25 - Solidified pure and surface scum salt samples

X-ray diffraction testing proved inconclusive, as there were no detectable contaminants in the dirty scum layer as compared to the clear salt sample. Fortunately, the scum layer did dissipate after the salt remained molten for several hours. In the interest of time, much of the foamy layer was ladled off and discarded before proceeding with the experiments. Subsequent trials using premelted salt did not exhibit the foamy layer upon melting, confirming the manufacturer's comments regarding the burn-off nature of the foamy layer. In a full-size system, any initial foamy salt layer which forms can be removed using the weir salt extraction and pond skimming flow, as discussed in Chapter 3. Alternatively, the salt can be ordered in large-block form without the anti-caking additive, thereby eliminating any foaming issues.

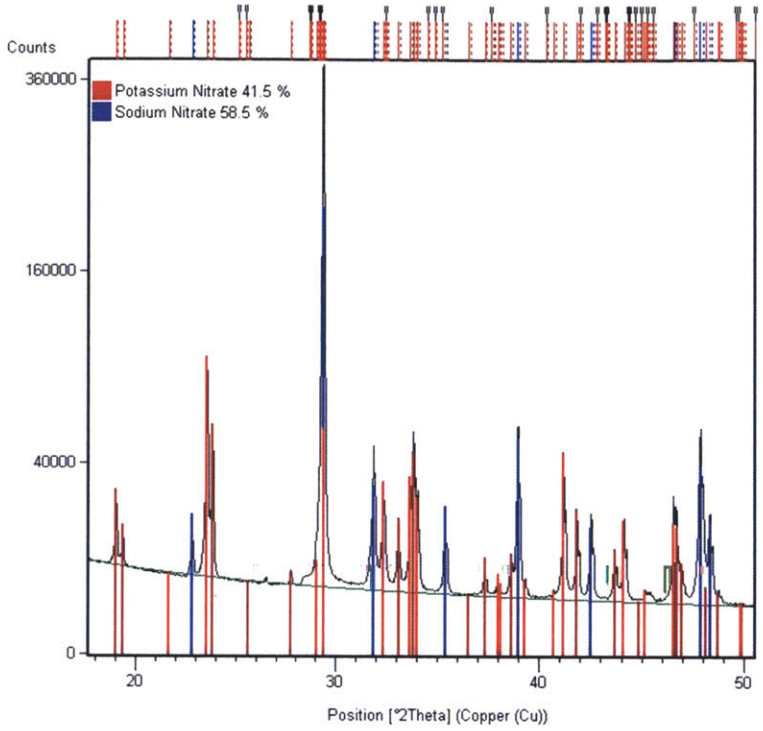

Figure 4.26 - X-ray diffraction data for pure solar salt

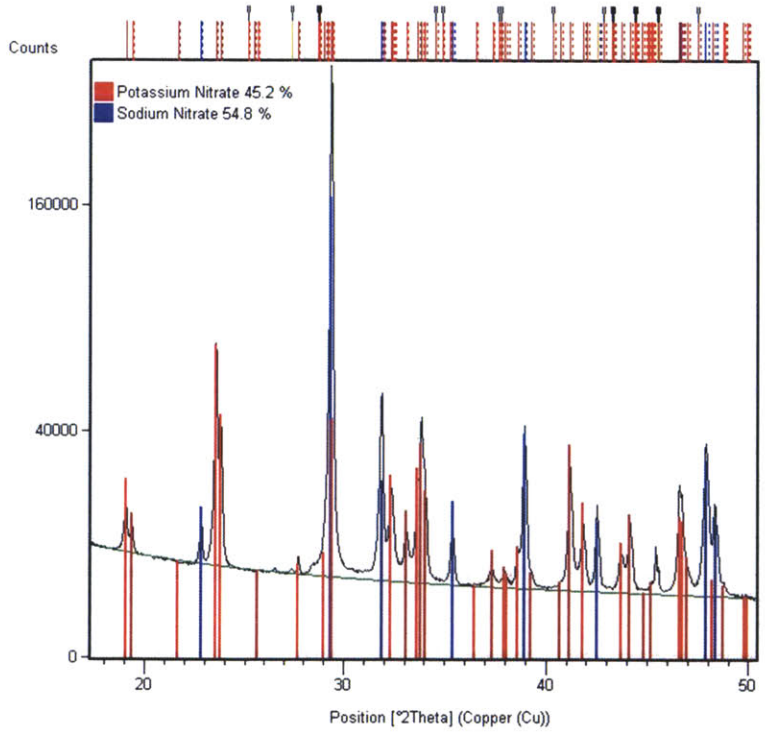

Figure 4.27 - X-ray diffraction data for brownish surface solar salt scum

CHAPTER 5: Idealized CSPonD System Design

This chapter is used to illustrate the design process for a generalized CSPonD receiver utilizing "idealized" hillside collector field geometry. Although the design is conducted for a single design point (solar noon on a specific summer day), a similar process can be employed using yearly solar position and historical meteorological data to provide a year-round optimal design catered to a site's specific solar resource and energy demand profiles.

Field geometry

Table 5.1 lists the site specific parameters for the idealized heliostat field under consideration, provided by Noone. Due to the site's south-facing slope, the fraction of ground area covered by heliostats can be greater than traditional level-ground central receiver CSP fields. Figures 5.1 and 5.2 plot top and side views of the field geometry. The *y*-axis of the staggered radial hillside field points towards true north and is aligned with the optical axis of the receiver; the receiver aperture is located at (0,0,0) and is denoted by a red dot.

Table 5.1 - Idealized heliostat field site parameters

Parameter	Value
Site location	San Diego, California
Site latitude	32.8°
Design point	solar noon, July 22
Solar elevation angle	77.5°
Direct normal irradiance (DNI)	1000 W/m^2
Mirror area	100 m^2
Mirror reflectivity	0.93
Mirror tracking and shape errors, net	1.2 mrad
Number of heliostats	813
Total heliostat area	81,300 m^2
Hill angle (grade)	36.9° (75%)
Land area	132,000 m^2

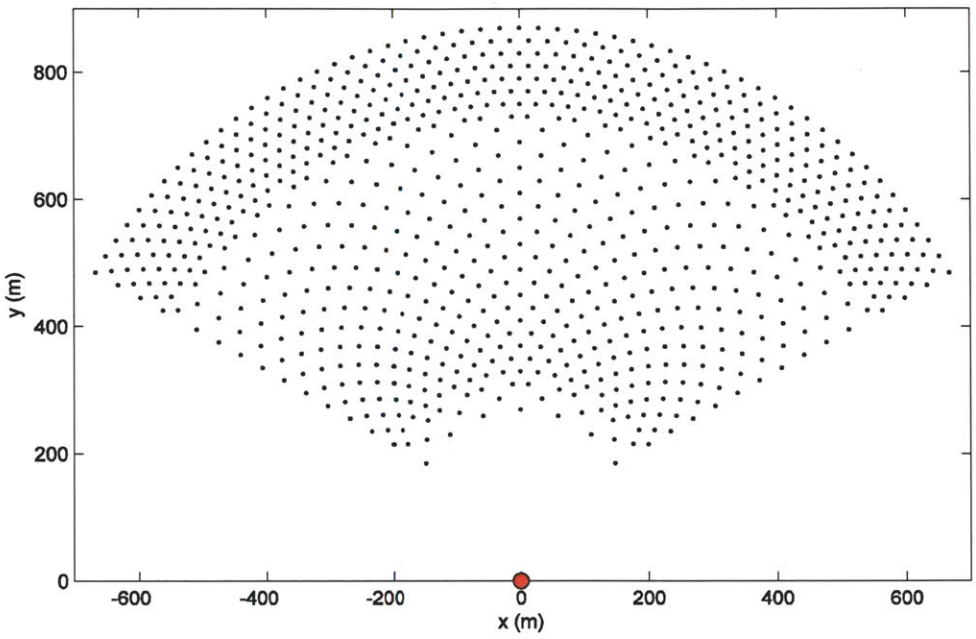

Figure 5.1 - Idealized hillside field: 813 heliostats, top view

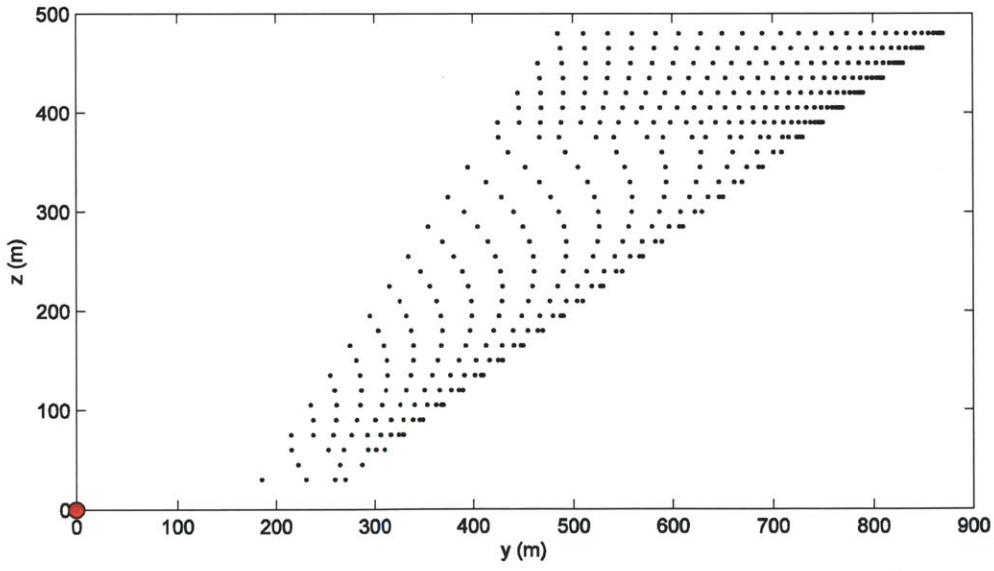

Figure 5.2 - Idealized hillside field: 813 heliostats, side view

Receiver flux distribution

The radiant intensity distribution at the aperture plane can be calculated by assuming each heliostat is aimed so its reflected beam is centered at the aperture. Although other aiming strategies may be employed, perhaps to illuminate the salt surface more uniformly or preferentially heat certain areas within the receiver, this allows for a simplified evaluation of peak flux values and corresponding spatial and angular distributions which are used to design the receiver aperture geometry.

Each heliostat mirror is spherically shaped to give a focal length equal to its slant range r. However, the finite size of the sun and heliostat optical errors results in beam spread and defocusing effects at the aperture. The total angular distribution of each heliostat is modeled as the convolution of an error cone and a Gaussian distribution with a root-mean-squared value defined as:

$$\sigma_{total}^2 = \sigma_{sun}^2 + \sigma_{optical}^2 \tag{5.1}$$

where σ_{sun} = 4.5 mrad. For example, if a heliostat is one kilometer from the receiver (r = 1 km), the projected sunspot image intensity at the receiver has a RMS radial width of 4.5 m, even without any mirror shape or tracking errors. The optical error $\sigma_{optical}$ includes sources such as mirror shape errors, surface imperfections and roughness, and tracking errors. Values of $\sigma_{optical}$ = 0.5-2.0 mrad are typical; an average value of $\sigma_{optical}$ = 1.2 mrad was assumed for this idealized field [136]. As a result of these errors, individual heliostat image beam spread radius becomes $r\sigma_{total}$, and the corresponding peak intensity obtained at the aperture is:

$$\Phi = \frac{\rho \eta_{\cos} \Phi_0 A}{2\pi (r\sigma_{total})^2} \tag{5.2}$$

where ρ is the mirror reflectivity, η_{cos} is the cosine efficiency of the heliostat in question, Φ_0 is the incident flux and A is the heliostat mirror area. More complex and accurate modeling schemes can be utilized with a "pillbox" distribution for the incoming solar irradiance and contour error models or ray-tracing simulations to arrive at the flux distribution at the receiver aperture, accounting for mirror shape and tracking errors; these methods are described by Winston and Vant-Hull [5], [28].

Figure 5.3 plots the relative peak intensities received at the aperture for each heliostat of the idealized field. Clearly, the heliostats closest to the receiver with small slant range r project the highest intensities upon the aperture. Conversely, heliostats with large slant ranges result in low peak intensities and large beam widths at the aperture. For this reason, peripheral heliostats added to very large fields (i.e., with $r > 1$ km) have minimal effect on overall system capacity for fixed aperture sizes.

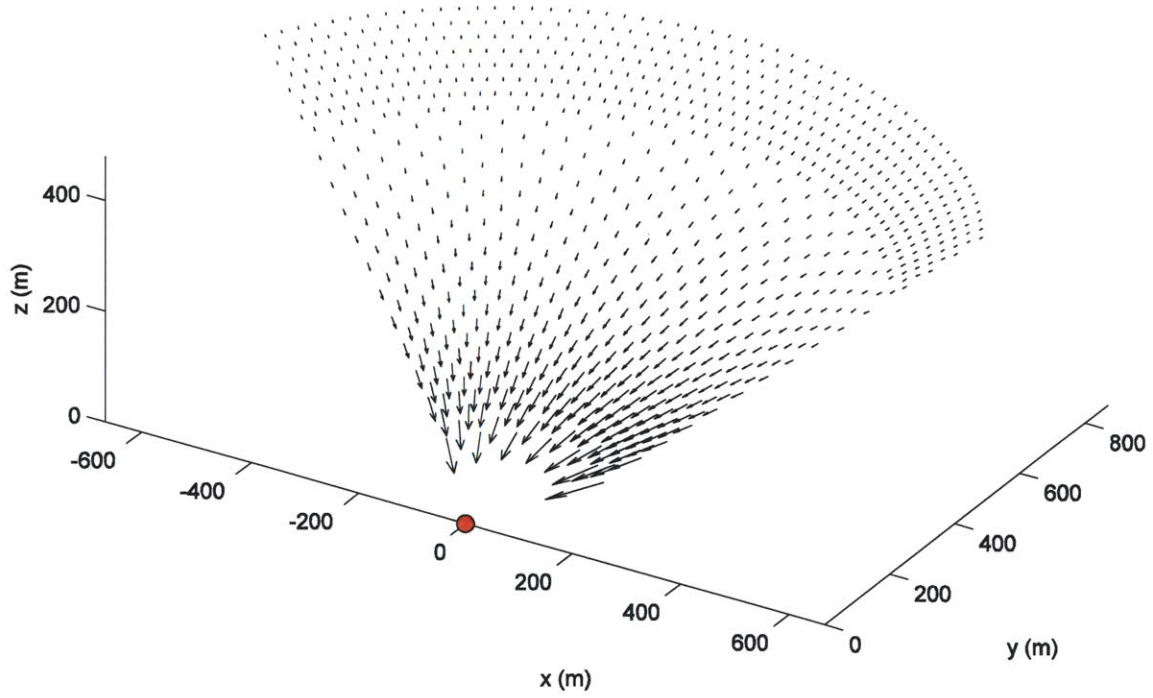

Figure 5.3 - Peak intensities at aperture for idealized heliostat field
Quiver-plot vector length denotes relative peak intensity value for individual heliostats.

The directional distribution of the concentrated flux at the aperture origin is shown in Figs 5.4 and 5.5. Again, the vector length denotes relative intensity corresponding to the particular heliostat location. These plots can be used to identify receiver acceptance angles and optimal orientations for the aperture plane, which does not necessarily have to be vertical. For example, the peak flux for this particular idealized field and receiver location is captured on an aperture whose normal is inclined approximately 22° upwards from horizontal. Figure 5.6 plots the flux distribution from the entire heliostat field for this particular inclined aperture plane. Note

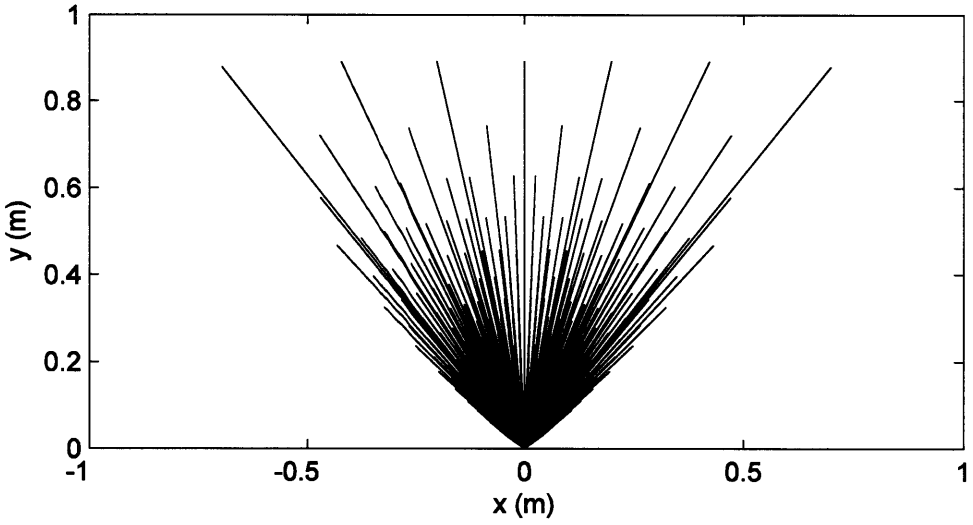

Figure 5.4 - Directional distribution of flux at the aperture origin: top view

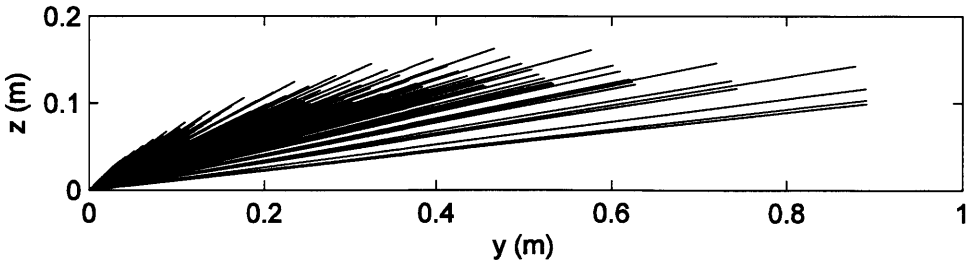

Figure 5.5 - Directional distribution of flux at the aperture origin: side view

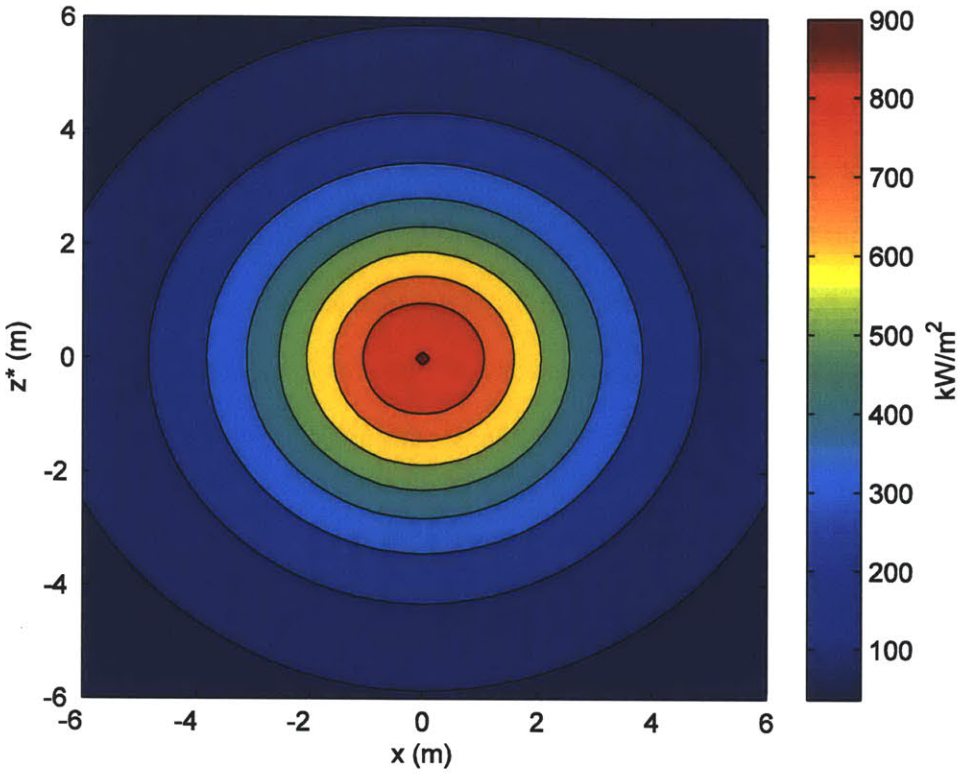

Figure 5.6 - Cumulative flux distribution projected on aperture plane
Calculated for 22° inclined aperture plane.

z^* is the local z-coordinate on this tilted plane; the peak flux at the design point is calculated as 901.4 kW/m^2. The net energy directed at the receiver, accounting for cosine and reflectivity losses is 46.4 MW$_t$, which is equivalent to an optical collection efficiency $\eta_{opt} = 0.57$ for the 81,300 m^2 heliostat field. The average cosine efficiency for the field at the design point is $\eta_{cos} = 0.61$. Shading and blocking losses are neglected under the assumption that the hillside staggered radial layout is selected to eliminate such effects at the design point [51].

Next, the aperture is sized to maximize the net energy gain to the receiver. For this CSPonD receiver, the lid is designed with integral CPC flux-boosting geometry. The profiles of the x-y and z-y 2D truncated parabolic concentrators are determined by the input flux directional distributions: the concentration ratio is selected as $C_x = 1.55$ across the x direction with a ± 30°

acceptance angle; $C_z = 3.5$ for the z^* direction with a ± 12° acceptance angle [28], [137]. However, the z^* direction maps to an elongated projection on the salt surface, as given by Eq. (3.1). For this specific case with the aperture tilt angle (equivalent to the nominal beam down angle ϕ) of 22°, the equivalent concentration ratio from the aperture to the salt surface is given as:

$$C = \frac{A_a}{A_{ip}} = C_x C_z \sin\phi = 2.0 \tag{5.3}$$

Thermal losses from the receiver are a function of lid and salt temperatures, and lid, pond and aperture areas; these are calculated as outlined in Chapter 3 for various aperture sizes and the CSPonD parameters given in Table 5.2. The lid area, no longer spherical, is composed of the converging walls at the exit of the truncated CPC geometry which redirect reflected light back towards the salt pond surface. The reflective CPC area as a function of the aperture area is given by Duffie and Beckman for the x direction as $A_{CPC}/A_a = 1$ and $A_{CPC}/A_a = 2.2$ for the z* direction [137]. Since the peripheral, low concentration radiation strikes the CPC walls at glancing angles of attack, pressed refractory board can be used in place of metallic or glass mirrors; providing reasonably high reflectivity while offering excellent durability in the salt vapor environment.

Figure 5.7 plots the intercepted optical energy and heat loss from the receiver for various aperture areas. To simplify calculations, the aperture width is fixed at 1.5 times the aperture height, a proportion suitable for this heliostat layout and resulting flux distribution. The net energy to the receiver is reaches a maximum value of 38.1 MW_t at an aperture area of 294 m^2, corresponding to a 21 m wide by 14 m high CPC aperture opening. At this size, the aperture intercepts 43.0 MW_t, or nearly 93% of the total flux directed towards the receiver. The spillage, or amount of concentrated radiation falling outside of the aperture, is 3.4 MW_t which is 7.3% of the total amount incident on receiver. Including spillage losses, the receiver efficiency is $\eta_{rec} = 0.82$; discounting spillage losses, $\eta_{rec} = 0.89$.

Table 5.2 - Idealized CSPonD receiver parameters

CSPonD Parameter	Value
Salt	Nitrate solar salt
Hot salt temperature	550 °C
Cold salt temperature	250 °C
Lid temperature	240 °C
Aperture inclination angle	22°
Aperture width	21 m
Aperture height	14 m
Aperture area	294 m^2
Lid CPC concentration ratio, width	1.55
Lid CPC concentration ratio, height	3.5
Lid opening width	13.6 m
Lid opening height	4 m
CPC aperture/exposed salt area	2.0

The average number of reflections undergone by radiation passing through a CPC can be found as:

$$N = 1 - \frac{1}{C} \tag{5.4}$$

where C is concentration ratio of the CPC in question. For this receiver, $N = 0.33$ in the x direction and $N = 0.71$ in the z^* direction, indicating a large portion of the incoming flux passes to the salt without impinging on the CPC inner walls. Indeed, comparing the lid opening size (13.6 m × 4 m) with Fig.5.6, the peak flux in the central region will pass directly through to the molten salt. It is assumed that the light which does impact the refractory-lined CPC does so at grazing angles, nearly parallel to the CPC walls. Even though the CPC walls are not specular reflecting

metallic mirrors, the grazing angle incidence results in high reflection coefficients and much of the energy will be reflected towards the salt. As the light progresses deeper within the CPC and lid structure, some rays will impinge at non-grazing angles and create greater heating loads on the lid. Hence it is reasonable to concentrate the lid heat extraction in this location.

Monte-Carlo ray tracing simulations, while beyond the scope of this thesis, can be used to find flux distributions on the salt surface, taking the reflective properties and geometry of the lid into consideration. The resulting flux distribution and subsequent radiative heat load to the molten salt and the lid can be found using the methods presented in Chapter 3.

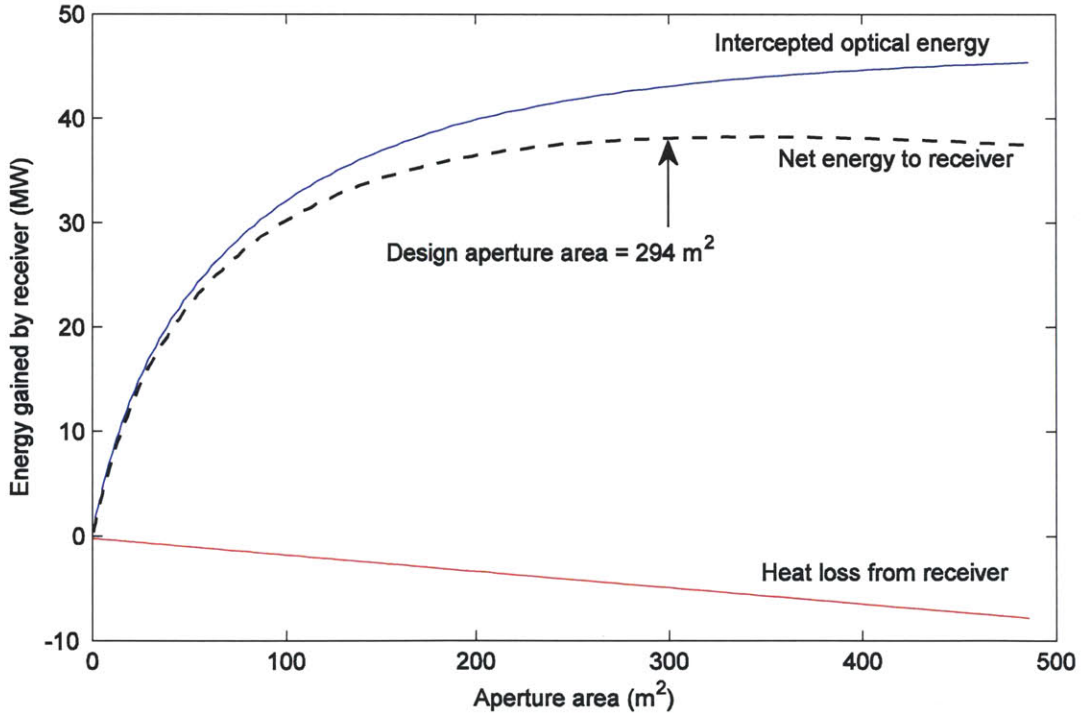

Figure 5.7 - Net energy flow into receiver for various aperture sizes Calculated for nitrate solar salt CSPonD receiver.

Thermal storage sizing

This particular CSPonD receiver is sized for 600 $MW_t h$ of energy storage. As described in Chapter 2, 2500 m^3 of solar salt contained in a 5 m deep × 25 m diameter tank and thermally cycled with a 300 K temperature difference provides this amount of sensible heat storage. Depending on heat extraction rates the system will take several sunny days to fully charge; a reasonable amount of daily energy input collected by the receiver for this particular heliostat field and an average DNI resource of 7.2 $kWh/m^2/day$, typical of CSP installation sites in the southwestern United States, is 275 $MW_t h$.

Assuming a modest heat extraction rate from the salt pond of 40 MW_t for six hours each day, the mass flow of salt for the heat exchanger required is:

$$\dot{m}_{salt} = \frac{\dot{Q}}{c_p \Delta T} = 41.5 \text{ kg/s} \tag{5.5}$$

The receiver will require 10 sunny days to completely charge the tank buffer volume, while still providing 240 $MW_t h$ of energy to the power cycle each day. Once fully charged, the system could provide full-load power from its 360 $MW_t h$ reserve for an extended cloudy period spanning an additional 9 hours, equivalent to an extra day and a half of operation.

Divider plate sizing

As explained in Chapter 2, divider plate sizing is a balancing act between thermal resistivity, neutral buoyancy and annular flow restriction during system charging. A nominal 20 cm annular gap is selected to ensure robust operation without risk of binding or damage to the tank walls. This gap results in an annular blow-by flow velocity v = 1.9 mm/s while the divider plate is stationary and the full-load flow of salt is circulating. Equation (4.4) can be used to find the Richardson number: with even a small 10 K temperature difference between the divider plate's upper surface and the cold upward annular flow at a depth of 1 m, Ri = 1.0×10^4. Again,

the Richardson number varies with divider plate position, relative speed and temperature difference, but this value illustrates that natural convection dominates the upper salt mixing behavior relative to forced convection.

Copeland has suggested making the barrier plate's thermal resistivity roughly equal to that of the fluids above and below [38]. To achieve this, the divider plate is outfitted with a 135 mm thick layer of closed-cell rigid glass insulation (i.e., Foamglas), which has thermal conductivity k = 0.042 W/m-K. The conductive heat transfer from the upper salt layer to the colder bottom layer can be modeled using a thermal resistance circuit as shown in Fig. 5.8, where the divider plate insulation provides one path for heat flow and the annular salt area between the divider plate and tank walls provides a parallel conduction path. The effects of the metal divider plate structure can be ignored due to its high conductivity relative to the salt and insulation. Using the thermal resistance analogy, the heat flow rate Q can be found as:

$$Q = \frac{\Delta T}{R_{eq}} \tag{5.6}$$

where R_{eq} is the equivalent resistance of the thermal network. For each conductive layer, or heat path, the thermal resistance R is:

$$R = \frac{L}{Ak} \tag{5.7}$$

The equivalent resistance of the parallel divider plate/salt annulus circuit is found as R_{eq} = 4.7 K/kW, giving a net axial heat transfer rate Q = 64 kW for ΔT = 300 K. Over a twenty-four hour period this is 1.5 $MW_t h$, or only 0.3% of the system capacity – sufficiently low for efficient thermocline storage. As a check, the equivalent salt thickness which gives a thermal resistance equal to the combined divider plate and salt annulus R_{eq} = 4.7 K/kW is found as 1.3 m which is well within reason for the 5 m deep receiver.

The divider plate's insulation lightweight density ρ = 120 kg/m^3 will "float" a substantial thickness of AISI type 321 (UNS S32100) stainless steel with a density of ρ = 7920 kg/m^3. Specifically, the insulation thickness of 135 mm results in a buoyancy force that will support over 135 tons of stainless steel. If this mass is distributed uniformly over the divider plate area, this equates to a 35.8 mm thick plate! A more logical and cost-effective approach utilizes a shelled divider plate with 6.35 mm thick upper and lower surfaces, supported by a network of structural beam reinforcements. If additional weight is needed, inexpensive ballast (i.e., steel plates) or heavier insulation (e.g., calcium silicate: ρ = 280-1400 kg/m^3, insulating firebricks: ρ up to 3100 kg/m^3) can be added to the interior, taking care not to short-circuit the desired insulating properties of the plate assembly. This shelled structure need not be totally sealed and salt-tight since the salt will not penetrate into the cellular glass foam. Indeed, an airtight construction may prove problematic as internal gas pressures may warp or rupture the structure. Pressure equalization ports eliminate any hydrostatic buckling forces on the plate. This particular grade of austenitic stainless steel is formulated for improved high temperature properties and resistance to carbide precipitation and intergranular sensitization-corrosion in the 400-800 °C range.

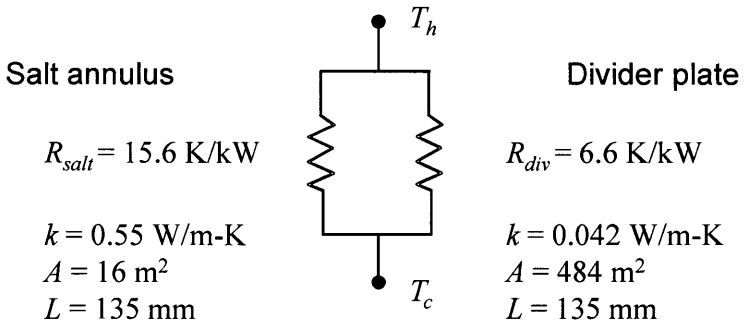

Figure 5.8 - Divider plate thermal resistance circuit

Tank and lid insulation considerations

Various refractory and insulating materials can be utilized to minimize thermal losses from the receiver and keep overall costs down. As discussed in Chapter 2, the salt bath heat treatment industry has decades of experience designing tanks which can withstand the high temperatures and corrosive environment created by molten salts. Typically, all but the lowest temperature tanks are designed with a super-duty firebrick liner. These bricks are laid dry in mortarless courses and provide excellent thermal shock resistance while their relatively high density and conductivity serves to stabilize the salt bath temperature. A typical product is alumina-silica KX-99 firebrick; if needed, a 99% silica firebrick such as SR-99 can be used for severely corrosive environments, perhaps near the salt-air interface. Firebrick is manufactured in various shapes, but the most common size is 9" × 4.5" × 3" (230 mm × 115 mm × 75 mm). Behind this layer, courses of less-dense, low conductivity insulating firebrick (IFB) provide the primary thermal barrier within the tank walls. This layer is designed with sufficient depth such that a "freeze plane" of salt is forms within the IFB.

Because the IFB layer contains and isolates the liquid salt, the tank can be constructed from low cost A36 structural steel or equivalent. The steel shell is sized to handle the hydrostatic load imposed by the molten salt and transferred by the refractory layers; standard codes and guidelines for field-erected water, oil or other liquid storage tanks can be used. The hydrostatic pressure at the bottom of the tank is simply:

$$P = \rho g H \tag{5.8}$$

where H is the depth of the tank. For this system $H = 5$ m and $P = 88$ kPa, which at 550 °C is well below the hot compressive load limits for typical IFB. For example, IFB class 20 (service temperature less than 2000 °F/1093 °C) does not measurably creep under a compressive load of 10 psi (69 kPa) at 1093 °C; allowable loads are much higher at reduced temperatures.

The exterior of the tank is covered in low-density, low conductivity fibrous insulation. Typical products include ceramic fiber insulation (i.e., Kaowool^{TM}) or mineral fiber insulation, as specified by ASTM C1393, Perpendicularly Oriented Mineral Fiber Roll and Sheet Thermal Insulation for Pipes and Tanks. Both materials possess thermal conductivity $k < 0.1$ W/m-K.

The fiber insulation is shielded and protected from moisture and degradation by metallic lagging. Typically, lagging is applied as thin overlapping or sealed-seam sheets made from galvanized steel, stainless steel or aluminum. Galvanized lagging has a zinc coating of at least 0.90 ounces per square foot (275 g/m^2) conforming to ASTM A924, Standard Specification for General Requirements for Steel Sheet, Metallic-Coated by the Hot-Dip Process, to prevent atmospheric corrosion. Stainless steel (typically AISI type 304, 2B cold-rolled exterior finish) and aluminum (7072 clad) lagging materials rely on the formation of chromium and aluminum oxides, respectively, to resist degradation. Additionally, any of the materials can be painted to enhance durability.

The proposed tank wall materials are listed in Table 5.3. The heat loss can be found using a series thermal resistance network and Eq. (5.6), substituting each layer's thickness and thermal conductivity data into Eq. (5.7). A convection coefficient of $h = 8$ W/m^2-K is assumed with ambient temperature $T_\infty = 25$ °C on the exterior surface of the lagging, whereby $R_{conv} = 1/hA$. The overall thermal resistance is $R_{eq} = 12$ K/kW; for $T_{salt} = 550$ °C, $q = 112$ W/m^2, $Q = 44$ kW at the tank periphery. Over an entire day, this is 1.1 MW$_t$h, only 0.2% of the system capacity.

Because the tank wall thickness is much less than the tank radius, this simple flat-plate analysis provides reasonably accurate results, within a few percent of the true values determined for cylindrical geometry. Figure 5.9 plots the temperature profile within the tank wall for the two temperature extremes: $T_{salt} = 250$ °C and 550 °C. The design goal of maintaining the salt freeze plane within the IFB is met and the exterior lagging temperature is less than 40 °C for both cases.

A similar analysis can be conducted for the tank bottom. Conduction losses into the earth are limited with an extra layer of cellular glass insulation or firebrick beneath the steel tank floor, in place of the fiber insulation and lagging material.

Table 5.3 - Tank wall materials

Layer	Specification/Trade name	Layer thickness (mm)	Thermal conductivity k (W/m-K)
Super-duty firebrick	KX-99	115	1.4
Insulating refractory brick	ASTM C155: IFB 20	460	0.15
Steel tank shell	ASTM A36	12.7	54
Ceramic fiber insulation	Kaowool (6 lb/ft^3)	101.6	0.070
Exterior lagging	ASTM B209: 7072 clad	1.6	250

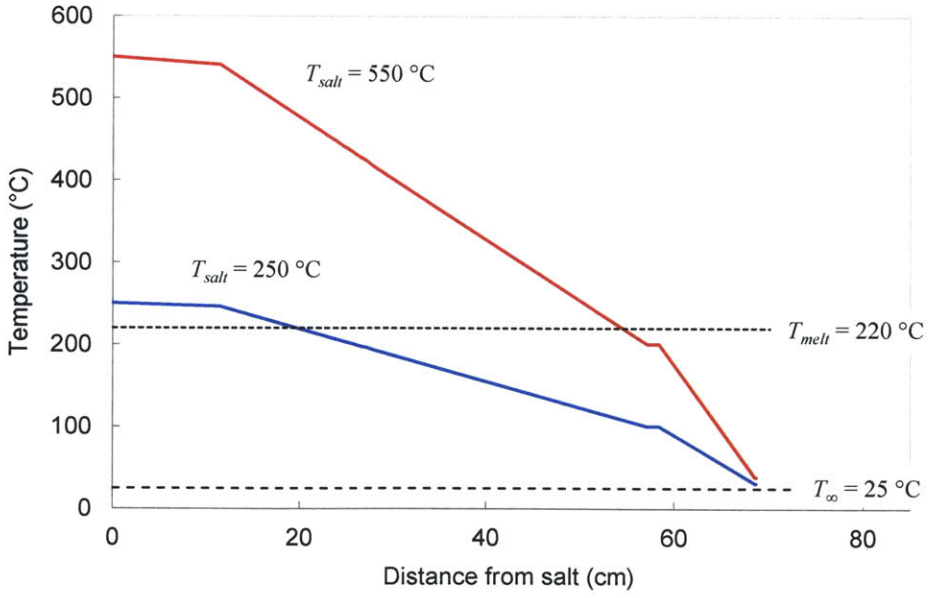

Figure 5.9 - Tank wall temperature profile

The lid insulation is designed similarly, except the heavy firebrick layers are replaced by lightweight ceramic fiber insulating board. The lightweight density ($\rho \sim 270\text{-}300$ kg/m^3) of these wet-formed alumina-silica fiber boards reduces the load on the lid support structure. These materials (i.e., Fiberfrax Duraboard) have high visible light reflectance and very low conductivity $k < 0.1$ W/m-K, which reduces overall heat loading to the lid. Additionally, the chopped-fiber construction is thermal-shock tolerant and limits crack propagation should any defects form. The rigid board layer contains a freeze plane similar to the IFB in the tank walls, behind which fiber insulation reduces temperatures such that a mild steel shell can be used for the lid structure. Again, this steel structure is covered on the exterior with fiber insulation and lagging. The low-temperature heat extraction loops can be integrated into the backside of the steel lid shell, thereby providing an extra barrier between the lid HTF (likely pressurized water/steam) and the receiver interior.

Table 5.4 lists the lid construction materials which can are used to find thermal losses as described previously with natural convection on the outer surface of the lagging. The overall thermal resistance of the lid is $R_{eq} = 1.6$ K/kW, an inner lid temperature $T_{lid} = 240$ °C results in $q = 133$ W/m^2 and $Q = 130$ kW for a hemispherical lid covering the entire salt surface. Over a twenty-four hour period this is 3.1 MW$_t$h or 0.5% of the system capacity. Figure 5.10 plots the temperature profile throughout the lid; note the steel lid structure is approximately 160 °C – an ideal temperature for power cycle water preheating. A similar insulation strategy is incorporated into the aperture door structure.

Table 5.4 - Lid construction materials

Layer	Specification/Trade name	Layer thickness (mm)	Thermal conductivity k (W/m-K)
Ceramic fiber insulating board	Fiberfrax Duraborard	19.1	0.084
Ceramic fiber insulation	Kaowool (6 lb/ft^3)	25.4	0.070
Steel lid shell	ASTM A36	6.4	54
Mineral fiber insulation	ASTM C1393 Type I	50.8	0.055
Exterior lagging	ASTM B209: 7072 clad	1.6	250

Daily conductive and convective heat losses from the external surfaces of receiver are very low, less than 1% of the 600 MW_th storage capacity. Equation (3.30) can be used to estimate the temperature drop in the molten salt at the tank wall as a function of time t, assuming isothermal initial conditions near the tank wall:

$$\Delta T = \frac{2q_{wall}}{k\sqrt{\pi}}\sqrt{\alpha' t} \tag{5.9}$$

Figure 5.11 plots Eq. (5.9) for the nitrate salt exposed to typical tank wall heat fluxes q_{wall} of this design. In extended periods of inclement weather, the system can idle for several days, or even weeks, without risk of the entire mass of salt freezing solid. The temperature drop calculated by Eq. (5.9) is an upper bound, since the physical system has additional thermal capacitance from the super-duty firebrick lining and convective mixing within the salt. Once salt begins freezing, the solidifying front is dictated by the Stefan problem as described in Chapter 3, which reduces the temperature gradient even further. Even so, the first region to freeze will be lower cold salt region below the divider plate. Hence, it is wise to incorporate a supplementary heater to underside of the tank bottom shell. Heating elements installed here can be turned on when the lower tank temperature is below a critical threshold, thereby preventing further heat loss and

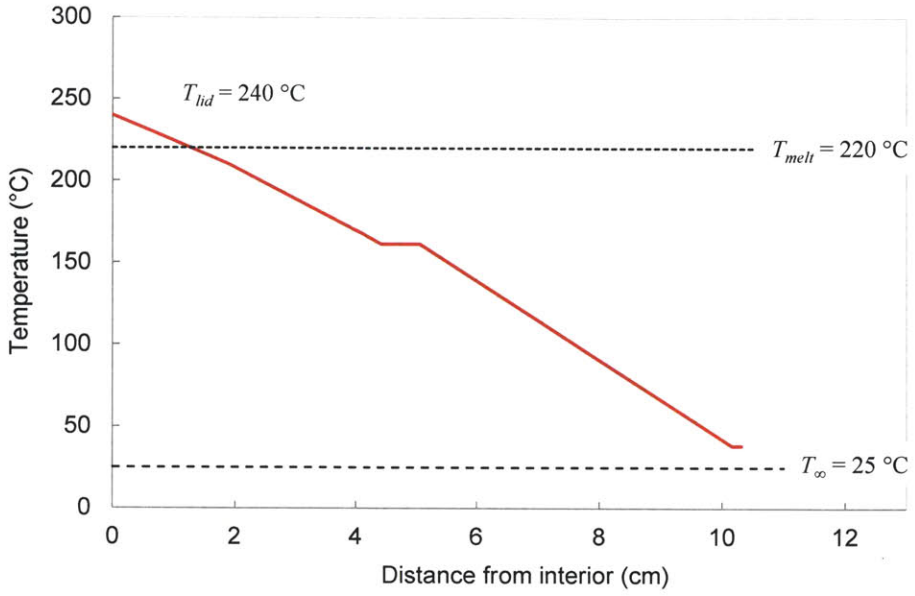

Figure 5.10 - Lid temperature profile

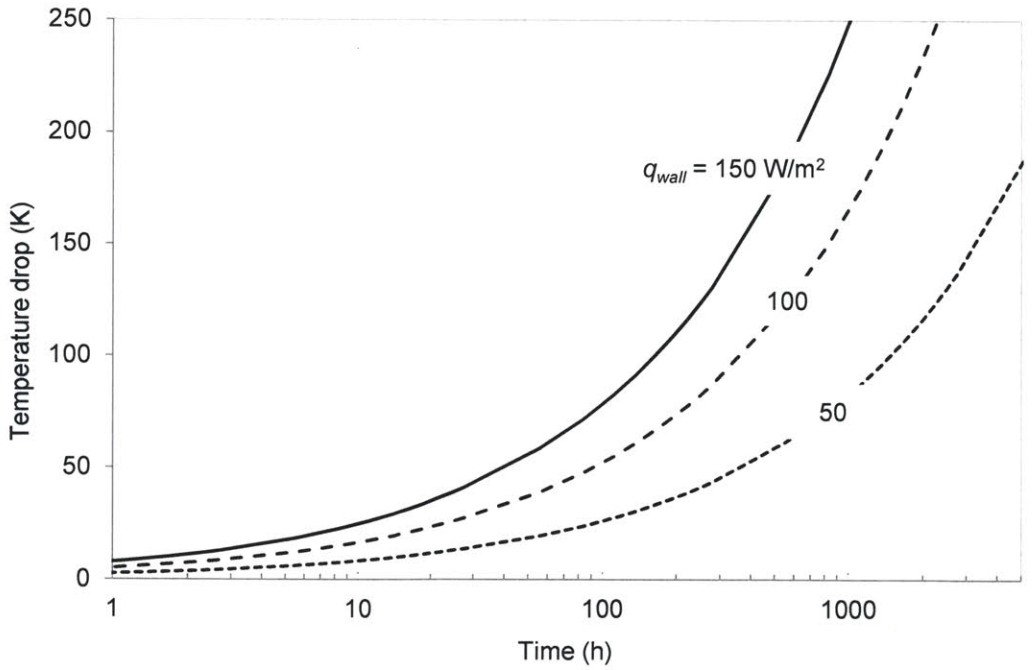

Figure 5.11 - Temperature drop in molten salt at tank wall interface
Calculated using Eq. (5.9) for nitrate salt with various tank wall heat loss q_{tank} values.

subsequent freezing. For this 25 m diameter design, a total of 50 kW of electric resistance heating elements (preferably several zones each wired in separate circuits for reliability purposes) is sufficient to overcome 100 W/m^2 losses through the tank bottom.

As a second contingency, the cold salt return line can be fitted with a "freeze valve" to allow passive draining of a majority of the salt volume in a worst-case situation. The freeze valve, as described by Briggs in the Molten Salt Reactor report, consists of nothing more than a nearly-flattened length of uninsulated stainless tubing, whereby a frozen salt plug forms [138]. During emergency drain scenarios, the exterior of this freeze valve is heated quickly and gravity-draining of the tank ensues. Salt flow can be stopped by blowing a stream of ambient air on the tube's exterior.

Power cycle considerations

The low temperature heat extraction from the lid is assumed to be fully utilized in feedwater preheating, or depending on plant layout, even in the evaporator section. The design heat extraction rate from the receiver is 40 MW_t – a fairly small value for large scale power generation equipment. Smaller steam turbines do exist in the 5-10 MW_e range, but larger 30-100 MW_e units are more efficient, reliable and cost less per watt power produced. If larger scale production is desired, a solution is to gang multiple CSPonD salt ponds together as discussed in Chapter 2. This has the added benefit of redundancy, increasing overall system reliability.

Some ganged unit designs will transfer hot salt to a central steam generation unit; others will use collocated steam generators to produce steam at the receiver and then transport this steam to a central turbine station. Still other designs may utilize an intermediate heat transfer fluid to extract heat from the individual receivers and transfer it to a centralized power block. The specifics of these implementations are beyond the scope of this thesis; for this idealized system, a single turbine is directly coupled to this pond with an assumed thermal efficiency for the heat exchanger-power cycle of $\eta_{th} = 0.38$.

Power cycle efficiencies are likely to vary depending on the use of water or air cooling, but this value represents a mid-range estimate. As a result, the gross electrical power produced by this receiver is 15.2 MW_e. Again, it is important to note that the CSPonD system produces this power continuously at this output during the power producing phase, unlike conventional PV system and CSP systems without storage which throttle output from peak, matching the solar resource available. This allows grid operators to easily integrate CSPonD-produced energy into their systems without worry of power variability and unexpected brownouts.

Parasitic power consumption

The salt pumping power can be found multiplying the nominal pressure drop across the steam generator, ΔP_{HX} = 450 kPa (taken from a representative molten salt steam generator [47]) with the volumetric flow rate of the salt:

$$P_{pump} = \frac{\dot{m}\Delta P_{HX}}{\rho} = 10.4\,\text{kW} \tag{5.10}$$

Although the value obtained with Eq. (5.10) does not account for fluid frictional losses in the piping or fittings between the tank and the steam generator or inefficiencies in the pump motor itself, the pumping power is only 0.15% of the total electrical power produced. This is in stark contrast to the pumping power requirements for traditional power tower designs, which must pump the HTF up to the top of the receiver tower at significant flow rates. For example, the proposed 150 MW_e SolarReserve Crossroads CSP plant uses a 200 m tall tower to support its external cylindrical receiver. With a reported ΔT = 277 K, pumping the required amount of nitrate solar salt to the tower – assuming no frictional losses in the long supply pipes or receiver – requires 1.9 MW_e, or 1.3% of the gross electrical output [139]. Additionally, conventional tubular receivers impose a significant restriction on the HTF flow, adding to the already large pumping power requirements. In this CSPonD system, a 152 mm (6") diameter pipe would have a salt flow

velocity of 1.3 m/s, resulting in a negligible pressure drop in comparison to ΔP_{HX} over the short pipe length needed. Similar low pumping power estimates can be obtained for the lid cooling loop.

With the divider plate properly ballasted and only slightly negatively buoyant, actuation forces are minimized. The speed requirements are minimal as well: extracting all of the storage energy in a short six hour 100 MW_t burst results in a maximum divider plate speed of 0.2 mm/s. The combined low force and low power requirements for the divider plate actuators make the positioning power negligible; six (for redundancy) continuous duty winch-type electric gearmotors can be used with a peak power draw of less than 1 kW each.

Central receiver system comparisons

It is worth comparing this CSPonD system design to other state-of-the-art central receiver designs, particularly those in planning or under development. A representative direct-steam generation system is eSolar's design, which employs a multitude of small 1.14 m^2 heliostat mirrors. Seven of these mirrors are aligned into individual "sticks" [140]. A module consists of one power tower and cavity-type tubular receiver with a dedicated heliostat field located north and south of the receiver. Twelve modules occupying roughly 80 hectares (200 acres) feed steam to a 46 MW_e eSolar power unit with a turbine generator set and a steam condenser [141]. There is only minimal thermal storage (15-30 minutes) associated with the eSolar plant. For reference purposes, the 81,300 m^2 mirror area CSPonD hillside field presented in this Chapter can be equivalently outfitted with a total of 71,315 eSolar heliostats, occupying 10,188 eSolar heliostat "stick" modules.

An alternate approach is utilized by SolarReserve and Brightsource, whereby one large 360° circular heliostat field heats a single receiver. Specifications for the proposed SolarReserve 100 MW_e Crescent Dunes Tonopah plant indicate that it will occupy 2.5 square miles (1,040 hectares) of Nevada desert [142]. The 30.5 m tall tubular cylindrical solar salt receiver sits atop a

168 m tall tower; a two-tank nitrate salt system is designed with ten hours of thermal storage and functions as the HTF [143]. The design presented by Brightsource for their 370 MW_e Ivanpah plant, composed of three circular field/receiver modules each with their own power block, is slated to occupy 5.5 square miles (1416 hectares); however the direct steam generator receivers are designed without thermal storage of any kind and requires natural gas firing during off-peak solar periods [144].

Table 5.5 compares the specific land usage and power production for the CSPonD, eSolar, SolarReserve and Brightsource CSP concepts. Clearly, the CSPonD system offers the best energy output per unit land area by exploiting parabolic dish-like hillside terrain, and more significantly, CSPonD's integral energy storage enables prolonged cloudy-day power generation. It is interesting to note the general trend regarding plant size as mentioned previously: smaller heliostat fields/receiver combos have greater optical efficiencies, which tends to outweigh very large plant gains in power block efficiency. As such, systems like CSPonD and eSolar, comprised of smaller optical modules connected in groups to larger power block units, will provide the most efficient land utilization.

To provide a direct solar-to-electric design point comparison, if the CSPonD receiver was producing electricity in-phase with the incident solar energy striking the collector field (i.e., without time-load shifting or daily accumulations to its "buffer" pond storage), $\eta_{solar\text{-}electric}$ as in Eq. (1.3) becomes:

$$\eta_{solar-electric} = \eta_{opt}\eta_{rec}\eta_{th}\eta_{ele} = (0.57)(0.82)(0.38)(0.98) = 17.4\% \qquad (5.11)$$

The parasitic electrical power efficiency is conservatively estimated as $\eta_{ele} = 0.98$ resulting from cooling fans, fluid pumps and generator losses. The overall efficiency found in Eq. (5.11) is greater than conventional designs, and as a result, the capital costs per installed megawatt are expected to be lower for CSPonD systems.

Table 5.5 - Comparison of central receiver CSP performance

Parameter	CSPonD[i]	eSolar [141]	SolarReserve Tonopah [142], [143]	Brightsource Ivanpah [144]
Receiver type	Volumetric: Cavity	Tubular: Cavity	Tubular: External	Tubular: External
Receiver HTF	solar salt	steam	solar salt	steam
Thermal storage capacity (h)	15	-	10	-
Module size (MW_e)	15.2	3.8	100	123.3
Number of modules per power block	3	12	1	1
System size (MW_e)	46	46	100	370
Daily power production duration (h)	6	4.8[ii]	13.3	4.8[ii]
Backup energy storage capacity (h)	9	-	-	-
Daily energy produced (MW_eh)	276	221	1330[iii]	1776[iv]
Average DNI ($kW_th/m^2/day$)	7.20[v]	7.20[v]	7.36	7.44
Heliostat mirror area (m^2)	243,900	218,880	1,071,361	2,295,960
Land area (hectares)	39.6	80	647	1416
Energy produced per mirror area ($kW_eh/m^2/day$)	1.13	1.01	1.24	0.77
Energy produced per land area ($kW_eh/m^2/day$)	0.70	0.28	0.21	0.13
$\eta_{solar\text{-}electric}$, based on mirror area	15.7%	14.0%	16.8%[iii]	10.4%
$\eta_{solar\text{-}electric}$, based on land area	9.7%	3.8%	2.8%[iii]	1.7%

Notes:

i) CSPonD power block assumed $\eta_{th} = 0.38$ for 46 MW_e unit, extracting 40 MW_t from each receiver.

ii) Daily power production duration for eSolar and Brightsource calculated for equivalent full-load solar power production (i.e., morning and late afternoon power output < peak power output due to lack of storage).

iii) SolarReserve Tonopah plant projected power output = 485,000 MW_eh/yr (13.3 h/day operation) which will deplete storage completely each day under certain circumstances. As such, the system will provide reduced output on days after depleting the thermal storage capacity. If a more realistic 10 h/day operation is used, $\eta_{solar\text{-}electric}$ becomes 12.6% and 2.1% based on mirror and land area, respectively.

iv) Brightsource plant capable of 8 hours full-load operation (2960 MWh) each day with natural gas assist heating.

v) Average DNI values assumed for typical CSPonD and eSolar southwestern US location.

It is important to note that the CSPonD summer solar noon design point calculations occur for the worst heliostat collector efficiency due to the beam down field geometry. Figure 5.12 plots the cosine efficiency for a heliostat on the optical axis with a beam down angle of 20°, roughly the average for the idealized field, at solar noon throughout the year. As can be seen, η_{cos} reaches a minimum during the summer months when the sun is at its highest in the sky. Conversely, η_{cos} increases dramatically in the winter months, when the solar elevation angle (complement of the solar zenith angle) is lower.

For comparison, the cosine efficiency for a power tower heliostat is shown in Fig. 5.12, which beams up at a 50° angle. This beam up angle is typical of the shorter-range mirrors which impose the greatest fluxes upon the receiver. While η_{cos} remains relatively high and constant throughout the year (hence the motivation for a high tower), the solar energy available to collect throughout the year follows the general trend illustrated by the solar elevation curve: peak energy is available during the longer days of summer, while winter's shorter days limit collection time and solar energy resources. As a result, conventional power towers are designed, and can provide their peak rated power during solar noon in the summer, but fall short during other seasons. In contrast, the increased relative collection efficiency of a CSPonD system during off-summer months allows for more uniform power production throughout the year, providing a higher capacity factor and annual energy output per rated peak power.

A similar analogy holds for early morning and late day collection when the sun is lower on the horizon: CSPonD systems will have an increased optical efficiency relative to solar noon. As a result, the net power as compared to the peak midday power to the receiver will fluctuate less than in conventional power tower systems. Further details are presented by Ghobeity, Noone and Mitsos, who analyze the CSPonD system collection behavior year-round to optimize heat extraction and power production for a given site [51], [77], [78].

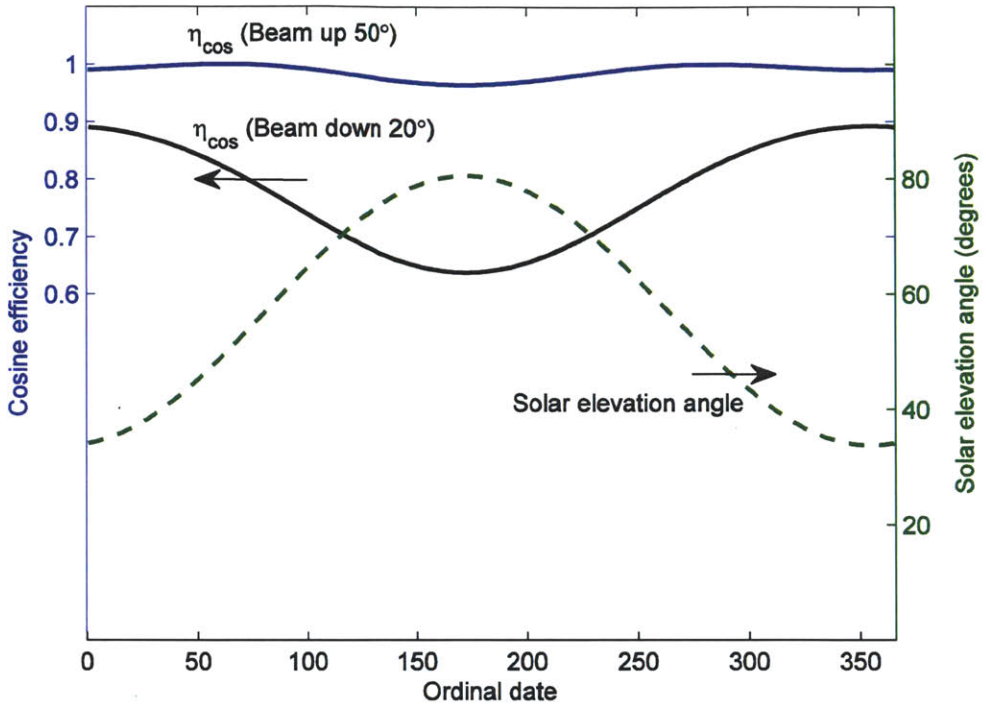

Figure 5.12 - Year-round cosine efficiency at solar noon
Calculated for San Diego, CA (latitude = 32.8°);
single heliostat located on the optical axis of the receiver.

Design details of receiver

Figures 5.13 through 5.20 illustrate design features as described in the previous section. The CSPonD receiver is shown on a concrete foundation pad; pilings support the cantilevered CPC which protrudes from the front of the tank. The aperture door assembly is not shown; it can be located in two places: large horizontal or vertical sliding doors covering the CPC inlet aperture; or a smaller set of doors at the CPC exit and lid interface. Locating the aperture door at the latter site would result in reduced heat losses while the receiver is off sun and the door is closed. However, additional design constraints would be imposed so that light is not impeded by the support structure when the door is open. A simple garage-type door which rotates up and out towards the heliostat field offers a possible solution, whereby the backside of the door forms a portion of the CPC's inner surface while open.

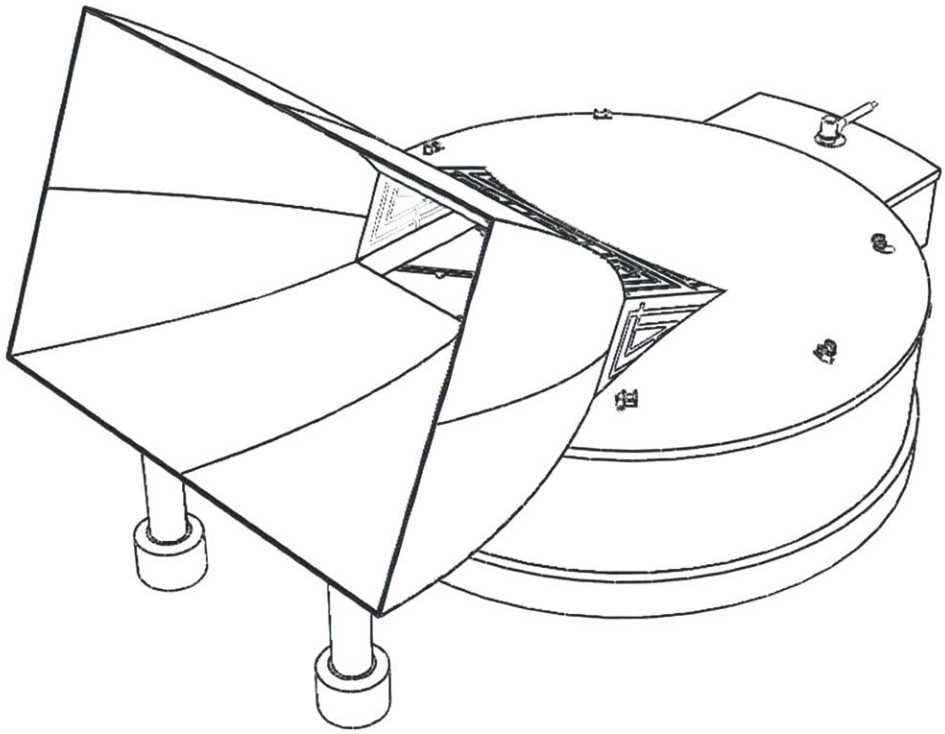

Figure 5.13 - Isometric perspective view of receiver

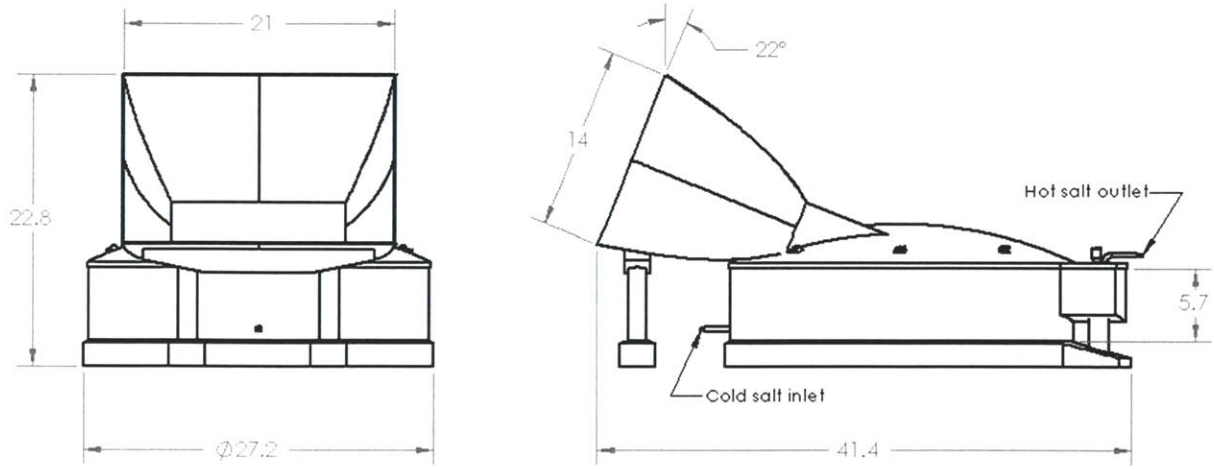

Figure 5.14 - Front and side views of receiver
(dimensions in meters)

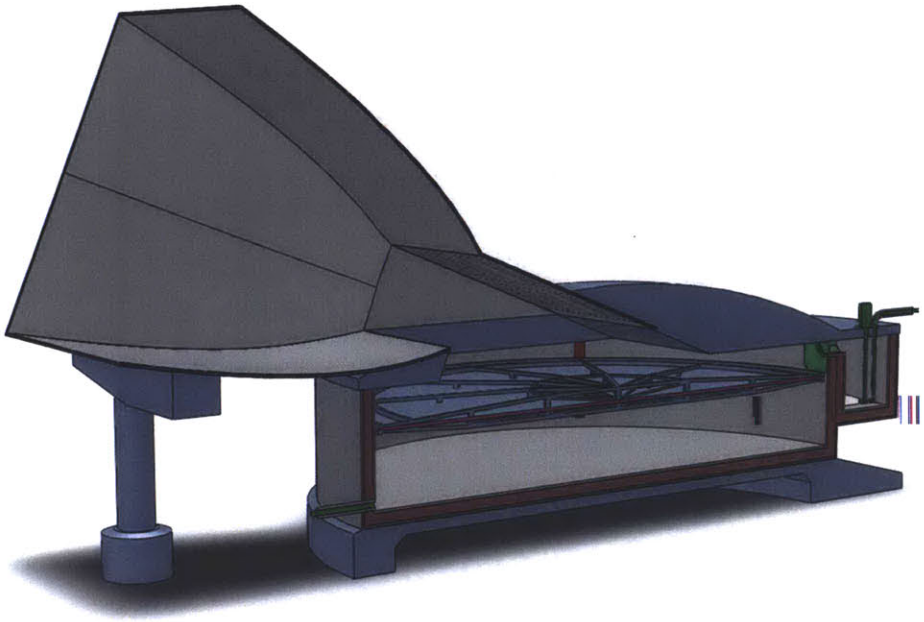

Figure 5.15 - Cross-section of receiver

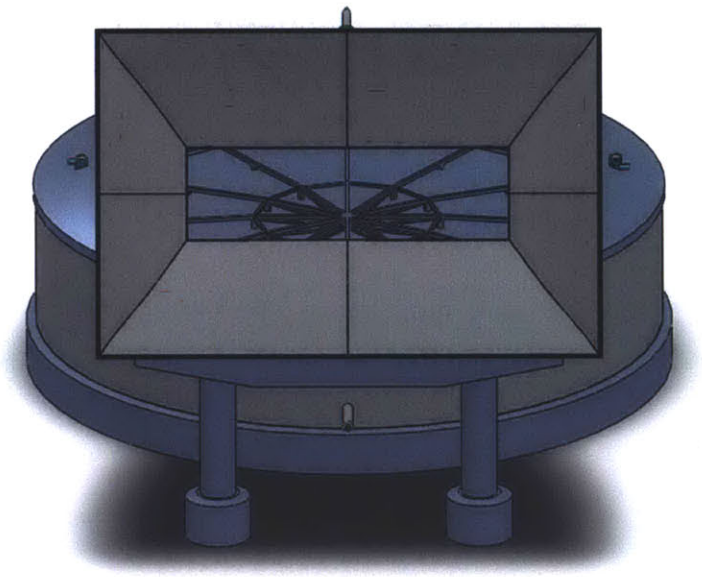

Figure 5.16 - View facing CPC entrance aperture

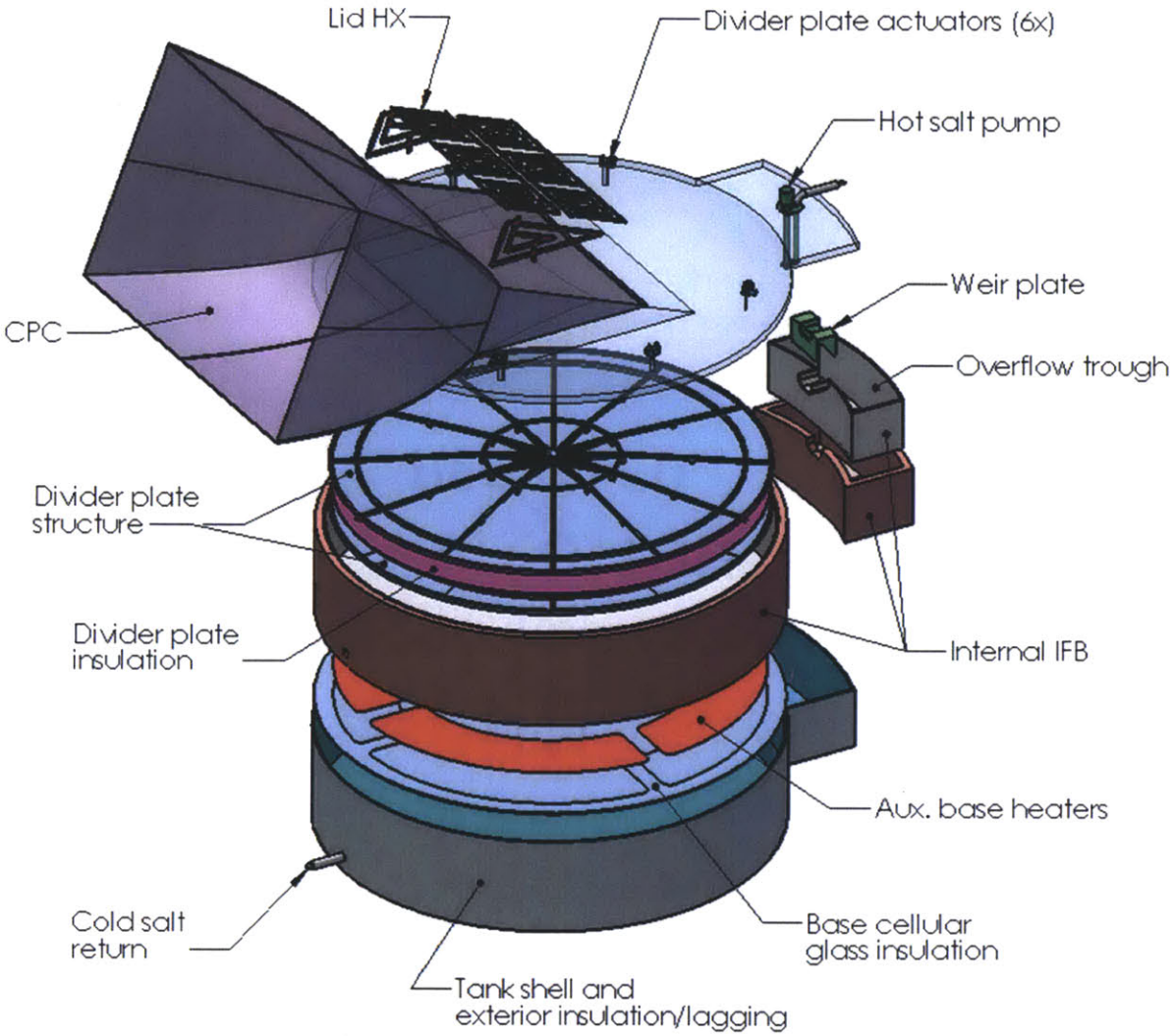

Figure 5.17 - Exploded view of CSPonD receiver

(Foundation removed and tank dome made transparent for clarity)

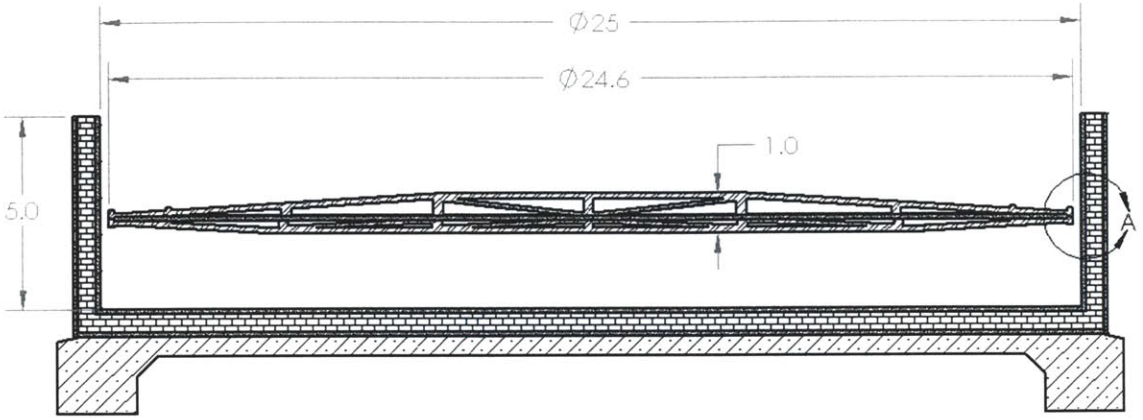

Figure 5.18 - Tank and divider plate cross-section detail
(dimensions in meters)

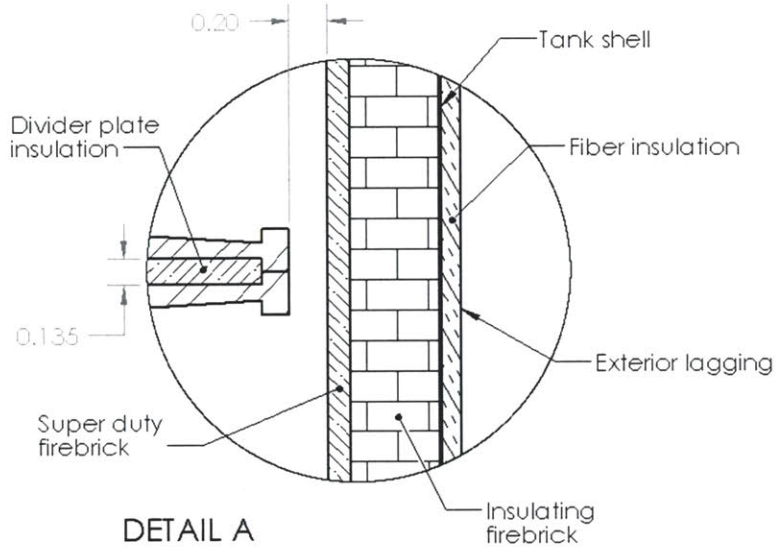

Figure 5.19 - Typical tank wall insulation details
(dimensions in meters)

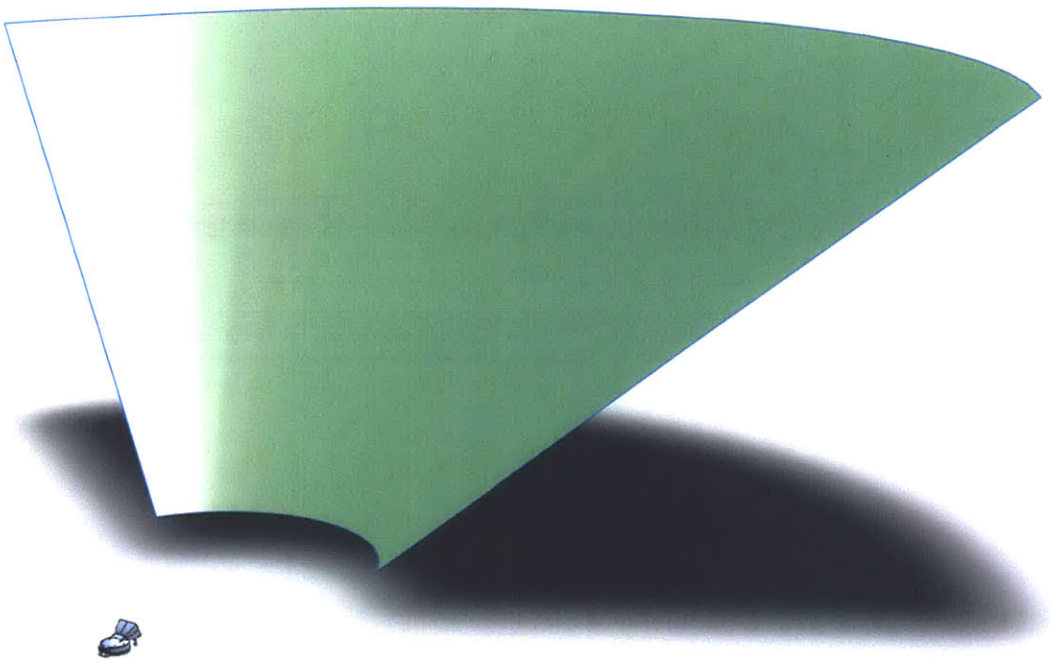

Figure 5.20 - Scale of receiver w.r.t. heliostat field area

CHAPTER 6: Concluding Remarks

Conclusions

A CSP system has been presented where hillside mounted heliostats direct sunlight into a volumetric absorption molten salt receiver with integral storage. The CSPonD DAR simplifies the system by eliminating the conventional tower based receiver, materials driven temperature limits on receiver structure, remote thermal storage system and high pressure heat transfer fluid pumps. Volumetric absorption into the passive molten salt pond results in increased performance and durability, enabling working fluid temperatures approaching 1000 °C and improved power cycle efficiency.

The receiver pond is internally insulated with firebrick and has a relatively small aperture and a refractory lined lid, whereby salt vapor condenses on the inner surface to form a self-healing reflective surface. This construction reduces secondary heat losses and avoids thermal fatigue associated with boiler tube-type receivers while achieving high temperatures needed for efficient power generation. In addition, the receiver volume also acts as the thermal storage volume. The use of low cost inorganic salts as the receiving medium, heat transfer fluid and thermal storage medium simplifies design; thermal storage media costs of 3.7 and 1.7 dollars per kilowatt-hour are achieved with binary sodium-potassium nitrate and chloride salt mixtures, respectively.

Hot salt is extracted from the top of the tank over a weir through a heat exchanger and then returned back into the bottom of the tank. An insulated divider plate provides an additional thermal barrier between the thermally stratified hot and cold layers within the tank, and the divider plate is moved axially up and down to provide high temperature thermal energy even as the average temperature of the salt in the tank decreases when the sun is not shining. The near-neutrally buoyant divider plate limits conductive heat transfer between the upper and lower salt regions to less than 1% of the storage capacity over a twenty four hour period.

CSPonD systems are expected to benefit from reduced capital and operational costs, resulting in lower levelized costs for energy produced. The capital cost for a CSPonD receiver

and integral thermal storage system is reduced through the extensive use of low-cost refractory materials, low-cost salts and by eliminating the need for a second cold salt storage tank. A majority of the capital expense in CSP systems is the heliostat field, and although hillside beam-down geometry results in additional cosine losses compared to conventional beam-up configurations, these cosine losses decrease in winter months. Thus, the CSPonD system can deliver power closer to its rated design capacity throughout the year, resulting in improved capacity factors relative to power tower designs. Operational cost, a portion of which can be measured in terms of parasitic energy consumption, is much lower in ground level CSPonD receivers as compared to that needed to pump heat transfer fluid to tall, tower mounted receivers.

Experiments with solar simulator heated lab-scale molten nitrate salt volumetric receivers indicate viability of the concept, while recent fundamental measurements of the attenuation properties of molten salts in the visible spectrum provide insight into large-scale volumetric absorption behavior [53]. Furthermore, an analysis of hillsides in the southwestern United States shows good potential for CSPonD system development at considerable scales [51]. A preliminary economic analysis using NREL's solar System Advisor Model indicates a levelized cost of electricity of 0.07-0.33 dollars per kilowatt-hour produced; the large variability is due in part to the pricing uncertainty of large numbers of heliostats and the relative uncertainty in predicting system efficiencies of such a novel and untested (at scale) system [67].

Perhaps the greatest benefit of the CSPonD system is its ability to provide dispatchable power as needed, likely during peak-power demand times when the cost of energy is high, using otherwise non-desirable hilly terrain in areas with high solar resources. Granted, very large contiguous gigawatt-scale hillside fields are neither practical nor likely to be available, but a hybrid desert system can be envisioned which combines the inherent storage and power time-shift capabilities of several CSPonD field/receiver modules with large tracts of photovoltaic or traditional CSP fields that produce power in phase with instantaneous solar irradiance. Such a hybrid system, utilizing high desert plains and surrounding foothills with CSPonD-storage would

enable wider adoption of solar into the electric grid, meeting the proposed Renewable Portfolio Standards (RPS) many states are enacting.

Thesis contributions

This thesis has provided a description of a new volumetric molten salt receiver solar thermal power system with integral storage, termed Concentrated Solar Power on Demand: CSPonD. Specific contributions have included:

- Design methodology & guidelines for the CSPonD system, including the hillside collector field
- Design guidelines for the collocated storage system, including the actuated divider plate
- First-order thermal and performance models for the CSPonD receiver
- Design rules for scaling, build & test of the receiver and storage system
- Development of a low cost high-flux solar simulator for indoor volumetric receiver testing
- Conducting volumetric absorption experiments with passive, high temperature molten salt receivers

Design parallels

It is worth mentioning other systems from which the CSPonD DAR can borrow, or has borrowed, inspiration. As an example, the aperture door mechanism and construction details can take inspiration from large observatory domes and retractable sporting stadium roofs.

The CSPonD beam down design was quickly termed the "doghouse" – and much to our surprise, a special type of glass pool furnace exists, known as a *doghouse furnace*! A low-

temperature variant of the doghouse design which many have unwittingly been exposed is the common open-hearth pizza oven. Newer designs incorporate active air extraction above the opening which increases heating within the oven and reduces heating of the *customers* outside the oven. The CSPonD salt fume extraction loop shares a similar goal: keeping salt in the receiver and reducing heat losses to the environment. Figure 6.1 depicts these analogies from which numerous lessons can be learned in design, materials and construction.

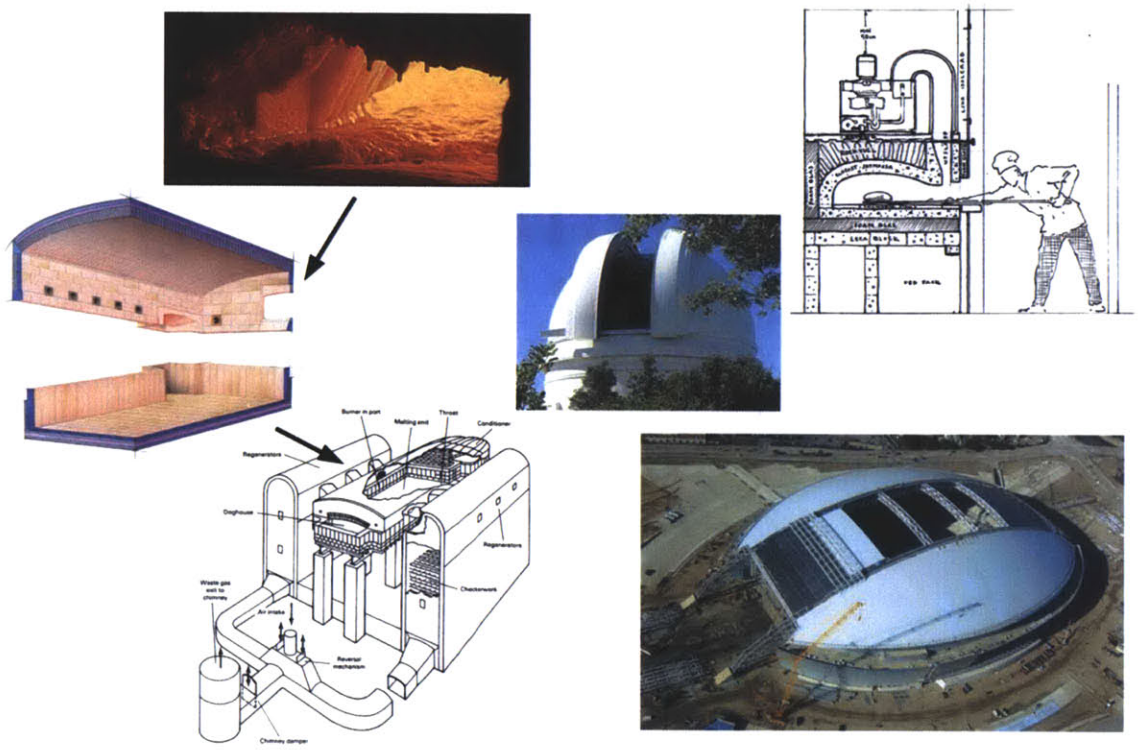

Figure 6.1 - Design parallels for the CSPonD system

Clockwise from bottom left: glass melting furnace; furnace interior; doghouse material entry; open-hearth pizza oven; observatory; stadium. Images from [71] and Creative Commons

Future work

The next step in the research is to design a 20-100 kW_t test receiver that has an aperture size to receive light from a typical concentrating heliostat, so a commercial array can be easily modified and used without needing additional concentrating optics at the aperture. This receiver would, however, be designed with the full anticipated depth of a larger system, so the optical penetration and convective mixing properties anticipated for the MW_e sized CSPonD system can be evaluated.

A detailed thermal and optical study of the receiver should be conducted using numerical methods, including modeling the convective flow field within the receiver. This is not a simple task, as it requires the simultaneous solution of the HTE, RTE and the Navier-Stokes equations. When combined with a site-specific ray tracing analysis of the heliostat field and proposed receiver lid and tank geometry needed to obtain accurate incoming radiation distributions, this task becomes quite the challenge – and is best left for computational savants. However, this modeling is mandatory before building a large-scale system to accurately characterize and predict year-round CSPonD performance.

On a smaller scale, experiments with material processing lasers can be used to verify the maximum flux limitations imposed on various solid and liquid molten salts as calculated in Chapter 3. Following on the lab-scale theme, other candidate salts can be examined for their use in a CSPonD open receiver, particularly the newly developed quaternary eutectic nitrate salts with very low melting points and high decomposition temperatures [98], [100].

Tangential research paths, perhaps to be explored by others in the field, include using the parts or all of the CSPonD system in diverse applications. One concept would use the solar-heated CSPonD molten salt receiver to feed molten salt pyrolysis reactions for production of hydrogen or other chemicals to displace fossil fuels in transportation applications. Yet another, somewhat more related application could incorporate molten salt volumetric receivers on a much

smaller scale (10-100 kW_e) for use in distributed parabolic dish power generation, providing much needed energy storage to these small, optically efficient systems. Yet another application of CSPonD technology incorporates the un-sealed divider plate concept into thermal storage tanks, for water, molten salt, or any other fluid tank combination. Indeed, SENER's large CSP solar trough plant, Andasol I: 49.9 MW_e with 6 hours thermal storage, is planning to install a 7 m diameter × 10 m high tank to test an insulated divider-plate equipped single tank thermocline system [84]. Data from these large scale tests, using solar salt (with only a 100 K temperature difference due to the low peak temperatures obtainable with a trough collection system) will be key to "selling" the CSPonD concept for commercial applications. Finally, research into the integration of CSP modules into larger power blocks is needed: particularly which chained-receiver configuration and thermal transport fluid provides optimal connectivity: molten salt, steam or yet another HTF.

On a research (as opposed to gargantuan commercial solar power purchase agreements) scale, the current funding trend towards "Micro CSP" systems with 0.1 – 50 MW_e output favors the development of individual CSPonD-type modules. Indeed, several funding opportunities exist for CSPonD proof-of-concept units located on government and public land in the western United States. Regardless of whether a CSPonD demonstration program is funded, the smaller scale of these projects will hopefully stimulate the development of more efficient and affordable heat engines in the Micro CSP range. This is greatly needed, as the poor thermal efficiency of smaller power blocks is the largest detractor from overall solar-to-electric CSP system performance.

APPENDIX – Solar Simulator Design

A low cost high-flux solar simulator

Solar simulators are an invaluable tool for solar energy research. Commercial off-the-shelf simulators are designed to provide small areas of uniform, nearly collimated light, matched to terrestrial solar spectra for photovoltaic (PV) cell testing. Typical flux output intensities are a few 'suns' (1 sun = 1 kW/m^2); thus they do not usually provide the high intensities required for concentrating solar power testing. Custom made solar simulators have been built to provide the intensities necessary for CSP research, ranging from 30-100 kW/m^2 (30-100 suns) and upward, but have cost hundreds of thousands of dollars. These research simulators utilize high power xenon arc lamps, precision engineered optical elements and active cooling circuits [145-148].

The design, development, and testing of a low-cost solar simulator, including details of its construction are provided in this Appendix. The goal was to design and build a solar simulator for under $10,000 that would offer similar testing capabilities to more expensive, high-flux research simulators. The only drawback is that the light is not collimated with the simple concentrating optics that are employed. Although the unit is designed for CSP thermal testing, specifically to study the absorption behavior of volumetric molten salt receivers, it could be utilized for concentrated PV testing provided collimated light was not needed.

Further characterization of output irradiance could be performed in accordance with ASTM 927, "Standard Specification for Solar Simulation for Photovoltaic Testing" to classify the simulator for more widespread use.

Detailed Design

The design of the solar simulator can be broken down into three subsystems: light source; adjustment structure; and concentrator. Table A.1 lists the primary functional requirements and associated specification targets for the solar simulator. Figure 1 shows the completed simulator.

Table A.1 - Solar simulator functional requirements & design specifications

Functional Requirement	Design Parameter	Specification
Emulate solar heating	Metal halide lights with metal reflective concentrating optics	Output flux $\geq$ 50 kW/m^2
Adjustable for different receivers	Aperture Height Adjustability via nested perforated tubing	0 $\leq$ Aperture height $\leq$ 1 m
Tiltable for non-normal incidence	Aperture Rotation pivot	0° $\leq$ Aperture angle $\leq$ 90°
Large output spot	Conical concentrator	Aperture diameter $\geq$ 20 cm
Low cost	Commercially available and simple components	Cost < $10,000

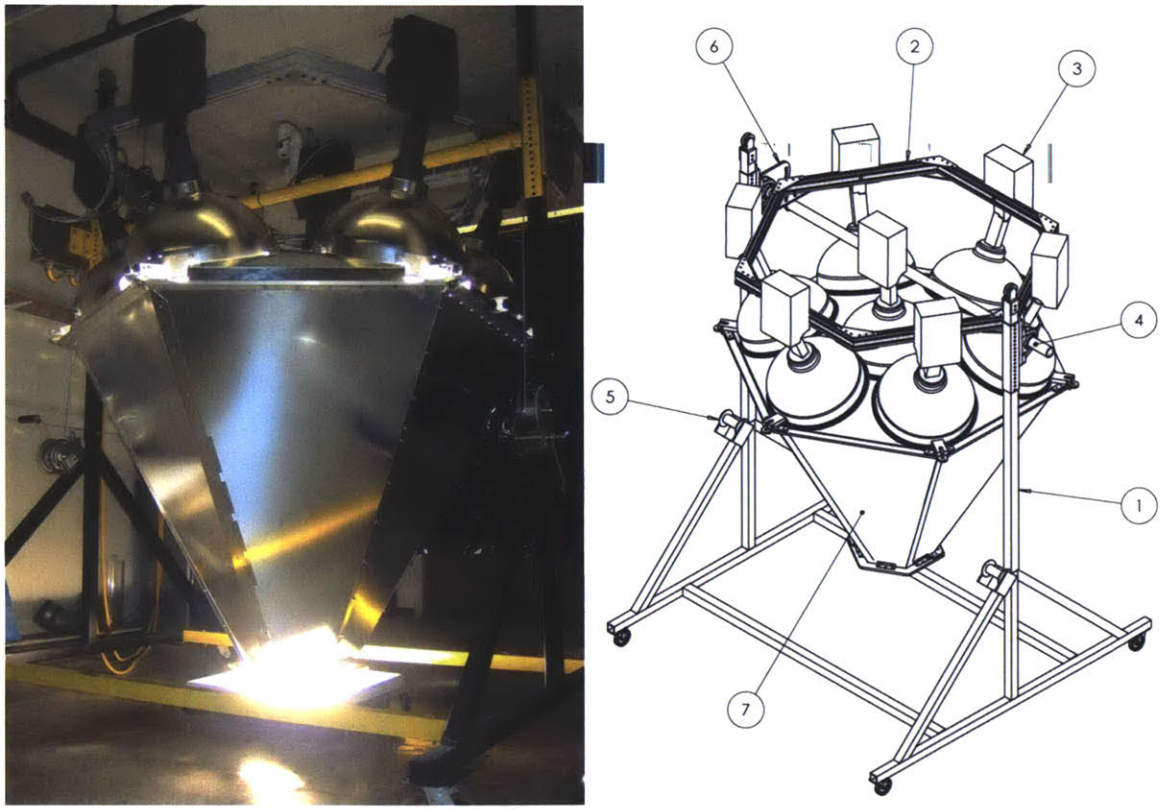

Figure A.1 - MIT metal-halide CSP solar simulator

10.5 kW; ∅38 cm hexagonal output aperture; 2.1 m x 2.1 m x 2.6 m (LxWxH) overall size. Subassemblies: (1) Frame; (2) Light Mounting Frame; (3) MH Light; (4) Pivot Tube; (5) Lifting Winch; (6) Tilt Adjustment Plate; (7) Secondary Concentrator.

Light Source

Xenon arc lamps, favored by commercial solar simulator manufacturers, can be filtered to have an emission spectrum closely matching that of terrestrial sunlight. They are available in high power single bulb configurations which can be coupled with a single ellipsoidal mirror, resulting in a tightly controlled spot size [148]. However, high power xenon arc lamps and their associated drive electronics are expensive products, with nearly 10 times the costs-per-watt than commodity light sources.

Metal halide (MH) lamps were determined to be the most practical light source due to the significant price difference. However, MH lamps come with quite a few drawbacks worth mentioning, although they were determined not to be detrimental to our CSP testing needs. The 'unfiltered' emission spectrum of does not match the emission spectrum of sunlight as closely as that of xenon arc lamps (see Fig. A.8 in the Testing & Characterization section). Also, the long 'filament' in large MH bulbs does not lend itself to precise focusing – resulting in an increased minimum achievable spot size relative to xenon arc lamps.

MH lamps are widely used in industrial and sports lighting applications, and are thus readily available and inexpensive. Common MH outdoor stadium lights utilize 1500 W BT-56 bulbs and NEMA standardized spun-aluminum ellipsoidal reflector geometries. Light distribution is described by NEMA 1-6 type ratings: Type 1 is a narrow beam (10-18°); Type 6 is a wide flood (100-130°) [149]. Figure A.2 shows the luminous intensity distributions for the most common types, NEMA 3 and 5. NEMA 3 reflectors were chosen for their narrow, high intensity output beam.

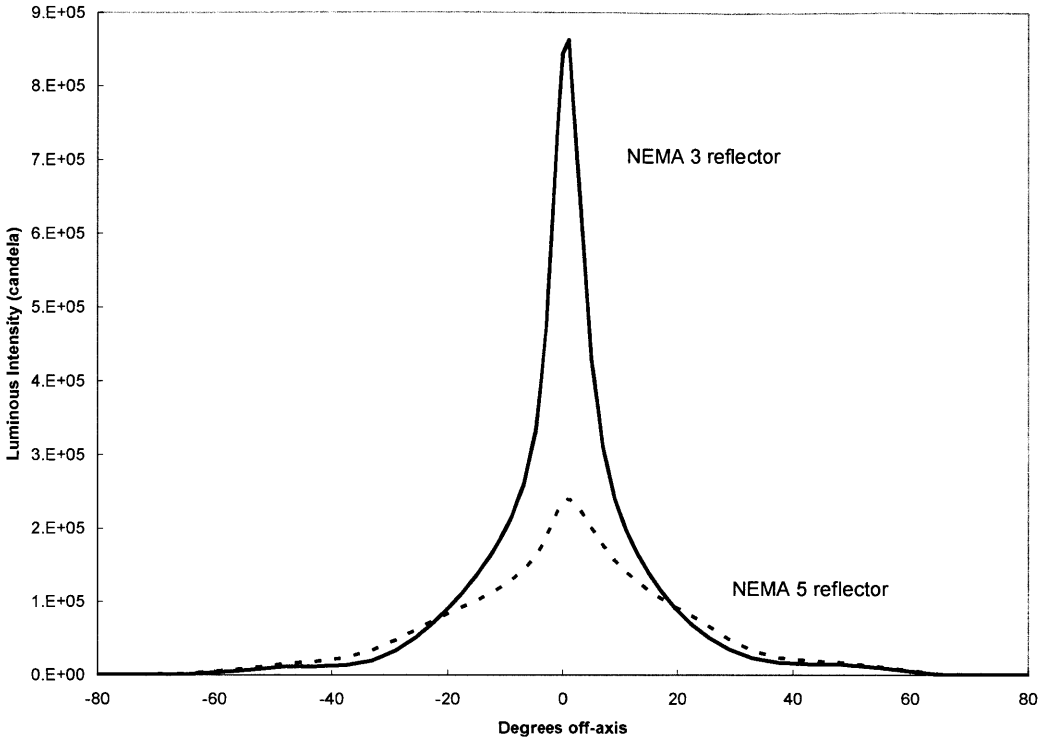

Figure A.2 - Luminous intensity distribution for various MH reflectors
1500 W MH sports lighting fixtures with NEMA 3 and NEMA 5 ellipsoidal reflector geometry. (Photometric data from [150])

Seven off-the-shelf (Complete Lighting Source: p/n SP1500MHMT) 1500 W outdoor MH units with integral ballasts, adjustable mounts and NEMA 3 reflectors are utilized for the solar simulator. The lights are arranged in a hexagonal array with the seventh light in the center. The simulator is configured for two 30A/208V power sources with fused safety cut-off switches and individual circuit breaker and in-line fuse protection.

Adjustment Structure

The frame must be easy to assemble, stiff, and support the weight for the MH lights, ballasts and secondary concentrator - about 160 kg. The frame also must be designed for ease of adjustment, disassembly and short range mobility so it can be moved within the lab, or between laboratories.

Base

Perforated steel tubing was chosen for its strength, stiffness, availability, low cost, and ability to safely set components at different heights with positive engagement pins. For portability, the frame is designed to separate into two A-frame style halves. The frame footprint measures approximately 2.1 m x 2.1 m. The base is equipped with casters for short-range mobility while assembled.

Adjustable Height

To accommodate test receivers/absorbers of various heights, perforated steel sleeves are employed over the frame uprights. The sliding sleeve assemblies are positioned using frame mounted load-lifting hand winches with integral safety brakes. Steel wire rope is used for the winches, extended over pulleys mounted to the top of each upright support and attached to an eyebolt on each sliding sleeve assembly (Fig. A.3). Zinc-plated steel quick release pins, 7/16" (11.1 mm) diameter, are used to lock the height adjustment sleeves in place.

Rotatable output

The simulator was designed to rotate about a horizontal axis to enable testing of various CSP receiver designs, some requiring non-vertical illumination – particularly the case of glancing angle irradiation over a liquid free-surface. Aluminum extrusions are assembled into a lightweight hexagonal frame, allowing direct mounting of the six peripheral MH light/ballast modules in a compact arrangement to enable pivoting of the entire light assembly.

The hexagonal frame assembly is mounted to a 2" schedule 40 (60.3 mm OD x 3.9 mm wall) steel pipe, supported on both ends by pillow-block mounted bearings. The central MH light is bolted to a bracket welded directly to the pipe's midsection. The pipe and aluminum extrusions

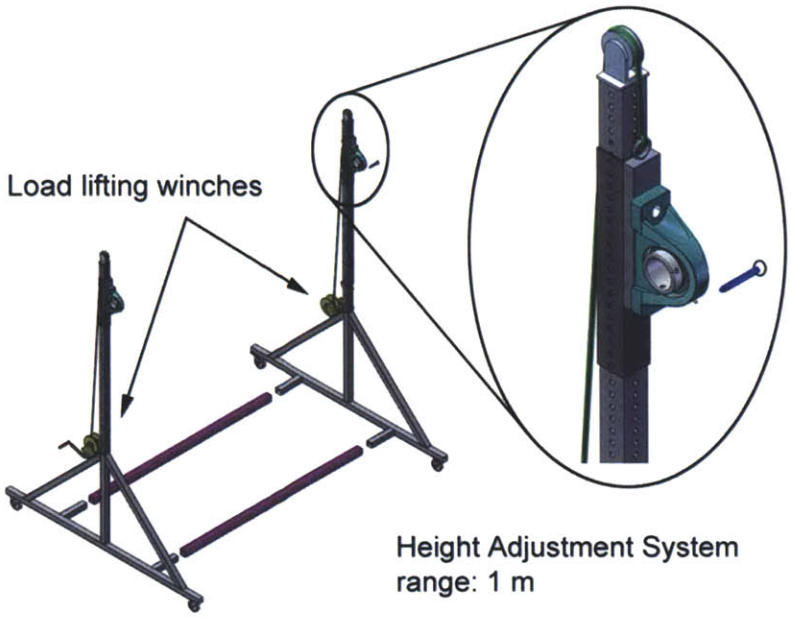

Figure A.3 - Simulator support frame

Nestable, perforated square tubing with pillow block bearing mount for height adjustments. Vertical adjustments accomplished with load-lifting winches (2X), located on support uprights.

were sized to keep deflection of the frame to a minimum, regardless of the tilt position. Efforts were made to keep the unit balanced so manual tilt adjustments can be made easily. An aluminum adjusting plate was designed to lock the simulator's rotation angle at 5 degree increments, and attached to the pipe with a captive stainless steel torque rod loaded in double shear (Fig. A.4). The torque rod serves as a "fuse" yielding to prevent tip-overs at torque of 11,800 lb-in (1,333 N-m), corresponding to an eccentric load of 380 lb (1.69 kN) applied at the edge of the 62" (1.6 m) wide light support frame. A single 7/16" (11.1 mm) diameter steel quick release pin locks the angular adjustment. The quick release pins are rated for 13,230 lb (58.8 kN) in single shear, which equates to a maximum load capacity of 3,400 lb (15.1 kN) at the outer extremes of the light support frame, more than adequate for the lights and mounting structure.

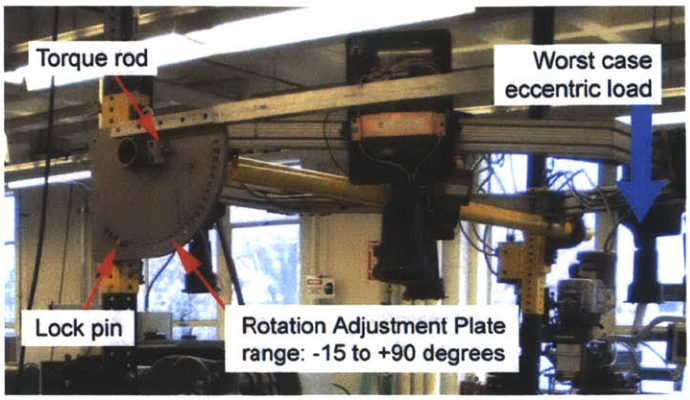

Figure A.4 - Rotation adjustment plate

Plate attached to MH support assembly, consisting of a steel 2" schedule 40 pipe mounted in pillow-block self-aligning bearings, supporting the hexagonal aluminum extrusion light support structure.

Secondary Concentrator

A simplified secondary concentrator is utilized to boost the flux available at the output aperture. Designs of non-imaging concentrators are well known – typical designs are variants of compound parabolic concentrators (CPCs) or flow-line concentrators (FLCs), as shown in Fig. A.5 [5]. A truncated FLC was selected for the simulator, resulting in a hexagonal conical structure with reasonable concentration performance that is very simple to manufacture.

As noted in the design of flat 2-dimensional cone concentrators, there is a distinct tradeoff between increased concentration, number of reflections, and the length of the concentrator. SolTrace, NREL's ray-tracing freeware, was used to simulate the optical performance of the secondary concentrator. However, the software did not allow for individual light sources (i.e., the array of seven MH lights) to be defined, so the entrance plane of secondary concentrator was illuminated with uniform, collimated input flux. Simulated output flux results are shown in Fig. A.6 for the conical design geometry with a 24.9° half-angle. Predicted concentration across the output aperture is boosted with noticeably increased concentration in the center.

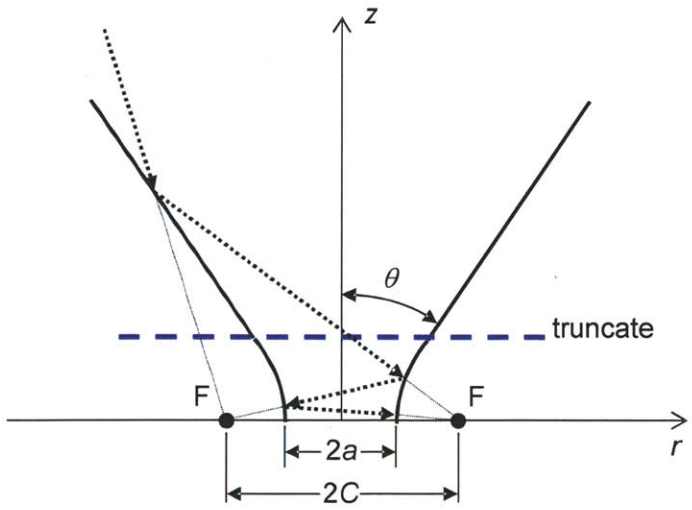

Figure A.5 - Flow-Line Concentrator geometry

Simplified flat-cone construction along hyperbolic asymptotes is utilized for the solar simulator. The asymptotes have a half angle θ relative to the z-axis. Flux aimed between ±C will be concentrated on to ±a, resulting in a concentration of C/a (C^2/a^2 for a hyperboloid of revolution). From [5]

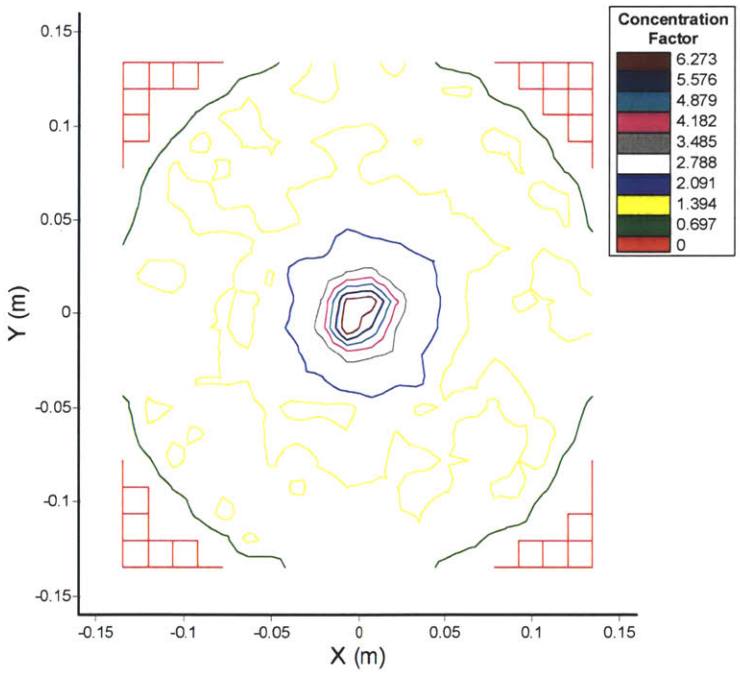

Figure A.6 - Output aperture flux ray tracing results

Ray-tracing simulation results, concentration ratio (output flux/input flux) at exit aperture of secondary concentrator. 24.9° conical secondary concentrator geometry; 300,000 rays with a uniform input flux directed parallel to the concentrator's z-axis. A "hot spot" of over 6x concentration is predicted in the center of the output aperture.

Commercial specular reflective 'bright' anodized aluminum (Lorin Industries ClearBrite® 1 mm thick Al 5657-H25) used in custom signs and lighting was chosen for the concentrator panels for its low cost, low mass and excellent heat dissipation characteristics. An aluminum frame was fabricated top and bottom for rigidity and ease of attachment to the lights. Additional provisions were made on the output aperture frame for mounting a hyperboloidal neck to further boost the concentration, if needed for future tests. Contoured aluminum adapter plates are used to distribute the stress of the concentrator load without deforming the thin MH primary reflectors, and top 'filler' reflectors close the gaps between the MH lights. (Fig. A.7)

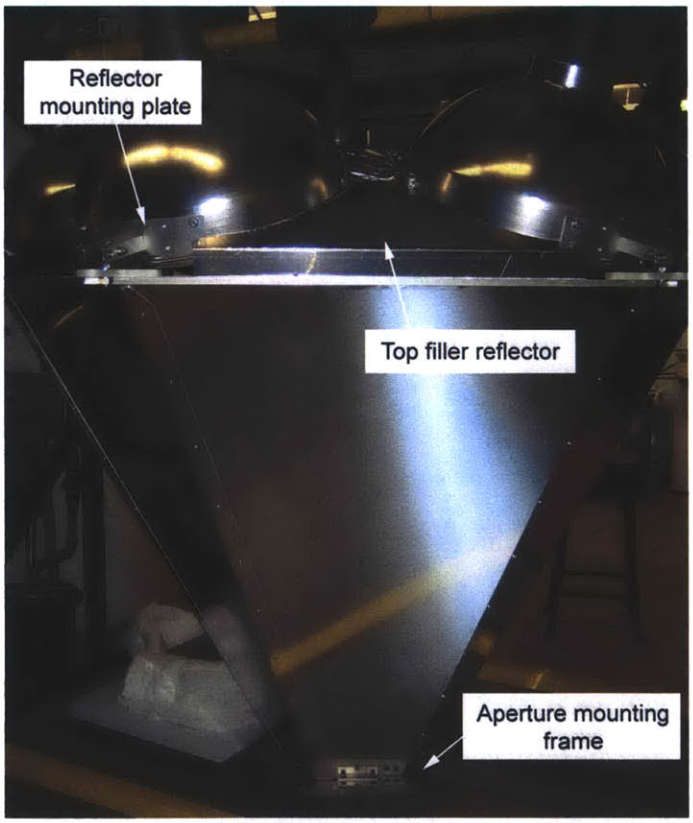

Figure A.7 - Secondary concentrator structure

Mounting plates distribute the load evenly on the reflector domes to avoid distortion. Specular anodized aluminum sheet (1 mm thickness) is utilized for the reflective surfaces.

It was assumed that natural convection over the concentrator's large outside surface would be sufficient to prevent overheating inside a climate-controlled laboratory environment with ambient temperatures near 25 °C. For example, a worst case calculation of all the input power (10.5 kW) reflected an average of two times over the secondary concentrator (assumed reflectivity = 0.89; surface area = 4.9 m^2) gives a heat flux of only 450 W/m^2 – much less than midday sun.

During operation, the upper portions of the simulator, including the primary MH light reflectors and the top of secondary concentrator, become slightly warm to the touch. However, during periods of prolonged operation exceeding several hours, the bottom 10 cm of the concentrator reaches temperatures of 140 °C. This is expected, as there are an increased number of reflections near the output aperture and heat from the receiver can conduct into the secondary concentrator. If needed, the concentrator's operating temperature can be reduced by adding external finned surfaces or water cooling the distal end of the panels, or cooling the output aperture mounting frame directly.

Testing & Characterization

After the solar simulator was assembled, the following tests were performed to determine its suitability for use in our CSP testing: solar spectral match and flux intensity determination.

Spectral Distribution

An Ocean Optics USB 650 spectrometer was used to compare the simulator output from 350-1000 nm (VIS-NIR) to midday sun. A pinhole aperture was placed over the sensor to avoid saturating the spectrometer while collecting the simulator's spectra. As shown in Fig. A.8, the spectral intensity of the simulator – while not a perfect match for sunlight – is a reasonable approximation in the range tested. The NIR intensity peaks typical of MH lights are clearly

visible beyond 800 nm. The MIT CSP simulator delivers 10.9% of its 350-1000 nm energy in the 800-1000 nm range, as opposed to the sun's measured 5.9% over the same range.

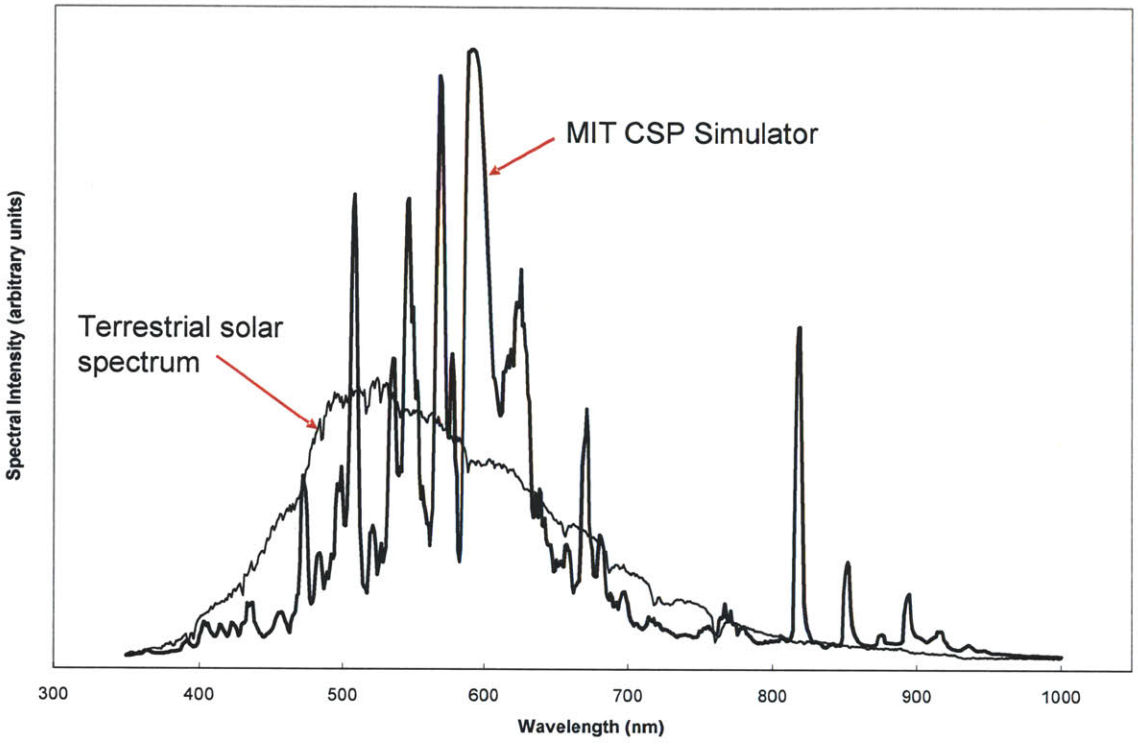

Figure A.8 - Spectral intensity comparison for the MIT CSP simulator

Comparison for the MIT MH CSP simulator vs. measured midday sun spectra. All curves were normalized to result in identical intensities when integrated over the test spectrum: 350 to 1000 nm.

Intensity Distribution

A simple calorimetric experiment was conducted to quantify the flux distribution across the output aperture. A flux gage was not available for use, so a small aluminum disc (∅29.3 mm x 1.3 mm thick) was instrumented with a thermocouple and placed in the output aperture. Figure A.9 plots the transient temperature behavior of the disc at various radial positions across the output aperture. After only 20 minutes under the simulator lights, the absorber disc temperature

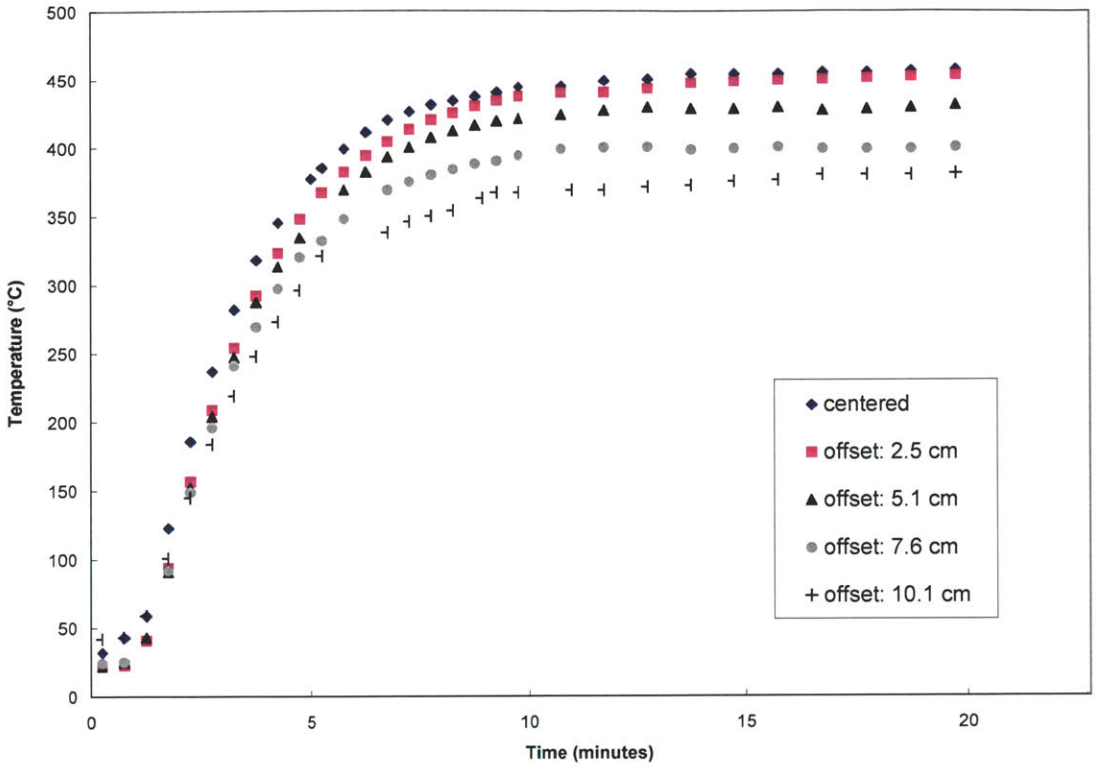

Figure A.9 - Calorimetric absorber target temperature

Al sheet disc, ∅29.3 mm x 1.3 mm thick, 6061-T6 mill finish. Note decreasing temperatures as the target is radially offset from the center of the output aperture.

approached steady-state values. Between each measurement run, the simulator was turned off and allowed to cool to ambient temperature. The absorber disc was examined after each run, but did not exhibit any noticeable change in appearance or oxidation discoloration. As expected, the peak temperature is reduced as the absorber was moved away from the center of the output aperture.

The small, conductive disc is assumed to be at a uniform temperature, which gives an indication of the average flux received onto its surface. Assuming steady-state conditions, a simple energy balance can be used to calculate the incoming flux in terms of the absorber temperature and its surface properties. The energy balance diagram is shown in Fig. A.10. Since the disc was placed on a thick layer of ceramic fiber insulation and the aperture opening was

lowered onto this insulation blanket, the horizontal disc can be modeled as well-insulated on the back side and without forced convection losses on the top surface. However, the hot disc promotes free convection to develop on its surface, and radiates heat to its lower temperature surroundings. The thin edge area of the absorber disc is ignored for these calculations.

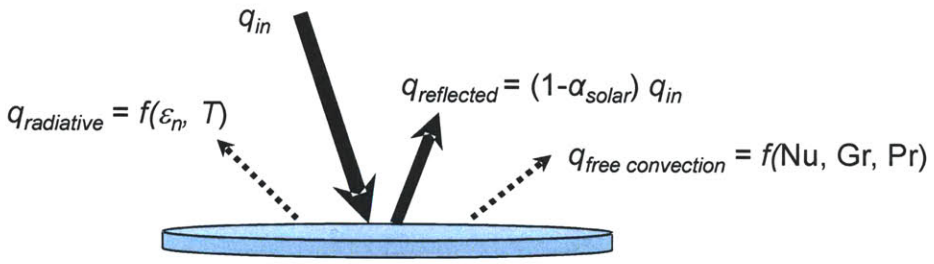

Figure A.10 - Heat flux balance for top surface of horizontal absorber test target. Back side is insulated.

Free convection losses can be estimated using correlations for natural convection above heated horizontal discs. These can be found in standard heat transfer textbooks and are of the form:

$$\mathrm{Nu_m} = c\ (\ \mathrm{Gr} \cdot \mathrm{Pr}\ )^n \tag{A.1}$$

The correlation coefficients for laminar flow over a hot horizontal plate given as c=0.54 and n = ¼ [120]. Nu is the Nusselt number, Gr is the Grashof number and Pr is the Prandtl number, evaluated at the mean air temperature, T_m and defined as:

$$\mathrm{Nu_m} = h_m \cdot L / k \tag{A.2}$$

$$\mathrm{Gr} = g\,\beta L^3\,(\,T - T_\infty)\,/\,\nu^2 \tag{A.3}$$

$$\mathrm{Pr} = \nu / \alpha \tag{A.4}$$

$$T_m = (T + T_\infty) / 2 \tag{A.5}$$

where

$$\beta = 1/T_m \tag{A.6}$$

In the case of a horizontal circular disc of diameter D, the characteristic length L to be used in Equations A.2 and A.3 is:

$$L = 0.9\,D \tag{A.7}$$

The free convection and radiative heat flux losses are calculated as:

$$q_{free\ convection} = h_m\,(T - T_\infty) \tag{A.8}$$

$$q_{radiative} = \varepsilon_n\,\sigma(T^4 - T_\infty^4) \tag{A.9}$$

The reflected heat flux, where α_{solar} is the disc's solar spectrum absorptivity, is simply:

$$q_{reflected} = (1 - \alpha_{solar}) \cdot q_{in} \tag{A.10}$$

The energy balance for the disc is:

$$q_{in} = q_{reflected} + q_{radiative} + q_{free\ convection} \tag{A.11}$$

combining Equations (A.9) and (A.10) to solve for the incoming flux provided by the simulator:

$$q_{in} = (1 / \alpha_{solar}) \cdot (\, q_{radiative} + q_{free\ convection}\,) \tag{A.12}$$

A Biot number $<< 0.1$, validates the assumption of the target disc as a lumped mass of uniform temperature. With the thermal conductivity of the disc denoted by k_{Al}, the Biot number, Bi, is defined as:

$$\mathrm{Bi} = h_m \cdot L / k_{Al} \tag{A.13}$$

Representative flux calculations for the absorber disc at each test position are presented in Tables A.2 and A.3. The calculated output intensity at various radial positions is shown in Fig. A.11. As expected, calculated optical power is greatest at the center of the output aperture. However, the ray-tracing predicted central "hot spot" was not observed, with calculated values decreasing only slightly as a function of the radial offset from center. One explanation for this discrepancy could be the ray-tracing modeling limitations which could not capture the seven discrete, aimed MH light sources – but instead required the use of a uniform input beam.

Table A.2 - Absorber disc properties

disc diameter, D (m)	characteristic length, L (m)	ambient temp, T_∞ (K)	α_{solar}	ε_n	k_{Al} (W/m-K)
0.0293	0.0264	298	0.11	0.05	164

It is worth noting the various sources of uncertainty in the above calculations; particularly the effects of ambient temperature (T_∞) and the absorber disc's surface properties (α_{solar} and ε_n). Before each run, the simulator and secondary concentrator were allowed to cool to the ambient temperature of the room, approximately 25 °C. The measurement runs were short, only 20 minutes duration, and the base of the secondary concentrator did not exceed 50 °C at the end of each run. Setting $T_\infty = 50$ °C (as opposed to $T_\infty = 25$ °C) equates to 6%, 1% and 6% difference in the values of flux calculated in Eqs. (A.8), (A.9) and (A.12), respectively.

The absorber disc surface property uncertainty has a much greater effect on the calculated performance. Tabulated values were used for the solar absorptivity and normal spectral emissivity of mill finish aluminum sheet. Ozisik [120] lists $\alpha_{solar} = 0.14$ and $\varepsilon_n = 0.06$, while Love [151] shows $\alpha_{solar} = 0.11$ and $\varepsilon_n = 0.05$. This large variation in the solar absorptivity (21%) translates to an equally large variation in calculated flux. In addition, the spectral output of the simulator does not match that of the sun exactly, and one would expect a slightly different value for the effective

"simulator absorptivity" of the aluminum absorber disc. Because the simulator has additional spectral output in the near infrared region, the "simulator absorptivity" should be bounded somewhere between the spectral emissivity (NIR-IR) and solar absorptivity (VIS-NIR). For this reason, the absorber disc's nominal values were set to those defined by Love, $\alpha_{solar} = 0.11$ and $\varepsilon_n = 0.05$. Bounding lines are shown on Figure 11 for Ozizik's values and the limiting case defined by Kirchhoff's law: $\varepsilon_n = \alpha_{solar} = 0.11$.

Table A.3 - Calculation of output flux levels

Parameter	disc offset from center (cm)					Equation from text
	0.0	2.5	5.1	7.6	10.2	
steady-state disc temp, T (K)	730	726	704	673	654	
T_m (K)	514	512	501	486	476	(A.5)
v (m^2/s)	3.96E-05	3.93E-05	3.80E-05	3.61E-05	3.49E-05	
α (m^2/s)	5.87E-05	5.84E-05	5.64E-05	5.36E-05	5.20E-05	
k (W/m-K)	4.20E-02	4.18E-02	4.11E-02	4.01E-02	3.95E-02	
Pr	0.674	0.674	0.673	0.672	0.672	(A.4)
Gr	9.64E+04	9.71E+04	1.01E+05	1.07E+05	1.10E+05	(A.3)
Nu_m	8.62	8.64	8.72	8.84	8.91	(A.1)
h_m (W/m^2-K)	13.72	13.71	13.61	13.45	13.35	(A.2)
$q_{free\ convection}$ (kW/m^2)	5.93	5.87	5.52	5.05	4.75	(A.8)
$q_{radiative}$ (kW/m^2)	0.78	0.77	0.67	0.56	0.50	(A.9)
q_{in} (kW/m^2)	**61.0**	**60.3**	**56.4**	**51.0**	**47.7**	(A.12)
Bi	0.0022	0.0022	0.0022	0.0022	0.0021	(A.13)

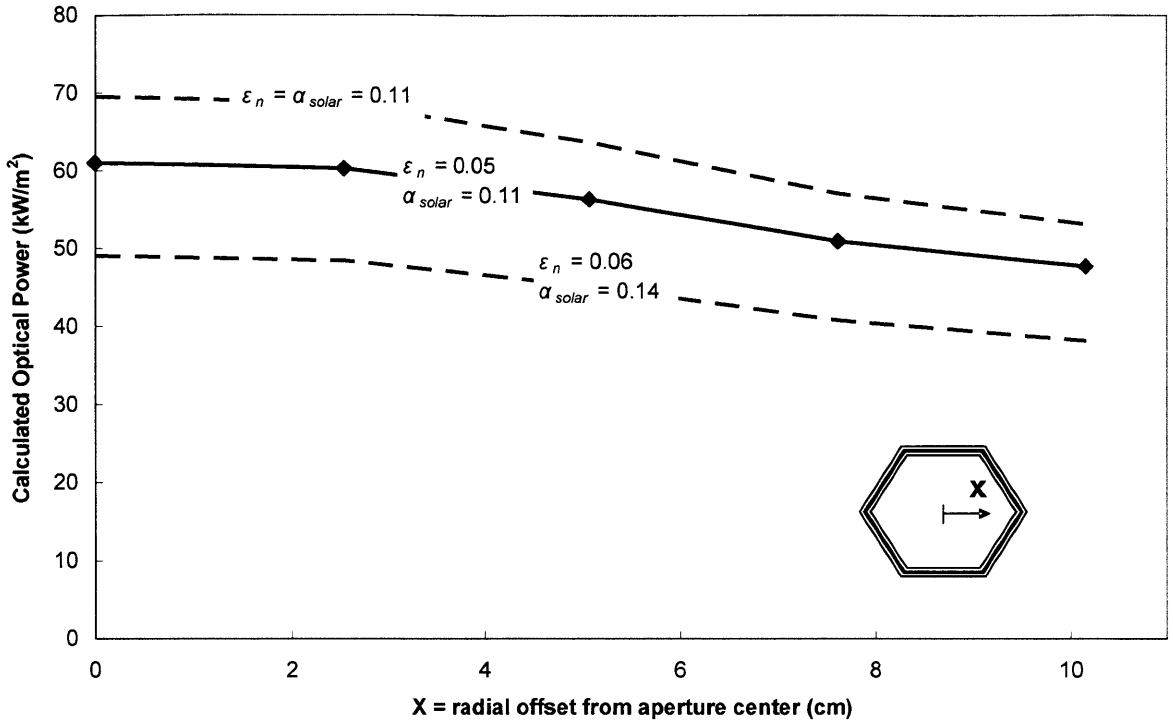

Figure A.11 - Calculated aperture flux distribution

Flux distribution, accounting for free-convection and radiative losses of the test target. Al sheet disc absorber, ∅29.3mm x 1.3mm thick, mill finish. Heavy solid line corresponds to absorber disc spectral emissivity, $\varepsilon_n = 0.05$, and solar absorptivity, $\alpha_{solar} = 0.11$ [151]. Bounding dotted lines correspond to $\varepsilon_n = 0.06$, $\alpha_{solar} = 0.14$ [120] and $\varepsilon_n = \alpha_{solar} = 0.11$.

The MIT CSP simulator was successful in heating nitrate salts and keeping them molten in small-scale receivers of various designs. It is interesting to note the divergent nature of the output rays, as shown in Fig. A.12, due to the non-imagining nature of the secondary concentrator optics.

Component Costs

The costs of the major subassemblies are detailed in the bill-of-materials listed in Table A.4. Direct material cost for the simulator is under $5,000.

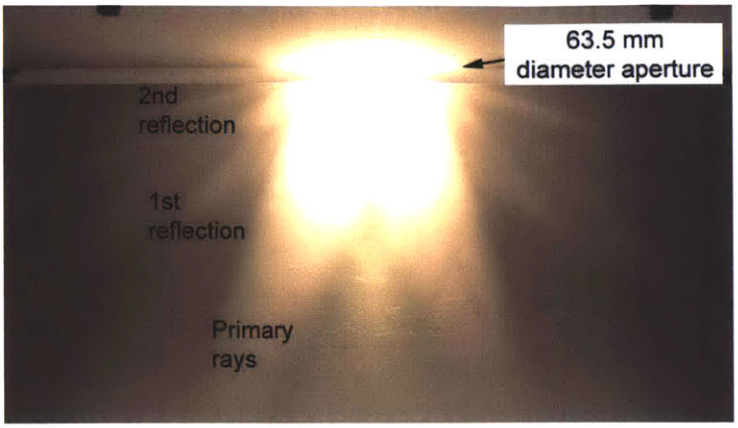

Figure A.12 - Appearance of output rays

Output limited by a 63.5 mm aperture. Clearly visible are the primary (from the MH lights) and secondary (reflected from the concentrator) rays. The non-imaging nature of the concentrator results in divergent rays as they travel away from the aperture.

Table A.4 - Bill of Materials for the MIT CSP solar simulator

Item No.	Assembly	Description	Quantity	Cost (ea.)	Cost (total)
1	Frame	Welded steel tubing & casters	1	$280	$280
2	Light Mounting	Hexagonal aluminum extrusion assembly	1	$510	$510
3	MH Light	1500W MH Stadium Lights with ballasts, NEMA 3 reflector	7	$285	$1,995
4	Pivot Tube	2" schedule 40 pipe & pillow block bearings	1	$170	$170
5	Winch	Load lifting winch & cable accessories	2	$100	$100
6	Adjustment Plate	Aluminum plate (waterjet) for angular adjustment	1	$200	$200
7	Concentrator	Aluminum (reflective anodized) concentrator and supports	1	$650	$650
-	Electrical	Wiring, conduit, breaker boxes, disconnect switches, etc	-	-	$600
-	Hardware	Assembly hardware and quick release adjustment pins	-	-	$350
				Hardware Total:	$4,855
			Assembly/Fabrication Labor: 50 h @ $25/h (Direct Labor+Overhead) Total:		$1,250
				Total:	$6,105

References

[1] B. Prior, "Greentech Media: US CSP Project Tracker.," 15-Sep-2010. [Online]. Available: http://www.greentechmedia.com/images/wysiwyg/research-blogs/USCSPProjectTracker.pdf. [Accessed: 08-Nov-2010].

[2] P. Viebahn, S. Kronshage, and Y. Lechon, *Deliverable n 12.2-RS Ia" Final report on technical data, costs, and life cycle inventories of solar thermal power plants*. NEEDS New Energy Externalities Developments for Sustainability: , 2008.

[3] Sargent & Lundy LLC, *Assessment of Parabolic Trough and Power Tower Solar Technology Cost and Performance Forecasts*. NREL, 2003.

[4] A. Steinfeld and M. Schubnell, "Optimum aperture size and operating temperature of a solar cavity-receiver," *Solar Energy*, vol. 50, no. 1, p. 19–25, 1993.

[5] *Solar Power Plants: Fundamentals, Technology, Systems, Economics*. Berlin: Springer-Verlag, 1991.

[6] H. E. Reilly and G. J. Kolb, *An Evaluation of Molten-Salt Power Towers Including Results of the Solar Two Project*. Sandia National Labs, Albuquerque, NM; Livermore, CA, 2001.

[7] W. Stoke, *Solar Two Central Receiver, P600-00-017*. California Energy Commission, 1999.

[8] J. C. Swearengen and S. L. Robinson, "Materials-related design issues in the solar central receiver pilot plant," *Journal of Materials for Energy Systems*, vol. 1, no. 3, p. 60–70, 1979.

[9] J. M. Lata, M. Rodríguez, and M. Á. de Lara, "High Flux Central Receivers of Molten Salts for the New Generation of Commercial Stand-Alone Solar Power Plants," *Journal of Solar Energy Engineering*, vol. 130, p. 021002, 2008.

[10] R. B. Diver, "Receiver/Reactor Concepts for Thermochemical Transport of Solar Energy," *Journal of Solar Energy Engineering*, vol. 109, no. 3, pp. 199-204, 1987.

[11] European Commision, *Solar hybrid gas turbine electric power system, EUR 21615 SOLGATE*. Luxembourg: Office for Official Publications of the European Communities, 2005.

[12] C. Singer, R. Buck, R. Pitz-Paal, and H. M\üller-Steinhagen, "Assessment of Solar Power Tower Driven Ultrasupercritical Steam Cycles Applying Tubular Central Receivers With Varied Heat Transfer Media," *Journal of Solar Energy Engineering*, vol. 132, p. 041010, 2010.

[13] A. Gil et al., "State of the art on high temperature thermal energy storage for power generation. Part 1–Concepts, materials and modellization," *Renewable and Sustainable Energy Reviews*, 2009.

[14] M. Medrano, A. Gil, I. Martorell, X. Potau, and L. F. Cabeza, "State of the art on high-temperature thermal energy storage for power generation. Part 2–Case studies," *Renewable and Sustainable Energy Reviews*, vol. 14, no. 1, p. 56–72, 2010.

[15] M. S. Bohn and H. J. Green, "Heat transfer in molten salt direct absorption receivers," *Solar Energy*, vol. 42, no. 1, pp. 57-66, 1989.

[16] M. S. Bohn, "Experimental investigation of the direct absorption receiver concept," *Energy*, vol. 12, no. 3-4, pp. 227-233, Mar. 1987.

[17] T. D. Brumleve, *A high temperature solar energy system, SAND74-8008*. Sandia National Labs, Livermore, CA, 1974.

[18] C. E. Tyner, *Status of the direct absorption receiver panel research experiment: Salt flow and solar test requirements and plans, SAND88-2455*. Sandia National Labs, Albuquerque, NM; Livermore, CA, 1989.

[19] R. E. West, "Direct absorption receiver system for high temperature," in *Solar Energy Utilization. Proceedings of the NATO Advanced Study Institute, 23 June-4 July 1986*, Dordrecht, Netherlands, 1987, pp. 361-73.

[20] D. C. Smith, E. E. Rush, C. W. Matthews, J. M. Chavez, and P. A. Bator, *Report on the test of the molten-salt pump and valve loops, SAND91-1747*. 1992.

[21] A. Rabl, "Tower reflector for solar power plant," *Solar Energy*, vol. 18, no. 3, pp. 269-271, 1976.

[22] A. Segal and M. Epstein, "Solar ground reformer," *Solar Energy*, vol. 75, no. 6, pp. 479-490, Dec. 2003.

[23] A. Yogev, "Heat storage device," U.S. Patent 5,685,2891997.

[24] M. Epstein, A. Segal, and A. Yogev, "A molten salt system with a ground base-integrated solar receiver storage tank," *Le Journal de Physique IV*, vol. 9, no. 3, 1999.

[25] M. Epstein and A. Segal, "A new concept for a molten-salt receiver/storage system," in *Proceedings of Solar 98: Renewable Energy for the Americas, 14-17 June 1998*, New York, NY, USA, 1998, pp. 383-90.

[26] A. Yogev, A. Kribus, M. Epstein, and A. Kogan, "Solar tower reflector systems: a new approach for high-temperature solar plants," *International journal of hydrogen energy*, vol. 23, no. 4, p. 239–245, 1998.

[27] A. Segal and M. Epstein, "Practical Considerations in Designing Large Scale 'Beam Down' Optical Systems," *Journal of Solar Energy Engineering*, vol. 130, p. 011009, 2008.

[28] R. Winston, *Nonimaging Optics*. Amsterdam: Elsevier Academic Press, 2005.

[29] F. Trombe and A. Le Phat Vinh, "Thousand kW solar furnace, built by the National Center of Scientific Research, in Odeillo (France)," *Solar Energy*, vol. 15, no. 1, p. 57–61, 1973.

[30] F. Trombe, L. Gion, C. Royere, and J. F. Robert, "First results obtained with the 1000 kW solar furnace," *Solar Energy*, vol. 15, no. 1, p. 63–66, 1973.

[31] A. C. Skinrood, T. D. Brumleve, C. T. Schafer, C. T. Yokomizo, and C. M. Leonard Jr, *Status report on a high temperature solar energy system, SAND74-8017*. Sandia Labs., Albuquerque, N. Mex.(USA), 1974.

[32] R. M. Green, D. K. Ottesen, J. J. Bartel, and T. T. Bramlette, "High temperature thermal energy storage," in *Sharing the sun: Solar technology in the seventies; Proceedings of the Joint Conference, Winnipeg, Canada, August 15-20, 1976*, 1976, vol. 8, p. 4–47.

[33] Z. Yang and S. V. Garimella, "Thermal analysis of solar thermal energy storage in a molten-salt thermocline," *Solar Energy*, vol. 84, no. 6, p. 974–985, 2010.

[34] U. Herrmann, B. Kelly, and H. Price, "Two-tank molten salt storage for parabolic trough solar power plants," *Energy*, vol. 29, no. 5-6, p. 883–893, 2004.

[35] J. E. Pacheco, S. K. Showalter, and W. J. Kolb, "Development of a molten-salt thermocline thermal storage system for parabolic trough plants," *Journal of Solar Energy Engineering*, vol. 124, p. 153, 2002.

[36] M. W. Jack and J. Wrobel, "Thermodynamic optimization of a stratified thermal storage device," *Applied Thermal Engineering*, vol. 29, no. 11-12, p. 2344–2349, 2009.

[37] D. Brosseau, J. W. Kelton, D. Ray, M. Edgar, K. Chisman, and B. Emms, "Testing of thermocline filler materials and molten-salt heat transfer fluids for thermal energy storage systems in parabolic trough power plants," *Transactions of the ASME. Journal of Solar Energy Engineering*, vol. 127, no. 1, pp. 109-16, Feb. 2005.

[38] R. J. Copeland and J. Green, "Raft thermocline thermal storage," in *Proceedings of the 18th Intersociety Energy Conversion Engineering Conference, 21-26 Aug. 1983*, New York, NY, USA, 1983, pp. 1801-5.

[39] R. J. Copeland, R. E. West, and F. Kreith, "Thermal energy storage at 900C," in *19th Intersociety Energy Conversion Engineering Conference (Cat. No. 84CH2101-4), 19-24 Aug. 1984*, LaGrange Park, IL, USA, 1984, pp. 1171-5.

[40] R. J. Copeland, "Method and apparatus for operating an improved thermocline storage unit," U.S. Patent 4,523,6291985.

[41] J. W. Andrews, "Hot water tank for use with a combination of solar energy and heat-pump desuperheating," U.S. Patent 4,390,0081983.

[42] K. Y. Wang, R. E. West, F. Kreith, and P. Lynn, "High-temperature sensible-heat storage options," *Energy*, vol. 10, no. 10, p. 1165–1175, 1985.

[43] D. Laing, W. D. Steinmann, and R. Tamme, "Sensible Heat Storage for Medium and High Temperatures," in *Proceedings of ISES World Congress 2007 (Vol. I–Vol. V)*, 2009, p. 2731–2735.

[44] P. Hejzlar, V. Dostal, and M. J. Driscoll, "A supercritical CO2 cycle- a promising power conversion system for Generation IV reactors," in *American Nuclear Society Embedded Topical Meeting - 2006 International Congress on Advances in Nuclear Power Plants, ICAPP'06, June 4, 2006 - June 8, 2006*, Reno, NV, United states, 2006, vol. 2006, pp. 722-731.

[45] A. H. Slocum and D. S. Codd, "Solar energy concentrator system with energy storage, US Patent Application 61/243763," 2010.

[46] A. H. Slocum, J. Buongiorno, C. W. Forsberg, D. S. Codd, and A. T. Paxson, "Concentrated Solar Power System, PCT Patent Application PCT/US10/49474," 2010.

[47] W. A. Allman, D. C. Smith, and C. R. Kakarala, "The design and testing of a molten salt steam generator for solar application," *Transactions of the ASME. Journal of Solar Energy Engineering*, vol. 110, no. 1, pp. 38-44, Feb. 1988.

[48] T. P. Otanicar, P. E. Phelan, and J. S. Golden, "Optical properties of liquids for direct absorption solar thermal energy systems," *Solar Energy*, vol. 83, no. 7, pp. 969-977, Jul. 2009.

[49] V. Velmurugan and K. Srithar, "Prospects and scopes of solar pond: A detailed review," *Renewable and Sustainable Energy Reviews*, vol. 12, no. 8, p. 2253–2263, 2008.

[50] F. A. Blake, T. R. Tracey, J. D. Walton, and S. Bomar, "One MWth bench model cavity receiver steam generator," *Solar Energy*, vol. 18, no. 6, p. 513–523, 1976.

[51] C. J. Noone, A. Ghobeity, A. H. Slocum, G. Tzamtzis, and A. Mitsos, "Site selection for hillside central receiver solar thermal plants," *Solar Energy*, vol. 85, no. 5, pp. 839-848, May. 2011.

[52] M. F. Modest, *Radiative Heat Transfer*, 2nd ed. Amsterdam: Academic, 2003.

[53] S. Passerini, "Optical and Chemical Properties of Molten Salt Mixtures for Use in High Temperature Power Systems," SM thesis, Massachusetts Institute of Technology, 2010.

[54] T. Makino, M. Edamura, A. Kato, and A. Yoshida, "Thermal radiation properties of molten salt (properties of alkali metal carbonates)," *Heat Transfer - Japanese Research*, vol. 21, no. 4, pp. 331-339, 1992.

[55] T. Makino, T. Maeda, T. Yasuo, and A. Yoshida, "Thermal radiation properties of molten salts (properties of alkali metal chlorides and conductive-radiative transfer in the salts)," *Heat Transfer - Japanese Research*, vol. 20, no. 7, pp. 711-721, 1991.

[56] T. Makino, T. Maeda, M. Edamura, and A. Yoshida, "Thermal radiation properties of molten salts (properties of alkali metal nitrates)," *Heat Transfer - Japanese Research*, vol. 20, no. 7, pp. 700-710, 1991.

[57] A. Lazaridis, R. J. Copeland, and J. Althof, "Temperature distribution in a solar irradiated liquid film flowing over a solid wall," *Solar Energy*, vol. 36, no. 6, pp. 565-72, 1986.

[58] H. Bloom and D. C. Rhodes, "Molten Salt Mixtures. Part 2. The Refractive Index Of Molten Nitrate Mixtures And Their Molar Refractivities," *The Journal of Physical Chemistry*, vol. 60, no. 6, p. 791–793, 1956.

[59] G. J. Janz, *Molten Salts Handbook*. New York: Academic Press, 1967.

[60] S. Kumar and C. L. Tien, "Analysis of combined radiation and convection in a particulate-laden liquid film," *Journal of solar energy engineering*, vol. 112, p. 293, 1990.

[61] F. M. White, *Fluid Mechanics*, 3rd ed. New York: McGraw-Hill, 1994.

[62] G. Chen, *Nanoscale energy transport and conversion: a parallel treatment of electrons, molecules, phonons, and photons*. Oxford University Press, USA, 2005.

[63] J. C. Nave, "Direct Numerical Simulation of Liquid Films," Ph.D. thesis, University of California, Santa Barbara, 2004.

[64] A. Lenert, "Nanofluid-based Receivers for High-Temperature,High-flux Direct Solar Collectors," SM thesis, Massachusetts Institute of Technology, 2010.

[65] H. Tyagi, P. Phelan, and R. Prasher, "Predicted Efficiency of a Low-Temperature Nanofluid-Based Direct Absorption Solar Collector," *Journal of Solar Energy Engineering*, vol. 131, p. 041004, 2009.

[66] T. P. Otanicar, P. E. Phelan, R. S. Prasher, G. Rosengarten, and R. A. Taylor, "Nanofluid-based direct absorption solar collector," *Journal of Renewable and Sustainable Energy*, vol. 2, p. 033102, 2010.

[67] A. H. Slocum et al., "Concentrated Solar Power on Demand," *Solar Energy*, in press, 2011.

[68] I. M. Bassett and G. H. Derrick, "An upper bound on the efficiency of a cavity absorber," *Optica Acta*, vol. 28, no. 1, pp. 57-63, Jan. 1981.

[69] G. H. Derrick and I. M. Bassett, "Optimization of imperfect diffuse reflectors," *Optica Acta*, vol. 32, no. 3, pp. 313-28, Mar. 1985.

[70] J. Hovis, "Infrared Spectral Reflectance of Some Common Minerals," *Applied Optics*, vol. 5, no. 2, pp. 245-248, Feb. 1966.

[71] ASM, *ASM Handbook: vol. 4: Heat Treating*, 10th ed., vol. 4. ASM International, 1991.

[72] Y. L. Chan and C. L. Tien, "A numerical study of two-dimensional natural convection in square open cavities," *Numerical heat transfer*, vol. 8, no. 1, p. 65–80, 1985.

[73] N. Sendhil Kumar and K. S. Reddy, "Numerical investigation of natural convection heat loss in modified cavity receiver for fuzzy focal solar dish concentrator," *Solar energy*, vol. 81, no. 7, p. 846–855, 2007.

[74] U. Leibfried and J. Ortjohann, "Convective heat loss from upward and downward-facing cavity solar receivers: measurements and calculations," *Journal of solar energy engineering*, vol. 117, p. 75, 1995.

[75] T. Taumoefolau, S. Paitoonsurikarn, G. Hughes, and K. Lovegrove, "Experimental investigation of natural convection heat loss from a model solar concentrator cavity receiver," *Journal of solar energy engineering*, vol. 126, p. 801, 2004.

[76] S. Y. Wu, L. Xiao, Y. R. Li, and Y. Cao, "Convection heat loss from cavity receiver in parabolic dish solar thermal power system: A review," *Solar Energy*, vol. 84, no. 8, 2010.

[77] A. Ghobeity, C. J. Noone, Papanicolas, C.N., and A. Mitsos, "Optimal Time-Invariant Operation of a Power and Water Cogeneration Solar-Thermal Plant," *Solar Energy*, submitted for publication, 2010.

[78] A. Ghobeity and A. Mitsos, "Optimal Use of Solar Thermal Energy for Combined Power Generation and Water Desalination," in *Proceedings of Distributed Renewable Energy Sources in the Mediterranean Region (DISTRES 2009)*, Nicosia, CY, 2009.

[79] M. F. A. Goosen, S. S. Sablani, S. S. Al-Maskari, R. H. Al-Belushi, and M. Wilf, "Effect of feed temperature on permeate flux and mass transfer coefficient in spiral-wound reverse osmosis systems* 1," *Desalination*, vol. 144, no. 1-3, p. 367–372, 2002.

[80] L. G. Semenyuk, "Exergy loss on mixing working bodies with different temperatures," *Journal of Engineering Physics*, vol. 44, no. 6, pp. 617-19, Jun. 1983.

[81] L. Pera and B. Gebhart, "Laminar plume interactions," *Journal of Fluid Mechanics*, vol. 68, no. 2, p. 259–271, 1975.

[82] M. M. Scase, C. P. Caulfield, S. B. Dalziel, and J. C. R. Hunt, "Time-dependent plumes and jets with decreasing source strengths," *Journal of Fluid Mechanics*, vol. 563, no. 1, p. 443–461, 2006.

[83] J. Zinoubi, A. Gammoudi, T. Naffouti, R. B. Maad, and A. Belghith, "Development of an Axisymmetric Thermal Plume between Vertical Plates," *American Journal of Applied Sciences*, vol. 4, no. 9, p. 679–685, 2007.

[84] J. Lata and J. Blanco, "Single tank thermal storage design for solar thermal power plants," in *16th SolarPACES Conference, Sept. 21-24, 2010*, Perpignan, France, 2010.

[85] C. W. Forsberg, C. Renault, B. Le, E. Merle-Lucotte, and V. Ignatiev, "Les applications des sels liquides et les réacteurs à sels fondus= Liquid salt applications and molten salt reactors," *Revue générale nucléaire*, no. 4, p. 63–71, 2007.

[86] A. G. Grindell, W. F. Boudreau, and H. W. Savage, "Development of Centrifugal Pumps for Operation with Liquid Metals and Molten Salts at 1100-1500 F," *Nuclear Sci. and Eng.*, vol. 7, 1960.

[87] D. F. Williams, "Assessment of Candidate Molten Salt Coolants for the NGNP/NHI Heat-Transfer Loop," *ORNL/TM-2006/69, Oak Ridge National Laboratory, Oak Ridge, Tennessee*, 2006.

[88] D. L. Barth, J. E. Pacheco, W. J. Kolb, and E. E. Rush, "Development of a high-temperature, long-shafted, molten-salt pump for power tower applications," in *2001 International Solar Energy Conference, a Part of Forum 2001, Solar Energy: The Power to Choose, April 21, 2001 - April 25, 2001*, Washington, DC, United states, 2001, pp. 381-386.

[89] C. C. Bland, "Method and apparatus for production of glass beads by dispersion of molten glass," U.S. Patent 3,243,2731966.

[90] J. C. Stultz, J. Capellman, and L. Knavish, "CONTINUOUSLY SKIMMING VISCOUS GLASS," U.S. Patent 3,771,9861973.

[91] C. W. Forsberg and D. L. Moses, *Safeguards Challenges for Pebble-Bed Reactors (PBRs): Peoples Republic of China (PRC)*. Oak Ridge National Laboratory (ORNL), 2009.

[92] G. J. Janz, C. B. Allen, N. P. Bansal, R. M. Murphy, and R. P. T. Tomkins, *Physical properties data compilations relevant to energy storage. II. Molten salts: Data on single and multi-component salt systems*. USA: Nat. Bur. Stand., Washington, DC, USA, 1979, p. 432.

[93] Q. D. Mehrkam, "An Introduction to Salt Bath Heat Treating," *Tooling & Production*, vol. 1967, no. June/July, 1967.

[94] Pont de Nemours & Company E.I., *Molten Salt Baths for Heat Treatment and Case Hardening of Steel*. [Wilmington: s.n, 1951.

[95] C. S. Byung, D. K. Sang, and W.-H. Park, "Heat transfer in a latent heat storage of ternary carbonate eutectic," in *26th National Heat Transfer Conference, August 6, 1989 - August 9, 1989*, Philadelphia, PA, USA, 1989, vol. 85, pp. 178-183.

[96] S. H. White and U. M. Twardoch, "The behavior of water in molten salts," *Journal of the Electrochemical Society*, vol. 134, p. 1080, 1987.

[97] D. A. Nissen and D. E. Meeker, "Nitrate/nitrite chemistry in sodium nitrate-potassium nitrate melts," *Inorganic Chemistry*, vol. 22, no. 5, p. 716–721, 1983.

[98] R. W. Bradshaw and N. P. Siegel, "Molten nitrate salt development for thermal energy storage in parabolic trough solar power systems," in *ES2008: Proceedings of the 2nd International Conference On Energy Sustainability*, 2009, vol. 2, p. 631–637.

[99] S. H. White and U. M. Twardoch, *A study of the interactions of molten sodium nitrate-potassium nitrate 50 mol% mixture with water vapor and carbon dioxide in air.* Sandia National Labs., Livermore, CA (USA); EIC Labs., Inc., Newton, MA (USA), 1981.

[100] R. W. Bradshaw and D. A. Brosseau, "Low-melting point inorganic nitrate salt heat transfer fluid," U.S. Patent 7,588,6942009.

[101] S. G. Lipsett, "Explosions from molten materials and water," *Fire Technology*, vol. 2, no. 2, pp. 118-126, 1966.

[102] Anon, "Potential hazards in molten salt baths for heat treatment," *Metal Progress*, vol. 51, no. 2, pp. 251-253, 1947.

[103] J. Li and P. K. Dasgupta, "A simple instrument for ultraviolet-visible absorption spectrophotometry in high temperature molten salt media," *Review of Scientific Instruments*, vol. 71, p. 2283, 2000.

[104] A. T. Paxson, "Design and Validation of an Air Window for a Molten Salt Solar Thermal Receiver," SB thesis, Massachusetts Institute of Technology, 2009.

[105] G. J. Kolb, "Thermal cycling of thermal energy storage tanks proposed for the solar two central receiver power plant," in *ASME International Solar Energy Conference, April 4, 1993 - April 9, 1993*, Washington, DC, USA, 1993, pp. 397-405.

[106] R. Gabbrielli and C. Zamparelli, "Optimal Design of a Molten Salt Thermal Storage Tank for Parabolic Trough Solar Power Plants," *Journal of Solar Energy Engineering*, vol. 131, no. 4, p. 041001, 2009.

[107] P. Sabharwall et al., *Molten Salts for High Temperature Reactors: University of Wisconsin Molten Salt Corrosion and Flow Loop Experiments–Issues Identified and Path Forward*. Idaho National Laboratory: , 2010.

[108] S. H. Goods and R. W. Bradshaw, "Corrosion of stainless steels and carbon steel by molten mixtures of commercial nitrate salts," *Journal of materials engineering and performance*, vol. 13, no. 1, p. 78–87, 2004.

[109] S. H. Goods, R. W. Bradshaw, M. R. Prairie, and J. M. Chavez, *Corrosion of stainless and carbon steels in molten mixtures of industrial nitrates*. Sandia National Labs., Livermore, CA (United States), 1994.

[110] U. Herrmann, B. Kelly, and H. Price, "Two-tank molten salt storage for parabolic trough solar power plants," *Energy*, vol. 29, no. 5-6, p. 883–893, 2004.

[111] F. Cardarelli, *Materials handbook*. Springer London etc., 2000.

[112] A. U. Seybolt, "Internal oxidation in heat-resisting stainless steels caused by presence of halides," *Oxidation of Metals*, vol. 2, no. 2, p. 161–171, 1970.

[113] "RA 253 MA Plate, Sheet, Bar, Pipe and Welding Products - Rolled Alloys." [Online]. Available: http://www.rolledalloys.com/productline/alloyspecs.aspx?alloy=ra253. [Accessed: 23-Mar-2011].

[114] M. P. Short, S. Morton, S. E. Ferry, and R. G. Ballinger, "Diffusional stability of ferritic-martensitic steel composite for service in advanced lead-bismuth cooled nuclear reactors," *International Heat Treatment and Surface Engineering*, vol. 4, no. 2, pp. 74-80, 2010.

[115] E. Hecht, *Optics*, 4th ed. Reading, Mass: Addison-Wesley, 2002.

[116] V. I. Haltrin, W. E. McBride III, and R. A. Arnone, "Spectral approach to calculate specular reflection of light from wavy water surface," 2001.

[117] R. Siegel, *Thermal Radiation Heat Transfer*, 4th ed. New York: Taylor & Francis, 2002.

[118] S. W. Gouse, J. J. Prifti, and J. Brown, *THERMAL RADIATION SHIELDING FOR HIGH TEMPERATURES*. 1969.

[119] G. Maag, C. Falter, and A. Steinfeld, "Temperature of a quartz/sapphire window in a solar cavity-receiver," *Journal of Solar Energy Engineering*, vol. 133, p. 014501, 2011.

[120] M. N. Özışık, *Heat Transfer: A Basic Approach*. New York: McGraw-Hill, 1985.

[121] T. Bauer, R. Tamme, M. Christ, and O. Öttinger, "PCM-graphite composites for high temperature thermal energy storage," in *Proc. of ECOSTOCK, 10th International Conference on Thermal Energy Storage, Stockton, USA*, 2006.

[122] H. G. Landau, "Heat conduction in a melting solid," *Quarterly of Applied Mathematics*, vol. 8, pp. 81-94, Apr. 1950.

[123] R. M. DiGuilio and A. S. Teja, "A rough hard-sphere model for the thermal conductivity of molten salts," *International journal of thermophysics*, vol. 13, no. 5, p. 855–871, 1992.

[124] R. L. Baker, "A steady-state melt layer model with absorption, conduction, and surface vaporization," *Letters in Heat and Mass Transfer*, vol. 9, no. 4, p. 299–308, 1982.

[125] C. C. Tseng and R. Viskanta, "Melting of a semitransparent bed of particles by convection and radiation," *Journal of the American Ceramic Society*, vol. 89, no. 8, pp. 2547-54, 2006.

[126] S. H. Chan, D. H. Cho, and G. Kocamustafaogullari, "Melting and solidification with internal radiative transfer–A generalized phase change model," *International Journal of Heat and Mass Transfer*, vol. 26, no. 4, p. 621–633, 1983.

[127] J. F. Ready and D. F. Farson, *LIA handbook of laser materials processing*. Laser Institute of America, 2001.

[128] W. S. Kim and B. C. Sim, "Study of thermal behavior and fluid flow during laser surface heating of alloys," *Numerical heat transfer. Part A, Applications*, vol. 31, no. 7, p. 703–723, 1997.

[129] S. Kou and Y. H. Wang, "Three-dimensional convection in laser melted pools," *Metallurgical Transactions A*, vol. 17, no. 12, pp. 2265-2270, Dec. 1986.

[130] B. W. Schumacher, "Quasi-adiabatic melting and vaporization due to a radiation beam of high power density," *Optik*, vol. 39, no. 5, pp. 558-80, 1974.

[131] F. Dabby and U. C. Paek, "High-intensity laser-induced vaporization and explosion of solid material," *Quantum Electronics, IEEE Journal of*, vol. 8, no. 2, p. 106–111, 1972.

[132] D. S. Codd, A. Carlson, J. Rees, and A. H. Slocum, "A low cost high flux solar simulator," *Solar Energy*, vol. 84, no. 12, pp. 2202-2212, Dec. 2010.

[133] J. Burch, G. Shoukas, M. Brandemuhl, and M. Krarti, *Test-and-Rate Methods for Thermosiphon Solar Water Heaters*. National Renewable Energy Laboratory (NREL), Golden, CO., 2007.

[134] J. Lu, J. Ding, and J. Yang, "Solidification and melting behaviors and characteristics of molten salt in cold filling pipe," *International Journal of Heat and Mass Transfer*, vol. 53, no. 9-10, p. 1628–1635, 2010.

[135] Folkers Rojas, "Heat Extraction for the CSPonD Thermal Storage Unit," SM thesis, Massachusetts Institute of Technology, 2011.

[136] S. A. Jones and K. W. Stone, *Analysis of Solar Two Heliostat Tracking Error Sources*. Sandia National Laboratories, Albuquerque, NM, and Livermore, CA, 1999.

[137] J. A. Duffie, *Solar Engineering of Thermal Processes*, 3rd ed. Hoboken, N.J: Wiley, 2006.

[138] R. B. Briggs, *Molten Salt Reactor Program Semiannual Progress Report for Period Ending July 31, 1964*. Oak Ridge National Laboratory: , 1964.

[139] "Crossroads Solar Energy Project HOME." [Online]. Available: http://crossroadssolar.com/index.html. [Accessed: 11-Apr-2011].

[140] S. Schell, "Design and evaluation of esolar's heliostat fields," *Solar Energy*, vol. 85, no. 4, pp. 614-619, Apr. 2011.

[141] "eSolar: Our Solution." [Online]. Available: http://www.esolar.com/our_solution/. [Accessed: 11-Apr-2011].

[142] "NREL: Concentrating Solar Power Projects - Crescent Dunes Solar Energy Project." [Online]. Available: http://www.nrel.gov/csp/solarpaces/project_detail.cfm/projectID=60. [Accessed: 17-Apr-2011].

[143] "Tonopah Solar Energy - HOME." [Online]. Available: http://www.tonopahsolar.com/index.html. [Accessed: 17-Apr-2011].

[144] "NREL: Concentrating Solar Power Projects - Ivanpah Solar Electric Generating Station." [Online]. Available: http://www.nrel.gov/csp/solarpaces/project_detail.cfm/projectID=62. [Accessed: 17-Apr-2011].

[145] D. Hirsch, P. v Zedtwitz, T. Osinga, J. Kinamore, and A. Steinfeld, "A new 75 kW high-flux solar simulator for high-temperature thermal and thermochemical research," *Transactions of the ASME. Journal of Solar Energy Engineering*, vol. 125, no. 1, pp. 117-20, Feb. 2003.

[146] D. A. Jaworske, K. S. Jefferies, and L. S. Mason, "Alignment and initial operation of an advanced solar simulator," *Journal of Spacecraft and Rockets*, vol. 33, no. 6, pp. 867-869, 1996.

[147] P. Kuhn and A. Hunt, "A new solar simulator to study high temperature solid-state reactions with highly concentrated radiation," in *5th Symposium on Solar High-Temperature Technologies, 27-31 Aug. 1990*, Netherlands, 1991, vol. 24, pp. 742-50.

[148] J. Petrasch et al., "A novel 50 kW 11,000 suns high-flux solar simulator based on an array of xenon arc lamps," *Transactions of the ASME. Journal of Solar Energy Engineering*, vol. 129, no. 4, pp. 405-11, Nov. 2007.

[149] J. Benya, L. Heschong, T. McGowan, N. Miller, and F. Rubinstein, *Advanced Lighting Guidelines*. New Buildings Institute, Inc, White Salmon, WA: , 2003.

[150] Hubble Lighting, *Photometric Report, 7-20-2004, CAT NO.:, TEST NUMBERS: HP-09844 (SLS-1500Hx-x3x), HP-09820 (SLS-1500Hx-x5x)*. Hubbel Lighting, Inc., Christiansburg, Virginia: , 2004.

[151] T. J. Love, *Radiative Heat Transfer*. Columbus, Ohio: C. E. Merrill Pub. Co, 1968.

List of Publications Related to this Thesis

Listed in alphabetical order by first author:

A. A. Adames, "Design Considerations of a 15kW Heat Exchanger for the CSPonD Project," SB thesis, Massachusetts Institute of Technology, 2010.

J. F. Alvarado, "Validation of a Numerical Model for the Analysis of Thermal-Fluid Behavior ina Solar Concentrator Vessel," SB thesis, Massachusetts Institute of Technology, 2010.

D. S. Codd, A. Carlson, J. Rees, and A. H. Slocum, "A low cost high flux solar simulator," *Solar Energy*, vol. 84, pp. 2202-2212, 2010.

D. S. Codd and A. H. Slocum, "Direct Absorption Volumetric Molten Salt Receiver with Integral Storage," in *ASME 5th International Conference on Energy Sustainability, ESFuelCell2011, August 7-10, 2011*, Washington, DC, United states, accepted for publication.

A. Ghobeity and A. Mitsos, "Optimal Use of Solar Thermal Energy for Combined Power Generation and Water Desalination," in *Proceedings of Distributed Renewable Energy Sources in the Mediterranean Region (DISTRES 2009)*, Nicosia, CY, 2009.

A. Ghobeity, C. J. Noone, C. N. Papanicolas, and A. Mitsos, "Optimal Time-Invariant Operation of a Power and Water Cogeneration Solar-Thermal Plant," *Solar Energy*, submitted for publication, 2011.

C. J. Noone, A. Ghobeity, A. H. Slocum, G. Tzamtzis, and A. Mitsos, "Site selection for hillside central receiver solar thermal plants," *Solar Energy*, vol. 85, pp. 839-848, 2011.

S. Passerini, "Optical and Chemical Properties of Molten Salt Mixtures for Use in High Temperature Power Systems," SM thesis, Massachusetts Institute of Technology, 2010.

A. T. Paxson, "Design and Validation of an Air Window for a Molten Salt Solar Thermal Receiver," SB thesis, Massachusetts Institute of Technology, 2009.

J. Rees, "Thermal Modeling of a Divided-Thermocline Molten Salt Volumetric Receiver," SB thesis, Massachusetts Institute of Technology, 2011.

F. Rojas, "Heat Extraction for the CSPonD Thermal Storage Unit," SM thesis, Massachusetts Institute of Technology, 2011.

A. H. Slocum, J. Buongiorno, C. W. Forsberg, D. S. Codd, and A. T. Paxson, "Concentrated Solar Power System, PCT Patent Application PCT/US10/49474," 2010.

A. H. Slocum and D. S. Codd, "Solar energy concentrator system with energy storage, US Patent Application 61/243763," 2010.

A. H. Slocum, D. S. Codd, J. Buongiorno, C. Forsberg, T. McKrell, J. C. Nave, C. N. Papanicolas, A. Ghobeity, C. J. Noone, S. Passerini, F. Rojas, and A. Mitsos, "Concentrated Solar Power on Demand," *Solar Energy*, in press, 2011.